Gravitational Signatures of Wave Dark Matter

Dissertation zur Erlangung des Doktorgrades an der Fakultät für Mathematik, Informatik und Naturwissenschaften Fachbereich Physik der Universität Hamburg

vorgelegt von

Alessandro Lenoci

Hamburg

2023

Gutachter/innen der Dissertation:	Prof. Dr. Géraldine Servant Dr. Hyungjin Kim
Zusammensetzung der Prüfungskommission:	Prof. Dr. Géraldine Servant Dr. Hyungjin Kim Prof. Dr. Dieter Horns Dr. Thomas Konstandin Prof. Dr. Marcus Brüggen
Vorsitzende/r der Prüfungskommission:	Prof. Dr. Dieter Horns
Datum der Disputation:	07.07.2023
Vorsitzender Fach-Promotionsausschuss PHYSIK:	Prof. Dr. Günter H. W. Sigl
Leiter des Fachbereichs PHYSIK:	Prof. Dr. Wolfgang J. Parak
Dekan der Fakultät MIN:	Prof. Dr.-Ing. Norbert Ritter

Declaration on oath

I hereby declare in lieu of oath that I have written this dissertation myself and that I have not used any auxiliary materials or sources other than those indicated.

Hamburg: 11.07.2023

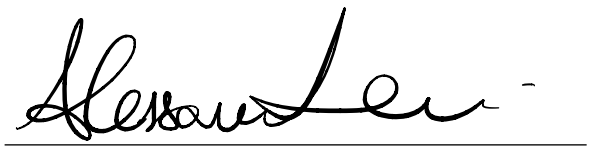

Signature of the doctoral student

"You're entitled to say: if you're so smart, why don't you tell me what that dark matter is? – And I'll have to confess I don't know. "

Jim Peebles

Abstract

This thesis explores wave dark matter and its intriguing phenomenological implications, namely the presence of wave-like signatures on astrophysical length scales. Specifically, we assume the dark matter is composed of light bosons with masses below 10 eV, allowing, due to the high phase space occupation number, for a classical wave description. We develop a formalism to describe the wave dark matter's response to gravity, accounting for the statistical properties of the field.

Our first subject of investigation is the behavior of the wave dark matter in the Solar system. Here we study the phenomenon of gravitational focusing, where a massive astrophysical object deforms the local distribution of dark matter, leading to a local overdensity. We calculate the response of observationally-motivated dark matter substructures to the Sun's potential and find unique signatures in the local overdensity and dark matter spectrum that can be relevant for direct detection experiments.

The second topic of discussion is the behavior of wave dark matter in a small dark matter halo. In particular, we investigate the wave dark matter response to the adiabatic growth of a black hole in the center of the halo. This phenomenon leads to a compression of the surrounding dark matter halo, resulting in a steeper density profile. We find significant wave features in the density profile of the compressed halo's inner region, where the semiclassical approximation breaks down.

As an application, we investigate the gravitational waves produced by the inspiral of a compact solar-mass object with a central intermediate-mass black hole within the compressed wave dark matter halo. Due to the enhanced mass density, the compressed halo exerts dynamical friction on the orbiting object which is stronger than in the uncompressed case, leading to a characteristic dephasing of the gravitational waves. This quantity being sensitive to the underlying dark matter model, we discuss concrete scenarios where the wave dark matter halo can be reconstructed from gravitational wave observations.

Zusammenfassung

Diese Dissertation untersucht wellenartige Dunkle Materie und ihre faszinierenden phänomenologischen Auswirkungen, insbesondere das Vorhandensein von wellenartigen Signaturen auf astrophysikalischen Längenskalen. Wir nehmen an, dass die Dunkle Materie aus leichten Bosonen mit Massen unter zehn Elektronenvolt besteht und aufgrund der hohen Besetzungszahl des Phasenraums eine klassische Wellenbeschreibung ermöglicht. Wir entwickeln einen Formalismus, mit dem wir die Reaktion der wellenartigen Dunklen Materie auf Gravitation beschreiben, und berücksichtigen dabei die statistischen Eigenschaften des Feldes.

Unser erster Untersuchungsgegenstand ist das Verhalten der wellenartigen Dunklen Materie im Sonnensystem. Hier untersuchen wir das Phänomen der gravitativen Fokussierung, bei dem ein massives astrophysikalisches Objekt die lokale Verteilung der Dunklen Materie verformt, welches zu einer lokalen Überdichte führt. Wir berechnen die Reaktion von Substrukturen der Dunklen Materie, welche durch Beobachtungen motiviert sind, auf das Potential der Sonne und finden eindeutige Signaturen in der lokalen Überdichte und im Spektrum der Dunklen Materie, die experimentell relevant sein können.

Das zweite Thema ist das Verhalten der wellenartigen Dunklen Materie in einem kleinen Halo Dunkler Materie. Insbesondere untersuchen wir die Reaktion der wellenartigen Dunklen Materie auf das adiabatische Wachstum eines Schwarzen Lochs im Zentrum des Halos. Dieses Phänomen führt zu einer Kompression des umgebenden Halo der Dunklen Materie, was in einem steileren Dichteprofil resultiert. Wir finden signifikante Merkmale der Wellennatur der Dunklen Materie im Dichteprofil der komprimierten, zentralen Region des Halos, in welcher die halbklassische Näherung nicht mehr gilt.

Als Anwendung untersuchen wir die Gravitationswellen, die emittiert werden, wenn ein Objekts mit Sonnenmasse ein zentrales schwarzen Loch mittlerer Masse innerhalb des komprimierten Halos der wellenartigen Dunklen Materie umkreist. Aufgrund der erhöhten Massendichte übt der komprimierte Halo eine dynamische Reibung auf das umlaufende Objekt aus, die stärker als im unkomprimierten Fall ist und zu einer charakteristischen Phasenverschiebung der Gravitationswellen führt. Diese Größe ist empfindlich gegenüber dem zugrunde liegenden Modell der dunklen Materie, daher untersuchen wir konkrete Szenarien, in denen der Halo der wellenartigen Dunklen Materie aus Gravitationswellenbeobachtungen rekonstruiert werden kann.

Acknowledgements

This thesis represents the culmination of the research work conducted during my doctoral studies in the Theory Cosmology group at DESY Hamburg, spanning the period from fall 2020 to spring 2023. As this has been a long and rewarding journey, I would like to thank the people who have supported me along the way and made this work possible.

First and foremost, I would like to thank my doctoral advisors, Géraldine Servant and Hyungjin Kim. I am deeply grateful to Géraldine Servant for her unwavering support, guidance, career advice and the opportunities she has provided me since the beginning of my doctoral studies.

It has been a privilege and a great learning experience to work under the supervision of Hyungjin Kim, whose passion, dedication, and curiosity have inspired many interesting discussions that have contributed to the development of this work. He has been an important source of motivation and has taught me to approach complex problems with diligence, tenacity, and method. I look forward to collaborating with him again in the future.

Next, I want to thank the people I have met here at DESY, and the reasons are countless, so I will just name a few for each person. My first thought goes to my 1a-O1.141 office mates during these years. I thank Yann Gouttenoire for his advice and the beautiful discussion during my visit at DESY in February 2020 and during the last days of his Ph.D. Thanks to Philip Sørensen for his enthusiasm that made my working days better, to Isak Stomberg for the interesting discussions throughout our collaboration and to Margherita Putti for her positive Italian energy she brought into our office.

I would also like to thank Thomas Konstandin for accepting to be my DESY mentor, for his insightful discussions, and for serving on my examination committee.

I would like to express my deepest appreciation to Aleksandr Chatrchyan, who has been more than just a colleague to me during my time at DESY. His unwavering support, encouragement, empathy, and friendship have been invaluable to me, especially during the process of writing this thesis. Merci, Sasha.

I would also like to extend my special thanks to Julián Rey for his advice and inspirational chats during my final year of Ph.D. I have to acknowledge the contributions of Matthias "Koschi" Koschnitzke and Peera Simakachorn. Koschi helped me with the writing of the Zusammenfassung of this thesis, and Peera provided valuable advice and assistance with the bureaucracy related to the thesis submission. Both Koschi and Peera have my gratitude for their precious work as cookie masters.

Last but not least, I would like to thank all the other people I have met in the DESY "cosmorridor" who have contributed to making it a pleasant environment. In order of (past or present) physical position in the corridor, I thank: Felix Giese, Henrique Rubira, Baptiste Filoche, Miguel Vanvlasselaer, Henda Mansour, Sonali Verma, Alice Albouy, Cem Eroncel, Andreas Ekstedt, Pablo Quílez, Felix Kling, Andrea Mitridate, Jacob Leedom, Inna Henning, Xiao Xue, Hyeonseok Seong, Ryusuke Jinno, Jorinde Van de Vis, Yohei Ema, Bibhushan Shakya.

Desidero esprimere la mia riconoscenza alle persone care che mi hanno sostenuto durante il mio dottorato ad Amburgo, nonostante la distanza fisica.

Innanzitutto, ringrazio Annachiara Picco per il suo immancabile supporto, la fiducia e i preziosi consigli nel corso di questi anni. Sono molto riconoscente anche a Omar Pagliarini, Paola Bogarelli, Barbara Gallazzi e Diana Istratii per la loro amicizia, il sostegno nelle scelte più ardue e le chiacchierate.

Non posso dimenticare di ringraziare i miei amici e compagni di università e il gruppo Persone. In particolare, ringrazio Nicola Barbieri per le discussioni patologiche e i consigli su LaTeX, Guglielmo Frittoli per la sua ospitalità durante la mia trasferta a Padova, Matteo Zatti per essere un esempio da seguire, Giovanni Ferrari per l'interesse quotidiano verso il nostro stato psicofisico, Umberto Maria Tomasini per la simpatia e l'energia che lo contraddistinguono. Un ringraziamento speciale va a Enrico Marchetto e Andrea Boido per l'aiuto nei momenti difficili e per tutti i bellissimi momenti trascorsi insieme.

Ringrazio di cuore Anna Vislapu per essere una continua fonte di ispirazione e per l'affetto e l'energia che mi trasmette ogni giorno.

Infine, vorrei ringraziare i miei genitori Maria Luisa Damiano e Sabino Lenoci per avermi sempre sostenuto e incoraggiato in tutte le mie scelte, e per la pazienza nell'aiutarmi a superare le difficoltà quotidiane.

Contents

List of Figures

List of Tables

List of Abbreviations

DM	**D**ark **M**atter
dB	**d**e **B**roglie
SM	**S**tandard **M**odel
GR	**G**eneral **R**elativity
WIMP	**W**eakly **I**nteracting **M**assive **P**article
ΛCDM	**C**old **D**ark **M**atter
GF	**G**ravitational **F**ocusing
IMRI	**I**ntermediate-**M**ass-**R**atio **I**nspiral
MB	**M**axwell-**B**oltzmann
GRC	**G**alactic **R**otation **C**urve
GW	**G**ravitational **W**aves
CMB	**C**osmic **M**icrowave **B**ackground
NFW	**N**avarro **F**renk **W**hite
SHM	**S**tandard **H**alo **M**odel
SP	**S**chrödinger-**P**oisson
QCD	**Q**uantum **C**hromodynamics **D**ynamics
PQ	**P**eccei-**Q**uinn
pNG	**p**seudo-**N**ambu-**G**oldstone
EDM	**E**lectric **D**ipole **M**oment
ALP	**A**xion-**L**ike-**P**article
FRW	**F**riedmann-**R**obertson-**W**alker
BBN	**B**ig-**B**ang **N**ucleosynthesis
BH	**B**lack **H**oles
IMBH	**I**ntermediate **M**ass **B**lack **H**oles
SMBH	**S**uper**M**assive **B**lack **H**oles
DF	**D**ynamical **F**riction
SNR	**S**ignal-to-**N**oise **R**atio

Introduction

Over the course of almost a century, the evidence for the existence of dark matter (DM) has continued to grow. This evidence is supported by observations at various astronomical scales, ranging from galaxy-sized systems [1–3] to cluster [4–8] and cosmological scales [9,10]. Alternative theories to dark matter, such as modified gravity theories [11,12], have been proposed and studied, but they fail to explain all astronomical observations without invoking dark matter [13,14].

It is worth noting that all of the evidence for dark matter comes from its gravitational interaction with ordinary matter, and as of now, it has not provided any insight into the possible interactions of dark matter with the Standard Model (SM) of particle physics. Additionally, since gravity is described by the theory of General Relativity (GR), we only possess information about the stress-energy tensor of dark matter at various times and scales throughout the history of the Universe. On the appropriate scales, the stress-energy tensor is typically represented through the perfect fluid assumption and expressed statistically through the phase-space distribution in the Boltzmann equation formalism. This provides information about the abundance and spectrum of dark matter, which is characterized as cold and collisionless on cosmological scales.

The search for dark matter is a daunting task due to the lack of information on non-gravitational interactions. As a result, the mass of potential candidates remains elusive. The viable parameter space is staggering, spanning 90 orders of magnitude, from ultra-light bosons with a mass of $m \sim 10^{-22}$ eV to solar mass-sized objects with $m \sim 10\ M_{\odot} \sim 10^{67}$ eV, depending on the assumptions of the fundamental nature of DM. This leads to an enormous diversity of dark matter models and production mechanisms, making the search even more challenging. Among these, a particular class of DM candidates, namely weakly interacting massive particles (WIMPs), has given particular attention in the last decades due to its predictive power and theoretical motivations. However, it has escaped intense scrutiny of terrestrial DM searches [15] as well as cosmological and astrophysical probes, signaling, perhaps, that either the couplings to SM or the mass of DM are not of the WIMP type. Nonetheless, the lack of positive results has motivated the exploration of novel ideas regarding the interplay of dark matter with the SM and its production mechanisms.

Given the challenges of dark matter detection, especially when taking into account the wide range of models and production mechanisms that exist, it is crucial to find ways to optimize the experimental search for dark matter. This is where precise astronomical observations come into play, as they have the unique advantage of probing a variety of scales and therefore, exploring larger areas in the parameter space. By taking advantage of these observations, we can gain a better understanding of the nature of dark matter and potentially detect it.

Wave dark matter

One of the most general constraints on the dark matter mass comes indeed from astronomical observations. The very existence of small dwarf galaxies implies that fermionic dark matter cannot be lighter than roughly 100 eV – 1 keV due to the Pauli exclusion principle: this is the Tremaine-Gunn bound [16–20]. This however does not exclude that dark matter can be made of light particles.

Indeed bosons lighter than roughly 10 eV are compelling alternative dark matter candidates. This mass scale appears to be a demarcation point in the vast available mass spectrum of the DM mass [21]. This has to do with the wavelength associated to a non-relativistic particle, the de Broglie wavelength $\lambda_{\rm dB} \sim (mv)^{-1}$, which is inversely proportional to the particle mass. We know that the density of dark matter in typical galactic environment is of order of $\rho \sim \text{GeV/cm}^3$ so we can compute the particle mass for which there is a virialized dark particle per de Broglie volume $\lambda_{\rm dB}^3$ and it turns out to be around 10 eV. For lighter masses, the occupation number in a de Broglie volume then increases quickly as m^{-4}. The huge occupation number motivates a treatment of these candidates as *classical* waves, analogously to how we describe photons in classical electrodynamics. Hence the collective name of *wave* dark matter as opposed to *particle* dark matter, for any heavier candidate. Here the word *classical* means that we can neglect quantum fluctuations in view of the large occupation number.

Particular interest has been raised by ultra-light dark matter candidates with mass around $10^{-22} - 10^{-21}$ eV [22–29], which show a fuzzy behavior [25] at galactic (kpc) scales, due to the astronomically-sized de Broglie wavelength. This fuzziness has been advocated as a possible solution of the small-scales shortcomings of the ΛCDM cosmological model [30]. Even though these small scale structure issues might be resolved by purely baryonic physics [31, 32], the possibility of such a light dark matter candidate is intriguing and phenomenologically interesting: astrophysical observations are able to constrain fuzzy dark matter putting lower bounds on the mass of these light bosons [33].

However, it would be very limiting to restrict the search for wave dark matter only to the light end of the mass spectrum. The wave nature of dark matter can manifest itself at various scales, depending on the mass and the velocity of the dark matter. While the mass is fixed, but unknown to us, the velocity depends on the system under consideration. For instances, just focusing on our surroundings, in the Sun's rest frame the speed of virialized dark matter component of our galactic halo is about 200 km/sec, but other dark matter components can have a very different speed, depending on their origin, or direction relative to the motion of the Sun around the center of the Milky Way. Therefore, for a chosen value of the mass, different dark matter components can exhibit wave features at substantially different scales. Also, the dark matter velocity dispersion can play an important role in erasing or smoothing out interference effects. The dependence of observable quantities on these effects can allow us to get some information on the wave nature of the dark matter, that, if detected, can give a strong hint on the value of the mass, with crucial implications for both theories beyond standard model and for experiments. For this reason, the wave dark matter hypothesis is extremely interesting for its testability and phenomenological value.

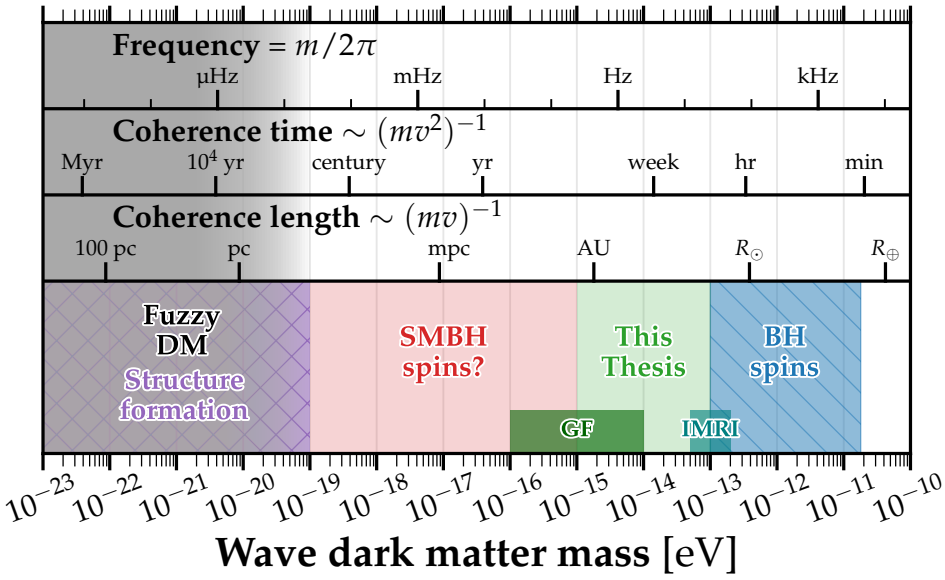

FIGURE 1: An illustration of the light end of the wave dark matter mass spectrum. We show the observational constraints based on the gravitational interactions and the mass range explored in our work. The gray area shows the natural mass ballpark for fuzzy dark matter, the purple band the range in tension with structure formation, the orange band and the blue band the regions probed via the superradiant instability effect with supermassive black holes and black hole spins, respectively. The range in green is the one mostly explored in this thesis, with GF (dark green) standing for the gravitational focusing in the solar system (Chapter 3) and IMRI (intermediate-mass ratio inspiral,teal) for the observation of wave dark matter spikes through the detection of gravitational waves (Chapter 5). Figure inspired by the cheatsheet in [34].

Remarkably, the density and velocity of wave dark matter particles are modified by their gravitational interaction with massive objects. The interplay of gravity with the wave nature of dark matter is crucial. First of all, in the unfortunate, but plausible case in which the dark matter does not interact with SM states but only through gravity, the wave nature might be the sole resource at our disposal to get hints on the dark matter mass. Furthermore the distortion of the dark matter phase space caused by the gravitational interaction with massive bodies is another way wave effects can manifest at different physical length scales and has the advantage of being independent on any assumption on the underlying model of dark matter.

In Figure 1 we show the wave dark matter mass spectrum constrained by observations based on the gravitational interaction. We also show the values of the coherence length $(mv)^{-1}$, timescale $(mv^2)^{-1}$ and frequency that correspond to the value of the mass. The ultralight end of the spectrum, i.e. fuzzy dark matter, is in tension with observations at small scales as structure formation is altered in cosmological scenarios involving $m \lesssim 10^{-20}$ eV. Observations of quasi-monochromatic gravitational radiation and gaps at large spin in the black holes spin-mass distribution due to the phenomenon of superradiant instability [35–39] can constrain heavier wave dark matter candidates. Constraints are already placed in the region $m \sim 10^{-14} - 10^{-11}$ eV, but future observations of supermassive black holes and low-frequency gravitational waves could allow the detection of boson masses in the

range $m \sim 10^{-19} - 10^{-15}$ eV [39–41].

This thesis focuses on bosons roughly in the gap between these superradiant constraints, as one can see in the bottom part of Figure 1. We will see how wave dark matter can leave gravitational signatures at lengthscales around the astronomical unit.

It is important to understand the origin of the wave features. The behavior of collisionless particle dark matter is described via the Boltzmann equation formalism in which the trajectories of individual particles are traced individually in phase space [42]. The main quantity is therefore the phase space distribution $f(t, \mathbf{x}, \mathbf{v})$, which solves the Liouville equation $df/dt = 0$. Wave features are better described in the formalism of a complex "wave function" $\psi(t, \mathbf{x})$ that satisfies the so-called Schrödinger-Poisson system [43]. The wave description allows for a reshuffling of the information that is originally contained in the phase-space distribution f into a wavefunction in position-space. This transformation can provide valuable insights, especially in simulations [44, 45], that may have been difficult to discern otherwise.

In the case of a collisional system, where the dark matter experiences weak gravitational scatterings with other objects, the Boltzmann equation $df/dt = \Gamma[f]$ proves to be a good formalism to describe both particle and wave dark matter, as long as the high phase-space occupancy is taken into account. It is possible to approximate this equation to the Fokker-Planck equation and describe the kinematics of objects in a dark matter medium through diffusion coefficients. These coefficients can be computed in the case of wave dark matter [46, 47] and can describe a plethora of astrophysical phenomena [21, 33], such as dynamical friction and gravitational cooling, which are sensibly altered by the wave nature of dark matter, as well as predict effects purely due to the stochasticity of the field .

It is crucial to remark that the wave description has to be equivalent to the particle one as soon as the typical length scale of the system under consideration is much larger than the typical wave length $\lambda_{\rm dB}$. In this limit we lose information not only on the wave nature, as spatial oscillations are averaged out, but also on the dark matter mass. Therefore, it is important to develop a formalism able to describe the interplay of the wave dark matter with gravity, as well as its stochastic properties, and able to recover the particle results in the appropriate limit. This formalism and its practical application to concrete astrophysical system is the central topic of this thesis.

The standard halo model

Thanks to precise observations of local objects' kinematics, we have gained an estimate of the typical value of the density of the virialized dark matter component of our galactic halo $\rho \sim 0.4\,\mathrm{GeV/cm^3}$ [48–50], at distances around 8 kpc from the galactic center, in the solar neighborhood, as well as its typical velocity dispersion, which is approximately $\sigma \sim 10^{-3}$ in natural units [51]. This information is of crucial importance for the design of detection experiments: we need to know how much dark matter is there and its probable kinematic properties in order to be able to predict what is the experimental reach of our detectors for a specific energy scale.

In other words, one crucial element in conducting terrestrial searches for dark matter is the local distribution of dark matter. Typically, the starting point is to assume that dark matter forms an isothermal halo and that its velocity follows the

Maxwell-Boltzmann distribution [52, 53]. This widely accepted model is referred to as the standard halo model and has been used as the basis for analyzing various terrestrial dark matter searches. While the standard halo model is straightforward and reasonably accurate, based on N-body studies [54, 55], it overlooks several important factors related to our current understanding of the local dark matter distribution. These factors may be critical in accurately mapping the local dark matter distribution.

First, the standard halo model fails to consider the possible presence of dark matter substructures in close proximity to the solar neighborhood. Recent studies employing precision astrometric data have identified a unique kinematic structure in a nearby population of stars [56, 57]. Dubbed Gaia-Enceladus or Gaia-Sausage due to its elongated shape in velocity space, this substructure is believed to have originated from a merger event with a satellite galaxy of mass approximately $10^{10} M_{\odot}$ around 8-10 billion years ago. It is expected that this same merger deposited dark matter into the Milky Way, with numerical simulations indicating that the kinematic structure of the accreted dark matter is very similar to its stellar counterpart [58, 59]. Consequently, a significant fraction of dark matter in the inner halo is presumed to exist in the form of substructures [60–62]. Besides Gaia-Enceladus, other substructures with distinct kinematic properties could also exist, such as streams with characteristically small velocity dispersion [63], and a dark disk that may have resulted from the merger events that gave rise to the thick stellar disk in the Milky Way [64]. This is of interest for this thesis: the variety of the kinematic properties of the different substructures in the Solar neighborhood can leave interesting imprints in the distribution of local dark matter, in particular if wave effects, that depend on the typical dark matter velocity, are present.

Gravitational focusing within the solar system

The standard halo model has another limitation in that it does not take into account the deformation of the local dark matter distribution caused by the Sun's gravitational potential. Since we are confined within the solar system, all our observations are inevitably affected by the presence of the Sun. The gravitational potential of the Sun modifies the trajectory of dark matter particles, resulting in the phenomenon of *gravitational focusing* within the solar system. This effect causes an excess of dark matter particles in the opposite direction to the solar system's motion in the Milky Way, creating a local overdensity. Therefore, it is crucial to study how the dark matter distribution near the solar system is influenced by the Sun, particularly along the Earth's orbital path.

Previous research has studied the gravitational focusing of dark matter in the search for weakly interacting massive particles [65–70]. Although the event rate due to the local overdensity remains low in the standard halo model, it can create a unique DM flux pattern on the sky map [68, 69] and modify the dark matter annual modulation signal [70].

In this thesis we investigate the gravitational focusing of wave dark matter and the response of dark matter substructures to the Sun's gravitational potential. Wave dark matter diffracts around massive objects, creating an interference pattern of

overdensity and underdensity fringes that depend on DM mass and velocity on typical length scale of $\lambda_{\rm dB} \sim (mv)^{-1}$. The wave gravitational focusing can have implications for theoretical predictions of the event rate and power spectrum of dark matter in direct detection experiments such as haloscopes [71–94] (see [95–97] and the relative section in [98] for a review of ultralight dark matter direct detection). Wave features in virialized halo components can be observed at wavelengths around or larger than the Sun-Earth distance. However, colder DM components like dark streams [63] can show a more definite interference pattern at smaller wavelengths due to smaller velocity dispersion, preserving a characteristic wave oscillation pattern over smaller angular scales. In the thesis we analyze the scenarios in which wave effects can have an impact on direct detection experiments.

Adiabatic compression of a dark matter halo

Another process through which the dark matter phase space distribution is reshaped by the gravitational potential of a massive body is the one of *adiabatic compression*. In the case of an adiabatically growing massive black hole at the center of a dark matter halo, the inner part of the halo gets compressed, leading to a steeper density profile. This phenomenon has been studied for particle WIMP dark matter [99], in particular in the context of dark matter annihilating into SM states [100]: the larger density increases the annihilation rate by ρ^2 and this could offer a striking indirect detection signal.

In the case of wave dark matter, self gravitating halos, at small radii, show a ground state, a cored solution of the Schrödinger-Poisson system, and at large radii they are characterized by a Navarro-Frenk-White-like profile. In this thesis we investigate how the compression works in the wave case. We expect that the wave halo can be analogously compressed by a growing central black hole and that, at distances larger than the soliton size, the dark matter density shows a spike as in the particle case. Depending on the values of the mass of the wave dark matter and of the black hole, the soliton can either survive over cosmological time scales or be absorbed by the central black hole, as already known in the literature [101].

Intermediate-mass-ratio inspirals in a dark matter spike

If we further assume the presence of a solar mass compact object orbiting around the central black hole, we can extract information about the dark matter density profile in the inner part of the halo. Due to the enhanced mass density, the compressed dark matter medium in the halo exerts a stronger dynamical friction force on the orbiting object: this is because the compact object is moving in a medium of dark matter particles which exerts a gravitational drag force on it. This additional source of energy loss causes a faster inspiral, hence a dephasing in the gravitational wave emission of the binary, which carries the signature of the nature of dark matter. This idea has appeared in the recent literature for the particle dark matter case [102–105].

The dephasing pattern will differ in the case of particle and wave dark matter because of the differences in the density profile and the different treatment of dynamical friction, where the gravitational effects can be suppressed at distances shorter

than the wavelength. In this thesis we study in which scenarios the wave dark matter halo can be reconstructed from gravitational wave observations and which information we can get on the dark matter mass.

Outline

The gravitational phenomenology of wave dark matter is the focus of this thesis. Therefore no assumption will be made regarding the specific particle model under consideration. Let us present the outline of the thesis.

The goal of Chapter 1 is to provide a primer on the phenomenology of dark matter that is useful for our discussion. We review the dark matter evidence on difference scales, the theory of structure formation and dark matter halos and we summarize important observational constraints on the dark matter candidates.

Chapter 2 is dedicated to an in-depth introduction on wave dark matter. We review the main particle physics motivations behind light scalars and we describe the properties of the wave field. First of all we consider the stochasticity of the field, which is crucial for a correct computation of the observables, such as the density or the field power spectrum, and we provide a formalism for the statistical description of wave dark matter. Next, we dive into the interplay between wave dark matter and gravity, mostly following [33]: we review why the wave field can be treated as a collection of classical waves and the formalism of the Schrödinger-Poisson system [43] through which the wave function embodies the field's response to gravity. The alternative fluid formulation, useful to study the small-scale suppression in the matter power spectrum ,characteristic of wave dark matter, is also presented. Furthermore, we overview some phenomenological consequences of the wave nature of the field, which lead to astrophysical constraints. We conclude the Chapter with an overview of the astrophysical and cosmological probes of wave dark matter and of the experimental searches for light bosonic DM.

Chapter 3, based on our work [106], considers, for the first time in the literature, the response of wave dark matter to the gravitational potential of a massive body. We study the phenomenon of gravitational focusing, for which the phase space of the dark matter medium is distorted by the presence of a massive object traveling inside it. After briefly reviewing the features of the focusing effect for particle dark matter, we move to the wave dark matter and show that we can find an analytical solution of the Schrödinger-Poisson system and compute observables. To obtain a physical understanding of the wave features of the system, we study to limits: (i) the monochromatic limit, in which the medium is uniquely characterized by the velocity of the dark matter and (ii) the semi-classical limit, in which the wave description has to match the particle one. Throughout the discussion we pay particular attention in highlighting the differences and similarities between wave and particle dark matter gravitational focusing.

The second part of Chapter 3 is devoted to the application of the formalism to dark matter components in the Solar system. We compute the density contrast and power spectrum for the halo dark matter component as well as for motivate dark matter substructures, which can constitute up to 10% of the local dark matter [60–62]: the so-called Gaia sausage [56, 57] a dark disk [64] and streams [63]. All these substructures have different response to gravitational focusing, due to their kinematic

properties, which we trace from the stellar observations, as shown by numerical studies [58, 59].

The adiabatic compression of a wave dark matter halo is the subject of Chapter 4, which explains the results of our work [107], where this topic is addressed for the first time in the literature. We review in detail the formation of the spike in the particle case, starting from a well-motivated initial Navarro-Frenk-White-like density profile. Next we proceed to study a wave dark matter halo, as done in the first part of [107]: as proven by numerical simulations [29, 108], the profile looks like the particle one at large distances from the center and shows a solitonic core at small radii. To describe the compression, we develop a semi-analytical approach: we model the initial halo as a superposition of wave functions as suggested in [93, 109] and we assign to these eigenstates the occupation numbers that reproduce a target density profile. Then the compression naturally follows from the conservation of quantum numbers, under the adiabatic assumption. The presence of the central black hole imposes peculiar boundary conditions, which further imply a finite lifetime for the eigenstates which form the halo. According to this, we find the final wave spike profile and we check that the relaxation process happens on timescales larger than the Gyr for the cases under inspection.

Chapter 5 explores a specific astrophysical scenario in which a wave dark matter spike can be observed, again expanding on the work done in [107]. We investigate the inspiral between a compact solar-mass object and an intermediate-mass black hole located within the compressed wave dark matter halo. The compressed wave dark matter halo exerts stronger dynamical friction on the orbiting object due to its enhanced mass density, leading to a distinctive pattern of dephasing in the gravitational waves emitted by the inspiral. This pattern of dephasing is different from that of inspirals in the particle dark matter halo because of the differences in density profile and the relatively suppressed dynamical friction force resulting from the wave nature of dark matter. We discuss the potential for using data from future gravitational wave detectors, such as the Laser Interferometer Space Antenna [110], to reconstruct the wave dark matter spike and distinguish it from the particle one.

Throughout this work, we use natural units $\hbar = c = 1$, unless stated otherwise.

Chapter 1

Dark Matter

In this Chapter we provide an overview on dark matter, constituting the necessary theoretical background of this thesis.

The content of the Chapter is taken from various sources, as it will be specified in each Section. Particular importance, was given to Section 1.2 where we produced the Figures ourselves. Section 1.1 reviews the evidence for dark matter on various scales, from galactic to the observable universe, Section 1.2 contains the computation of the linear matter power spectrum and a discussion on the typical mass of dark matter halos which will be of use in Chapter 4. We provide an overview on the standard halo model and the constraints on local dark matter in Section 1.3, which will be of use in Chapter 3. We conclude with a summary on the general properties of dark matter in Section 1.4.

1.1 Evidence

In this Section, we provide a review of the most significant evidence for dark matter accumulated by the scientific community in recent decades, following mostly [111–114]. This evidence spans scales ranging from (sub-)galactic scales (parsecs to 100 kpc) and clusters of galaxies (1 to 100 Mpc) to cosmological scales up to the size of the observable universe (100 to 10^4 Mpc). What is remarkable is that the abundance of dark matter is inferred solely from its gravitational effects on visible matter (baryons and radiation), and we presently have no information other than bounds regarding interactions between dark matter and visible matter or among dark matter particles themselves.

1.1.1 Galactic scales

In this work we take for granted the presence of dark matter in galaxies. Here we provide a brief review of why we think that dark matter is essential in the galactic dynamics.

Galactic rotation curves

Currently, the most compelling evidence for the presence of dark matter on a galactic scale is derived from observing galactic rotation curves (GRCs), which measure the circular velocity of stars and gas at varying distances from the galactic center.

This is accomplished by combining observations of redshifts of the 21cm line with optical surface photometry. Given the density profile of visible matter, organized in a disk, $\rho_b(r)$, and the enclosed mass, $M(r) = 4\pi \int dr'\ r'^2 \rho_b(r)$, we can derive the expected circular velocity, $v(r)$, of a visible object based on the equation of motion. We assume that, given $r_{\rm ch}$ some kpc-scale characteristic radius which marks the size of the galactic disk, the enclosed mass scales with volume for $r < r_{\rm ch}$ and saturates for $r > r_{\rm ch}$. So we have

$$v(r) = \sqrt{\frac{GM(r)}{r}} \propto \begin{cases} r & r \ll r_{\rm ch} \quad M(r) \propto \rho_b r^3 \\ r^{-1/2} & r \gg r_{\rm ch} \quad M(r) \simeq \text{const} \end{cases} \tag{1.1}$$

The Newtonian prediction based on visible matter is that the enclosed mass is increasing with the volume inside the disk while it is saturated outside the disk. In the top panel of Figure 1.1 we show how this prediction is in conflict with the actual data. As an example, we take the rotation curve of the NGC 6503 galaxy among the many analyzed in [115]: velocity data points flatten at large distances. The data can be fit if we consider a superimposed dark density profile, a so-called dark matter halo, with $M(r) \propto r$ at large radii, hence a density profile $\rho(r) \propto r^{-2}$ for $r \gg r_{\rm ch}$.

At present, we possess a more extensive collection of GRCs, which comprise data points beyond the 100 kpc range where no stars are present, but only hydrogen gas layers. All of the galaxies observed so far exhibit flat velocity profiles at the greatest probed radii. Among these galaxies, is our very own Milky Way, whose rotation curve is crucial for determining the local dark matter density - a crucial parameter for detecting dark matter in laboratories. The outcome of one of the earliest measurements [116] is depicted in the lower panel of Figure 1.1. More recently, a study on DM in the Milky Way [117] has been carried out, with the authors contending that current data overwhelmingly refutes the notion of baryons as the sole constituents in the galactic mass budget and positing the presence of a dark matter component, regardless of any assumed distribution.

Another possible explanation for GRCs data, instead of dark matter, could be a modification of Newton's universal gravitation on galactic scales. This has led to theories of modified gravity, such as MOND [11] and TeVeS [12], which have gained attention for their ability to reproduce observations of hundreds of GRCs [111]. However, these theories have a large number of free parameters and they are rather phenomenological descriptions that can hardly be derived from first principles. They have not been able to consistently reproduce all observations on larger scales, such as cluster scales [13]. TeVeS was definitively ruled out by the LIGO-Virgo observation of the gravitational wave signal GW170817 and the electromagnetic counterpart [118], which showed that the gravitational wave propagation velocity is equal to the speed of light up to a part over 10^{15}.

Gravitational lensing

The main drawback of GRCs is that they can only provide information on the presence of dark matter halos up to a certain distance, roughly 100 kpc, limited by the presence of light or neutral hydrogen. Therefore, they cannot precisely locate the bulk of the dark matter, despite sensing the presence of a DM halo. To overcome this

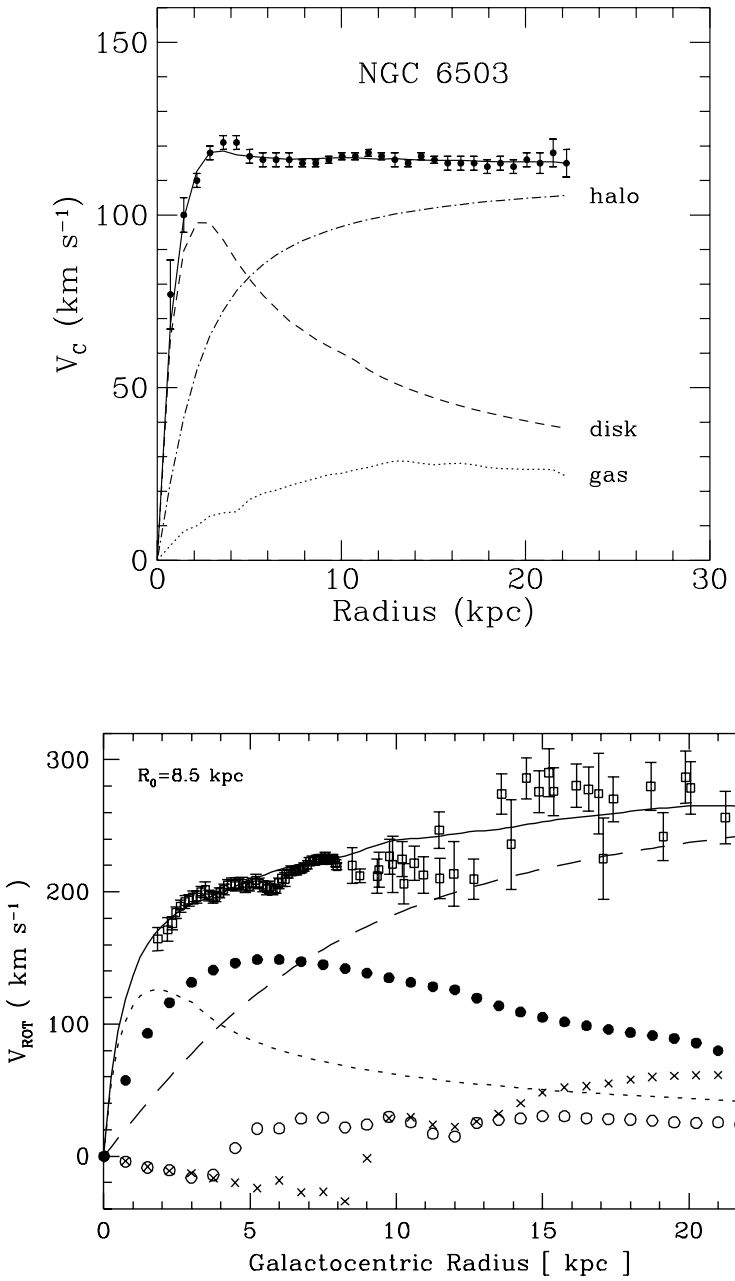

FIGURE 1.1: **Top**: the rotation curve of NGC 6503, from [115]. The contributions of gas, disk, and DM are represented by the dotted, dashed, and dash-dotted lines, respectively, while the solid line corresponds to the sum of all contributions. **Bottom**: the rotation curve of the Milky Way from [116]. The dotted line represents the contribution of the bulge, while the filled circles, crosses, and circles represent the contributions from the stellar disk, the HI gas layer, and the H2 gas layer, respectively. Finally, the dashed line corresponds to the contribution of a smooth dark halo, and the solid line represents the sum of all contributions.

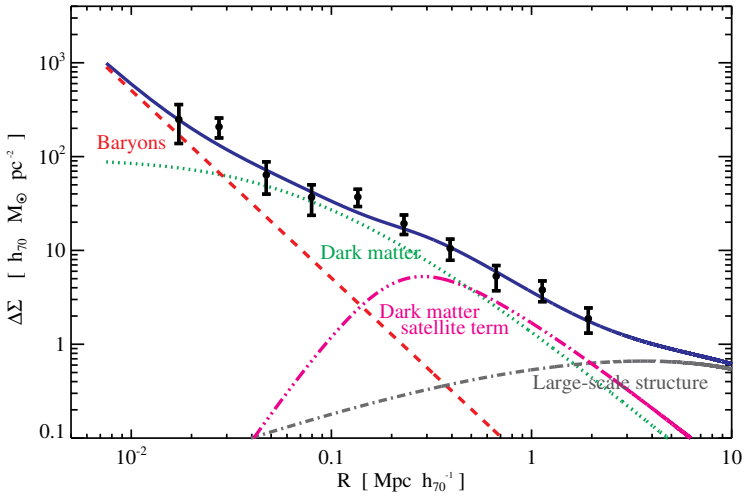

FIGURE 1.2: The radial mass density around elliptical galaxies, as observed in the Hubble Space Telescope COSMOS survey, broken down into its constituent components (see [119] and references therein). The blue solid curve represents the total "galaxy-galaxy" weak gravitational lensing signal. On small scales of approximately 10 kpc, the signal is dominated by the baryonic matter content of galaxies, as shown by the red dashed curve. On intermediate scales of around 100 kpc, DM halos become the dominant factor, with the main $\rho \propto r^{-2}$ halo term represented by the green dotted curve, and an additional contribution from subhalos hosting satellite galaxies shown by the magenta triple-dot-dash curve. At larger scales above 3 Mpc, the lensing signal is solely the cosmic shear signal from large-scale structure surrounding the galaxy, as indicated by the grey dot-dash curve.

limitation, gravitational lensing can be used. This is the phenomenon predicted by GR that causes mass to bend light as it passes nearby. In practice, the light emitted by distant objects, such as quasars, is bent by the gravitational field of galaxies located far (> 100 kpc) from their centers. Lensing measurements have confirmed the existence of enormous amounts of DM in both galaxies and clusters of galaxies, which we will discuss in the next Section.

It is interesting to note that both the dark matter and baryonic components contribute to the production of an isothermal density profile, with $\rho \propto r^{-2}$, out to very large radii, as confirmed by both gravitational lensing and dynamical analysis. As illustrated in Figure 1.2 extracted from [119], to account for the observed lensing signal in this wide range of scales, several factors must be considered, including baryonic matter at small scales, the dark matter halo of the galaxy, and the haloes of neighboring galaxies at greater distances. Furthermore, the agreement between the location of the transition from the host halo to large-scale structure and the expected size of DM structures from N-body simulations provides compelling evidence for the cold dark matter paradigm.

Additional support for the existence of DM, at both small and large scales, can be found in numerous sources of data (see [111] for more details). These include weak gravitational lensing measurements and velocity dispersion studies of dwarf spheroidal galaxies and satellite galaxies of spiral galaxies, which exhibit subtle deviations from what can be explained by visible matter alone.

1.1.2 Galaxy cluster scales

The presence of DM is also evident when observing clusters of galaxies, which are gravitationally bound systems spanning from 1 to 10 Mpc in size. Clusters were actually the first type of system where the evidence of dark matter was discovered. Zwicky [4] measured the velocity dispersion of galaxies in the Coma cluster and found it to be too large for the system to be stable if the mass was only due to visible matter. In other words, he estimated a mass-to-light ratio of approximately 400 $M_\odot$ by comparing the mass density obtained from the velocity dispersion using the virial theorem with the value estimated from visible matter, which was the average mass of a galaxy multiplied by the number of galaxies in the cluster: $\sim 10^9\ M_\odot \times 10^3$.

A different approach for estimating the mass of a cluster involves comparing the weak gravitational lensing signal with the observed X-ray emission profile, which traces the distribution of hot gas in clusters. The presence of this gas in the cluster can only be accounted for by the existence of a significant DM component, which provides the gravitational potential necessary to keep the gas in hydrostatic equilibrium. Assuming that the gas is indeed in hydrostatic equilibrium and modeling it as an ideal gas which is a good approximation, the pressure is $P = k_B T \times [\rho/(\mu m_p)]$ where ρ, T are the gas mass density and temperature, k_B is the Boltzmann constant, m_p is the proton mass and $\mu \simeq 0.6$ the average molecular weight, we have

$$\begin{aligned} -\frac{GM(r)}{r^2} = \frac{1}{\rho}\frac{dP}{dr} &= \frac{1}{\rho}\left[\frac{\rho}{\mu m_p} k_B T\right] \\ &= \frac{k_B}{\mu m_p} \times \frac{T}{r}\left[\frac{d\log\rho}{d\log r} + \frac{d\log T}{d\log r}\right]. \end{aligned} \tag{1.2}$$

Here $M(r)$ is the mass of the gas within radius r. Assuming constant temperature and $\rho \propto r^{-2}$ at large radii, we find that the temperature of the gas at hydrostatic equilibrium should be of order of

$$k_B T \simeq \frac{G\mu m_p M(r)}{r} \simeq 1.5\,\mathrm{keV}\left(\frac{M}{10^{14}\ M_\odot}\right)\left(\frac{1\,\mathrm{Mpc}}{r}\right), \tag{1.3}$$

having normalized to typical cluster values, with M the enclosed baryonic mass. This value of the temperature is an order of magnitude smaller than the observed value, around 10 keV. This fact gives us the hint of the presence of a large amount of dark matter in the cluster, about 6 times the visible matter.

These estimates can be compared to a gravitational map obtained from the lensing of distant objects by the gravitational potential of the cluster. In a classic study by Clowe et al. [8], this technique was applied to the Bullet cluster, a pair of merging clusters, studying the gravitational lensing. The collision caused the distribution of stars and galaxies to be spatially separated from the baryonic mass of the system, which was traced by the hot gas emitting in the X-ray band. By comparing the X-ray image to the lensing map, the authors found a significant 8σ spatial offset between the center of the total mass and the center of the baryonic mass. This offset cannot be explained by modified gravity, providing further evidence for the existence of DM.

1.1.3 Cosmological scales

While the evidence for dark matter on galactic and cluster scales is very robust, it is challenging to precisely determine the total amount of DM in the universe based on the observations discussed thus far. These observations only allow for rough estimates based on the mass-to-light ratio. However, observations on cosmological scales, beyond redshift $z > 0.03$ or distances > 100 Mpc, such as Lyman-α forest, galaxy surveys, or the Cosmic Microwave Background (CMB), can provide valuable information on the energy budget of the universe. Only on such large scales does DM reveal its intrinsic non-baryonic nature.

Cosmic Microwave Background

One of the strongest pieces of evidence for DM is derived from the analysis of the fluctuations in the Cosmic Microwave Background (CMB), which also provides the most precise estimate of its density. We briefly review the importance of dark matter in the CMB analysis following the discussion in [120] and the review in [113].

The CMB is a background of radiation originating from the propagation of photons in the early universe decoupled from baryons at a temperature about 0.1 eV. It has been extensively measured by various experiments over the past few decades, and the most precise measurement was done by the Planck satellite [9, 121]. The CMB has been found to resemble the spectrum of a black body at a temperature of $T_0 = 2.726$ K at an extreme level of precision. The CMB provides two main observables: the intensity of photons, which corresponds to temperature, and polarization, which is less relevant for our discussion about dark matter. The physical quantity of interest are temperature fluctuations, or anisotropies, in different directions in the sky. Any deviation from an isotropic and homogeneous early universe, consisting of a thermal bath of photons, baryons, neutrinos, and DM particles, is manifested as a modification of the constant photon temperature over the so-called last scattering surface, which is the way we can think of the CMB.

The main source of temperature fluctuation in the CMB is the relative motion of observers such as the Earth, solar system, and Milky Way, with respect to the CMB. By subtracting this dipole correlation, we obtain an isotropic background with temperature fluctuations of approximately $\delta T/T_0 \simeq 10^{-5}$. The isotropy observed at such large scales suggests the existence of an early inflationary phase. this has two main outcomes. First, it offers a scenario where all scales were initially in causal contact. Second, it provides the primordial seeds for large scale perturbations, including the CMB anisotropies, from the density fluctuations of the field responsible for inflation.

The symmetry of the problem suggests to conveniently expand the temperature fluctuations at a certain angular position $\delta T(\theta, \phi)$ in spherical harmonics

$$\delta T(\theta, \phi) = \sum_{\ell=0}^{\infty} \sum_{m=-\ell}^{\ell} a_{\ell m} Y_{\ell m}(\theta, \phi) \, . \tag{1.4}$$

Observationally, the sum over the multipoles ℓ needs to start from $\ell = 2$, because the monopole is an overall nonphysical constant and the dipole has been subtracted. On

the other hand, the sum has a upper cutoff at $\ell_{\max} \sim \pi/\theta_{\min}$ set by the resolution of the experiment. The Planck satellite was able to reach $\ell_{\max} \simeq 2500$.

If the fluctuations are assumed to be Gaussian, all the information is included in the power spectrum , which attains a diagonal form thanks to isotropy

$$\langle a_{\ell m} a_{\ell' m'} \rangle = C_\ell \delta_{\ell\ell'} \delta_{mm'} \,, \tag{1.5}$$

We can compute the correlation between fluctuations at different angular position:

$$\left\langle \delta T(\theta_i, \phi_i) \delta T(\theta_j, \phi_j) \right\rangle = \sum_\ell (2\ell + 1) C_\ell P_\ell(\cos\theta_{ij}) \tag{1.6}$$

with P_ℓ the Legendre polynomial and θ_{ij} the angle between the directions i and j. The power spectrum coefficients C_ℓ encode the dependence of the observable on the cosmological parameters. In Figure 1.3 we show the angular power spectrum coefficients reparameterized as $\mathcal{D}_\ell^{TT} = \ell(\ell+1)C_\ell/(2\pi)$ as measured by the Planck satellite together with the best fit that allows for the estimation of cosmological parameters [9]. This power spectrum displays a set of peaks known as acoustic peaks, where each peak corresponds to an angular scale with a significant contribution to the temperature fluctuations. The acoustic peaks are generated by several physical effects that must involve a non-baryonic dark matter component:

- *acoustic oscillations* of the coupled baryon-photon fluid. Initially, photons are tightly coupled to electrons through Thomson scattering, and baryons are coupled to electrons through Coulomb scattering. This fluid interacts gravitationally with dark matter, which pulls it into gravitational wells. As the fluid falls into these wells, it gets compressed adiabatically, increasing its pressure and countering gravity. This results in an oscillation in the energy of the photons in regions of high dark matter density. These oscillations can be decomposed into a set of fluctuation modes in reciprocal space, each with an associated power characterized by multipole moments. The power associated with each mode is an imprint of the gravitational potential around the electron-photon decoupling.

- *Sachs-Wolfe effect*, the impact of gravity on the propagation of the photons from the last scattering surface to us. The effect is mainly due to dark matter overdensities , which create a time-dependent gravitational potential through which the CMB photons travel to reach us. As the photons escape the potential wells, they lose energy due to the redshift effect, which dominates over the temperature gain associated with the overdensity. Thus, the cold spots in the CMB we observe today are associated with overdense regions at recombination, while hot spots are associated with underdense regions. The Sachs-Wolfe effect, which is caused by the free-streaming of photons, results in a power spectrum that depends on multipole moments as $C_\ell \propto [\ell(\ell+1)]^{-1}$.

Both of these effects demonstrate the important role played by DM in creating potential wells that affect the oscillations of the photon-baryon fluid and the streaming of decoupled photons.

Fitting the positions of the CMB spectrum peaks, which depend in a non-trivial way on the cosmological parameters, one can obtain best fit values for the energy budget of the universe today $t = t_0$ and the Hubble constant $H_0 = 100h$ km/s/Mpc [9]:

$$\begin{aligned} \Omega_b(t_0)h^2 &= 0.0224 \pm 0.0001 && \text{baryon density ,} \\ \Omega_m(t_0)h^2 &= 0.142 \pm 0.001 && \text{matter density} \\ \Omega_\Lambda(t_0)h^2 &= 0.684 \pm 0.009 && \text{dark energy density ,} \\ h &= 0.674 \pm 0.005 && \text{Hubble constant ,} \\ |1 - \Omega(t_0)| &< 10^{-3} && \text{flatness .} \end{aligned} \tag{1.7}$$

Notice the high precision of these parameters. Most importantly for us,

$$\Omega_{\rm dm}(t_0)h^2 = 0.1198 \pm 0.0012 \,. \tag{1.8}$$

Throughout the entire discussion, it was necessary to treat DM as a completely distinct component of the universe in comparison to baryons. This is because DM interacts with CMB photons solely through gravitational interactions, unlike baryons. This confirms that DM is non-baryonic in nature and cannot be composed of ultra-faint ordinary matter objects.

There are at least two additional independent observables on cosmological scales that can be used to probe $\Omega_b h^2$ and Ω_m. The former can be measured from Big Bang Nucleosynthesis (BBN) in the very early universe [122], while the latter can be analyzed through Supernovae Ia as a late universe measurement [123]. We will not review these topics, but we mention that the consistency provides strong evidence for the existence of dark matter as a crucial non-baryonic ingredient in the cosmic inventory.

Structure formation

A common method to understand the necessity for dark matter at different length scales is to compare the observed distribution of matter to the theory of structure formation, which is discussed in greater detail in Section 1.2. The goal of this Section is to outline why the dark matter is essential for the very existence of the Milky Way.

According to the standard paradigm, all the structures we observe in our universe, such as galaxies, clusters, and superclusters, originated from small primordial inhomogeneities that were generated during the inflationary epoch. These initially small and linear fluctuations evolved over time under the competing effects of gravity and the Hubble expansion. The presence of DM played a pivotal role in allowing the formation of such structures.

We want to study the properties of the matter density contrast. Here we parameterize as

$$\delta(\mathbf{x}, t) = \frac{\rho(\mathbf{x}, t) - \bar{\rho}}{\bar{\rho}} = \int \frac{d^3k}{(2\pi)^3} \delta_{\mathbf{k}}(t) e^{-i\mathbf{k}\cdot\mathbf{x}} \,, \tag{1.9}$$

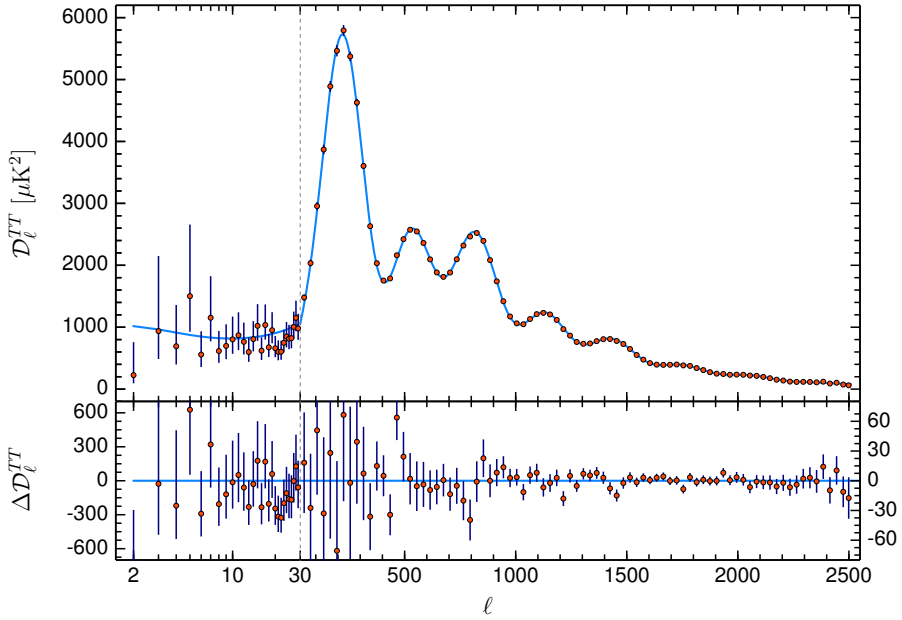

FIGURE 1.3: The Planck 2018 temperature anisotropies power spectrum from [9]. The upper panel displays the theoretical spectrum of the base-ΛCDM model that best fits the Planck data, while the lower panel shows the residuals relative to this model. The error bars represent the 1σ diagonal uncertainties, accounting for cosmic variance. It is worth noting that the vertical scale changes at $\ell = 30$, which is also the point where the horizontal axis switches from a logarithmic to a linear scale. This scale serves as a boundary between large and small scales, which are analyzed using different techniques.

with $\bar{\rho}(t)$ is the background mean matter density. The evolution of non-relativistic matter density fluctuations on sub-horizon scales, i.e. $\lambda < \lambda_H = H^{-1}$ can be described by Newtonian gravity, or, better by the small scalar perturbation limit of the Friedmann-Robertson-Walker metric (see Appendix A for more). Indeed, considering the Poisson equation for the gravitational potential Φ, on sub-horizon scales, for small perturbations

$$\nabla^2\Phi = 4\pi G\bar{\rho}\delta = \frac{3}{2}H^2\delta \Longrightarrow \Phi \sim \left(\frac{\lambda}{\lambda_H}\right)^2 \delta \ll 1 \tag{1.10}$$

consistently. One can show that combining the Poisson equation with the Friedmann equations and the continuity and Euler equation for the matter fluid, in Fourier space, the perturbation has to satisfy the *Jeans equation*

$$\ddot{\delta}_{\mathbf{k}} + 2H\dot{\delta}_{\mathbf{k}} + \left[\frac{c_s^2k^2}{a^2} - 4\pi G\bar{\rho}\right]\delta_{\mathbf{k}} = 0\,. \tag{1.11}$$

Here a is the scale factor and c_s the matter sound speed, which is non-zero if the matter has pressure, for example when baryons are coupled to photons. The brackets contain the battle between gravity and pressure for the growth of the overdensity. The scale at which these effects are balanced is called *Jeans scale*:

$$\lambda_J = \frac{2\pi}{k_J} = 2\pi\left(\frac{c_s^2}{4\pi G a^2\bar{\rho}}\right)^{1/2} = 2\pi r_H\sqrt{\frac{2}{3}}c_s \tag{1.12}$$

with $r_H = (aH)^{-1}$ the comoving Hubble radius. Perturbations on scales $\lambda < \lambda_J$ get washed out by pressure while those at larger scales $\lambda > \lambda_J$ undergo gravitational collapse. We can solve the Jeans equation in the different regimes.

- $\lambda \ll \lambda_J, \lambda_H$ (perturbations on sub-Jeans and sub-horizon scales). The gravity term can be neglected and the Jeans equation has the form of a damped harmonic oscillator with frequency $\omega_{\mathbf{k}}(a) = c_s k/a$ and amplitude of the form

  $$\delta_{\mathbf{k}}(t) = A_{\mathbf{k}}(t)e^{-i\omega t} + B_{\mathbf{k}}(t)e^{i\omega t} \tag{1.13}$$

  Perturbations on sub-Jeans scales undergo damped acoustic oscillations.

- $\lambda_J \ll \lambda < \lambda_H$ (perturbations on super-Jeans and sub-horizon scales). We should consider two different cases. In radiation domination $a \propto t^{1/2}$, $H = (2t)^{-1}$ and $\bar{\rho}$ is negligible, so the equation has the form $\ddot{\delta}_{\mathbf{k}} + \dot{\delta}_{\mathbf{k}}/t = 0$ with solution

  $$\delta_{\mathbf{k}}(t) = A_{\mathbf{k}} + B_{\mathbf{k}}\log t \sim B_{\mathbf{k}}\log a \qquad \text{radiation domination}\,. \tag{1.14}$$

  Perturbations grow only logarithmically in time.

  In matter domination $a \propto t^{2/3}$, $H^2 = 8\pi G\bar{\rho}/3 = 4/9 \times t^{-2}$. The equation gets $\ddot{\delta}_{\mathbf{k}} + 4/3t^{-1}\dot{\delta}_{\mathbf{k}} - 2/3t^{-2}\delta_{\mathbf{k}} = 0$ with solution

  $$\delta_{\mathbf{k}}(t) = A_{\mathbf{k}}t^{-1} + B_{\mathbf{k}}t^{2/3} \sim B_{\mathbf{k}}a \qquad \text{matter domination}\,. \tag{1.15}$$

We can use the formula for the sub-horizon and super-Jeans perturbations in a matter-dominated era to compute the density perturbations today. We know that during decoupling $\delta_{\rm CMB} \sim 10^{-5}$. We neglect the impact of the cosmological constant at late times. Since in this regime $\delta \propto a$, we obtain

$$\delta(t_0) = \frac{a(t_0)}{a(t_{\rm CMB})}\delta_{\rm CMB} \simeq \frac{T(t_{\rm CMB})}{T(t_0)}\delta_{\rm CMB} \sim 10^3 \times 10^{-5} \sim 10^{-2}\,. \tag{1.16}$$

The measured value of CMB fluctuations in the baryon-photon plasma is too small to explain the existence of present structures, even on the largest scales where the density perturbations are of the order of $\delta \sim 1 - 10^5$. The fact that we observe such small fluctuations is a strong indication that we are missing a crucial ingredient in the formation of structures: cold dark matter. DM provides the potential wells necessary to allow the perturbations to go non-linear, and without it, the universe would be still quite homogeneous, with just some percent fluctuations in density.

To understand the impact of DM on the theory of structure formation, we model the fluctuations as Gaussian random fields with statistical properties described by the linear matter power spectrum $P(k)$, which is defined from the two-point function of the Fourier perturbations.

$$\langle \delta_{\mathbf{k}}(t)\delta_{\mathbf{k}'}(t)\rangle = (2\pi)^3\delta^{(3)}(\mathbf{k}-\mathbf{k}')P(k)\,. \tag{1.17}$$

This quantity is computed carefully in Section 1.2. For now, we just present in Figure 1.4 the result of the theoretical prediction of the ΛCDM model with the data at the different cosmological scales. The agreement supports the evidence of dark matter.

1.2 Dark matter structures

Cosmological structures on different scales, such as galaxies and galaxy clusters, are formed through the process of gravitational instability, whereby small initial overdensities grow due to gravity. Although the initial overdensities were incredibly small (of the order of 10^{-4}), the accumulation of matter over the age of the universe eventually led to the formation of the significant structures that we observe in the present-day. The growth of perturbations and the resulting clustering of galaxies depend on the contents of the universe in a non-trivial way. First of all, perturbations on a given scale can only grow once that scale is smaller than the horizon scale $d_{\rm hor} = a(t)\int_0^t dt'/a(t') \sim H^{-1}$. When the inverse of a comoving scale, k, is equal to the comoving horizon scale H^{-1}/a, i.e. $k = aH$, it is said to have "entered the horizon". The specific time at which this happens depends on the cosmological history of the universe. Secondly, interactions between the components of the universe are important: dark matter perturbation start growing earlier than baryons, which are coupled to photons until recombination and whose perturbation cannot grow. After recombination baryons fall in the gravitational wells previously made by dark matter and we can treat matter as a whole.

In this Section, we discuss the evolution of perturbations and the formation of matter structures (halos), clarifying the notation and providing useful concepts for

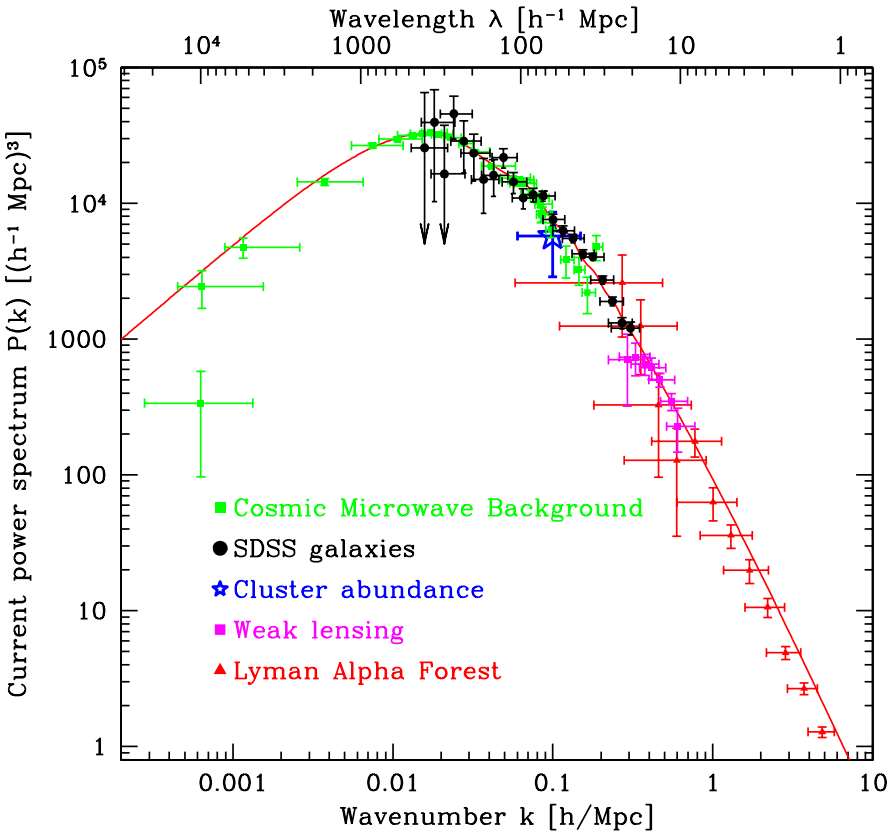

FIGURE 1.4: The theoretically predicted linear matter power spectrum from the ΛCDM model (see Section 1.2 for details) compared to observations at different scales: CMB (combination of [124] and [125]), SDSS galaxy counting [126], lensing [127], Lyman-α forest [128] reanalyzed by [129]. Figure from [126].

the investigation of compressed dark matter halos in Chapter 4. The structure of content of the Section relies on [120], focusing on the key points relevant for this work.

1.2.1 Linear matter power spectrum

Consider the gravitational potential on the scale $\mathbf{k}$ at redshift z, related to the scale factor as $1+z = a_0/a$ ($a_0 = 1$ today, usually). At early times all of the modes are outside the horizon $k/(aH) \ll 1$ and the potential is constant. At intermediate times wavelengths enter the horizon and the matter content starts dominating the energy density of the universe over radiation and therefore the potential evolves. At late times, deep in matter domination epoch, the potential is constant again. This history is expressed as [120]

$$\Phi(\mathbf{k}, z) = \frac{3}{5}\mathcal{R}(\mathbf{k})\mathcal{T}(k)(1+z)D_+(z)\,. \tag{1.18}$$

We explain each contribution. $\mathcal{R}$ is the primordial curvature (adiabatic) perturbation generated during inflation. $\mathcal{T}$ is the transfer function, which describes the evolution of perturbations through the epochs of horizon crossing and radiation/matter transition, defined as

$$\mathcal{T}(k) \equiv \frac{\Phi(\mathbf{k}, z_{\rm late})}{\Phi_{\rm ls}(\mathbf{k}, z_{\rm late})}\,, \tag{1.19}$$

where $z_{\rm late}$ is a sufficiently late-time redshift, deep in matter domination ($z_{\rm late} \ll z_{\rm eq}$) and $\Phi_{\rm ls}$ is the large-scale potential, i.e. solution of the gravitational potential for modes that entered the horizon well in the matter-dominated epoch. In particular it is 9/10 of the primordial potential. The growth factor $D_+(z)$ parameterizes the evolution of perturbations, and it is defined as the ratio of the potential to its value right after the transfer function regime, for $z < z_{\rm late}$

$$(1+z)D_+(z) \equiv \frac{\Phi(\mathbf{k}, z)}{\Phi(\mathbf{k}, z_{\rm late})}\,. \tag{1.20}$$

During matter domination, the potential is constant so $D_+(z) = 1/(1+z) = a$, hence the normalization. Perturbations at late times grow in time $\propto D_+(z)$.

In the late universe, i.e. well after recombination, baryons closely follow the dark matter, so they are cosmologically described together in form of the total matter overdensity field

$$\delta(\mathbf{x}, z) = \frac{\rho_{\rm m}(\mathbf{x}, z)}{\bar{\rho}_{\rm m}} - 1 \tag{1.21}$$

as a random field realized in space. The amplitude of the density perturbations at a given time is quantified statistically via the power spectrum. Assuming homogeneity and isotropy makes the power spectrum diagonal in Fourier space

$$\left\langle \delta(\mathbf{k}, z)\delta(\mathbf{k}', z)\right\rangle = (2\pi)^3\delta(\mathbf{k}-\mathbf{k}')P_\delta(k, z)\,. \tag{1.22}$$

The *dimensionless* power spectrum is also introduced $\Delta^2_\delta(k,z) = k^3/(2\pi^2)P_\delta(k,z)$. Thanks to these definitions the ensemble average of the matter overdensity reads

$$\left\langle \delta^2(\mathbf{x},z)\right\rangle = \int \frac{d^3k}{(2\pi)^3}\, P_\delta(k,z) = \int d\log k\, \Delta^2_\delta(k,z)\,. \tag{1.23}$$

We want to express the power spectrum of the matter distribution as a function of the gravitational potential $\Phi(\mathbf{k},z)$. The overdensity and the gravitational potential are related by the Poisson equation. On sub-horizon scales $k \gg aH$ and in matter domination $z < z_{\rm late}$,

$$\Phi(\mathbf{k},z) = \frac{4\pi G\bar\rho_{\rm m}a^2}{k^2}\delta(\mathbf{k},z)\,. \tag{1.24}$$

We substitute $\bar\rho_{\rm m} = \Omega_{\rm m}\rho_{\rm cr}/a^3$ and $H_0^2 = 8\pi G\rho_{\rm cr}/3$ and use Eq. (1.18)

$$\delta(\mathbf{k},z) = \frac{2k^2a}{3\Omega_{\rm m}H_0^2}\Phi(\mathbf{k},z) = \frac{2k^2}{5\Omega_{\rm m}H_0^2}\mathcal{R}(\mathbf{k})\mathcal{T}(k)D_+(z)\,. \tag{1.25}$$

Therefore the linear matter power spectrum is written as

$$P_\delta(k,z) = \frac{4}{25\Omega_{\rm m}^2H_0}\left(\frac{k}{H_0}\right)^4 P_{\mathcal{R}}(k)D_+^2(z)\mathcal{T}^2(k)\,. \tag{1.26}$$

The primordial curvature power spectrum is given by [120]

$$P_{\mathcal{R}}(k) = A_{\mathcal{R}}\left(\frac{k}{k_\star}\right)^{n_s-1}\,, \tag{1.27}$$

with $A_{\mathcal{R}} \simeq 2\times10^{-9}$, $n_s = 0.968$ and $k_{\rm p} = 0.05\,{\rm Mpc}^{-1}$ [9]. The transfer function $\mathcal{T}(k)$ can be obtained numerically, but it is enough for our purposes to use the analytical expression by Eisenstein and Hu [130]. The growth function can be found solving the evolution equation for the matter perturbation in a matter-dominated universe [120]

$$D_+(z) = \frac{5}{2}\Omega_{\rm m}(t_0)\frac{H(z)}{H_0}\int_z^\infty dz'\,(1+z')\frac{H_0^3}{H^3(z')}\,. \tag{1.28}$$

We can exploit $\Delta^2_\delta(k,z)$ to find the scale $k_{\rm nl}(z)$ at which perturbations are non-linear. This corresponds to $\Delta^2_\delta(k,z) \gtrsim 1$. Solving for this condition at redshift $z = 0$ gives $k_{\rm nl}(0) \simeq 0.25h$ Mpc^{-1}. At higher redshifts, structures were not as evolved, so the nonlinear scale was smaller, that means $k_{\rm nl}$ larger.

In Figure 1.5, we show the linear matter power spectrum today and at earlier times for the fiducial ΛCDM cosmology. On large scales, where the transfer function goes to unity, the spectrum goes as $P_\delta \propto k^{n_s}$. The spectrum shows a peak corresponding roughly to the scale $k_{\rm eq} \simeq 0.015h$ Mpc^{-1} that enters the horizon at matter/radiation equality. This can be explained easily with the fact that scales smaller than $k_{\rm eq}$ enter the horizon earlier, and the earlier they do, the later they start growing. Thus, the power spectrum is a decreasing function of k on small scales.

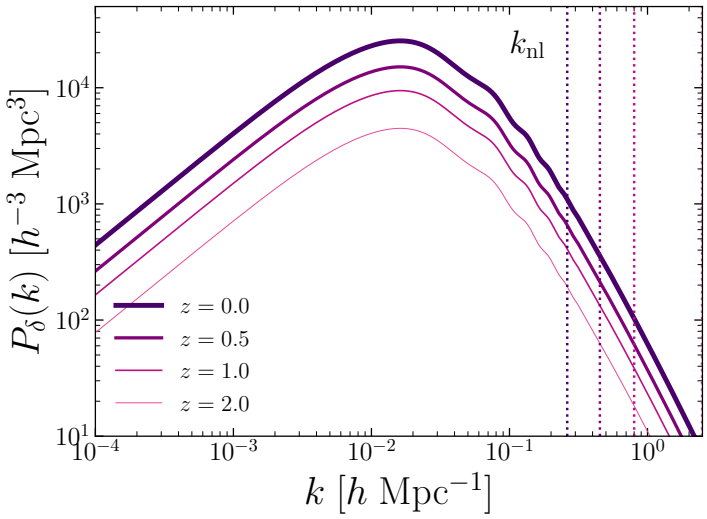

FIGURE 1.5: The linear matter power spectrum in the fiducial ΛCDM cosmology for Planck [121] parameters at different redshifts. The vertical dotted lines show the scales $k_{\rm nl}$ at which linearities cannot be ignored.

1.2.2 Halos

Dark matter forms structures called halos. Even though the intricate structure of individual halos can be highly complex, their average characteristics are surprisingly straightforward. Essentially, at a given point in time, the properties of a halo are primarily determined by one factor: its mass. However, before leveraging this information, it is important to establish a clear definition of a halo's mass. A practical way is to consider all matter enclosed in a sphere of a certain radius to achieve an enclosed density of some multiple Δ of the mean matter density $\bar{\rho}_{\rm m} = \Omega_{\rm m}\rho_{\rm cr}$. A common choice is to define the virial radius $r_{\rm vir}$ and the virial mass

$$M_{\rm vir} \equiv M_{\rm dm}(< r_{\rm vir}) = \frac{4\pi}{3}\Delta_{\rm vir}\bar{\rho}_{\rm m}(z_{\rm vir})r_{\rm vir}^3 \tag{1.29}$$

with $z_{\rm vir}$ the redshift at which virialization happens. The other conventional way to define the halo mass is through

$$M_{200} \equiv M_{\rm dm}(< r_{200}) = \frac{4\pi}{3}\Delta_{200}\rho_{\rm cr}(z_{\rm vir})r_{200}^3 \tag{1.30}$$

which is the mass enclosed within the radius r_{200} where the average mass density is $\Delta_{200} = 200$ times the critical density. This choice is motivated by the fact that, as we are about to see, $\Delta_{\rm vir} \approx 200$.

Spherical collapse and critical overdensity

Let us consider briefly the spherical collapse model. According to this simple model, the radius R of a spherical overdense region evolves via the parametric solutions to the Friedmann equation for a closed universe. With $\delta_i \ll 1$ as the initial density of

size R_i at time t_i,

$$R = \frac{R_{\rm ta}}{2}(1-\cos\theta) = \frac{R_i}{2}\frac{3}{5\delta_i}(1-\cos\theta)\,, \tag{1.31}$$

$$t = \frac{t_{\rm ta}}{\pi}(\theta-\sin\theta) = \frac{1}{2H_i}\frac{3}{5\delta_i}(\theta-\sin\theta)\,. \tag{1.32}$$

Here $R_{\rm ta}$ is the size at turnaround, that happens at time $t_{\rm ta}$. One can show that the overdensity evolves as

$$1+\delta = \frac{9}{2}(1+\delta_i)\frac{(\theta-\sin\theta)^2}{(1-\cos\theta)^3} \approx (1+\delta_i)\left(1+\frac{3\theta^2}{20}\right)\,. \tag{1.33}$$

The last expression is the expansion for $\theta \ll \pi$, where the linear theory is valid.

At early times, $\theta \ll \pi$ we have $R \propto t^{2/3}$ and the overdensity grows as $\delta \propto R$. The expansion subsequently slows down, and at $\theta = \pi$ the region "turns around" and starts collapsing. However, even though $R = 0$ at $\theta = 2\pi$, the assumptions behind spherical collapse that matter is in spherical shells with small random velocities breaks down and the region actually reaches virialization. We can determine the overdensity at collapse in the linear theory. We expand the formulae for t and $1+\delta$ for $\theta \ll \pi$ and eliminating θ we get [131]

$$1+\delta \approx (1+\delta_i)\left[1+\delta_i\left(\frac{3}{2}H_i t\right)^{2/3}\right]\,. \tag{1.34}$$

The spherical region collapses (and virializes) if the overdensity in the linear theory exceeds the critical value $\delta_{\rm c} = \delta(t_{\rm c})$. We can find this by evaluating Eq. (1.34) for $t_{\rm c} = 2t_{\rm ta}$. We find

$$\delta_{\rm c} = \frac{3}{5}\left(\frac{3\pi}{2}\right)^{2/3} \simeq 1.686\,. \tag{1.35}$$

The threshold for spherical collapse is used to identify which regions within an initial (linear) density field may undergo collapse to create halos. It is noteworthy that the collapse threshold is independent of the size and mass of the collapsing region, as a result of the scale-free characteristic of an Euclidean matter-dominated universe.

One can also estimate the typical overdensity within scale R during spherical halo virialization. This is done by utilizing the fact that virialization necessitates the kinetic energy to be $-1/2$ of the potential energy. Remarkably, the outcome is not affected by the size or mass of the region and is determined to be, for a flat matter-dominated universe, $\Delta_{\rm vir} = 18\pi^2 \simeq 180$. This is why $\Delta = 200$ is chosen as the threshold density for defining halo mass and radius. Due to the rough nature of this approximation, it has become the norm to round off the value of Δ to the nearest whole number.

Including the cosmological constant Λ, no closed-form solution for the spherical collapse exist. However the effect on $\Delta_{\rm vir}$ and $\delta_{\rm cr}$ is small. In [132], for example, it is

found for $\chi = \Omega_{\rm m}(z_{\rm vir}) - 1$

$$\Delta_{\rm vir} \approx \frac{18\pi^2 + 82\chi - 39\chi^2}{\chi + 1} \,. \tag{1.36}$$

The reason for this is that during the early stages of collapse in matter domination, Λ is not the primary factor, while during the later stages when dark energy becomes significant, the collapsing region has already achieved a much higher density than the background and is mostly separated from the Hubble flow.

The mass variance

We want to describe the typical amplitude of a perturbation on scale R. We define a smoothed density field on the (comoving) scale R

$$\delta_R(\mathbf{x}, z) = \int d^3x' \; W_R(\mathbf{x} - \mathbf{x}')\delta(\mathbf{x}, z) \,, \tag{1.37}$$

through a window function W_R normalized to $\int d^3x \, W_R(\mathbf{x}) = 1$. We choose a top-hat filter, which is unity inside the sphere of radius R and zero outside:

$$W_R(r) = \frac{3}{4\pi R^3}\Theta(R - r) \,. \tag{1.38}$$

The typical amplitude of perturbations on scale R is given by the mass variance

$$\sigma_R^2(z) = \left\langle \delta_R^2(\mathbf{x}, z) \right\rangle = \frac{1}{2\pi^2} \int_0^\infty dk \, k^2 |W_R(k)|^2 P_\delta(k, z) \,, \tag{1.39}$$

where $W_R(k)$ is the Fourier transform of the top-hat function

$$W_R(k) = \frac{3}{(kR)^3} \left[\sin(kR) - (kR)\cos(kR)\right] \,. \tag{1.40}$$

The filter was introduced to regularize the integral in Eq. (1.39) defining σ_R^2, which is divergent for the matter power spectrum. We can replace at will the filter over the size R with a filter over the mass $M(R) = 4\pi\bar{\rho}_{\rm m}(0)R^3/3$ enclosed in R. In Figure 1.6 we show the mass variance of cosmological perturbation, averaged over a scale R such that $M(R) = M$ for different redshifts. The mass scales for which $\sigma_M^2 \gtrsim 1$ signals that structure formation is happening. The plot of mass variance shows that small dark matter structures form first at every redshift, because their mass variance is order one earlier than for larger masses. Smaller object formed from larger perturbations, hence at earlier times. This is the essence of hierarchical clustering of cold dark matter.

We want to compute the typical halo mass M at redshift z. A good statistical description is given by the Press-Schechter formalism [133]. This method relies on knowing the fraction of collapsed objects of mass M or smaller $F(\sigma_M, \delta_{\rm c})$, making use of the critical overdensity found in the spherical collapse case. Assuming that δ_R

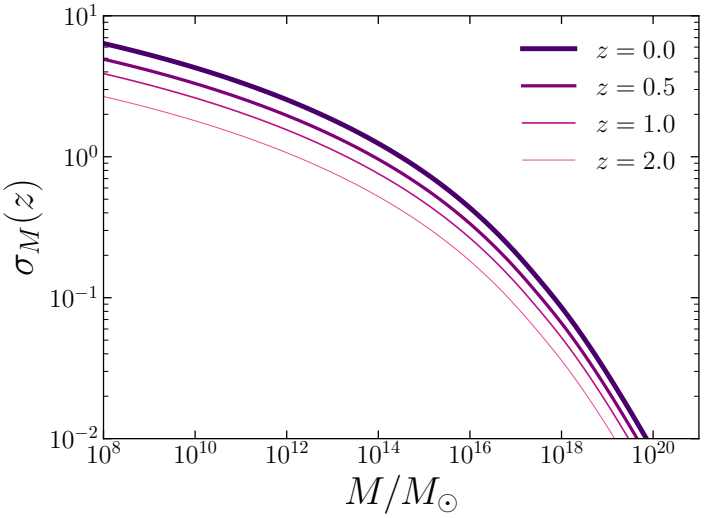

FIGURE 1.6: The mass variance of cosmological perturbations filtered over the mass scale M for different redshifts. This figure shows the hierarchical clustering of CDM structure formation.

is a Gaussian random field, with variance σ_R, then it follows that [134]

$$F(\sigma_M, \delta_c) = 2 \int_{\delta_c}^{\infty} \frac{1}{\sqrt{2\pi}\sigma_R} e^{-\delta_R^2/(2\sigma_R^2)} = \mathrm{erfc}\left(\frac{\nu}{\sqrt{2}}\right), \tag{1.41}$$

with

$$\nu(z) = \frac{\delta_c}{\sigma_M(z)}, \tag{1.42}$$

the so-called peak height. This parameter tells us how rare (in $\nu\sigma$ terms) is to find a certain structure with mass M at given redshift z. Typical halo masses formed at redshift z in the ΛCDM cosmology are then obtained finding the value M from Eq. (1.42) with ν of order unity. Note that $\lim_{M\to 0} F(\sigma_M, \delta_c) = 1$ as we expect (all the structure collapse) thanks to the factor of 2, exactly introduced by Press & Schechter.

We show the results of this analysis in Figure 1.7. The lines are the isocontours for the halo mass distribution as a function of redshift. For a fixed redshift, the most likely values are the ones below the 1σ contour line, while the halo masses above become more and more unlikely. Notice that at high redshift large structures are much more unlikely compared to today, where all the lines appear to be closer.

Navarro-Frenk-White density profile

Navarro, Frenk, and White [135, 136] found that the equilibrium density profile of collisionless cold dark matter in N-body simulation are well fitted, over two orders of magnitude in radius for a wide spectrum of halo masses and cosmological parameters by a universal profile of the form

$$\rho_{\mathrm{NFW}}(r) = \frac{\rho_{\mathrm{cr}}(z_{\mathrm{vir}})\delta_{\mathrm{ch}}}{(r/r_s)(1 + r/r_s)^2}, \tag{1.43}$$

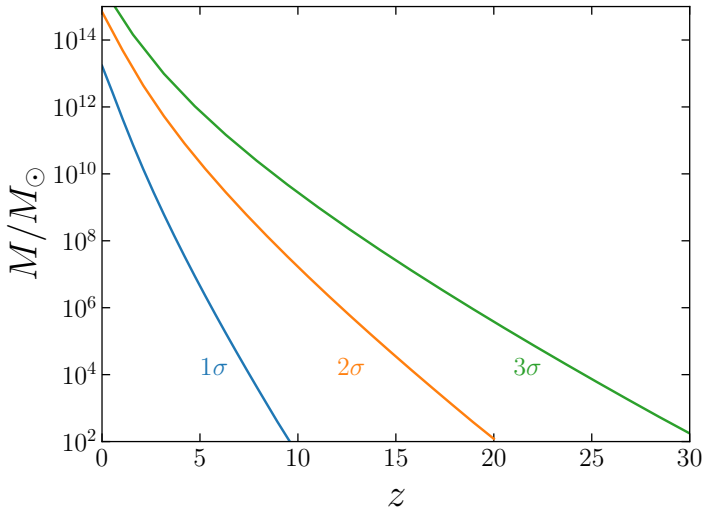

FIGURE 1.7: Typical halo masses formed at redshift z in the fiducial ΛCDM cosmology. We choose the peak height $\nu = 1,\ 2,\ 3$, that correspond to the contours in the M, z plane for values likely at the $1\sigma,\ 2\sigma,\ 3\sigma$ level, respectively.

where r_s is the scale radius, i.e. the radius at which the logarithmic derivative of the density profile is equal to -2:

$$\left.\frac{d\log\rho_{\rm NFW}}{d\log r}\right|_{r=r_s} = -2\,. \tag{1.44}$$

This definition is general and independent on the NFW profile itself. $\rho_{\rm cr}(z_{\rm vir})$ is the critical density at halo formation and $\delta_{\rm ch}$ is the characteristic overdensity. The scale density, i.e. the density at scale radius is then defined as $\rho_s = \rho_{\rm cr}\delta_{\rm ch}$. For $r \ll r_s$, $\rho_{\rm NFW} \propto r^{-1}$, so the inner NFW profile can be effectively described by a power-law profile.

The enclosed dark matter mass and dark matter self-gravity potential are found analytically [42]

$$M_{\rm NFW}(r) = 4\pi_s\rho_s r_s^3\left[\log\left(1+\frac{r}{r_s}\right) - \frac{r/r_s}{1+r/r_s}\right], \tag{1.45}$$

$$\Phi_{\rm NFW}(r) = -\frac{4\pi\rho r_s^3}{r}\log\left(1+\frac{r}{r_s}\right). \tag{1.46}$$

Notice that the enclosed mass logarithmically diverge for large radii. This is why the NFW profile cannot describe realistic bound halos at large radii, where $r \gg r_s$, $\rho_{\rm NFW} \propto r^{-3}$. The real halo profiles become steeper at $r > r_{\rm vir}, r_{200}$. An exponential cutoff at large radii is appropriate to parameterize this behavior.

1.3 Dark matter distribution

It is of crucial interest to understand the distribution of dark matter around us and how it is shaped by gravity. This is the topic of Chapter 3, but for now we want to

outline the formalism to model both the abundance and the kinematic properties of the dark matter particles in our neighborhood. In other words we want to know what observations of the kinematics of stars in the Milky Way tell us about the phase-space distribution of dark matter. For this section we largely refer to the review [114] and the references therein.

We denote with $f(\mathbf{x}, \mathbf{v}, t)$ the phase space distribution. It is normalized such that $\int d^3v\, f = \rho$ and $\int d^3x\, d^3v\, f = M$. In the collisionless regime, the phase space distribution has to satisfy the Liouville equation [42]

$$\frac{df}{dt} = 0. \tag{1.47}$$

Once the total derivative is expanded, we find

$$\frac{\partial f}{\partial t} + \mathbf{v} \cdot \nabla f - \nabla\Phi \cdot \frac{\partial f}{\partial \mathbf{v}} = 0 \tag{1.48}$$

Here Φ is the potential, from the particle's equation of motion $\dot{\mathbf{v}} = -\nabla\Phi$. This equation tells us how the phase space distribution evolves on the particle's trajectory.

Standard Halo Model We have seen in Section 1.2 that dark matter forms halos which embed galaxies. For simplicity, the velocity distribution of the dark matter in the Milky Way halo is taken to be a Maxwell-Boltzmann distribution,

$$f(\mathbf{v}) = \frac{\rho}{(2\pi\sigma^2)^{3/2}} \exp\left[-\frac{v^2}{2\sigma^2}\right] \tag{1.49}$$

which corresponds to the assumption of a isothermal density profile, that provides a flat galaxy rotation curve, having $\rho \propto r^{-2}$ at large radii. This is the so-called Standard Halo Model (SHM) [52, 53]. This has been used as the basis for analyzing various terrestrial dark matter searches. A feature of the isothermal sphere is that the circular velocity is given by $v_c(r) = r[d\Phi/dr] = \sqrt{2}\sigma$.

The density distribution isothermal sphere extends to infinity, which means that the velocity distribution also would allow to infinite velocities. However, the Milky Way halo is finite and particles with velocities greater than the escape speed of the Milky Way $v_e(r) = \sqrt{2|\Phi(r)|}$, are not gravitationally bound to it. To account for this, the velocity distribution is often truncated at the measured local escape speed.

Local density There are two categories of techniques used to constrain the local dark matter density, namely local methods that use kinematics of nearby stars and global ones that involve mass modeling of the Milky Way through rotation curves and velocity dispersion of stars. While the error on the measurement can be small, the estimates of $\rho(R_\odot)$ are spread in the $0.3 - 0.6\ \mathrm{GeV/cm^3}$ range, e.g. [48–50] indicating that systematics may be relevant (see the reviews [137,138] for more details). It is worth noticing that this value of the density appears when we average over scales larger than the parsec, which is the average distance between local stars. Bounds on the actual density *inside* the solar system are much weaker [139].

Local circular speed The circular speed at the Sun's position $v_c(R_\odot)$ was determined in [140] from the proper motion of the Milky Way's central black hole Srg A* to be $v_c(R_\odot)/R_\odot = (30.3 \pm 0.9)$ km/sec/kpc. From a recent precise determination of the radial distance of the Sun from the galactic center [141], we can obtain $v_c(R_\odot) = (248 \pm 7)$ km/sec. A complementary method is a Jeans analysis through tracer stars which give $v_c(R_\odot) = (229.0 \pm 0.2)$ km/sec [51]. We stick to this more precise result.

Local escape speed The local escape speed $v(R_\odot)$ is estimated from the population of high velocity stars. Using GAIA data without assumptions in the gravitational potential, it is found $v_e(R_\odot) = (580 \pm 63)$ km/sec [142].

Shortcomings The standard halo model appears to be reasonably accurate, according to N-body studies [54, 55], but does not take into account the history of mergers that Milky Way has undergone, which could lead to peculiar dark matter substructures. In other words, the velocity distribution contains imprints of the archaeology of Milky Way's halo.

A considerable portion of the local dark matter belongs to the Gaia-Enceladus sausage, which originated from the aftermath of a major merger with a $M < 10^8\, M_\odot$ dwarf galaxy about 8-10 billion years ago [57]. It is called so because the stellar component has radially biased orbits, resulting in a sausage-like distribution of radial velocity component [56]. The dark matter in the Gaia sausage constitutes about 10 to 30% of the local DM density. Ref. [60] presents an updated version of the standard halo model that includes this component. In addition to this, the local stellar halo has narrow tidal streams from smaller or more recent mergers such as S1 [143], the Helmi streams [144] and Nyx [145]. Since all these components have characteristic kinematic properties, they must be modeled independently and added to the total local dark matter distribution.

1.4 General constraints and properties

The nature of dark matter is still unknown, although we know its abundance and distribution in the universe, as well as its gravitational interaction and pressureless fluid behavior. Its microscopic properties such as mass, spin, and couplings with the visible sector are still uncertain, making the quest to unveil the DM theory one of the main goals of physicists today. Despite decades of attempts to detect non-gravitational interactions of DM particles, no success has been achieved. However, the null results from dark matter searches have provided valuable information, as we now know what DM *cannot be*. This chapter aims to overview the properties any dark matter candidate must have. We follow the recent review [146].

Cosmological density Thanks to the fit of the CMB data by the Planck collaboration [9] we know the present value of the mass density of dark matter on cosmological scales:

$$\Omega_{\rm dm}(t_0)h^2 = \frac{\rho_{\rm dm}}{\rho_{\rm cr}h^{-2}} = 0.1198 \pm 0.0012\,. \tag{1.50}$$

Coldness Based on constraints from structure formation, e.g. Lyman-α [147], it is established that dark matter must be cold, meaning it was non-relativistic when the universe was at a temperature of approximately $T \sim$ keV, in order to avoid a velocity dispersion that would hinder structure formation. Below this temperature, dark matter behaves as a pressure-less fluid. This leads to the exclusion of thermal candidates with mass $m < 1 - 10$ keV, such as Standard Model neutrinos. These constraints imply that light DM candidates should be produced non-thermally.

Charge neutrality Dark matter is indeed *dark* because it does not interact electromagnetically. If it did, it would have been visible and would have had a significant impact on the Cosmic Microwave Background (CMB) power spectrum due to its coupling with the photon fluid. However, it is still possible that dark matter has a tiny electric charge, although current observations do not completely rule out this possibility, at least for a fraction of dark matter [148].

Self-interactions We have established that DM is a collision-less particle, which means it has a weak interaction with itself. As a result, the DM halo around our galaxy remains spherical: if dark matter had the ability to dissipate energy like baryonic matter, a dark matter disk would form. At present, the bounds on DM self-interactions are derived from systems like the bullet cluster, which is a well-known visual demonstration of evidence for DM. It consists of two colliding clusters, each containing gas and a spherical dark matter halo. The gas is collisional, which prevents the two gas clouds from passing through each other, leading to an increase in temperature, which is observable through X-ray emission. Lensing observations prove instead that the DM halos continue their motion, behaving in a collision-less way. this allows to put a bound on the self-interactions [149]

$$\frac{\sigma_{\text{self}}}{m} \lesssim 1 \text{ cm}^2 g^{-1} \simeq 1 \text{ barn GeV}^{-1} . \tag{1.51}$$

This bound is actually weak, corresponding to a self-interaction cross-section smaller than the typical strong interaction cross-section. Dark matter self interactions have been advocated to alleviate the presence of too many structures at small scales [150].

Stability The particles accounting for the present dark matter relic density must be stable over the timescale of the age of the universe $H^{-1} \sim 14$ Gyr $\sim 4 \times 10^{17}$ s. However, the bound is stronger than this.

The most robust bound is independent on the decay products. its essence is the fact that the decay products, whatever they are, must be much lighter than the DM: this would imply a conversion of energy into radiation, affecting structure formation. The limit is [151]

$$\tau_{\text{dm}} \gtrsim 200 \text{ Gyr} \sim 10^{19} \text{ s} . \tag{1.52}$$

If the decay products are visible, the bound is even stronger, since the CMB would be affected: $\tau \gtrsim 10^{25-29}$ s [152].

Mass There is no specific mass scale identified by astronomical observations for the microscopic component of dark matter. If the DM is a new elementary particle it has a natural upper bound at the mass $M_{\rm pl}$. For super-Planckian values of the mass. The Compton wavelength of the particle would be smaller than its Schwarzschild radius, forming a black hole.

Lower bounds come from astronomical observations. We observe small dark matter-dominated structures, such as dwarf spheroidal galaxies with size $R_{\rm dSph} \sim$ kpc $\sim 10^{26}$ eV^{-1}. Dark matter needs to be localized within the length scale of these systems. We know that the localization of the particles have to take into account the statistics.

- **Bosons**. The smallest DM structures would be erased if particles could not be confined in a system of size. this would be the case for very light dark matter, see the next Chapter, for which the de Broglie wavelength is astronomical. If we fix $v \sim 100$ km/sec and impose $\lambda_{\rm dB} < R_{\rm dSph}$, we obtain the bound

$$m > \frac{2\pi}{v R_{\rm dSph}} \simeq 10^{-22}\ {\rm eV}\ . \tag{1.53}$$

- **Fermions**. The constrain is inevitably much stronger for fermions because of the Pauli exclusion principle. Let us consider the case in which all the energy levels are occupied. We consider an isothermal dark matter sphere of radius $R_{\rm dSph}$ and mass $M_{\rm dSph} = \frac{4\pi}{3}\rho R^3_{\rm dSph}$. If DM is fermionic with g internal degrees of freedom, the energy distribution is given by the Fermi-Dirac

$$f(E) = \frac{g}{\exp[(E-\mu)/T]+1}\ , \tag{1.54}$$

  where μ is the chemical potential. For a degenerate system it is appropriate to approximate $f(E)$ as

$$f(E) \approx \begin{cases} g & E < \mu \\ 0 & E > \mu \end{cases}\ . \tag{1.55}$$

  We can obtain the mass density integrating the phase space distribution over all the occupied level, i.e. up to the Fermi velocity $v_{\rm F}$

$$\rho = m \int \frac{d^3p}{(2\pi)^3} f(E) = g\frac{m^4}{2\pi^2}\int_0^{v_{\rm F}} dv\ v^2 = \frac{g m^4 v_{\rm F}^3}{6\pi^2}\ . \tag{1.56}$$

  Substituting this value of ρ in the formula for the mass and inverting to find the Fermi velocity

$$v_{\rm F} = \left[\frac{9\pi}{2g}\frac{M_{\rm dSph}}{m^4 R^3_{\rm dSph}}\right]^{1/3}\ . \tag{1.57}$$

We can obtain a bound on the mass imposing the Fermi velocity is smaller than the escape velocity $v_e = (2GM_{\rm dSph}/R_{\rm dSph})^{1/2}$. We find

$$m > \left[\frac{9\pi}{4\sqrt{2}g}\frac{1}{\sqrt{G^3 M_{\rm dSph} R_{\rm dSph}^3}}\right]^{1/4} \simeq 145\ {\rm eV}\left(\frac{10^8\ M_\odot}{M_{\rm dSph}}\right)^{1/8}\left(\frac{\rm kpc}{R_{\rm dSph}}\right)^{3/8}. \quad (1.58)$$

This is the so-called Tremaine-Gunn bound [16]. The direct implication is that if dark matter is lighter than the 10-100 eV scale, it must be bosonic.

Chapter 2

Wave Dark Matter

The goal of this Chapter is to provide an overview of the theoretical and phenomenological background on wave dark matter.

Wave dark matter can be simply defined as dark matter which exhibits wave features on macroscopic, or even astronomic scales. The origin of these wave features is the light mass of the dark matter candidate, smaller than roughly 10 eV. Since this mass scale is roughly one order of magnitude smaller than the Tremaine-Gunn bound [16–20], the particle candidates of wave dark matter are light bosons. The Bose-Einstein statistics, unlike the Fermi-Dirac one, allows for huge occupation numbers in phase space and this is the crucial feature which pushes for a wave description of dark matter.

Let us see what is special about the 10 eV mass scale. Astronomical measurements in the Milky Way give us information about the dark matter mass density in the solar neighborhood. Despite not being conclusive, all the measurements [48–50] converge on values around $\rho \sim 0.4\ \mathrm{GeV/cm^3}$. From this information, we are able to compute the average dark matter inter-particle separation in a Milky Way-like galaxy as a function of mass

$$d \sim \left(\frac{\rho}{m}\right)^{-1/3} \simeq 3 \times 10^{-3}\mathrm{cm} \left(\frac{10\ \mathrm{eV}}{m}\right)^{-1/3} . \tag{2.1}$$

Let us compare this distance with the de Broglie wavelength of a particle with mass 10 eV and with the typical virialized velocity in the solar neighborhood

$$\lambda_{\mathrm{dB}} \sim \frac{1}{mv} \simeq 3 \times 10^{-3}\mathrm{cm} \left(\frac{10\ \mathrm{eV}}{m}\right) \left(\frac{250\ \mathrm{km/s}}{v}\right) . \tag{2.2}$$

The fact that $d \sim \lambda_{\mathrm{dB}}$ allows us to set the value of the mass for which this happens $m \sim 10$ eV as a demarcation point in the dark matter mass spectrum [21]. The number of particles in a de Broglie volume $N_{\mathrm{dB}} = (\rho/m)\lambda_{\mathrm{dB}}^3 \propto m^{-4}$ is a sharply increasing function for a decreasing dark matter mass. This means that occupation number gets so large that the dark matter particles is best described by classical[1] waves, very much similarly to how photons are described as electromagnetic waves. At the same time, for smaller masses, the de Broglie wavelength gets larger and larger, reaching

[1] We will use the word *classical* in two ways: (i) to say that we can neglect quantum fluctuations, thanks to the large occupation number (see Section 2.3); (ii) to express the transition between wave dark matter and (classical) dark matter. The distinction should be clear based on the context.

astronomical-sized values:

$$\begin{aligned} \lambda_{\rm dB} &\simeq 1\ {\rm km} \left(\frac{10^{-6}\ {\rm eV}}{m}\right) , \\ &\simeq 0.1\ {\rm AU} \left(\frac{10^{-14}\ {\rm eV}}{m}\right) , \\ &\simeq 0.1\ {\rm kpc} \left(\frac{10^{-22}\ {\rm eV}}{m}\right) . \end{aligned} \tag{2.3}$$

Being the length scale at which wave features become observable, the de Broglie wavelength will always be a central quantity in our analyses. Here we provided the scalings according to three different values of the mass, for fixed $v \sim 250$ km/sec. The 10^{-6} eV case corresponds to the ballpark of the QCD axion, where most of the experimental searches have focused so far, see Section 2.1.1 and 2.7. The 10^{-14} eV case is particularly interesting since the de Broglie wavelength is close to the distance between Sun and Earth, for reasons that will be explored in Chapter 3. Other, slightly larger values of the mass can have features in smaller systems, such as the inner part of compressed dark matter halos, as we will see in Chapters 4 and 5. Finally, the ultralight scenario, or *fuzzy dark matter* [25], $m \sim 10^{-22}$ eV is the case in which wave dark matter has the most striking phenomenological consequences. The idea of such light scalars [22–29] has attracted recent interest to address small (sub kpc) scales structure issues in the standard cold dark matter paradigm [30, 31] in the case they cannot be solved by baryonic physics. Even lighter wave dark matter is excluded by observations of small structures, such as dwarfs spheroidal galaxies, which would be wiped out by interference effects. In this Chapter and throughout this thesis, we will mostly focus on the (ultra)-light end of the spectrum $m \sim 10^{-22} - 10^{-10}$ eV.

Most of the material presented in this Chapter is based on a number of reviews. Section 2.1 follows [21, 33, 153] mainly. Section 2.2 is inspired by the discussion in [153]. Section 2.3 presents our original work that can be found in the correspondent section of [106]. The description of wave dark matter and gravity in Section 2.4 as well as the main phenomenological implications in Section 2.5 integrate the content from [21, 25, 33] with our own arguments and explanations. Section 2.6 is based on the corresponding section of [96]. Finally, Section 2.7 borrows a lot of material and references from [95–97].

The outline is the following. In Section 2.1 we present a few motivated particle physics models that can accommodate for a wave dark matter candidate: these include axion-like particles (ALPs) and the dark photon. In the axion case, we show, studying the evolution of the field in 2.2, that these candidates are able to reproduce the observed relic density. Section 2.3 presents our treatment of the wave dark matter stochasticity and outlines the formalism we use in this thesis to describe the statistical properties of the field. Section 2.4 reviews the formalism to describe the interplay of wave dark matter and gravity: the Schrödinger-Poisson system, the fluid description and its implication for perturbation theory and structure formation. In Section 2.5 we present some phenomenological consequences on the gravitational dynamics of wave dark matter: the gravitational cooling, or relaxation, wave features in dynamical friction and the phenomenon of subhalo tidal disruption which

is of importance in addressing wave dark matter substructures and small scales. Section 2.6 reviews cosmological and astrophysical probes of ultralight scalars and vectors and Section 2.7 concludes, attempting a review of the many ideas for direct detection of wave dark matter.

2.1 Particle physics motivation

In this Section, we provide a brief theoretical overview of the particle physics models motivating wave dark matter candidates. We mostly refer to the reviews [21,95,153].

Historically, the first appearance of beyond standard model bosons so light to fall in the mentioned mass range characteristic of wave dark matter is the *axion*. This scalar particle, specifically dubbed the QCD axion, was originally proposed in the Peccei-Quinn (PQ) mechanism [154, 155] as a solution to the strong CP problem in the standard model, which refers to the observed lack of charge-parity (CP) violation in strong interactions. Weinberg [156] and Wilczek [157] identified axions as the pseudo-Nambu-Goldstone (pNG) boson of the newly broken global symmetry proposed by Peccei and Quinn.

However, nowadays, the term *axion* more freely refers to scenarios involving a pNG boson, with low mass and coupling that arises naturally from a broken symmetry at high energy scales. These models are usually less constrained than the QCD axion and do not relate to the PQ mechanism.

Another possibility which we can consider is that wave dark matter is constituted by a new vector boson, rather than a scalar particle. A scenario studied in the literature is the *dark photon*. The idea of adding to the SM a new $U(1)$ gauge boson [158,159], similar to the photon, was early on considered in the context of supersymmetric theories [160,161] and later extended to more general contexts [162,163]. We consider the scenario in which the dark photon is light and makes up the wave dark matter.

2.1.1 QCD axion

The strong CP problem The QCD Lagrangian suffers from the *strong CP problem*. Let us explain why. The following CP-violating terms are allowed in the QCD Lagrangian

$$\mathcal{L}_{\rm QCD} \supset \theta \frac{\alpha_s}{8\pi} G^a_{\mu\nu} \tilde{G}^{\mu\nu}_a - \left[\bar{q}_R M_q e^{i\theta_q} q_L + \text{h.c.} \right] . \tag{2.4}$$

Here $G_{\mu\nu}$ is the gluon field, $\tilde{G}_{\mu\nu} \equiv \frac{1}{2}\epsilon_{\mu\nu\rho\sigma}G^{\rho\sigma}$, its dual, $q_{L,R}$ left and right quark fields, M_q a quark mass matrix. The first term arises from the θ-vacua of QCD, meaning that θ can be understood as an angle setting the vacuum of the theory (see Appendix A of [153] and references therein for more details). Only a combination of the θ and θ_q parameter is physical. Indeed, performing a chiral rotation of the quark fields, the second term disappears. However, the gauge anomaly implies that a term identical to the first one appears but with $\arg\det M_q$ in place of θ. Therefore we are left with

$$\mathcal{L}_{\rm QCD} \supset \theta_{\rm QCD} \frac{\alpha_s}{8\pi} G^a_{\mu\nu} \tilde{G}^{\mu\nu}_a , \tag{2.5}$$

where $\theta_{\rm QCD} = \theta + \arg\det M_q$. This CP-violating term has the phenomenological consequence of predicting a electric dipole moment (EDM) for the neutron [164]

$$d_n = 3.6 \times 10^{-16} \theta_{\rm QCD}\, e\,\text{cm}, \tag{2.6}$$

with e the electron charge. However, experiments have not detected any neutron EDM so far, with the most stringent current bound being $|d_n| < 1.8 \times 10^{-26}\ e$ cm [165], implying $|\theta_{\rm QCD}| \lesssim 10^{-10}$. The strong CP problem is a fine tuning problem: why is $\theta_{\rm QCD}$ so small if it arises from two phases of different origin?

The Peccei-Quinn solution An elegant solution to the strong CP problem was proposed by Peccei and Quinn [154,155]. They postulated a new $U(1)$ global symmetry, called the PQ-symmetry, which is spontaneously broken at a high energy scale $f_{\rm PQ}$. This symmetry group acts as a chiral rotation, under which the $SU(3)$ color group is anomalous and produces the $\theta G\tilde{G}$ term. The fact that the PQ symmetry is spontaneously broken implies the existence of an uneaten Goldstone boson, whose phase ϕ, is a pseudoscalar field called the *axion* by Wilczek, as it is the field which washes the strong CP problem away. Indeed, thanks to the PQ mechanism, the low energy effective Lagrangian includes the term

$$\mathcal{L}_{\rm QCD} \supset \frac{\phi}{f_{\rm PQ}} \frac{\alpha_s}{8\pi} G^a_{\mu\nu} \tilde{G}^{\mu\nu}_a\,, \tag{2.7}$$

which replaces the $\theta_{\rm QCD}$ term of Eq. (2.5) absorbing it into a redefinition of the axion field ϕ. The crucial point in the discussion is that the above term, below the non-perturbativity QCD scale $\Lambda_{\rm QCD} \approx 200$ MeV is such that the axion gets a potential which allows it to relax to the CP-conserving value $\phi = 0$ [166], solving the strong CP problem.

The above coupling of the axions with the gluon field has important consequences, which are to a certain extent, independent on the specific way the axion is implemented in the SM. First of all it shows a suppression by a $f_{\rm PQ}$ factor. This implies that any phenomenological effect of axions will be suppressed. Indeed the original model (PQWW) or Peccei-Quinn-Weinberg-Wilczek), which has $f_{\rm PQ}$ at the electroweak scale, could be excluded by lack of observation of the rare kaon decay $K^\pm \to \pi^\pm \phi$. Values $f_{\rm PQ} \gtrsim 10^9$ GeV are usually required, mainly because of astrophysical bounds.

Secondly, the QCD non-perturbative effects generate a (small) mass for the axion field through the mixing with QCD mesons, making the axion a pseudo-Nambu-Goldstone boson. The mass is found to be

$$m_\phi \simeq \left(\frac{\sqrt{m_u/m_d}}{1+m_u/m_d}\right) \frac{m_\pi f_\pi}{f} \simeq 5.70 \times 10^{-6}\ \text{eV} \left(\frac{10^{12}\ \text{GeV}}{f_{\rm PQ}}\right) \tag{2.8}$$

and its small value is again due to the large value of $f_{\rm PQ}$. The fact that the mass is determined by QCD dynamics is crucial: the only free parameter is $f_{\rm PQ}$. The axion mass is actually temperature dependent, again due to QCD non-perturbative effects and the value in the above equation is only valid at zero temperature. This fact is of

importance when treating the cosmology of the QCD axion, see [167] and references therein. We will not deal with this effect.

Thirdly, the presence of the $\phi G\tilde{G}$ operator in the Lagrangian naturally implies a series of other couplings of the axion to the standard model field. After PQ symmetry breaking and non-perturbative effects have switched on, i.e. at energies below $\Lambda_{\rm QCD}$, the operators of interest are

$$\begin{aligned}\mathcal{L}_\phi \supset \quad & \frac{\phi}{f_{\rm PQ}}\frac{C_{\phi\gamma\gamma}}{8\pi}F_{\mu\nu}\tilde{F}^{\mu\nu} + \frac{\phi^2}{f_{\rm PQ}^2}\frac{C^{(2)}_{\phi\gamma\gamma}}{4\pi}F_{\mu\nu}F^{\mu\nu} \\ & + \frac{\partial_\mu\phi}{2f_{\rm PQ}}\sum_f C_\psi\bar{\psi}\gamma^\mu\gamma_5 f\psi + \frac{\phi^2}{f_{\rm PQ}^2}\sum_\psi C^{(2)}_\psi m_\psi\bar{\psi}\psi \\ & - \frac{iC_N}{2}\frac{\phi}{f_{\rm PQ}}\bar{N}\sigma_{\mu\nu}\gamma_5 N F^{\mu\nu}\,,\end{aligned} \tag{2.9}$$

i.e. the couplings to photons (first row) and to SM fermions (nucleons or leptons) (second row), including the nucleon N (proton or neutron) EDM coupling (third row). Here $\sigma_{\mu\nu} = \frac{i}{2}[\gamma_\mu, \gamma_\nu]$. Expressions for all standard model couplings of the QCD axion can be found in [168] and the EDM coupling is discussed in [169]. Experimental searches of axions are based on these operators, see Section 2.7.

2.1.2 Axion-like particles

The above discussion can be generalized for any other $U(1)$ spontaneously broken at a high energy scale f_ϕ. In this case, the pNG boson arising is not linked to the PQ mechanism or the strong CP problem whatsoever and therefore their mass m doesn't follow the relation with f_ϕ that we showed in Eq. (2.8), but a more general one, depending on the considered potential for the theory. In this cases we talk about axion-like particles (ALPs). For example we can think of a coupling of the type $\phi G\tilde{G}$ where G is now the field strength of a generic $SU(N)$ that shows non-perturbative effects at a scale Λ. ALPs which can be dark matter can also arise from the compactification of theories with extra-dimensions, including string theory [170–173] or from models which aim to solve either dynamically or anthropically the electroweak hierarchy problem [174–182].

A common way to write the potential of these models is [21]

$$V(\phi) = \Lambda^4\left[1 - \cos\frac{\phi}{f_\phi}\right]. \tag{2.10}$$

Here both f_ϕ and Λ are free parameters. At energy scales below Λ the ALP gets a mass $m \sim \Lambda^2/f_\phi$, which can be very tiny if f_ϕ is sufficiently high.

Finally, the couplings in Eq. (2.9), except the coupling to gluons which defines the QCD axion, can be introduced in a effective theory approach or just derived from the explicit model. If present, these operators can allow for direct detection of the ALPs, see Section 2.7.

2.1.3 Dark photon

Dark photons are another possibility for light bosonic dark matter. We refer to the recent review [183] to summarize the main properties of these candidates.

The Lagrangian Consider the Lagrangian with two abelian $U(1)$ gauge bosons coupled, respectively to SM matter current J_μ and to dark-sector matter J'_μ.

$$\mathcal{L} \supset -\frac{1}{4}F_{1\mu\nu}F_1^{\mu\nu} - \frac{1}{4}F_{2\mu\nu}F_2^{\mu\nu} - \frac{\epsilon}{2}F_{1\mu\nu}F_2^{\mu\nu} + eJ_\mu A_2^\mu + e'J'_\mu A_1^\mu \,. \tag{2.11}$$

The kinetic part of the Lagrangian can be diagonalized with the rotation [158]

$$\begin{pmatrix} A_1^\mu \\ A_2^\mu \end{pmatrix} = \begin{pmatrix} \frac{1}{\sqrt{1-\epsilon^2}} & 0 \\ -\frac{\epsilon}{\sqrt{1-\epsilon^2}} & 1 \end{pmatrix} \begin{pmatrix} \cos\theta & -\sin\theta \\ \sin\theta & \cos\theta \end{pmatrix} \begin{pmatrix} A'^\mu \\ A^\mu \end{pmatrix} \,. \tag{2.12}$$

We now can identify A_μ with the ordinary photon and A'_μ with the dark photon. The angle θ is arbitrary if the gauge bosons are massless. This freedom allows, in the massless case, either the dark photon to couple to both SM and dark current and the photon to just the SM, or, for another choice of θ, the dark photon couples only to the dark sector and the photon to both SM and dark particles, which then become "millicharged".

Instead, if the bosons get mass with a Higgs mechanism, the diagonalization of the mass terms sets θ to be the value required to rotate to the mass eigenstates. So we cannot have the freedom to set one of the bosons to couple just to one current. This is also what happens when the $U(1)$ gauge bosons acquire a mass by means of the Stueckelberg mechanism [184]. To diagonalize the Lagrangian

$$\mathcal{L} \supset -\frac{1}{2}M_1^2 A_{1\mu}A_1^\mu - \frac{1}{2}M_2^2 A_{2\mu}A_2^\mu - M_1 M_2 A_{1\mu}A_2^\mu \,, \tag{2.13}$$

θ is fixed by

$$\cos\theta = \frac{1-\delta\epsilon}{\sqrt{1-2\delta\epsilon+\delta^2}} \,, \tag{2.14}$$

with $\delta = M_2/M_1$. However, the most frequent case is when only one of the gauge boson gets a mass. In this case, the mass states are already diagonal. So, for $\delta = 0$, we obtain that the ordinary photon couples only to visible matter and the massive dark photon couples to the electromagnetic current of the SM as

$$\mathcal{L} \supset \left[\frac{e'}{\sqrt{1-\epsilon^2}}J'^\mu - \frac{e\epsilon}{\sqrt{1-\epsilon^2}}J^\mu\right]A'_\mu + eJ^\mu A_\mu \approx [e'J'^\mu - e\epsilon J^\mu]A'_\mu + eJ^\mu A_\mu \,. \tag{2.15}$$

This is the standard choice for the massive dark photon, and the portal interaction to the visible matter is suppressed by the kinetic mixing parameter ϵ. Notice that we do not actually need to assume the existence of a dark sector current J'_μ.

In another large class of models, the dark photon couples to the SM through direct gauge couplings, with Lagrangian

$$\mathcal{L} \supset -\frac{1}{4}F_{\mu\nu}F^{\mu\nu} - \frac{1}{4}F'_{\mu\nu}F'^{\mu\nu} + \frac{1}{2}m^2_{A'}A'_\mu A'^\mu + eJ^\mu A_\mu - gJ^\mu_{\rm SM}A'_\mu \tag{2.16}$$

with $J^\mu_{\rm SM}$ not necessarily the electromagnetic current. Examples include gauging of the baryon number or $U(1)_{B-L}$ and/or $U(1)_{L_e-L_\mu}$.

Dark photon dark matter If produced non-thermally as a condensate in the early universe, a very light massive dark photon could be a candidate for dark matter produced through the misalignment mechanism associated with an early inflationary epoch [185–188]. However, it cannot be produced in the vanilla misalignment mechanism, like in the case of ALPs [185]: a non-minimal coupling to gravity is needed [186]. The mechanism involves the value of the field being frozen by the rapidly expanding universe to the value it had at the initial moment. The rate of expansion is much larger than the mass, and the field does not have time to relax to the minimum of the potential. Although there is an unavoidable and problematic violation of Lorentz invariance, it is estimated to be small and undetectable.

The Stueckelberg mechanism is responsible for the mass of the dark photon in this scenario, requiring a non-minimal coupling to gravity. As the value of the Hubble constant drops below the mass of the dark photon, its field begins to oscillate, behaving like cold dark matter.

However, there are two important constraints that must be considered in this dark photon scenario. Firstly, the initial value must be finely tuned to match the critical density. Secondly, the decay into photons and SM leptons should not affect the cosmic microwave background. This means that the mixing parameter ϵ must not exceed a certain threshold (roughly less than 10^{-9}), and the mass $m_{A'}$ should be less than 1 MeV [186]. This is indeed not a problem if the dark matter is much lighter than the eV scale.

Other possibilities for non-thermal production of dark photon dark matter include production via parametric resonances [189], tachyonic instabilities developed via the rolling of an ALP [190–192] or the inflaton [193] and decay of topological defects such as global cosmic strings [194].

2.2 Ultralight scalars in cosmology

We focus on ultralight scalars, as they will be the reference case considered in this thesis; we put aside the dark photons for now. Axions are potentially crucial in various cosmological scenarios, including inflation, dark radiation, dark energy, and the physics of the cosmic microwave background. However, their most significant role could be as a potential candidate for (wave) dark matter [195–198]. Being this light, axions cannot be produced thermally, if they have to account for cold dark matter, so a peculiar mechanism must be studied.

Considering generic ALPs, they appear after the spontaneous symmetry breaking of a global $U(1)$. The most common production mechanism is the misalignment mechanism, or vacuum realignment. At high temperatures, the field is stuck due

to Hubble friction in a initial value $\theta_i = \phi_i/f_\phi \in [-\pi, \pi]$. Later on, when non-perturbative effects generate the axion mass and this value overcomes the Hubble parameter, the field starts oscillating around the minimum, behaving as a perfect cold dark matter candidate. We will see how the relic density can be reproduced. Alternatives and modification to the standard misalignment, e.g. when the field has an initial non-negligible kinetic energy, have also been studied [199–203], or when the ALP potential is non periodic [204].

In a full cosmological context, the phase transition from which the ALP originates can happen before inflation or after. This fact impacts the dynamics of the field. In the first case, the pre-inflationary scenario, the value of θ_i is unique for the whole observable universe, but it is in principle unknown. In the post-inflationary scenario, instead, θ_i takes random values in the angular domain in the different patches of the universe, so an average value $\theta_i = \pi/\sqrt{3}$ can be considered. However, in this case, the topological defects that arise from the phase transition are not wiped out by inflation so they can decay to produce lots of axions. Their contribution is subject of active debate, but the results seem to point to a contribution one [205, 206] or two [207, 208] orders of magnitude larger than the one from misalignment, with implications on the mass of the axion that reproduces the observed value of the dark matter relic density.

2.2.1 Relic density

Let us understand the evolution of the ALP field in a cosmological context and show that ALPs are good wave dark matter candidates. We taked a Friedmann-Robertson-Walker (FRW) universe with metric

$$ds^2 = dt^2 - a^2(t)\delta_{ij}dx^i dx^j \,, \tag{2.17}$$

where a is the scale factor. We consider the following Lagrangian for the ALP

$$\mathcal{L}_\phi \supset \frac{1}{2}\partial_\mu\phi\partial^\mu\phi - V(\phi) \,, \tag{2.18}$$

with $V \approx m^2\phi^2/2$ when the universe is colder than the strong coupling scale Λ. The mass is given by $m = \Lambda^2/f$ where f is the breaking scale of the $U(1)$ defining the axion. The stress-energy tensor of the field can be found $T_{\mu\nu} = \partial_\mu\phi\partial_\nu\phi - g_{\mu\nu}\mathcal{L}$:

$$T^0_0 = \rho_\phi = \frac{1}{2}f^2\dot{\theta}^2 + V(\theta) \,, \tag{2.19}$$

$$T^i_j = -P_\phi\delta^i_j = \left[\frac{1}{2}f_\phi^2\dot{\theta}^2 - V(\theta)\right]\delta^i_j \,. \tag{2.20}$$

The equation of motion for the field is the Klein-Gordon equation (see Appendix A for a derivation). We write it for $\theta = \phi/f$:

$$\ddot{\theta} + 3H\dot{\theta} + m^2\theta = 0 \tag{2.21}$$

and appears to be the equation of motion of a damped oscillator. We have two regimes

- $m \ll 3H$. The axion field is frozen to the initial value θ_i by the Hubble friction term. If $f_\phi^2\dot{\theta}^2 \ll 2V$ the field slow rolls and $w = P_\phi/\rho_\phi \simeq -1$, therefore the axion behaves as a contribution to dark energy.

- $m \gg 3H$. As the universe cools down and H decreases, the ALP field begins to coherently oscillate about the potential minimum. Let us focus on the oscillation phase. We denote with $a_{\rm osc}$ the scale factor when $m \approx 3H(a_{\rm osc})$. The field starts oscillating with frequency $\sim m$ and, subsequently, in the fast oscillation regime $m \gg 3H$. We average on timescales larger than $1/m$ and we find, thanks to the virial theorem

$$\langle \rho_\phi \rangle = \left\langle \frac{1}{2} f^2 \dot{\theta}^2 \right\rangle + \langle V(\theta) \rangle = m^2 f^2 \theta^2 \,, \tag{2.22}$$

$$\langle P_\phi \rangle = 0 \,. \tag{2.23}$$

  Therefore the axion-like field behaves as pressure-less matter, hence $\langle \rho_\phi \rangle \propto a^{-3}$ like we expect from cold dark matter.

We can estimate f from the requirement that matter-radiation equality is achieved at $T_{\rm eq}$. We assume that the oscillation started in the radiation-dominated era and that the mass is temperature-independent. The temperature $T_{\rm osc}$ can be found from $m \approx 3H(a_{\rm osc}) \sim 3T_{\rm osc}^2/M_{\rm pl}$. So

$$T_{\rm osc} \sim \sqrt{\frac{M_{\rm pl} m}{3}} \sim 300 \text{ eV} \left(\frac{m}{10^{-22} \text{ eV}}\right)^{1/2} \,. \tag{2.24}$$

This is after BBN, so the axion behaves during BBN as a negligible contribution to dark energy. At the $T_{\rm osc}$ the ratio of radiation and matter energy density is $\rho_{\rm r}/\rho_m \sim T_{\rm osc}^4/\Lambda^4$ and it grows as $\propto a^{-1} \propto T$. We impose the ratio to be about unity at matter-radiation equality, $T_{\rm eq} \sim$ eV and use $\Lambda^4 = m^2 f^2$. Assuming $\theta_i \sim 1$

$$1 \sim \frac{\rho_{\rm r}(a_{\rm eq})}{\rho_{\rm m}(a_{\rm eq})} = \frac{T_{\rm osc}^4}{m^2 f^2} \frac{T_{\rm eq}}{T_{\rm osc}} \,, \tag{2.25}$$

from which

$$f \sim \frac{M_{\rm pl}^{3/4} T_{\rm eq}^{1/2}}{m^{1/4}} \sim 0.5 \times 10^{17} \text{ GeV} \left(\frac{m}{10^{-22} \text{ eV}}\right)^{-1/4} \,. \tag{2.26}$$

This is consistent with our assumptions on the ALP model with $f < M_{\rm pl}$.

Let us find the relic density today, assuming as before, that $a_{\rm osc} < a_{\rm eq}$. After the ALP has started to oscillate, the number of axions in a comoving volume is conserved and $\rho_\phi \propto a^{-3}$, so

$$\Omega_\phi = \frac{\rho_\phi(a_{\rm osc})}{\rho_{\rm cr}} a_{\rm osc}^3 \,. \tag{2.27}$$

Substituting the Friedmann equation for a radiation-dominated universe, we can find the value of $a_{\rm osc} = (9\Omega_{\rm r} H_0^2/m^2)^{1/4}$. Now we average over fast oscillations and

assume $\rho_\phi(a_{\rm osc}) \approx m^2 f^2 \theta^2 \sim m^2 f^2 \theta_i^2$, with θ_i the starting random value and obtain

$$\begin{aligned} \Omega_\phi &= \frac{1}{3}(9\Omega_{\rm r})^{3/4} \left(\frac{m}{H_0}\right)^{1/2} \left(\frac{f}{M_{\rm pl}}\right)^2 \theta_i^2 \\ &\simeq 0.13\theta_i^2 \left(\frac{\Omega_{\rm r}}{10^{-5}}\right)^{3/4} \left(\frac{m}{10^{-22}\,{\rm eV}}\right)^{1/2} \left(\frac{f}{10^{17}\,{\rm GeV}}\right)^2 , \end{aligned} \tag{2.28}$$

using again the fuzzy dark matter mass as a reference point. For larger values of the mass, the value of f should be considered accordingly, as in Eq. (2.26). We see that the ALP produced through the misalignment mechanism is able to reproduce the dark matter relic density today.

2.2.2 Self-interactions

What is the impact of self-interactions? The ALP potential includes higher order terms which may spoil the evolution of the field. We follow the discussion in [33]. Including the next-to-leading order in the equation of motion, we get

$$\Box\theta + m^2\theta - \frac{m^2}{6}\theta^3 = 0\,. \tag{2.29}$$

The box operator contains the contribution from gravity. The cubic term is attractive and has to be compared to gravity. We can estimate $\Box\theta \sim \Phi m^2\theta$; therefore the θ^3 term will be important if $\theta^2 \gtrsim \Phi$. We can test this condition in the early universe and today.

At the temperature $T_{\rm osc}$, we have $\theta^2 \sim 1$, while the primordial gravitational perturbation is $\Phi \sim 10^{-5}$. Therefore $\theta^2 \gg \Phi$ and self-interactions dominate over gravity. However, $\theta^2 \propto a^{-3}$ so $\theta^2 \sim \Phi$ at temperatures $10^{-5/3} T_{\rm osc} \sim 7$ eV, which is before equality (we used the $T_{\rm osc}$ found in the computation of the relic density). So as soon as matter perturbation can grow, gravity surely dominates, and structure formation is not spoiled.

Consider instead a bound structure of ALPs of density ρ and size R in today's universe. From the Poisson equation $\Phi \sim \rho R^2/(8\pi M_{\rm pl}^2)$. Since the density is $\rho \sim f^2 m^2 \theta^2$, we have that $\theta^2 \gtrsim \Phi$ when

$$R \lesssim \frac{\sqrt{8\pi} M_{\rm pl}}{mf} \sim 10\,{\rm pc} \left(\frac{10^{-22}\,{\rm eV}}{m}\right) \left(\frac{10^{17}\,{\rm GeV}}{f}\right)\,. \tag{2.30}$$

This means that in a ALP structure of size greater than 10 pc, gravity dominates over self interactions.

2.3 Statistical properties

In this section, our focus is on investigating the statistical properties of the wave dark matter field. Our approach is based on the corresponding section in [106]. We introduce a formalism that enables us to account for the stochastic nature of the field and its behavior as a collection of classical waves in computing observable quantities

such as correlation functions. While our analysis assumes a spinless boson with mass m for simplicity, it can be readily extended to vector bosons.

We start from a QFT-like decomposition of the field, that is as a superposition of (complex) wave modes φ_i and annihilation and creation operators. If the quantization of the field is realized in a finite volume V, we can write

$$\hat{\phi}(x) = \sum_i \frac{1}{\sqrt{2\omega_i V}} \left[\hat{a}_i \varphi_i(x) + \hat{a}_i^\dagger \varphi_i^\star(x)\right] . \tag{2.31}$$

The annihilation and creation operators $\hat{a}_i, \hat{a}_i^\dagger$ satisfy the canonical commutation relations $[\hat{a}_i, \hat{a}_j^\dagger] = \delta_{ij}$. The sum over the index i denotes all the quantum numbers. If the field is free in flat space-time, the mode functions take the simple plane wave form $\varphi_i = e^{-ik_i \cdot x}$. Here $k_i = (\omega_i, \mathbf{k}_i)$ is the four-momentum associated to the plane wave.

Usually the three-momentum $\mathbf{k}$ is taken itself as a quantum number for the free particles and the continuum limit is performed. In this case the field has the expansion

$$\hat{\phi}(x) = \int \frac{d^3k}{(2\pi)^3} \frac{1}{\sqrt{2\omega_\mathbf{k}}} \left[\hat{a}_\mathbf{k} \varphi_\mathbf{k}(x) + \hat{a}_\mathbf{k}^\dagger \varphi_\mathbf{k}^\star(x)\right] , \tag{2.32}$$

and the annihilation and creation operators satisfy the commutation relation in the form $[\hat{a}_\mathbf{k}, \hat{a}_{\mathbf{k}'}^\dagger] = (2\pi)^3 \, \delta^{(3)}(\mathbf{k} - \mathbf{k}')$. Our goal is to examine the statistical characteristics of this field, specifically to determine the density operator, which is utilized to calculate the expectation values of operators in this theory.

2.3.1 Density operator of a harmonic oscillator

We begin with a simple example: the harmonic oscillator in quantum mechanics with Hamiltonian operator

$$\hat{H} = \omega \left(\hat{a}^\dagger \hat{a} + \frac{1}{2}\right) . \tag{2.33}$$

The statistical properties of the harmonic oscillator are described by the density operator $\hat{\rho}$. A way to write the operator is in the bases constructed from the eigenstates $|n\rangle$ of the number operator $\hat{N} = \hat{a}^\dagger \hat{a}$. Therefore we can write

$$\hat{\rho} = \sum_n P_n \, |n\rangle \, \langle n| . \tag{2.34}$$

The coefficients P_n are the probabilities of finding the oscillator in the eigenstate $|n\rangle$. They have to satisfy the following constraints:

$$\mathrm{Tr}[\hat{\rho}] = \sum_n P_n = 1 , \tag{2.35}$$

$$\mathrm{Tr}[\hat{N}\hat{\rho}] = \sum_n n P_n = \langle n \rangle , \tag{2.36}$$

with $\langle n \rangle$ the occupation number of eigenstate $|n\rangle$.

We want to find the form of P_n that maximizes the von Neumann entropy

$$\mathcal{S} = -\operatorname{Tr}[\hat{\rho}\log\hat{\rho}] = -\sum_n P_n \log P_n \,, \tag{2.37}$$

subject to the above two constraints. The maximization can be performed introducing two Lagrange multipliers λ_1 and λ_N. We maximize

$$\mathcal{L} = -\sum_n P_n \log P_n + \lambda_1 \left(\sum_n P_n - 1\right) + \lambda_N \left(\sum_n n P_n - \langle n\rangle\right) \,, \tag{2.38}$$

that is

$$0 = \delta\mathcal{L} = -\sum_n [\log P_n + 1 - \lambda_1 - \lambda_N n]\, \delta P_n. \tag{2.39}$$

We find $P_n = e^{\lambda_1 - 1 + n\lambda_N}$ and imposing the constraints, we can rewrite the probability coefficients as

$$P_n = \frac{1}{1+\langle n\rangle}\left(\frac{\langle n\rangle}{1+\langle n\rangle}\right)^n \,, \tag{2.40}$$

from which the density matrix reads

$$\hat{\rho} = \frac{1}{1+\langle n\rangle}\sum_n \left(\frac{\langle n\rangle}{1+\langle n\rangle}\right)^n |n\rangle\langle n| \,. \tag{2.41}$$

The above procedure applies as long as the statistical properties of the excitation are chaotic, as detailed in [209]. Therefore, we can express the density matrix as a function of the occupation number. This is of primary importance for our study of the statistical properties of the scalar field.

As an example, one can verify this procedure in the case of thermal equilibrium. If one throws in this assumption, with inverse temperature β, then the density operator is

$$\hat{\rho} = \frac{1}{\operatorname{Tr}[e^{-\beta\hat{H}}]}\exp[-\beta\hat{H}] \,. \tag{2.42}$$

The occupation number is fixed in the thermal case by the Bose-Einstein distribution

$$\langle n\rangle = \frac{1}{e^{\beta\omega}-1} \tag{2.43}$$

and one can see that this satisfies the form of P_n required to reproduce the thermal form of $\hat{\rho}$.

Ultimately, we want to apply this statistical formalism to wave dark matter. Being interested in a system with a large occupation number, it is convenient to rewrite the above density matrix in the coherent state representation. Coherent states are defined from number states as

$$|\alpha\rangle = e^{-|\alpha|^2/2}\sum_{n=0}^{\infty}\frac{\alpha^n}{\sqrt{n!}}|n\rangle \,. \tag{2.44}$$

They are constructed to be eigenstates of the annihilation operator, i.e. $\hat{a}\,|\alpha\rangle = \alpha\,|\alpha\rangle$, with α a complex number. With the coherent state, the density operator can be expressed in the Glauber-Sudarshan representation [210, 211] as

$$\hat{\rho} = \int d^2\alpha\; P(\alpha)\,|\alpha\rangle\,\langle\alpha|\;, \tag{2.45}$$

where $P(\alpha)$ is a quasi-probability distribution, defined as

$$P(\alpha) = \frac{1}{\pi\,\langle n\rangle}\exp\left[-\frac{|\alpha|^2}{\langle n\rangle}\right]\;. \tag{2.46}$$

For the density matrix in Eq. (2.45), the quasi-probability distribution has the desired properties to be interpreted as a probability distribution for a complex number α; it is positive $P(\alpha) \geq 0$ and integrates to one $\int d^2\alpha\; P(\alpha) = 1$. Interestingly, it can be factorized into two probability distributions, one for the modulus $|\alpha|$ and one for the the phase $\theta = \arg(\alpha)$ as

$$P(\alpha) = P(|\alpha|)P(\theta)\;, \tag{2.47}$$

where the modulus follows the Rayleigh distribution and the phase is uniformly distributed

$$P(|\alpha|) = \frac{2|\alpha|}{\langle n\rangle}\exp\left[-\frac{|\alpha|^2}{\langle n\rangle}\right]\;, \tag{2.48}$$

$$P(\theta) = \frac{1}{2\pi}\;. \tag{2.49}$$

Being equipped with an explicit form for the density matrix, we are able to compute expectation values of any operator decomposed in annihilation and creation operators, we denote as $\hat{A}(\hat{a},\hat{a}^\dagger)$

$$\left\langle\hat{A}\right\rangle = \mathrm{Tr}[\hat{A}\hat{\rho}] = \int d^2\alpha\,\langle\alpha|\,\hat{A}\hat{\rho}\,|\alpha\rangle\;. \tag{2.50}$$

As a simple example, we can compute the expectation value of the number operator:

$$\begin{aligned}
\left\langle\hat{N}\right\rangle &= \int d^2\alpha\,\langle\alpha|\,\hat{a}^\dagger\hat{a}\hat{\rho}\,|\alpha\rangle \\
&= \int d^2\alpha\int d^2\alpha'\;P(\alpha')\,\langle\alpha|\,\hat{a}^\dagger\hat{a}\,|\alpha'\rangle\,\langle\alpha'|\alpha\rangle \\
&= \int d^2\alpha\int d^2\alpha'\;P(\alpha')\alpha^\star\alpha'\delta^{(2)}(\alpha-\alpha') \\
&= \int d^2\alpha\;P(\alpha)|\alpha|^2 = \langle n\rangle\;,
\end{aligned} \tag{2.51}$$

as we expected. If we were to compute the expectation value of $\hat{N}^\dagger$ instead, since $\hat{a}\hat{a}^\dagger = \hat{a}^\dagger\hat{a}+1$, we would have obtained $\left\langle\hat{N}^\dagger\right\rangle = \langle n\rangle + 1$. However we are interested in a situation in which $\langle n\rangle$ is huge. Therefore, when computing expectation values, we can safely ignore the non-commutativity of annihilation and creation operator, knowing that the resulting terms will be suppressed by a $1/\langle n\rangle$ factor.

The above exercise teaches us that, since the coherent states are eigenstates of the

annihilation operator, we can replace the bracketed operator with a function A of complex variables $\alpha,\ \alpha^\star$

$$\langle\alpha|\,\hat{A}(\hat{a},\hat{a}^\dagger)\,|\alpha\rangle = A(\alpha,\alpha^\star) + \mathcal{O}\left(\frac{1}{\langle n\rangle}\right) \tag{2.52}$$

up to terms suppressed by the occupation number. Consequently, modulo these sub-leading terms,

$$\left\langle\hat{A}\right\rangle \approx \int d^2\alpha\ P(\alpha)A(\alpha,\alpha^\star)\ . \tag{2.53}$$

2.3.2 Density operator of wave dark matter

Let us now consider the case of wave dark matter. Our field $\hat{\phi}$ is decomposed in a linear combination of modes. It is natural to consider each mode as an independent harmonic oscillator. Therefore the density operator is given by the product of density operators for each mode of quantum number i:

$$\hat{\rho} = \prod_i \hat{\rho}_i = \left[\prod_i \int d^2\alpha_i P(\alpha_i)\right] |\{\alpha_i\}\rangle\,\langle\{\alpha_i\}|\ . \tag{2.54}$$

The form of the probability distribution for each α_i is the same as in Eq. (2.46). We have introduced a multi-mode coherent state, defined as $\hat{a}_j\,|\{\alpha_k\}\rangle = \delta_{jk}\alpha_k\,|\{\alpha_k\}\rangle$.

The density operator in Eq. (2.54) completely determines the statistical properties of the scalar dark matter field, meaning that we are able to compute any operator constructed from $\hat{\phi}$. We can generalize what we understood for the single mode harmonic oscillator. We can replace any operator $\hat{A}(\hat{a}_i,\hat{a}_j^\dagger)$ with a function of complex variables $A(\alpha_i,\alpha_j^\star)$ each of which follows the probability distribution $P(\alpha_i)$. Any term arising from the non-vanishing commutation relations between creation and annihilation operator is suppressed by the occupation number of the mode.

In other words, we find

$$\begin{aligned}
\left\langle\hat{a}_i^\dagger\hat{a}_j\right\rangle &= \delta_{ij}\,\langle n_i\rangle \\
\left\langle\hat{a}_i\hat{a}_j^\dagger\right\rangle &= \delta_{ij}[\langle n_i\rangle + 1] \approx \left\langle\hat{a}_i^\dagger\hat{a}_j\right\rangle \\
\left\langle\hat{a}_i\hat{a}_j\right\rangle &= \left\langle\hat{a}_i^\dagger\hat{a}_j^\dagger\right\rangle = 0
\end{aligned} \tag{2.55}$$

Therefore, any expectation value will be given by, up to sub-leading terms,

$$\left\langle\hat{A}(\hat{a}_i,\hat{a}_j^\dagger)\right\rangle \approx \left[\prod_{k=i,j}\int d^2\alpha_k\ P(\alpha_k)\right]\ A(\alpha_i,\alpha_j^\star)\ . \tag{2.56}$$

From the discussion above, we deduce that, when computing expectation values of the field $\hat{\phi}$, we can instead consider the function

$$\phi(x) = \sum_i \frac{1}{\sqrt{2\omega_i V}}\left[\alpha_i\varphi_i(x) + \alpha_i^\star\varphi_i^\star(x)\right]\ . \tag{2.57}$$

We treat each α_i as a random variable, following the probability distribution in Eq. (2.46), while ignoring possible quantum fluctuation suppressed by $1/\langle n_i \rangle$. In depth, this is the essence of the treatment of wave dark matter as classical waves. The huge occupation number in each mode allows us to neglect quantum fluctuations and the field manifests a classical wave behavior, with all the related interference and diffraction phenomena linked to it.

The discussion above can be easily generalized in case of continuous quantum number(s) and the continuum limit can be performed. This formalism reproduces the statistical properties of the scalar field obtained in other approaches [212,213] for the plane wave decomposition $\varphi_i(x) = e^{-ik_i \cdot x}$. The stochasticity of the field proves to be crucial for wave dark matter detection experiments, as it may affect the correct interpretation of the data as shown in [71–73,212–216].

2.4 Wave dark matter and gravity

In this Section, we outline the formalism to describe the wave dark matter in presence of gravity, which is the central topic of this thesis. More details about the derivation of the various equations, under the different assumptions, are in Appendix A.

Let us consider a spinless bosonic dark matter particle with a mass m, minimally coupled to gravity. We start from the action

$$S = \int d^4x \, \sqrt{-g} \left[\frac{M_{\rm pl}^2}{2} R + \frac{1}{2} g^{\mu\nu} (\partial_\mu \phi)(\partial_\nu \phi) - \frac{1}{2} m^2 \phi^2 \right] . \tag{2.58}$$

We make an assumption on the metric, which we take to be the perturbed Friedmann-Robertson-Walker (FRW) metric [33] in Newtonian gauge

$$ds^2 = [1 + 2\Phi(t, \mathbf{x})] dt^2 - a^2(t) [1 - 2\Phi(t, \mathbf{x})] \delta_{ij} dx^i dx^j . \tag{2.59}$$

here $a(t)$ is the scale factor and $\Phi(t, \mathbf{x})$ is a (small) gravitational potential that is treated perturbatively. As we explain in Appendix A, while it is possible to consider even a more general metric, with two scalar potentials, Φ and Ψ, for most of the applications involving wave dark matter, $\Phi = \Psi$ is enforced by the Einstein's equations.

We want to write the equation of motion for the wave dark matter field ϕ in a curved spacetime. This is the so-called Klein-Gordon equation

$$\frac{1}{\sqrt{-g}} \partial_\mu [g^{\mu\nu} \sqrt{-g} \, \partial_\nu \phi] + m^2 \phi = 0 . \tag{2.60}$$

The equations of motion, in general, are coupled to the equations for the scale factor, i.e. the Friedmann equations, and for the potential Φ, obtained from the Einstein equations for the metric. We show the general form of both the Einstein and the Klein-Gordon equations and their declination in the specific approximations in Appendix A.

2.4.1 The Schrödinger-Poisson system

Wave dark matter is non-relativistic in most physical systems and scales. It is therefore useful to write the Klein-Gordon equation Eq. (2.60) in a form more suited for the treatment of non-relativistic dark matter. The idea is to factor out the fast time oscillations at frequency m and focus on the oscillations at smaller frequency mv^2 where $v \ll 1$ is the dark matter velocity. In this way, we can study the de Broglie-wavelength oscillations of the wave dark matter field.

We consider the field expansion in Eq. (2.57), we approximate $\omega_i \approx m + \mathbf{k}^2/(2m)$ and factor out the fast time oscillation of the wave mode function, that is we introduce wave functions for the single modes $\varphi_i = \psi_i e^{-imt}$:

$$\phi(x) = \sum_i \frac{1}{\sqrt{2m}} \left[\alpha_i \psi_i(x) e^{-imt} + \alpha_i^\star \psi_i^\star(x) e^{imt} \right] . \tag{2.61}$$

For compactness, we can introduce the wave function of the full system $\psi(x)$, summing all the modes $\psi = \sum_i f_i \psi_i$ with appropriate coefficients f_i, we get then

$$\phi(t, \mathbf{x}) = \frac{1}{\sqrt{2m}} \left[\psi(t, \mathbf{x}) e^{-imt} + \psi(t, \mathbf{x}) e^{imt} \right] . \tag{2.62}$$

Notice that ψ has mass dimension $3/2$. Since the Klein-Gordon equation is linear and homogeneous in ϕ, the constant numerical prefactors do not matter, and we can obtain easily an equation for either ψ or each i-mode, ψ_i. To be consistent with our non-relativistic expansion, we assume that the wave function is slowly varying, that is $|\partial_t^2 \psi| \ll m |\partial_t \psi|$ i.e. the time scale over which ψ varies is much longer than $1/m$. Under these assumptions we obtain [33]

$$i \left[\partial_t \psi + \frac{3}{2} H \psi \right] = \left[-\frac{\nabla^2}{2ma^2} + m\Phi \right] \psi . \tag{2.63}$$

The steps for the derivation of this equation from the general Klein-Gordon equations are outlined in Appendix A.

Notice that the above equation depends on $a(t)$ and $\Phi(t, \mathbf{x})$. In our case, the equations for the background expansion of the universe, i.e. the Friedmann equations, can be decoupled from the one of the perturbations and solved independently. Once this is done, under the assumption that Φ is slowly-varying or time-independent, the remaining part of the Einstein equation becomes the Poisson equation

$$\nabla^2 \Phi = 4\pi G a^2 (\rho_{\text{ext}} + \rho_\phi) , \tag{2.64}$$

as shown in Appendix A. This leads to the Schrödinger-Poisson (SP) system on cosmological scales, for which Eq. (2.63) and Eq. (2.64) have to be solved at the same time. Indeed we see that the right-hand-side of the Poisson equation contains the dark matter energy density $\rho_\phi = m|\psi|^2$ (in the non-relativistic approximation, as shown in Appendix A) but may also include any external matter density ρ_{ext}. The context imposes which one of the two terms dominates or if we have to consider both.

For many galactic dynamics applications or on even smaller scales, it is a good

approximation to set the scale factor to unity and the Hubble parameter to zero. This will be the case for wave dark matter in the Solar system, which we investigate in Chapter 3 and inside the inner part of wave dark matter halos, the subject of Chapters 4 and 5. Under the small-scale assumption, we obtain the well-known SP system [43]

$$\begin{aligned} i\partial_t\psi &= \left[-\frac{\nabla^2}{2m}+m\Phi\right]\psi\,, \\ \nabla^2\Phi &= 4\pi G(\rho_{\rm ext}+m|\psi|^2)\,. \end{aligned} \tag{2.65}$$

We stress that the ψ should be thought of as a (complex) classical field and not as a quantum wave function. We will still refer to ψ as the wavefunction anyway. The situation is very similar to the formalism adopted in modeling quantum fluids such as Bose condensates, by means of a mean field approach (e.g. the Gross-Pitaevskii equation). Notice that, in deriving the SP system, we treated perturbatively only the gravitational potential, therefore the results will be valid even in the non-linear regime in terms of density fluctuations around $|\psi|^2$. This makes the SP system particularly suitable for simulations of structure formation on non-linear scales and in general to deal with wave dark matter dynamics on small scales.

2.4.2 Fluid description

From the Schrödinger picture, it is easy to move to a fluid description of the wave equation through the Madelung formulation [217, 218]. We rewrite the Schrödinger equation in terms of a fluid density $\rho(t,\mathbf{x})$ defined such as

$$\psi \equiv \sqrt{\frac{\rho}{m}}e^{i\theta}\,. \tag{2.66}$$

The phase $\theta(t,\mathbf{x})$ is the potential for the fluid velocity $\mathbf{v}(t,\mathbf{x})$:

$$\mathbf{v} \equiv \frac{1}{ma}\nabla\theta = \frac{1}{2ima|\psi|^2}\left[\psi^\star\nabla\psi-\psi\nabla\psi^\star\right]\,. \tag{2.67}$$

Being the gradient of the phase, the velocity is irrotational, i.e. its curl is zero, $\nabla\times\mathbf{v}=0$. Moreover, the fluid velocity is a gradient flow, resembling that of a superfluid. Substituting the new form of ψ in the Schrödinger-Poisson system, and splitting the real and imaginary part of Eq. (2.63), we obtain the set of equations

$$\begin{aligned} &\partial_t\rho+3H\rho+\frac{1}{a}\nabla\cdot(\rho\mathbf{v})=0\,, \\ &\partial_t\mathbf{v}+H\mathbf{v}+\frac{1}{a}(\mathbf{v}\cdot\nabla)\mathbf{v}=-\frac{1}{a}\nabla\Phi+\frac{1}{2a^3m^2}\nabla\left[\frac{\nabla^2\sqrt{\rho}}{\sqrt{\rho}}\right]\,, \\ &\nabla^2\Phi=4\pi Ga^2(\rho_{\rm ext}+\rho)\,. \end{aligned} \tag{2.68}$$

These are known as Madelung equations, generalized to a perturbed FRW metric. They resemble the continuity (mass conservation) and Euler equations for a perfect unviscous fluid. These are the equations commonly used in the Jeans analysis of linear perturbation theory and are well-suited to numerical simulations, because

standard hydrodynamics codes can be modified to incorporate the additional term in the Euler equation [29, 219, 220]. The Euler equation shows how the particle limit is obtained: for large m, it reduces to that for a pressureless fluid, as it is appropriate for particle dark matter.

The wave nature of the fluid provides us an additional term with respect to the pressureless fluid case. It is called the *quantum pressure* term, even though it arises from the classical wave description:

$$Q = -\frac{1}{2a^3m^2}\nabla\left[\frac{\nabla^2\sqrt{\rho}}{\sqrt{\rho}}\right] . \tag{2.69}$$

Notice the minus sign: this term opposes gravity compression. An easy estimate shows on which scales λ the quantum pressure term beats the gravity gradient in a self-gravitating system. We approximate, thanks to the Poisson equation, $\Phi \sim G\rho\lambda^2$

$$\frac{\text{quantum pressure}}{\text{gravity gradient}} = \frac{1}{a^3m^2\lambda^3}\frac{a\lambda}{G\rho\lambda^2} \gtrsim 1 , \tag{2.70}$$

which gives

$$\lambda \gtrsim \lambda_J = \left(\frac{1}{am\sqrt{G\rho}}\right)^{1/2} . \tag{2.71}$$

As we shall prove in the next section, this is precisely the so-called *Jeans scale* in the wave dark matter case, which sets the typical size of an overdense region that is going to collapse under gravity, forming a bound structure. Notice that this scale is the geometric mean of the Compton length $1/m$ and the dynamical scale of a gravitating system $(G\rho)^{-1/2}$. The peculiarity of our system is actually even deeper: the Jeans scale is the de Broglie wavelength of the ground state of a particle in the gravitational potential well [25]. Notice that the velocity of the fluid is given by $v \sim Hr \sim (G\rho)^{-1/2}r$, because of the Friedmann equation. Hence $\lambda_{\rm dB} \sim (mv)^{-1} \sim (G\rho)^{-1/2}(mr)^{-1}$. Setting $r \sim \lambda_{\rm dB}$, returns the Jeans scale λ_J.

We can understand this fundamental result from two main points of view. The first is from the wave-particle duality: the stability below the Jeans scale is guaranteed by the uncertainty principle, since an increase in momentum opposes any attempt to confine the particle further. The second is from the fluid picture: below the Jeans-De Broglie scale the quantum pressure term prevents further confinement of the fluid. The two pictures are of course equivalent and can be summarized in the fuzziness property of our wave dark matter candidate.

2.4.3 Perturbation theory

The standard fluid picture we derived in the previous section is particularly suitable to study linear perturbations in Fourier space in order to see differences in the evolution of perturbations with respect to (particle) cold dark matter.

We start from the system of Eq. (2.68) and we linearly perturb it:

$$\begin{aligned} \rho(t,\mathbf{x}) &= \bar{\rho}(t) + \varrho(t,\mathbf{x}) + \mathcal{O}(\varrho^2)\,, \\ \mathbf{v}(t,\mathbf{x}) &= \mathbf{v}(t,\mathbf{x}) + \mathcal{O}(v^2) \\ \Phi(\mathbf{x}) &= \bar{\Phi} + \epsilon(\mathbf{x}) + \mathcal{O}(\epsilon^2) \end{aligned} \tag{2.72}$$

Notice that the velocity is already perturbed at first order, i.e. the background component is zero. The background density follows $\partial_t\bar{\rho} + 3H\bar{\rho} = 0$. We obtain

$$\begin{aligned} &\partial_t\varrho + \frac{\bar{\rho}}{a}\nabla\cdot\mathbf{v} = 0\,, \\ &\partial_t\mathbf{v} + H\mathbf{v} + \frac{1}{a}\nabla\epsilon - \frac{1}{2m^2a^3}\nabla\frac{\nabla^2\varrho}{2\bar{\rho}} = 0\,, \\ &\nabla^2\epsilon - 4\pi G a^2\varrho = 0\,. \end{aligned} \tag{2.73}$$

Now we spatially Fourier transform the system, obtaining

$$\begin{aligned} &\partial_t\varrho_{\mathbf{k}} + ik^2\frac{\bar{\rho}}{a}u_{\mathbf{k}} = 0\,, \\ &\partial_t u_{\mathbf{k}} + Hu_{\mathbf{k}} + \frac{ik}{a}\left[-\frac{4\pi G a^2}{k^2} + \frac{k^2}{4a^2m^2\bar{\rho}}\right] = 0\,, \\ &\epsilon + \frac{4\pi G a^2\varrho}{k^2} = 0\,, \end{aligned} \tag{2.74}$$

where we have used $\mathbf{v}_{\mathbf{k}} = u_{\mathbf{k}}\hat{k}$, since the velocity is irrotational. Nevertheless, even if some vorticity was there, the component orthogonal to $\mathbf{k}$ would disappear as the universe expands: $\mathbf{v}_\perp \propto a^{-1}$. We introduce the density contrast $\delta_{\mathbf{k}} = \varrho_{\mathbf{k}}/\bar{\rho}$ and an effective sound speed

$$c_{\rm eff}^2 \equiv \frac{k^2}{4a^2m^2}\,, \tag{2.75}$$

which originates from the quantum pressure term. Now we differentiate the first equation with respect to time, substitute $\partial_t u_{\mathbf{k}}$ from the second one and exploit $u_{\mathbf{k}} = ia\partial_t\delta_{\mathbf{k}}/k^2$, finding

$$\partial_t^2\delta_{\mathbf{k}} + 2H\partial_t\delta_{\mathbf{k}} + \left[c_{\rm eff}^2\frac{k^2}{a^2} - 4\pi G\bar{\rho}\right]\delta_{\mathbf{k}} = 0\,. \tag{2.76}$$

Comparing this equation with the usual one for linear perturbations in cold dark matter, we note that the only difference is in the effective sound speed. Also notice that, requesting the square bracket to be zero, we obtain the same Jeans scale predicted from dimensional arguments in the previous section, modulo order one factors:

$$k_J = (16\pi G\bar{\rho})^{1/4}(ma^2)^{1/2} \simeq 70\,{\rm Mpc}^{-1}\left(\frac{m}{10^{-22}\,{\rm eV}}\right)^{1/2}\,, \tag{2.77}$$

where the scalings imply $a = 1$ and $\bar{\rho} = 3H_0^2/(8\pi G)$. On large length scales $k < k_J$, gravity beats the quantum pressure while on small length scales $k > k_J$ the latter

dominates. The differences between cold dark matter and wave dark matter lay in the different Jeans scale that causes a suppression in the power spectrum at small scales.

Notice that the effective sound speed shows a pathology for $a < k/2m$, since it overcomes the speed of light in vacuum. This is due to our assumption of the limit $k/am \ll 1$ in the derivation of the fluid equation. If this limit is not satisfied, the non-relativistic plus Newtonian approximation breaks down and the scalar field is not in the oscillating phase, as it should to be dark matter, but behaves like a fluid with $c_{\rm eff} = 1$. Therefore the two behaviors can simply be joined [25],

$$c_{\rm eff}^2 = \begin{cases} 1 & a \leq \dfrac{k}{2m} \\ \dfrac{k^2}{4a^2m^2} & a > \dfrac{k}{2m} \end{cases} \tag{2.78}$$

We have that $k_J \propto a\bar{\rho}(a)^{1/4}$, hence it is constant in the radiation-dominated epoch, while it slightly grows in the matter-dominated epoch as $k_J \propto a^{1/4}$: because of this, it becomes easier and easier as time passes to form collapsed structures. We can also rewrite the Jeans scale using the Friedmann equation as $k_J \propto a(Hm)^{1/2}$. Since the wave dark matter starts oscillating in the radiation dominated epoch, at equality we still have $H > m$. Hence $k_J > k_H$, with k_H the wavenumber corresponding to the Hubble radius. The Jeans length will always be smaller than the Hubble radius during the whole matter-dominated epoch, allowing for structure formation. However, unlike cold dark matter, the wave dark matter perturbations on scales smaller than the Jeans length at matter-radiation equality $k > k_J(a_{\rm eq})$ need to wait to gravitationally collapse until k crosses the Jeans scale, at $a_\star = a_{\rm eq}[k/k_J(a_{\rm eq})]^4$. This feature produces a sharp cutoff in the matter power spectrum [25] at a critical scale given by the Jeans scale at equality

$$k_J(a_{\rm eq}) \simeq 9\ {\rm Mpc}^{-1} \left(\frac{m}{10^{-22}\ {\rm eV}}\right)^{1/2} . \tag{2.79}$$

In [25] the authors numerically found that the wave dark matter power spectrum is suppressed with respect to the particle dark matter one by a transfer function

$$T^2(k) \equiv \frac{P_{\rm wave}}{P_{\rm particle}} \approx \left[\frac{\cos \jmath^3}{1+\jmath^8}\right]^2 . \tag{2.80}$$

with $\jmath = 1.61 k/k_J(a_{\rm eq})[m/10^{-22}\ {\rm eV}]^{1/18}$. From this, one finds that the spectrum is suppressed by a factor of 2 at

$$k_{1/2} \approx 4.5\ {\rm Mpc}^{-1} \left(\frac{m}{10^{-22}\ {\rm eV}}\right)^{4/9} , \tag{2.81}$$

which is very close to $k_J(a_{\rm eq})$. The sharp cutoff, provided by the transfer function, can provide a suppression of small-lengthscale perturbations in the case of fuzzy dark matter. This is interesting because it can solve small-scales shortcomings of ΛCDM, in the case baryonic physics fails to explain them. In [221], by analyzing subhalos in very massive halos similar to the Milky Way ones, the authors argue

that indeed a sharp cutoff at $k \simeq 4.5\ \mathrm{Mpc}^{-1}$ could solve both the cusp-core and the missing satellite problems, see [31] for a review.

2.5 General gravitational phenomenology

In this Section, we present several implications of the wave dark matter at the phenomenological level, considering only the gravitational interaction. In particular we explore the existence of solitons, i.e. ground state solutions of the Schrödinger-Poisson system and we sketch its properties. We then briefly review the process of gravitational cooling or relaxation, which, in the wave dark matter case, is much more effective than in the particle case, due to the high occupation number and the wave granularity of the field. Particular wave features also appear in the context of energy exchange through weak encounters with other massive bodies, leading to differences in the dynamical friction and to new phenomena like stochastic heating. Another phenomenological implication, that regards the number of dark matter structures, is the phenomenon of subhalo tidal disruption, which we briefly review. The Section is inspired by the approach of [33].

2.5.1 Solitons and boson stars

The Euler equation and the Schrödinger-Poisson system provide a nice understanding of the properties of non-linear bound wave dark matter structures. These stable configurations are called *solitons* or boson stars.

A quick comparison of the relative importance of the gravity term versus the quantum pressure term in the Euler equation Eq. (2.68) reveals that a bound structure of size R and mass M should satisfy

$$\frac{GM}{R} \sim \frac{1}{m^2 R^2}\,. \tag{2.82}$$

This implies that the size of such structure is inversely proportional to its mass

$$\begin{aligned} R \gtrsim \frac{1}{GMm^2} &\simeq 1\ \mathrm{kpc}\left(\frac{10^{10}\,M_\odot}{M}\right)\left(\frac{10^{-23}\,\mathrm{eV}}{m}\right)^2\,, \\ &\simeq 10^{-3}\ \mathrm{pc}\left(\frac{10^{-4}\,M_\odot}{M}\right)\left(\frac{10^{-13}\,\mathrm{eV}}{m}\right)^2\,. \end{aligned} \tag{2.83}$$

The scalings are for the fuzzy dark matter case and for the wave halos that can be probed by intermediate mass ratio inspirals, that we consider in Chapters 4 and 5. This bound on the size directly comes from the fact that the particles constituting the bound structure have to be localized in a volume smaller than the virial radius of this structure. This is only possible if the de Broglie wavelength at the virial radius is smaller than the virial radius. The inequality is saturated for the ground state stable solution. This implies the size is determined by the solution of $R \sim \lambda(R)/(2\pi) \sim 1/\sqrt{GMm^2/R}$ which gives the same result as in Eq. (2.83).

The above size of the structure is just a lower bound, that is saturated for a soliton. The soliton has also a maximum mass. If the size is given by Eq. (2.83), the maximum mass M_{max} is the one for which this size corresponds to the Schwarzschild

radius of a black hole of this mass:

$$M_{\rm max} \sim \frac{1}{Gm} \simeq 10^{13}\, M_\odot \left(\frac{10^{-23}\,{\rm eV}}{m}\right), \quad (2.84)$$
$$\simeq 10^{3}\, M_\odot \left(\frac{10^{-13}\,{\rm eV}}{m}\right).$$

Naturally, solitons are not the only bound structures that wave dark matter can form. Indeed most dark matter halos are bound structures for which gravity is balanced by virialized motion. This happens as long as the velocity is large enough to beat the quantum pressure term. Therefore at small radii, where quantum pressure dominates, a soliton core would form. Let us investigate the properties of this solitonic solution.

Spherical ground state solutions of the SP system

We follow [33, 167, 222] and references therein. We start from the SP system on small scales (i.e. with unit scale factor and zero Hubble expansion), Eq. (2.65). Since the dark matter is self gravitating, the gravitational potential is sourced only by the dark matter density via the Poisson equation. We look for eigenstate solutions of the time-independent SP system. Therefore we consider [223, 224]

$$0 = \left[\nabla^2 - 2m^2(\Phi - \epsilon)\right]\psi \quad (2.85)$$
$$\nabla^2\Phi = 4\pi G m |\psi|^2.$$

Here ϵ is the energy per unit mass of the eigenstate. We assume both ψ and Φ are regular at the origin and vanish at infinity. The wave function is normalized such as the total mass M is

$$M = \int d^3x\, \rho = m \int d^3x\, |\psi|^2 . \quad (2.86)$$

We focus on spherical solutions, for which $\psi(r) > 0$ is real. The system becomes

$$\psi'' + \frac{2}{r}\psi' + 2m^2[\epsilon - \Phi]\psi = 0 \quad (2.87)$$
$$\Phi'' + \frac{2}{r}\Phi' = 4\pi G m \psi^2$$

here the prime denotes the derivative with respect to the radial coordinate. We can rewrite the equation with dimensionless quantities $\psi \to \psi/\sqrt{4\pi G m^3}$, $r \to mr$.

$$\psi'' + \frac{2}{r}\psi' + 2[\epsilon - \Phi]\psi = 0 \quad (2.88)$$
$$\Phi'' + \frac{2}{r}\Phi' = \psi^2$$

The mass disappeared from the equations. It is important to note that the SP system satisfies the scaling symmetry [225],

$$(r, \psi, \Phi, \epsilon, M, \rho) \to (g^{-1}r, g^2\psi, g^2\Phi, g^2\epsilon, gM, g^4\rho) \quad (2.89)$$

where g is the scaling factor. Therefore, whichever the solutions, they can be rescaled, e.g. for a system on a smaller spatial scale $r' = r/g$, it will correspond a larger mass $M' = gM$. We can take the soliton mass M or the soliton size, e.g. the half-mass radius $r_{1/2}$, or whichever other quantity as the only free parameter of the SP system.

The solutions of the SP system can be obtained numerically. We list the energy eigenvalue, the soliton energy per mass, the radius and the central density of the ground state solitonic solution, i.e. the one with the smallest energy eigenvalue [33, 222–224]:

$$\epsilon = -0.16(GMm)^2 , \tag{2.90}$$
$$E/M = -0.05(GMm)^2 , \tag{2.91}$$
$$r_c = 2.67(GMm^2)^{-1} , \tag{2.92}$$
$$\rho(0) = 0.004\, M(GMm^2)^3 . \tag{2.93}$$

The soliton radius r_c is defined as the distance at which the density drops by a factor of 2 compared to its central value, i.e. $\rho(r_c) = \rho(0)/2$. Another parameter often used is the soliton mass enclosed in r_c, i.e. $M_c = M_{\rm dm}(< r_c)$; this quantity is related to the total mass by $M_c \simeq 0.24M$.

Soliton host-halo relation

Numerical simulations have also found a so-called soliton-host halo relation [29, 108], relating the mass of the soliton core M_c to the mass of the host halo $M_{\rm vir}$. In particular [108]

$$M_c \simeq 6.7\times 10^7\, M_\odot \left(\frac{10^{-22}\,{\rm eV}}{m}\right)\left(\frac{M_{\rm vir}}{10^{10}\, M_\odot}\right)^{1/3} . \tag{2.94}$$

We do not provide right away the scalings for larger wave dark matter masses for the following reason. The above relation is well-tested only for halo masses in the limited range $10^8 - 10^{11}\ M_\odot$ and redshifts $z \in [0, 10]$, see [108], because of the difficulty in simulating wave dark matter in large boxes (see the review of Hui [21]) while maintaining the necessary resolution.

The $M_c \propto M_{\rm vir}^{1/3}$ relation can be understood as follows. Assume the halo and the soliton have the same gravitational potential at their respective sizes (that is, assume a kind of isothermal equilibrium condition)

$$\frac{GM_c}{r_c} \sim \frac{GM_{\rm vir}}{r_{\rm vir}} . \tag{2.95}$$

Remember now that $r_c \propto M_c^{-1}$ from Eq. (2.83) and $M_{\rm vir}/r_{\rm vir}^3 \sim$ const so that $r_{\rm vir} \propto M_{\rm vir}^{1/3}$. Then $M_c \propto M_{\rm vir}^{1/3}$ follows.

We can wonder why we have to assume this isothermality condition. Note that Eq. (2.94) is originally written [108] in the form

$$GM_c m = \sqrt{\frac{E_{\rm vir}}{M_{\rm vir}}} , \tag{2.96}$$

where on the right hand side we see total energy of the halo per unit mass. Notice that this corresponds to $E_{\rm vir}/M_{\rm vir} \sim 0.05(GMm)^2$, very similar to what we obtained for the soliton solution of the SP system. Indeed, Bar et al. [222, 226, 227] rewrite the above condition as

$$\sqrt{\frac{K}{M}}\bigg|_{\rm soliton} \approx \sqrt{\frac{K}{M}}\bigg|_{\rm halo}, \tag{2.97}$$

where the two sides, under the square root, are the kinetic energy per unit mass of the soliton and of the halo, respectively. All these arguments converge to indicate that the prescription to determine the soliton-core mass, or equivalently the radius, is

$$r_c \sim \frac{1}{m v_{\rm vir}}, \tag{2.98}$$

where $v_{\rm vir} = \sqrt{GM_{\rm vir}/r_{\rm vir}}$. Considering that $v_{\rm vir} \simeq 0.33(GMm)$ from the SP system ground state solution [33], we obtain exactly Eq. (2.98) once we consider $r_c \simeq 2.67/(GMm^2)$.

We come back to this prescription in Section 4.2.1. We will see that it provides unrealistically small values for the core radius, hence huge core densities [228] when applied to wave dark matter of mass $m \sim 10^{-13}$ eV. The problem arises when the dark matter de Broglie wavelength is hierarchically smaller than the size of the system so that the virial velocity is not representative for the actual dark matter particle velocity at the scale of the soliton. Hence the relation in Eq. (2.98) can be applied only in the fuzzy dark matter case, where the wavelength is not hierachically distant from the virial radius, which is at the kpc scale.

2.5.2 Relaxation

How does the soliton form in a wave dark matter halo? The condensation, or gravitational cooling process, has a characteristic timescale [33], called *relaxation* timescale. In a collisionless system of radius R filled with N stars, of mass m, the stars exchange kinetic energy by an order-one factor after a timescale $t_{\rm relax} \simeq 0.1 t_{\rm cr} N/\log N$ [42]. Here $t_{\rm cr} \sim R/v$ is the crossing time and the typical velocity is $v \sim \sqrt{GNm/R}$ for the virial theorem. The system is approximately collisionless, i.e. the constituent particles move under the influence of the gravitational field generated by a smooth mass distribution, rather than a collection of mass points, only for $t < t_{\rm relax}$. After $t_{\rm relax}$ the objects start exchanging energy. In standard cold dark matter models the particle mass m is so small that the relaxation time is many orders of magnitude larger than the age of the universe, hence it does not play any physical role.

The relaxation timescale can be estimated in the quasiparticle picture of wave dark matter. The wave interference between different finite modes localized in the halo produces granules, or quasiparticles of size of the de Broglie wavelength. Considering the inner part of a halo of radius R, the number of granules is $N_{\rm dB} \sim (R/\lambda_{\rm dB})^3$. The condensation happens on a timescale for which these granules change

their kinetic energy by some order-one factor. Therefore we get [33]

$$t_{\rm relax} \sim 0.1\frac{2R}{v}N_{\rm dB} \simeq 0.1\,{\rm Gyr}\left(\frac{R}{\rm kpc}\right)^4\left(\frac{v}{100\,{\rm km/sec}}\right)^2\left(\frac{m}{10^{-22}\,{\rm eV}}\right)^3 \simeq 10^{-4}\,{\rm Gyr}\left(\frac{R}{10^{-3}\,{\rm pc}}\right)^4\left(\frac{v}{0.1\,{\rm km/sec}}\right)^2\left(\frac{m}{10^{-13}\,{\rm eV}}\right)^3 \tag{2.99}$$

We see that, for the fuzzy dark matter case, the relaxation time around the radii corresponding to the typical de Broglie wavelength can be considerably shorter than the age of the universe. In the larger wave dark matter case, where $\lambda_{\rm dB}$ is smaller, for realistic values of halo size and velocity, the relaxation timescale around $R \sim \lambda_{\rm dB}$ is even shorter. We will investigate this scenario in more detail in Section 4.2.2.

A wave halo develops a compact soliton from the mass originally in the radius R, with R given by $t_{\rm relax}(R) = t_{\rm age}$ with $t_{\rm age}$ the age of the halo. A good definition of the relaxation timescale comes from the diffusion coefficients we discuss in detail in Appendix C.2. The physical meaning of $t_{\rm relax}$ is the timescale for which the objects exchange order one kinetic energy, i.e. $(\Delta E)^2/E^2 \sim \mathcal{O}(1)$. The diffusion coefficient indicates the variation of the quantity in the unit time. Therefore $(\Delta E)^2/E^2 \sim D[(\Delta E)^2]/E^2 \times t = v^2 D[(\Delta v_\parallel)^2]/v^4 \times t \sim 1$, from which [42]

$$t_{\rm relax} \equiv \frac{1}{3}\frac{v^2}{D[(\Delta v_\parallel)^2]}\,. \tag{2.100}$$

Some ambiguity still remains regarding the velocity to consider in the above formula. It is reasonable to think that the velocity above has to be a representative of the (quasi-)particles in the system, so depending on the speed distribution, the choice of v can vary. For a Maxwell-Boltzmann speed distribution with one-dimensional velocity dispersion σ it is natural to consider $v = \sqrt{3}\sigma$, hence the factor $1/3$ in the definition of the relaxation timescale.

2.5.3 Dynamical friction and stochastic heating

Wave dark matter impacts *dynamical friction*, which is one of the most important sources of cooling of astrophysical objects. When a massive objects of mass M, like a star, travels through the dark matter medium with velocity v, the particles get focused, creating an overdensity wake which pulls the massive object, slowing it down. This phenomenon was studied by Chandrasekhar in the context of friction exerted on a test star moving through a medium of other stars [229–231]. Here we just outline the main features of the wave dark matter in modifying the friction force. As we will see in Chapter 3 the overdensity is smoothed at scales smaller than the de Broglie wavelength. Effectively, the wavelength sets a lower cutoff on the minimum impact parameter. An order-one deflection occurs if the impact parameter is $b_{90} \sim GM/v^2$; the particle limit occurs when the de Broglie wavelength is smaller than this value as no suppression of scales is imposed. We compare these scales

$$\frac{b_{90}}{\lambda_{\rm dB}} \sim \frac{GMm}{v} \sim 10^{-3}\left(\frac{M}{10^6\,M_\odot}\right)\left(\frac{m}{10^{-22}\,{\rm eV}}\right)\left(\frac{100{\rm km/sec}}{v}\right)\,. \tag{2.101}$$

Therefore, in the fuzzy dark matter case, the dynamical friction can be strongly suppressed. Studies of dynamical friction in realistic scenarios with fuzzy dark matter [46, 232, 233] confirm the above estimate. We compute the dynamical friction for the particle and wave case in Appendix E. We come back to the topic in Chapter 5 as this effect will be of primary importance to the evolution of a binary in a wave halo.

The wave nature of dark matter can lead to an energy transfer to the massive object traveling in the medium. The fluctuations of the wave dark matter can be thought as quasiparticles with macroscopic mass $m_{\rm eff} = \rho(\lambda_{\rm dB}/2)^3$ that continuously hit the massive object, transferring energy to it [33,46,47]. This is called *stochastic heating*. A full calculation of the wave effects in the case of weak gravitational encounters is presented in Appendix C, where the diffusion coefficients describing the dynamics of massive objects in a dark matter halo are derived.

2.5.4 Subhalo tidal disruption

We have seen that wave dark matter, specially in the fuzzy limit of the mass spectrum, leads to a considerable suppression of small scales structures. Another reason why small-scales structures are suppressed is the vulnerability of subhalos to tidal disruption. We review this phenomenon referring to [33].

There are two main reasons for the subhalo tidal disruption. Firstly, there is a maximum value of the mass density of wave dark matter halos, and it is given by the ground state value of the Schrödinger-Poisson system: $\rho(0) = 0.004M(GMm^2)^3$. Secondly, the wave dark matter can tunnel through the gravitational potential barrier out of the so-called *tidal radius* r_t. Let us estimate the timescale of the subhalo tidal disruption. The tidal radius is the equilibrium solution of the equation of motion of a test particle of mass M orbiting around a host mass $M_{\rm host}$, at distance R and angular speed ω:

$$r_t \equiv R\left(\frac{M}{2M_{\rm host}}\right)^{1/3} . \tag{2.102}$$

If the mass M is subject to a spherically symmetric tidal potential $\Omega = -3/2 \times \omega^2 r^2$, this has to be included in the Schrödinger-Poisson system through the replacement $\Phi \to \Phi + \Omega$. In contrast to the particle case, where particles can orbit forever if they are inside the tidal radius, in the wave case, the Schrödinger equation allows a tunneling of the barrier at r_t. The disruption timescale is found solving numerically the Schrödinger-Poisson system with the added tidal potential; the energy eigenvalue acquires an imaginary part, which is proportional to the mass rate $\dot{M} = 2M{\rm Im}E$. A typical massive galaxy (Milky Way-like) has circular speed of 100 km/sec so it orbits about 15(30 kpc$/r$) times in a Hubble time. If we impose that the soliton of the subhalo survives at least for 10 orbits on a radius R around a host of mass $M_{\rm host}$, we obtain that the soliton density is $\rho \gtrsim 60\rho_{\rm host}$. This implies a lower bound on the subhalo soliton mass

$$M > 6.7\times 10^8\, M_\odot \left(\frac{M_{\rm host}}{10^{11}\, M_\odot}\right)^{1/4} \left(\frac{10\ {\rm kpc}}{R}\right)^{3/4} \left(\frac{10^{-22}\ {\rm eV}}{m}\right)^{3/2} . \tag{2.103}$$

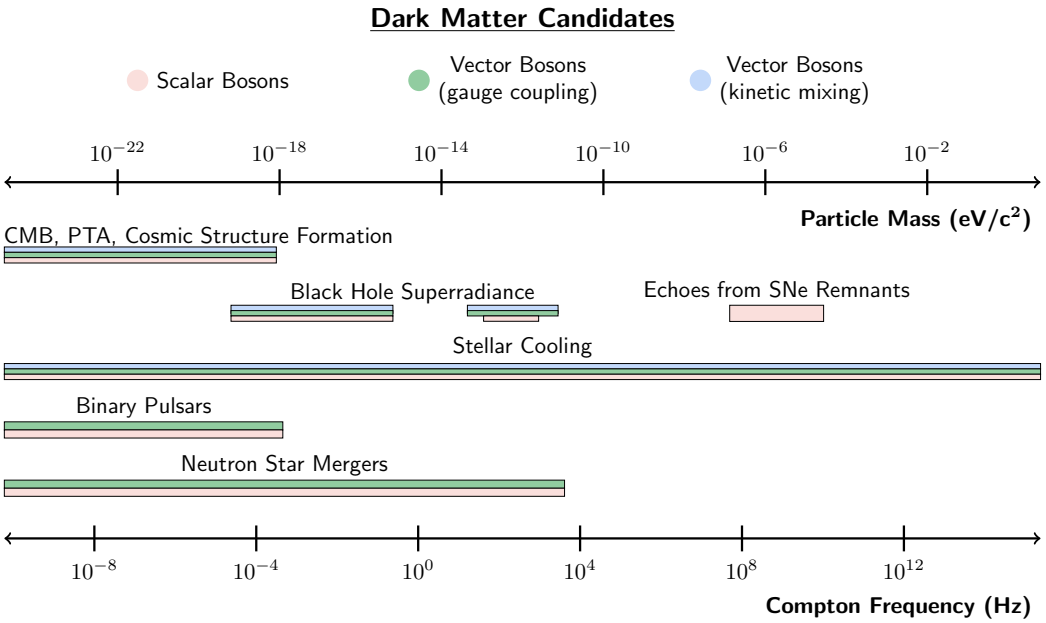

FIGURE 2.1: Overview of the current and future probes of wave dark matter (scalar, vector both from kinetic mixing and gauge coupling with SM). Figure taken from [96]. See the main text for the details

This lower bound is consistent with numerical simulations which find that halo substructure is suppressed below a few times $10^8 M_\odot$ [232]. These estimates can be tested observationally determining the subhalo mass function. This can be accomplished by analyzing gravitational lensing of background galaxies by the subhalos and studying the evolution of tidal streams.

2.6 Cosmological and astrophysical probes

The goal of this Section is to provide a broad but simple and exhaustive overview of the cosmological and astrophysical probes of wave dark matter both in case it interacts only gravitationally with ordinary matter and in the case it also has additional interactions with the SM. The wave features at different scales have important phenomenological consequences that can be translated into bounds on the mass or other parameters once an explicit model is assumed. This section is heavily based on [96]. From this reference, we take Figure 2.1 that summarizes the type of constraints on the wave dark matter mass spectrum. The Figure does not show exclusion or limits but only which observables are able to probe which part of the spectrum, depending on the assumption that wave dark matter is a scalar boson, or a vector boson, with kinetic mixing or gauge coupling with the SM. Cosmological measurements probe the light end of the wave dark matter mass spectrum because these candidates are able to show wave-like features on astronomical lengthscales. As we discussed in Section 1.2, the constraining power of these observation comes mainly from the fact that wave dark matter suppresses power at scales smaller than the Jeans scale at equality, which depends on the wave dark matter mass. Generally, these constraints apply to all the wave DM candidates.

Cosmic Microwave Background The CMB data from Planck [9] probe the mass range 10^{-32} eV $< m < 10^{-26}$ eV and exclude density fraction larger than the percent. This is possible because such light scalars would spoil the standard picture of structure formation. Future CMB experiments like Simons Observatory [234], CMB Stage-4 [235] or CMB-HD [236] will improve the constraints and extend the mass range. Additional information from the Sunayev-Zeldovich effect can further extend the range up to $m \sim 10^{-22}$ eV [237]. Couplings to the electromagnetic sector would also give detectable spectral distortions in the CMB, through cosmic birefringence [238–242].

High-redshift clustering Wave dark matter suppresses structure formation at high redshift. This can be probed by measurement of the Lyman-α forest of neutral hydrogen absorption in the intergalactic medium for $z \sim 5$, effectively measuring the quasi-linear matter power spectrum at scales smaller than the Mpc. The strongest current bound is $m > 2 \times 10^{-20}$ eV at 95% if all the dark matter is ultralight [147,243–245]. At even higher redshift, intensity mapping of lines like the neutral hydrogen 21 cm transition by surveys like HIRAX [246] and the Square Kilometre Array [247] would be sensitive to a 10% density component with mass $m < 10^{-22}$ eV [248]. Measurements of the velocity acoustic oscillation feature in the power spectrum of the 21cm lines in e.g. HERA [249] could even probe $m \sim 10^{-18}$ eV [250].

Galaxies and subhalos Wave dark matter suppresses galaxy formation and delays cosmic reionization, excluding the possibility that wave dark matter with mass $m < 10^{-23}$ eV makes 50% of the DM relic density via a combination of Hubble Space Telescope Ultra Deep Field UV luminosity function and the CMB optical depth [251]. Measurements with the James Webb Space telescope can extend these constraints by more than one order of magnitude in the spectrum. The wave suppression of the matter power spectrum also translates into a low-mass cutoff subhalo abundance, also due to the phenomenon of subhalo tidal disruption. Dark Energy Survey (DES) detection of satellite galaxies [252], subhalos inferred from strong lensing [253, 254] and stellar streams perturbations in the Milky Way impose $m \gtrsim 2 \times 10^{-21}$ eV [255], with possible improvements in future surveys.

Time oscillations In [256] it is shown that the wave nature of dark matter would imply oscillations in the gravitational potential of the Milky Way on timescales

$$t \sim 6.6 \text{ yr} \left(\frac{10^{-23} \text{ eV}}{m} \right) , \tag{2.104}$$

which is accessible by NANOGrav [257] and Parkes Pulsar Timing Array [258]. Indeed the claim of a recent detection of a stochastic background component by NANO-Grav [259–261] could be a spectral feature of ultralight dark matter [262]. The survival of the star cluster in the dwarf galaxy Eridanus-II to time oscillations of the potential impose bounds around 10^{-21} eV [263].

Black hole superradiance When the Compton wavelength of ultralight bosons becomes comparable to the Schwarzschild radius of a black hole, a superradiant instability can be triggered. This phenomenon causes the rotational energy of the black hole to be depleted, as discussed in [35, 171]. The ultralight bosons are excited and form a macroscopic cloud around the black hole due to the gravitational interactions of the particles, regardless of whether they are scalars or vectors. The efficiency of this process is reduced for particles with large self-interactions and interactions with the SM, which makes it an excellent complement to laboratory searches. There are two main observable consequences of this process: quasi-monochromatic gravitational radiation and gaps at large spin in the BH spin-mass distribution [35–39]. The most promising range of interest for this phenomenon is for boson masses in the range of $m \sim 10^{-14} - 10^{-11}$ eV. Observations of supermassive black holes and low-frequency gravitational waves in the future will be capable of detecting boson masses within the range of $m \sim 10^{-19} - 10^{-15}$ eV [39–41]. The whole mass range probed by black hole superradiance is of interest for this thesis.

Neutron stars: pulsar binaries and mergers Ultralight bosons can affect neutron star binaries. New vector-mediated forces can induce a faster decay of the orbital period due to the emission of dark dipole radiation. Moreover, if light bosons couple to muons, which are naturally abundant in neutrons stars, the neutron star merger observed through gravitational waves would be modified by the additional Yukawa force and radiation of the dark boson. This effect can probe masses $m < 10^{-11}$ eV [264, 265] in both the scalar and vector case.

Stellar cooling Particles that couple to SM states can be produced abundantly within the cores of stars, resulting in unusual cooling [266–272]. Electromagnetic excitations exist in the stellar plasma, and both transverse and longitudinal modes can have unconventional dispersion relations. In the dark photon case, when its mass is similar to the plasma frequency of the SM photon, resonant production of dark photons occurs, with the lower masses being suppressed due to the small kinetic mixing, while heavier masses are Boltzmann suppressed. Scalars, in particular axions [272], can mix with the longitudinal mode of photons and be produced resonantly at any value of the small mass. Scalars with coupling to muons can be constrained through horizontal branch stars and supernovae [273]. All the bounds span the whole mass spectrum for wave dark matter and are often the dominant ones.

Galactic dynamics Finally, a category of observational constraints not included in Figure 2.1 is the one of galaxy rotation curves and velocity dispersion of stars in ultra-faint dwarf galaxies. In [227] find that the soliton-host halo relation in rotation-dominated galaxies is disfavored for a broad ranges of masses, or, assuming the validity of the soliton-host halo relation, ultralight DM is disfavored in the region $m \sim 10^{-24} - 10^{-20}$ eV for wave dark matter density fractions down to 30%. The heating of stellar orbits in ultra-faint dwarf galaxies by wave dark matter is used in [274] to put bounds on the fuzzy dark matter mass at the level of $m > 3 \times 10^{-19}$ eV.

2.7 Experimental searches

The aim of this section is to give a partial overview of the perspective for detection of wave dark matter, depending on the mass range under consideration and on the couplings to the SM states, other than just the gravitational one. This field is experiencing an outstandingly rapid evolution [96–98].

In Figure 2.2, taken from [34], we illustrate the different timescales, lengthscales of interest throughout the mass spectrum of wave dark matter as well as the diverse experimental strategies for direct detection of wave dark matter. The different methodologies group together several experiments which share a common main idea or experimental setup and are divided in different categories depending on the underlying assumption on the dark matter coupling with SM states and spin (vector or boson). From the Figure, we see that all the dark matter spectrum is covered by various direct detection techniques and notably several searches populate the range of interest for this thesis $m \sim 10^{-15} \sim 10^{-13}$ eV. We consider these cases separately, even though there can be intersections. We follow the reviews [95–97].

2.7.1 Coupling to photons

The coupling between ultralight dark matter and photons is of fundamental importance for experiments and it is common in most models.

Pseudoscalar coupling In the QCD axion case, the coupling to photon arises via the mixing of the axion with pions. We can write it in a general way as

$$\mathcal{L} \supset -\frac{C_{\phi\gamma}}{f}\frac{\alpha}{2\pi}\phi F_{\mu\nu}\tilde{F}^{\mu\nu} = g_{\phi\gamma}\mathbf{E}\cdot\mathbf{B} \tag{2.105}$$

where $\mathbf{E}$ and $\mathbf{B}$ are the electric and magnetic fields, respectively. Here we refer to the pseudoscalar coupling. In the case of a dark photon, the coupling with a photon is the kinetic mixing, see Section 2.1.3. In most of the cases the phenomenology is the same, so we consider the two cases together.

We already mentioned the importance of the **CMB** in probing ultralight dark matter in Section 2.6.

Figure 2.2 includes the label **Earth** which represents the constraints imposed by the oscillations of the terrestrial magnetic field when ultralight DM is coupled to photons. This can happen either through kinetic mixing in the case of hidden photons [275, 276] or via ALP coupling to photons [277]. The presence of ultralight dark matter induces a monochromatic oscillating magnetic field with a specific global vectorial pattern. This pattern can be detected by using a network of unshielded magnetometers, see below for more details.

The term **Cavities** in Figure 2.2 denotes collectively the conventional haloscopes that enhance the conversion of ultralight fields to photons by exploiting the resonance between the frequency of the cavity and the ultralight field. This process amplifies the power by the quality factor $Q \sim 1/\sigma^2 \sim 10^6$, and the photons produced manifest as an excited mode of the cavity. A suitable port can be used to extract this power from the cavity and connect it to a low-noise amplifier in a radio-frequency

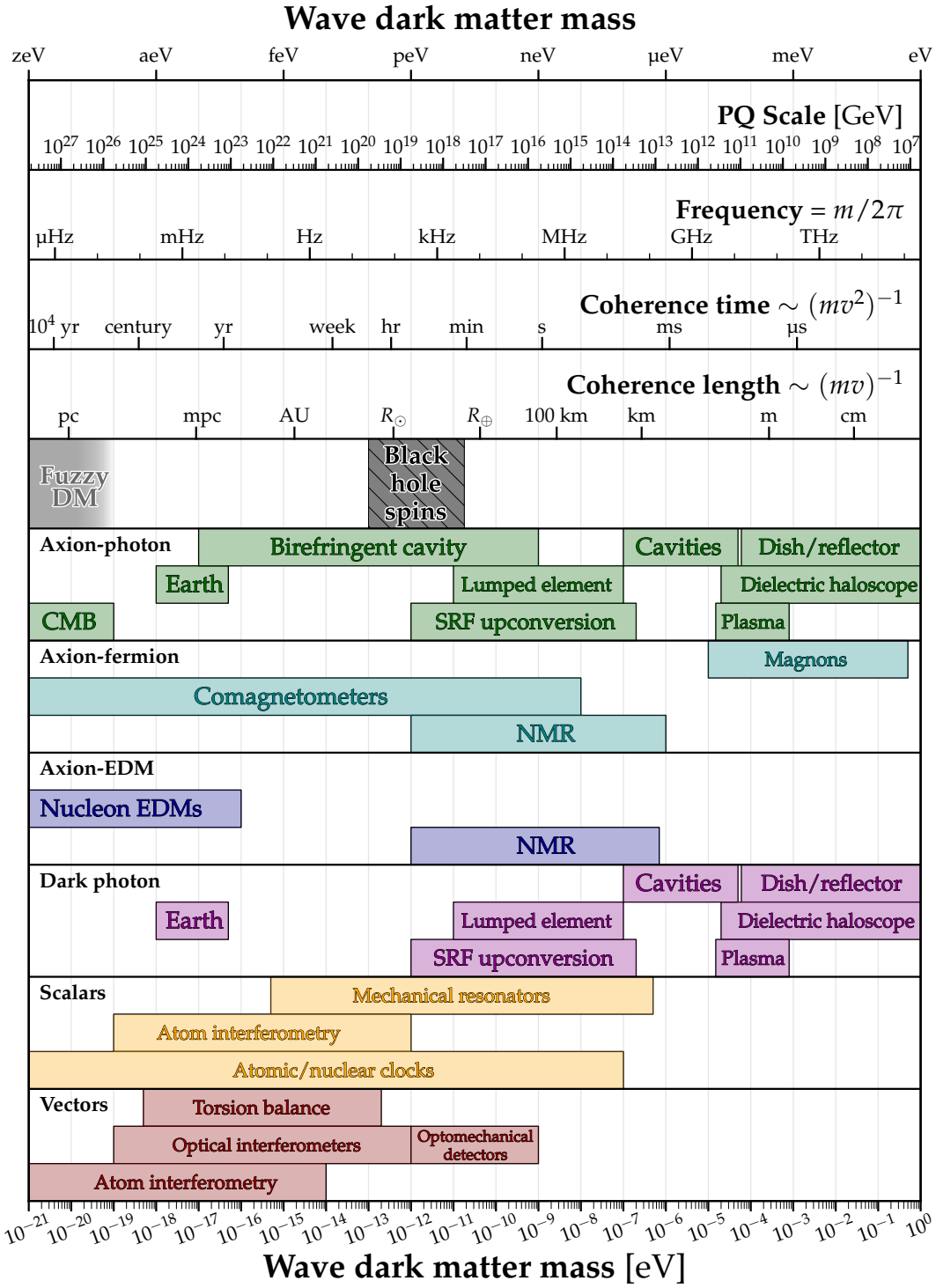

FIGURE 2.2: Cheatsheet for the conversion between the wave dark matter mass and a few other quantities, and some rough order-of-magnitude estimates for the mass range reach of different experimental searches, explained in the main text. Figure from [34].

(RF) detection chain. Most of the constraints are around the μeV and the main disadvantage is the narrow band of the resonance, that implies the need of an inefficient continuous scan of the mass spectrum. Many current and planned experiments exploit and improve this technique: ADMX [71–73], HAYSTAC [74, 75], CAPP [79], ORGAN [81], QUAX a-γ [82, 83], the last two being non-tunable. See [95, 97, 98] for more details.

Birefringent cavity refers to haloscopes for ALPs with cavities that exhibit birefringence between its two linearly polarized laser eigenmodes [278], allowing to explore smaller frequencies than with normal cavities.

Moving to higher frequencies necessitates completely different methods of detection. One of the most significant is the magnetized **Dish antenna** (or **reflector**) and its derivative, the **Dielectric haloscope**. When a dielectric interface, such as a mirror or the surface of a dielectric slab, is placed in a magnetic field parallel to its surface, it should emit electromagnetic radiation perpendicular to its surface due to the presence of the dark matter axion field or dark photon [84]. This radiation is tiny and can only be detected if the emission of a large surface is focused on a small point, such as in the case of a spherical surface. This approach has the benefit of being broadband and sensitive to all axion masses simultaneously. Since there is no resonance involved, the sensitivity can be scaled up increasing the area. Dielectric haloscopes use this idea stacking together several dielectric slabs inside a magnetic field and putting them in front of a metallic mirror, increasing constructed interference. This is the functioning principle of the planned experiment MADMAX [80]

Another idea to detect dark matter at frequencies above the GHz is the **Plasma** haloscope. When operating at high frequencies, the signal power in simple cavities diminishes significantly due to their small size. To overcome this issue it has been proposed [279, 280] to modify the wavelength of light inside the device, giving the photon an effective mass, or plasma frequency. By matching the plasma frequency with the dark matter mass, regardless of the size of the device, resonant conversion can be achieved, enabling the search for high-mass axions between 5-50 GHz, depending on the chosen detector technology. One way to tune the plasma is to use a wire metamaterial [281, 282], so that, being the plasma frequency a function of the wire geometry, it can be tuned easily. Using superconducting wires can further increase the sensitivity of the device.

Detecting the oscillating magnetic field associated with axion dark matter or dark photon field at much lower masses (well below μeV and therefore in the radio band) can be more effective by placing a pick-up coil inside a large external constant magnetic field as explored in [76, 283, 284]. This is called **Lumped element** in Figure 2.2. The detector can be operated in two modes: resonant, where the amplification is obtained via an external LC circuit and, remarkably, broad-band [76]. The idea is under development by different collaborations [76, 285, 286]. Among them, ABRACADABRA [77, 287] and SHAFT [86] have released preliminary result for a smaller-scale version of the planned experiment in the $10^{-11} - 10^{-8}$ eV mass range. We also mention here BEAST [288] and BASE [87].

Another technique for particles in the radio band is the heterodyne method, which can be used to detect axions using SRF (superconducting radio-frequency)

cavities [91,289,290], dubbed **SRF upconversion** in Figure 2.2. This technique separates the dark matter frequency from the mode frequency by using a superconducting cavity that contains an oscillating magnetic field. Although this method introduces new sources of noise, it also significantly increases the signal power, particularly at low masses. Consequently, this approach achieves comparable sensitivity without necessitating large, high-field magnets or quantum sensing methods.

Scalar coupling The linear and quadratic scalar coupling to photons are often parameterized as

$$\mathcal{L} \supset \frac{d_e \phi}{\sqrt{2} M_{\rm pl}} \frac{1}{4} F_{\mu\nu} F^{\mu\nu} = \frac{g_{\phi\gamma\gamma}\phi}{4} F_{\mu\nu} F^{\mu\nu} \,, \tag{2.106}$$

$$\mathcal{L} \supset \frac{g^{(2)}_{\phi\gamma\gamma}\phi^2}{4} F_{\mu\nu} F^{\mu\nu} \,, \tag{2.107}$$

for both linear and quadratic interactions in ϕ. Some of the techniques to detect this operators are in common with the ones mentioned in the ALP case, see Table 2.1. Note that, in the axion case, the quadratic coupling is allowed and arises at loop level in the chiral Lagrangian, from $\phi G\tilde{G}$, while the linear one is forbidden. New important effects are present with $\phi FF, \phi^2 FF$ operators. These terms effectively change the electromagnetic fine structure constant to

$$\begin{aligned} \alpha &\to \frac{\alpha}{1 - g_{\phi\gamma\gamma}\phi} \approx \alpha(1 + g_{\phi\gamma\gamma}\phi) \,, \\ \alpha &\to \frac{\alpha}{1 - g^{(2)}_{\phi\gamma\gamma}\phi^2} \approx \alpha(1 + g^{(2)}_{\phi\gamma\gamma}\phi^2) \,. \end{aligned} \tag{2.108}$$

As a result, the coupling to the SM fields of the oscillating scalar DM field $\phi = \phi_0 \cos(mt)$ leads to an apparent oscillation of fundamental constants at frequency equal to m in the linear case and $2m$ in the quadratic case. Such oscillations can alter several physical quantities which experiments are sensitive to, such as energy levels in atoms [40,291] and the length of solids [291,292].

A first class of experiments that is sensitive to the aforementioned effect is the one of **Atomic, molecular and nuclear clocks**, often collectively dubbed *quantum clocks*. These clocks have reached an outstanding frequency precision below 10^{-18} [293], becoming therefore sensitive to the oscillation of fundamental constants that leads to variations in the atomic, molecular or nuclear spectra, changing the clock frequency. These clock searches are broad-band and sensitive to masses $m < 10^{-12}$ eV depending on the total measurement time and the clock specifics. If the period is longer than the experiment's timescale, the signal would arise as a peak in frequency space at $\omega = m$. A dark matter signal could manifest in the oscillation of the ratio between two reference frequencies ν_1, ν_2 which have different sensitivities to fundamental constants. For the structure constant,

$$\frac{\partial}{\partial t} \log \frac{\nu_2}{\nu_1} = (K_2 - K_1) \frac{\partial}{\partial t} \log \alpha \tag{2.109}$$

where K_1, K_2 are dimensionless sensitivity factors that depend on the clock's transition. All the presently operating clocks can be divided on the basis of the transition type exploited: transitions between hyperfine substates of the atom's ground state are used in microwave clocks (GHz frequencies), while transitions between electronic levels are used in optical clocks [294] (10^{15} Hz frequencies). Optical clocks are mainly sensitive to variations of α. Current bounds on ultralight dark matter come from re-analyses of α drift data for Dy/Dy [295], Rb/Cs microwave clocks [296] and Al^+/Hg^+ optical clocks [297]. New experiments count clock-comparison setups with Yb/Al^+ and Yb/Sr clock pair limits [297] and comparison of H maser and Sr optical clock with cryogenic crystalline Si cavity (H/Si and Sr/Si) [298]. We refer to [96] for an overview of new ideas on molecular and nuclear clocks.

Atom interferometry is a method that utilizes the comparison of the phase accumulated by an atom cloud that is excited by laser pulses and moves in space. By combining two atom interferometers that share common laser pulses from a single laser, a clock gradiometer can be created to measure the phase difference between the two interferometers, allowing for cancellation of laser noise. Ultralight dark matter can influence the phase of the atom cloud by either affecting the internal energy splitting or by exerting an additional force on the cloud. In the first case, if dark matter produces oscillations of fundamental constants, the atom levels will oscillate at the Compton frequency of DM. In the second case, dark matter that causes acceleration of the clouds can be searched comparing atom interferometers with clouds made of different isotopes. Both scalars and vectors can be constrained by MAGIS-100, an atom interferometer under development [299].

The variation of α directly implies the variation of the Bohr radius $a = (m_e\alpha)^{-1}$, hence of the length of a solid $\delta L/L = -\delta\alpha/\alpha$. **Optical cavities** use this phenomenon to detect wave dark matter, as they are sensitive to the variation of the cavity reference frequency. Cavities can be compared with atomic clocks as mentioned above, or with other cavities [300].

Also **Optical interferometers**, including gravitational wave detectors, are sensitive to scalar and vector wave dark matter. In a Michelson interferometer with identical arms, scalars change the optical path length difference between the arms, due to the oscillation in the beam-splitter thickness as well as of the beam-splitter refractive index. Searches for these effects have been performed with old datasets from GEO600 [301] and Fermilab Holometer [302]. If the interferometer has Fabry-Perot cavities, the sensitivity to scalars is generally suppressed compared to the pure Michelson interferometer, but can be improved exploiting mirrors with different thickness in the two arms [303]. Wave DM can also exert time-varying accelerations on test bodies, $\mathbf{a} \propto \nabla\phi, \partial_t \mathbf{A}'$ for the scalar and the vector, respectively. In the scalar case, the gradient gives a velocity suppression, while in the vector case there is no such suppression, this is why optical interferometers are listed in the vector section of Figure 2.2 and not in the scalar.

Another interesting idea is to use **Torsion balances** to detect ultralight DM [169]. Torsion balances can detect accelerations as small as 10^{-15} m/s^2 on gram-mass objects. Torsion balances are used to search for equivalence principle violations, but can be used to detect differential forces by dark matter or time. Bounds have been obtained on vector DM with $B - L$ gauge coupling from equivalence principle tests

[304] and the Microscope satellite [305].

We have seen that the detection of ultralight dark matter can be achieved through the measurement of the deformation of an elastic body produced by a weak force, which is the basis of both torsion balances and optical-cavity-based ultralight DM searches. If the elastic body has internal resonances at $\omega = m$, the deformation can be amplified by the resonance Q factor, resulting in massive sensitivity enhancement over a narrow bandwidth. There have been several proposals in recent years for **Mechanical resonator**-based detection, as summarized in [306]. These proposals span a huge range in the mass $m \sim 10^{-14} - 10^{-5}$ eV. Resonant mass detectors for scalars are limited by the fact that the high-quality resonant enhancement comes at the price of a small bandwidth. Constraints include the ones from AURIGA [307], DAMNED [308] and Halometer [302]. The vector case may favor the use of **Optomechanical detectors**, which involve a mechanical resonator coupled with an optical cavity made of a different material [309]. This is because vectors cause an oscillating center-of-mass acceleration of a test mass dependent on its material composition [310].

2.7.2 Coupling to fermions

The coupling of wave dark matter to fermions is also of primary importance for detection.

Pseudoscalar coupling The first case is the pseudoscalar coupling to a fermionic axial current, the one characteristic of ALPs, that we can write as

$$\mathcal{L} \supset \frac{\partial_\mu \phi}{f} \sum_\psi C_\psi \bar{\psi} \gamma^\mu \gamma_5 \bar{\psi} \,. \tag{2.110}$$

In the non-relativistic limit, this term corresponds to the Hamiltonian coupling with spin $\mathbf{S}_\psi$

$$\mathcal{H} \supset - \sum_\psi \frac{2 C_\psi}{f} \mathbf{S}_\psi \cdot \nabla \phi \,. \tag{2.111}$$

This implies that the ALP can couple with nuclear spins like a fictitious magnetic field and produce the precession of nuclear spins. This spin coupling can be exploited for detection in atomic **Magnetometers** [311, 312] and **Comagnetometers** [313–315] (magnetometers that measure the nuclear spin precession of a material containing two different nuclear spins, used as very sensitive gyroscopes). A detector exploiting nuclear magnetic resonances (**NMR**) is CASPEr [169, 316]. CASPEr-electric uses precision solid-state magnetic resonance to search for an oscillating spin torque induced by interaction of axion-like dark matter with nuclear spins, while CASPEr-gradient is only sensitive to the nucleon spin gradient coupling [97].

An interesting approach is to use a network of quantum sensors based on spin. The Global Network of Optical Magnetometers for Exotic physics searches (GNOME) [317, 318] employs this strategy. It consists of over a dozen optical atomic magnetometers operating within magnetically-shielded environments at stations worldwide [319].

For ALPs detection, it has been proposed to utilize quantum non-demolition detection of **Magnons** [320], collective spin excitations in a solid, that are expected to be excited by the axion-electron interaction. The prototype detector includes a ferromagnetic sphere as an electronic spin target and a superconducting qubit, embedded inside a microwave cavity to create a coherent effective interaction between the uniform magnetostatic mode in the ferromagnetic crystal and the qubit.

In general, an ALP can couple to gluons via the operator

$$\mathcal{L} \supset \frac{C_G}{f}\frac{g^2}{32\pi^2}\phi G^a_{\mu\nu}\tilde{G}^{\mu\nu}_a \,. \tag{2.112}$$

This coupling induces an oscillating electric dipole moment (EDM) of a nucleon [169]

$$\mathcal{L} \supset -\frac{iC_N}{2}\frac{\phi}{f}\bar{N}\sigma_{\mu\nu}\gamma_5 N F^{\mu\nu} \,, \tag{2.113}$$

and of atoms and molecules [321]. Searches for an oscillating neutron EDM constrain C_G/f over 10^{-24} eV $< m < 10^{-17}$ eV [165], while searching for oscillating EDM in the HfF^+ molecule constrains the range 10^{-22} eV $< m < 10^{-15}$ eV [322]. It has been also proposed to search for the ALP induced EDM in the future proton storage ring to measure the static proton EDM [323]. We group these bounds as **Nucleon-EDM**. The coupling to gluons can be detected also through nuclear magnetic resonance (**NMR**) methods. The CASPEr project [169,316] is exploring this direction. The coupling to gluons can be accessed also via the phenomenology of the quadratic operators that arise at loop level, such as $\phi^2 FF$ and $\phi^2\bar{\psi}\psi$ [324]. For this, we refer to the discussions on these operators.

Scalar coupling The scalar coupling to fermions can be written as

$$\mathcal{L} \supset -\sum_\psi g_\psi \phi\bar{\psi}\psi - \sum_\psi g^{(2)}_\psi \phi^2\bar{\psi}\psi \,. \tag{2.114}$$

The second term arises also in the axion case from the chiral Lagrangian. These operators effectively modify the mass of the fermions $m_\psi \to m_\psi + g_\psi\phi$ (or $m_\psi \to m_\psi + g^{(2)}_\psi\phi^2$ in the case of quadratic coupling) and produce oscillations in this quantity at frequency m in the linear case and $2m$ in the quadratic case. The phenomenological consequences are clear: fundamental constants and parameters in the experimental setup are modified and experience oscillations. Therefore, many of the above mentioned experiments are also sensitive, even if with some suppression, to this couplings. These include quantum clocks, atom interferometers, optical cavities, optical interferometers, mechanical resonators and equivalence principle violation searches.

We conclude with Table 2.1, taken from [96], that summarizes experimental and astrophysical probes for scalar and vector fields coupled to the SM states.

DM	Couplings	Experimental and astrophysical probes
ϕ	Gravity	CMB, Matter power spectrum (Lyαf, Halo Mass Function) Galactic rotation curves, Black hole superradiance
	Electromagnetism $(\phi F_{\mu\nu}F^{\mu\nu})$	EP violation and fifth-force searches All optical and microwave clocks, Optical cavities Optical and atom interferometers (including GW detectors) LC oscillators, Cosmic distance measurement Stellar observations, DM stimulated emission
	Electrons $(\phi\bar{e}e)$	EP violation and fifth-force searches Stellar observations Microwave and molecular clocks, Optical cavities Optical and atom interferometers (including GW detectors) Mechanical resonators, Molecular absorption
	Muons $(\phi\bar{\mu}\mu)$	$g_\mu - 2$, Stellar observations, Neutron star mergers
	Gluons $(\phi G_{\mu\nu}G^{\mu\nu})$	Microwave, molecular, and nuclear clocks EP violation and fifth-force searches
	Quarks $(\phi\bar{q}q)$ / Nucleons $(\phi\bar{N}N)$	Microwave, molecular, and nuclear clocks EP violation and fifth-force searches
A'_μ	Gravity	CMB, Matter power spectrum (Lyαf, Halo Mass Function) Black hole superradiance
	Kinetic Mixing	Coulomb's law, Light-shining-through-a-wall, CMB Stellar observations, Resonant cavities, LC circuits Quantum materials, Molecular absorption, Magnetometers Broadband reflectors, Plasma haloscopes, Dielectric haloscopes
	Minimal Gauge Coupling $(B, L, B-L)$	EP violation and fifth-force searches Stellar observations Optical and atom interferometers (including GW detectors) Molecular absorption Mechanical resonators
	Minimal Gauge Coupling $(L_\mu - L_\tau)$	Neutron star mergers

TABLE 2.1: Experimental and astrophysical probes for scalar and vector fields coupling to the SM particles. Couplings that can be induced at loop level are not considered. Pseudoscalar couplings are not included, see Figure 2.2 for axions. Table taken from [96] to which we refer for a full overview of the mentioned probes.

Chapter 3

Gravitational Focusing

In this Chapter, we study the distortion of the dark matter distribution via the gravitational interaction with a massive body, an effect called *gravitational focusing*. We explore the gravitational focusing of light bosonic dark matter and its unique signatures in the local overdensity and spectrum. We provide a formalism that captures the gravitational focusing effects of wave dark matter and highlights the similarities and differences with particle dark matter. While gravitational focusing effects are generally small, they could be much larger for dark matter substructures. Wherefore, we investigate how dark matter substructures (motivated by the observations of stars whose kinematic properties suggest the presence of a non-halo DM counterpart [58, 59] with same properties) respond to the gravitational potential of the Sun. A cartoon description of the geometry of gravitational focusing is shown in Figure 3.1.

The content of this Chapter is substantially based on [106]. The outline is the following. In Section 3.1, we review the main features of the focusing effect in the particle case mainly following [68, 69] for the sake of a later comparison with the wave dark matter. In Section 3.2, we derive the wave DM response to the gravitational potential of the massive object and we compute observables making use of the statistical formalism presented in Section 2.3. To gain insights on the wave features and to compare with particle DM, the monochromatic limit is explored as well as the particle, or semi-classical limit in the discussion Section 3.3. The main application of our formalism is presented in Section 3.4, devoted to the computation of the response of wave dark matter components to the gravitational potential of the Sun. We conclude in Section 3.5.

3.1 Particle focusing

We start reviewing the gravitational focusing of particle dark matter to set up the notation and formalism for a comparison with the wave focusing, that is the topic of next section. The treatment follows [68, 69].

3.1.1 Naive understanding

Let us consider the dark matter phase space distribution $f(t, \mathbf{x}, \mathbf{v})$. In the collisionless system, the phase space density is conserved, i.e. $df/dt = 0$. This is also the

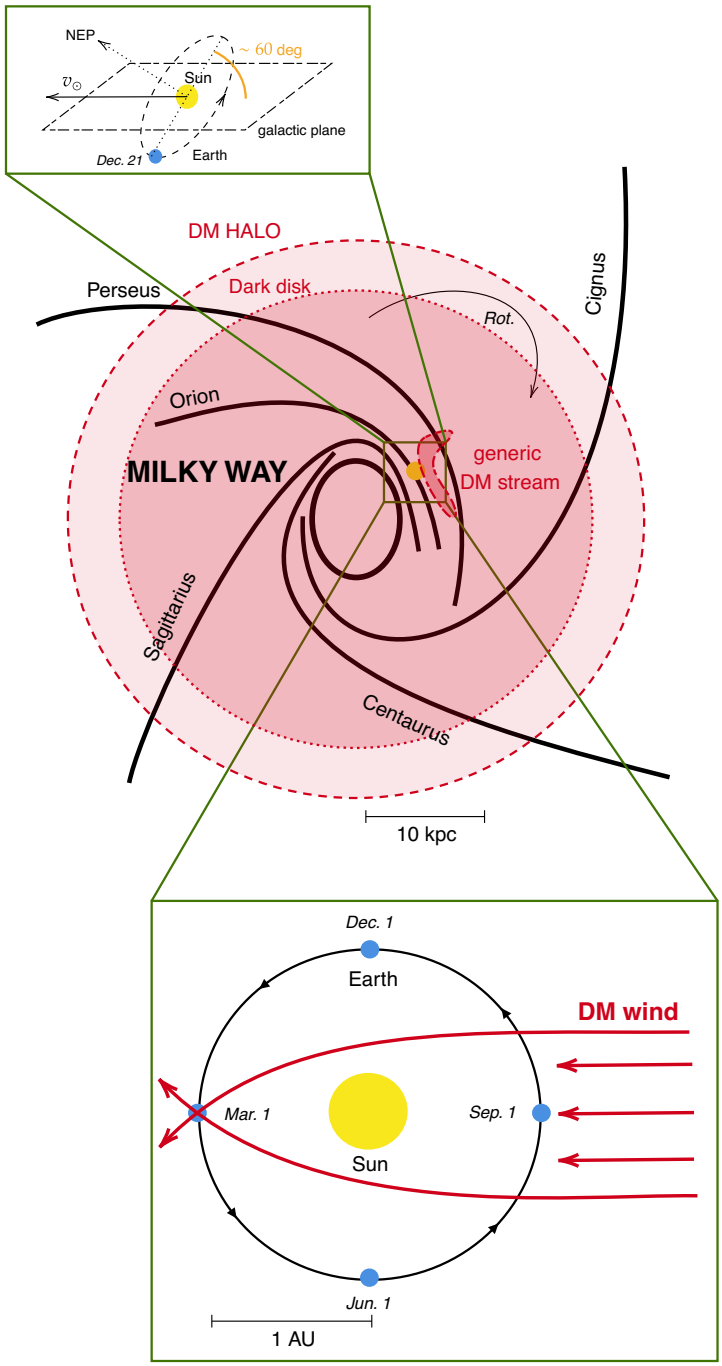

FIGURE 3.1: A cartoon illustrating the gravitational focusing effect. Different dark matter components, represented in the central figure, can be present in the solar neighborhood. Due to its orbit in the Orion arm around the Milky Way, the Sun experiences, in its rest frame, a dark matter "wind". This wind is focused behind the Sun and the Earth experiences an overdensity around March due to the geometry of its orbit.

case in the scenario under consideration, in which dark matter particles feel only an (external) pull force due to the gravitational potential of a massive object.

We can have a first understanding of gravitational focusing thanks to Liouville's theorem. According to this result, the phase space volume is conserved along the particle trajectory obtained by solving the equation of motion from the system's Hamiltonian.

Consider particles localized in an infinitesimal phase space volume $d^3x_0\, d^3v_0$ ally far away from a source of mass M. We work in the rest frame of the source. Let us assume, for simplicity, that the phase space density f is constant over this volume, that is, we choose this volume sufficiently small. When particles approach the source they get pulled and, falling in its gravitational well, they accelerate. At distance r from the source, the speed is

$$v(r) = \sqrt{v_0^2 + v_e^2(r)}\,. \tag{3.1}$$

Here v_0 is the asymptotic value of the particles' speed, far away from the massive body and $v_e^2(r) = 2GM/r$ is the escape velocity.

If we impose the conservation of the phase space volume by the Liouville's theorem, $d^3x_0\, d^3v_0 = d^3x\, d^3v$, where the right-hand side is the volume at distance r from the source, we find $d^3x = [v_0/v(r)]d^3x_0$, that is, the spatial volume is reduced by the factor $v_0/v(r) < 1$ and the dark matter particles are *focused*. As a consequence, the density at r is enhanced from the asymptotic value ρ_0

$$\rho(r) \approx \frac{\rho_0 v(r)}{v_0} = \rho_0 \sqrt{1 + \frac{v_e^2(r)}{v_0^2}}. \tag{3.2}$$

This expression gives us the intuitive understanding that the focusing effect is stronger closer to the source, where the escape velocity is larger, and is particularly important for slow particles (in the rest frame of the massive body).

3.1.2 Quantitative analysis

Let us be more quantitative now. Our boundary condition is $f = f(\mathbf{v}_0)$, the velocity distribution at $r \to \infty$, which we assume independent on position and normalized as $\int d^3v_0\, f(\mathbf{v}_0) = 1$. The mass in the infinitesimal phase space volume asymptotically far away from M is, for the Liouville's theorem,

$$\rho_0 f(\mathbf{v}_0) d^3x_0\, d^3v_0 = \rho_0 f(\mathbf{v}_0) d^3x\, d^3v\,. \tag{3.3}$$

The mass density at position $\mathbf{x}$ relative to the source is found by integrating the velocity distribution, which is conserved

$$\begin{aligned} \rho(\mathbf{x}) &= \rho_0[1 + \delta(\mathbf{x})] \\ &= \rho_0 \int d^3v\, f(\mathbf{v}_0) \\ &= \rho_0 \int d^3v_0\, J(\mathbf{v}_0, \mathbf{x})\, f(\mathbf{v}_0)\,. \end{aligned} \tag{3.4}$$

The Jacobian $J(\mathbf{v}_0, \mathbf{x}) = |dv/dv_0|$ is given by [68]

$$J(\mathbf{v}_0, \mathbf{x}) = \frac{1}{2}\left[\left(1 + \frac{2v_e^2/v_0^2}{1 - \hat{v_0}\cdot\hat{x}}\right)^{\frac{1}{2}} + \left(1 + \frac{2v_e^2/v_0^2}{1 - \hat{v_0}\cdot\hat{x}}\right)^{-\frac{1}{2}}\right] . \tag{3.5}$$

For a given velocity distribution, the integral in the third line of Eq. (3.3) can be performed numerically. Alternatively, one can compute the integral in the second line using the expression for $\mathbf{v}_0(\mathbf{v}, \mathbf{x})$ that can be obtained via the conservation of the Laplace-Runge-Lenz vector [68, 69].

$$\mathbf{v}_0(\mathbf{v}, \mathbf{x}) = \frac{v_0^2\mathbf{v} + \frac{1}{2}v_e^2 v_0 \hat{x} - v_0\mathbf{v}(\mathbf{v}\cdot\hat{x})}{v_0^2 + \frac{1}{2}v_e^2 - v_0(\mathbf{v}\cdot\hat{x})} . \tag{3.6}$$

The expressions for $J(\mathbf{v}_0, \mathbf{x})$ and $\mathbf{v}_0(\mathbf{v}, \mathbf{x})$ can be expanded in the case of small escape velocity and analytical expressions can be obtained for a Maxwell-Boltzmann distribution distribution [213].

To proceed, let us consider a Maxwell-Boltzmann distribution for the dark matter velocity distribution asymptotically far away from the massive body

$$f(\mathbf{v}_0) = \frac{1}{(2\pi\sigma^2)^{3/2}} \exp\left[-\frac{(\mathbf{v}_0 - \mathbf{v}_{\rm dm})^2}{2\sigma^2}\right] , \tag{3.7}$$

with mean velocity $\mathbf{v}_{\rm dm}$ and dispersion σ. In this way, the density contrast δ of the focused DM is completely determined once three parameters are specified

$$v_{\rm dm}/\sigma, \qquad r/\bar{r}, \qquad \mu \equiv \hat{v}_{\rm dm}\cdot\hat{x} . \tag{3.8}$$

Here

(i) $v_{\rm dm}/\sigma$ is the asymptotic speed in units of the dispersion;

(ii) $r/\bar{r}$ is the radial distance from the source in units of the radius of gravitational influence

$$\bar{r} = \frac{GM}{\sigma^2} = 0.03\ \text{AU}\ \left(\frac{M}{M_\odot}\right)\left(\frac{240\ \text{km/sec}}{\sqrt{2}\sigma}\right)^2 , \tag{3.9}$$

where we normalized to the typical value of the dark matter velocity dispersion for the Milky Way virialized halo. An equivalent choice would be v_e/σ instead of $r/\bar{r}$.

(iii) $\mu \equiv \hat{v}_{\rm dm}\cdot\hat{x}$ is giving the angular dependence.

We show the density contrast of focused particle dark matter in Figure 3.2. We choose $\mathbf{v}_{\rm dm} = (-240, 0, 0)$ km/s and change the value of the ratio $v_{\rm dm}/\sigma$. Increasing this parameter, the dark matter approaches the monochromatic limit. We see that if the dispersion is too large, the system is supported by pressure and the focusing is very weak and isotropic, while for very cold dark matter a well defined order-one overdensity tail forms. The central plot shows the case for virialized halo-like dark matter, $v_{\rm dm}/\sigma = \sqrt{2}$. The density contrast is invariant under the rotation with respect to the $\hat{v}_{\rm dm}$ axis, due to the azimuthal symmetry of the system.

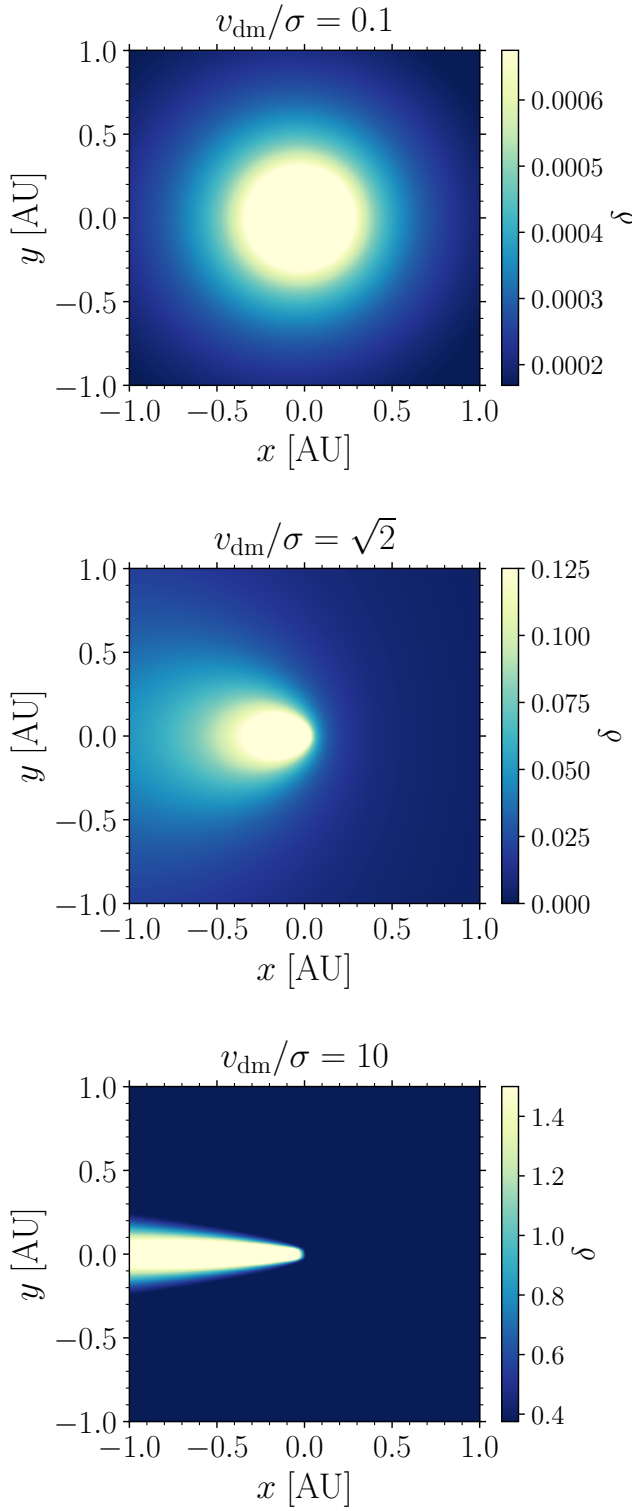

FIGURE 3.2: The density contrast of the focused particle dark matter. We choose $\mathbf{v}_{\rm dm} = (-240, 0, 0)$ km/s and the source mass to be the solar mass. We plot the density contrast for increasing values of $v_{\rm dm}/\sigma$.

In the limit $v_e \ll \sigma$, we can obtain an analytic expression for the density contrast [42]

$$\delta(\mathbf{x}) \approx \frac{v_e^2}{2\sigma^2} \exp\left[-\frac{v_e^2}{2\sigma^2}(1-\mu^2)\right] \mathrm{erfc}\left(-\frac{v_{\rm dm}\mu}{\sqrt{2}\sigma}\right) . \tag{3.10}$$

This expression can be used to study the dark matter substructures with $v_e < \sigma$.

3.1.3 Downstream density and angular average

To better understand the properties of the overdensity profile, we can consider two quantities

$$\delta_{\rm ds}(r) = \delta(r, \mu = 1) , \tag{3.11}$$

$$\delta_{\rm avg}(r) = \frac{1}{4\pi}\int d\Omega_{\hat{x}}\, \delta(\mathbf{x}) = \frac{1}{2}\int d\mu\, \delta(r,\mu) . \tag{3.12}$$

$\delta_{\rm ds}$ is the density along the downstream direction ($\hat{v}_{\rm dm}\cdot\hat{x} = \mu = 1$) and $\delta_{\rm avg}$ is the density contrast averaged over a sphere of radius r. Although these quantities depend on two parameters, $v_{\rm dm}/\sigma$ and $r/\bar{r}$, they only depend on a specific combination of them. For the downstream, we obtain

$$1 + \delta_{\rm ds} \approx \sqrt{1 + \frac{v_e^2}{\sigma^2}} = \sqrt{1 + \frac{2\bar{r}}{r}} . \tag{3.13}$$

This approximation follows easily from the approximation in Eq. (3.10), if $v_e/\sigma < 1$. Notice that $\frac{1}{2}\int_{-1}^{1} d\mu\, J(v_0,\mu) = \sqrt{1 + v_e^2/v_0^2}$, so the exact result for $\delta_{\rm avg}$ is

$$1 + \delta_{\rm avg} = \int d^3v_0\, f(\mathbf{v}_0)\sqrt{1 + \frac{v_e^2}{v_0^2}} . \tag{3.14}$$

However, since $\langle v_0^2\rangle = \int d^3v_0\, v_0^2 f(\mathbf{v}_0) = v_{\rm dm}^2 + 3\sigma^2$, we can approximate

$$\begin{aligned} 1 + \delta_{\rm avg} &= \left\langle\sqrt{1 + \frac{v_e^2}{v_0^2}}\right\rangle \approx \sqrt{1 + \frac{v_e^2}{\langle v_0^2\rangle}} \\ &\approx \sqrt{1 + \frac{v_e^2}{v_{\rm dm}^2 + \sigma^2}} = \sqrt{1 + \frac{2\bar{r}/r}{1 + v_{\rm dm}^2/\sigma^2}} . \end{aligned} \tag{3.15}$$

We neglected the factor of 3 in front of the σ^2 for the sake of simplicity.

We validate these approximations numerically and present a comparison with exact results in Figure 3.3. In the left panel, we plot $\delta_{\rm ds}$ for $v_{\rm dm}/\sigma \in [0.1, 10]$ and find that the result is weakly dependence on $v_{\rm dm}/\sigma$. The red dashed line corresponds to the approximation of $\delta_{\rm ds}$ in Eq. (3.13) matching the exact result within a factor of two over a two-order-of-magnitude range of $v_{\rm dm}/\sigma$. We repeat the exercise in the right panel for $\delta_{\rm avg}$ and compare the exact result with the approximation in Eq. (3.15). Again, for $v_{\rm dm}/\sigma \in [0.1, 10]$ the approximation matches the exact result well. This agreement highlights the sensitivity of the result on the combination $(r/\bar{r})[1 + v_{\rm dm}^2/\sigma^2]$ only.

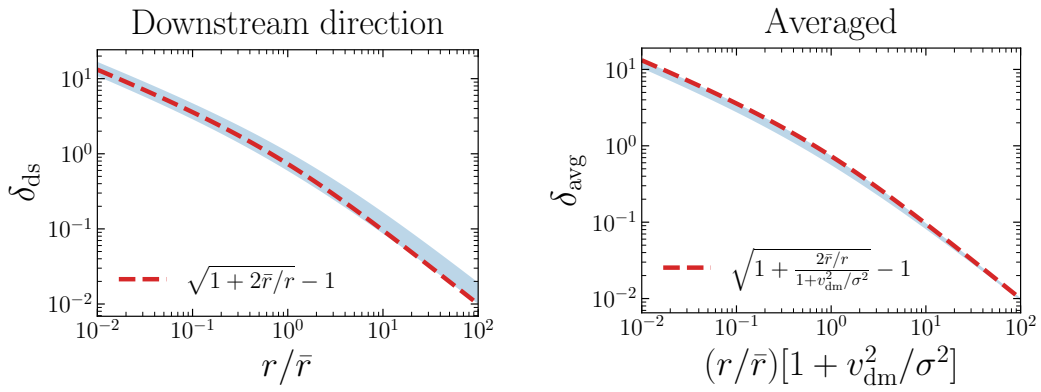

FIGURE 3.3: **Left**: the density contrast $\delta_{\rm ds}$ of the focused particle dark matter on the downstream direction, $\hat{v}_{\rm dm}\cdot\hat{x}=1$. **Right**: the density contrast averaged over the solid angle. In both panels, the lower and upper boundary of the blue band correspond to $v_{\rm dm}/\sigma = 0.1$ and 10, respectively.

Remarkably, the ratio $\delta_{\rm avg}/\delta_{\rm ds}$ represents the angular scale over which the density contrast is non-vanishing. In the reasonable limit $v_e < \sigma < v_{\rm dm}$, one obtains the following behavior, expanding the above approximations:

$$\Delta\mu \sim \frac{\delta_{\rm avg}}{\delta_{\rm ds}} \approx \frac{\sigma^2}{v_{\rm dm}^2}\,. \tag{3.16}$$

Thus, the ratio of $v_{\rm dm}/\sigma$ alone can explain the angular scale of the density contrast. This provides an explanation for the observations in Figure 3.2, as well as the transition to the monochromatic limit regime where the density contrast is highly concentrated around the downstream direction.

3.2 Wave focusing

In this Section, we develop the formalism to describe the focusing of wave dark matter. Much of this formalism was already established in Section 2.3 for the stochasticity of the wave field and in Section 2.4 for the description of the wave dark matter in curved space-time.

As previously done, we consider a free spinless bosonic dark matter particle with a mass m, minimally coupled to gravity. The action of the system reads

$$S = \int d^4x\,\sqrt{-g}\left[\frac{M_{\rm pl}^2}{2}R + \frac{1}{2}g^{\mu\nu}(\partial_\mu\phi)(\partial_\nu\phi) - \frac{1}{2}m^2\phi^2\right]\,. \tag{3.17}$$

Here $g = \det g_{\mu\nu}$ is the determinant of the metric tensor, $g_{\mu\nu}$ and $M_{\rm pl}$ is the reduced Planck mass. We consider the weak-gravity metric

$$ds^2 = (1+2\Phi)dt^2 - (1-2\Phi)[dr^2 + r^2 d\Omega]\,, \tag{3.18}$$

with $\Phi(\mathbf{x})$ the gravitational potential. We assume this gravitational potential to be static, or that it evolves on timescales much longer than several years.

To analyze non-relativistic dark matter, we adopt a similar approach as in Section 2.4.1 by expanding the field and separating the fast oscillations due to the mass. This allows us to focus on the wave oscillations at the characteristic wavelength $\lambda_{\rm dB} \sim 1/k$ with k. In the continuum limit, the field is expressed in terms of modes with wavenumber $\mathbf{k} = m\mathbf{v}$, which correspond to plane waves far from the gravitational potential source. We approximate $\omega_{\mathbf{k}} = \sqrt{\mathbf{k}^2 + m} \approx m + \mathbf{k}^2/2m$ and rewrite the field as

$$\hat{\phi}(x) = \int \frac{d^3k}{(2\pi)^3} \frac{1}{\sqrt{2m}} \left[\hat{a}_{\mathbf{k}} \psi_{\mathbf{k}}(x) e^{-imt} + \hat{a}^\dagger_{\mathbf{k}} \psi^\star_{\mathbf{k}}(x) e^{imt} \right] . \tag{3.19}$$

The annihilation and creation operators $\hat{a}_{\mathbf{k}}$, $\hat{a}^\dagger_{\mathbf{k}}$ satisfy canonical commutation relations. To obtain ensemble averages of the field, which were discussed in Section 2.3, we can rewrite the field in the following way

$$\phi(x) = \int \frac{d^3k}{(2\pi)^3} \frac{1}{\sqrt{2m}} \left[\alpha_{\mathbf{k}} \psi_{\mathbf{k}}(x) e^{-imt} + \alpha^\star_{\mathbf{k}} \psi^\star_{\mathbf{k}}(x) e^{imt} \right] . \tag{3.20}$$

Here, the annihilation and creation operators have been replaced with complex number α whose modulus follows the Reyleigh distribution and phase is uniformly distributed. These numbers reflect the stochastic nature of the wave field. Since the occupation number is large, we can neglect the non-vanishing commutator between the annihilation and creation operators.

On the other hand, the mode functions $\psi_{\mathbf{k}}$ encode the response of wave dark matter to the gravitational potential and are obtained by solving the equation of motion. Assuming that $\psi_{\mathbf{k}}$ is proportional to $e^{i\mathbf{k}\cdot\mathbf{x}}$, where the gravitational potential Φ vanishes, is a boundary condition for the problem, given the definition and physical interpretation of the continuous quantum number $\mathbf{k}$.

3.2.1 Wave function

Let us solve the equation of motion for the mode function. In Section 2.4.1, we found that the Klein-Gordon equation Eq. (2.60) on small scales and in the non-relativistic approximation gets into the form of the Schrödinger equation. Since this equation is linear, we can write it for each mode function $\psi_{\mathbf{k}}$

$$i\partial_t \psi_{\mathbf{k}} = \left[-\frac{1}{2m}\nabla^2 + m\Phi \right] \psi_{\mathbf{k}} . \tag{3.21}$$

The gravitational potential Φ is determined by the Poisson equation,

$$\nabla^2 \Phi = 4\pi G(\rho_M + \rho_{\rm dm}) , \tag{3.22}$$

where ρ_M and $\rho_{\rm dm}$ are the mass density profile of the source and of the dark matter, respectively. We treat the source as point-like, of mass M, and we neglect the self-gravity contribution $\rho_{\rm dm}$ compared to ρ_M. Under these assumptions, the gravitational potential is a simple $1/r$-central potential, $\Phi(r) = -GM/r$ and the Schrödinger equation can be solved independently, with Φ treated an external potential. Actually, the problem is identical to the Coulomb scattering of an electron with a proton: the

wave dark matter plays the role of the electron, the point mass M of the proton and the electromagnetic force is replaced by Newton's gravitational pull.

To solve Eq. (3.21), we factor out the remaining plane wave time dependence $\psi_{\mathbf{k}}(t,\mathbf{x}) = e^{-iE_{\mathbf{k}}t}\psi_{\mathbf{k}}(\mathbf{x})$ with $E_{\mathbf{k}} = k^2/2m$. The Schrödinger equation becomes

$$\left[\nabla^2 + k^2 + \frac{2m\alpha_G}{r}\right]\psi_{\mathbf{k}}(\mathbf{x}) = 0\,. \tag{3.23}$$

Here $\alpha_G = GMm$ is the gravitational fine structure constant, highlighting the analogy with the electron-proton scattering case. We impose a plane wave boundary condition, i.e. $\psi_{\mathbf{k}} = e^{i\mathbf{k}\cdot\mathbf{x}}$ at $r \to \infty$. The analytical solution is given by [33, 325]

$$\boxed{\psi_{\mathbf{k}}(\mathbf{x}) = e^{i\mathbf{k}\cdot\mathbf{x}}\Gamma[1-i\beta]e^{\pi\beta/2}{}_1F_1\left[i\beta, 1, ikr(1-\hat{k}\cdot\hat{x})\right]\,.} \tag{3.24}$$

Here $\beta = GMm^2/k = \alpha_G/v$, $\Gamma[z]$ is the Euler gamma function, ${}_1F_1(a,b,z)$ is the confluent hypergeometric function. Let us have a physical intuition of this expression considering the large and small distance asymptotic behaviors.

For a large argument $|z| \gg 1$ and $\arg(z) \in (-\pi/2, 3\pi/2)$, the confluent hypergeometric function can be expanded as

$${}_1F_1(a,b,z) \approx \frac{e^z z^{a-b}}{\Gamma[a]} + \frac{e^{i\pi a} z^{-a}}{\Gamma[b-a]}\,. \tag{3.25}$$

This limit corresponds to a large distance expansion. If we introduce $\cos\theta = \hat{k}\cdot\hat{x}$ and $q = kr(1-\cos\theta)$, we can rewrite the wave function in the large q limit in the form

$$\psi_{\mathbf{k}}(\mathbf{x}) \approx e^{i(\mathbf{k}\cdot\mathbf{x} - \beta\log q)} + \frac{f_R(\theta)}{r} e^{i(kr + \beta\log q)}\,, \tag{3.26}$$

with the function $f_R(\theta)$ given by

$$f_R(\theta) = \frac{\Gamma[1-i\beta]}{\Gamma[1+i\beta]}\frac{r\beta}{q} = \frac{\Gamma[1-i\beta]}{\Gamma[1+i\beta]}\frac{m\alpha_G}{2k^2\sin^2(\theta/2)}\,. \tag{3.27}$$

The asymptotic expansion shows that the solution is the sum of a plane wave $e^{i\mathbf{k}\cdot\mathbf{x}}$, as requested by the boundary conditions and an outgoing spherical wave after the collision $f_R(\theta)e^{ikr}/r$, modulo some logarithmic corrections. This large-distance expansion is the form predicted by the scattering theory of quantum mechanics and, remarkably, it agrees with the Rutherford scattering cross section

$$\frac{d\sigma}{d\Omega} = |f_R(\theta)|^2 = \frac{m^2\alpha_G^2}{4k^4\sin^4(\theta/2)}\,. \tag{3.28}$$

In the opposite limit, $|z| \ll 1$, the hypergeometric function approaches unity. This corresponds to the small distance expansion. The squared wave function becomes

$$|\psi_{\mathbf{k}}(0)|^2 = \frac{2\pi\beta}{1-e^{-2\pi\beta}}\,. \tag{3.29}$$

The above expression is identical to the Sommerfeld enhancement factor for dark matter annihilation when the interaction is mediated by the Coulomb interaction [326]. For large values of $\beta = \alpha_G/v \gg 1$, e.g. when the dark matter velocity is smaller than α_G, this expression shows indeed an enhancement proportional to β. Instead, for $\beta \ll 1$ the value of the squared function at the origin converges to unity.

3.2.2 Density contrast and power spectrum

We can now use the density operator of the wave dark matter field $\hat{\phi}$ found in Section 2.3 to find ensemble averages, i.e. moments of the field. These physical quantities are directly connected to observables in dark matter detection experiments.

We are particularly interested in the second moment of the field $\langle\hat{\phi}^2\rangle$, because it is related to the density contrast δ of wave dark matter

$$1 + \delta(\mathbf{x}) = \frac{\langle\hat{\phi}^2\rangle}{\phi_0^2} \,. \tag{3.30}$$

Here $\phi_0 = \sqrt{\rho_0}/m$ is the root mean square of the field value measured asymptotically far away from the source, which is determined by the asymptotic value of the wave dark matter mass density ρ_0 and mass m. The second moment of the field is related to the power of any dark matter signal; indeed, naively, it measures how much energy is stored in the field in a given spatial position.

This information is of primary importance for wave dark matter direct detection experiments such as in axion and axion-like particle searches relying on interactions with the photon field mediated by the operator $\mathcal{L} \supset \phi F\tilde{F}$, see Section 2.7[1], the total signal power is proportional to $\langle\hat{\phi}^2\rangle$. The same holds for scalar dark matter searches that look for couplings to fermions or photons $\mathcal{L} \supset \phi\bar{\psi}\psi$, ϕFF via the oscillations of fundamental constants as reviewed in Section 2.7 [2].

Let us find an explicit expression for the second moment of the field. We can write it in terms of the expectation value of products of annihilation and creator operators, which have been computed in Eq. (2.55) exploiting the density operator in Eq. (2.54). Explicity,

$$\begin{aligned}\langle\hat{\phi}^2(x)\rangle \;=\; & \frac{1}{2m}\int\frac{d^3k}{(2\pi)^3}\int\frac{d^3k'}{(2\pi)^3}\Big[\left\langle\hat{a}_{\mathbf{k}}\hat{a}^\dagger_{\mathbf{k}'}\right\rangle\psi_{\mathbf{k}}\psi^\star_{\mathbf{k}'} + \left\langle\hat{a}_{\mathbf{k}}\hat{a}_{\mathbf{k}'}\right\rangle\psi_{\mathbf{k}}\psi_{\mathbf{k}'}e^{-2imt} \\ & + \left\langle\hat{a}^\dagger_{\mathbf{k}}\hat{a}_{\mathbf{k}'}\right\rangle\psi^\star_{\mathbf{k}}\psi_{\mathbf{k}'} + \left\langle\hat{a}^\dagger_{\mathbf{k}}\hat{a}^\dagger_{\mathbf{k}'}\right\rangle\psi_{\mathbf{k}}\psi^\star_{\mathbf{k}}e^{2imt}\Big] \,.\end{aligned} \tag{3.31}$$

We adapt the results from Eq. (2.55) to the continuum limit,

$$\begin{aligned}\left\langle\hat{a}^\dagger_{\mathbf{k}}\hat{a}_{\mathbf{k}'}\right\rangle &= (2\pi)^3\delta^{(3)}(\mathbf{k}-\mathbf{k}')n_{\mathbf{k}} \,, \\ \left\langle\hat{a}_{\mathbf{k}}\hat{a}^\dagger_{\mathbf{k}'}\right\rangle &= (2\pi)^3\delta^{(3)}(\mathbf{k}-\mathbf{k}')[n_{\mathbf{k}}+1] \approx \left\langle\hat{a}^\dagger_{\mathbf{k}}\hat{a}_{\mathbf{k}'}\right\rangle \\ \left\langle\hat{a}_{\mathbf{k}}\hat{a}_{\mathbf{k}'}\right\rangle &= \left\langle\hat{a}^\dagger_{\mathbf{k}}\hat{a}^\dagger_{\mathbf{k}'}\right\rangle = 0 \,,\end{aligned} \tag{3.32}$$

[1] For instance, ADMX [71–73], HAYSTAC [74, 75], ABRACADABRA [76, 77, 287], DM-Radio [78], CAPP [79], MADMAX [80], ORGAN [81] and so on.

[2] For instance, atomic clocks [40, 295, 296, 298, 308, 327, 328], atomic and molecular spectroscopy searches [94, 329], and interferometry [301–303, 330, 331].

where $n_{\mathbf{k}}$ is the occupation number of mode $\mathbf{k}$. It follows that

$$\langle \hat{\phi}^2(x) \rangle = \int \frac{d^3k}{(2\pi)^3} \frac{n_{\mathbf{k}}}{m} |\psi_{\mathbf{k}}(x)|^2 \,. \tag{3.33}$$

In the non relativistic limit, the three-momentum asymptotically far away from the source is given in terms of the velocity $\mathbf{k} = m\mathbf{v}$. Therefore, it is natural to rewrite the integral above as an integral over asymptotic velocities[3]. We define the velocity probability distribution as

$$f(\mathbf{v}) \equiv \frac{m^4}{(2\pi)^3} \frac{n_{\mathbf{k}}}{\rho_0} \,, \tag{3.34}$$

normalized as $\int d^3v \, f(\mathbf{v}) = 1$. Notice that any $e^{iE_{\mathbf{k}}t}$ factor in $\psi_{\mathbf{k}}$ gets canceled and $|\psi_{\mathbf{k}}|^2$ has no time dependence. We can finally write the density contrast as

$$\boxed{1 + \delta(\mathbf{x}) = \int d^3v \, f(\mathbf{v}) |\psi_{\mathbf{v}}(\mathbf{x})|^2 \,.} \tag{3.35}$$

This compact expression can be compared with the corresponding expression for particle dark matter in Eq. (3.4): the Jacobian factor $J(\mathbf{v}_0, \mathbf{x})$ in the second line of Eq. (3.4) that describes the particle trajectory is now replaced with the squared amplitude of the wave function $|\psi_{\mathbf{v}}(\mathbf{x})|^2$. Both factors are weighted by the velocity distribution asymptotically far away from the source to give the density contrast.

To proceed, we assume a Maxwell-Boltzmann velocity distribution Eq. (3.7) as in Section 3.1.2. Then, the density contrast depends on four parameters

$$v_{\rm dm}/\sigma, \qquad r/\bar{r}, \qquad \mu \equiv \hat{v}_{\rm dm} \cdot \hat{x}, \qquad 2\pi\bar{r}/\lambda_{\rm dB} \qquad . \tag{3.36}$$

The first three parameters are the same introduced in Section 3.1.2 for the particle dark matter. The fourth is (2π) times the ratio of the radius of gravitational influence $\bar{r}$ and the de Broglie wavelength

$$\lambda_{\rm dB} = \frac{2\pi}{mv} \simeq 1 \text{ AU} \left(\frac{10^{-14} \text{ eV}}{m}\right) \left(\frac{240 \text{ km/s}}{v}\right) \,. \tag{3.37}$$

where we scaled to typical values of interest. As we will see in the next section, the de Broglie wavelength is a key quantity that controls the gravitational response of the wave dark matter.

We also compute the spectrum of the field fluctuations in the frequency space. The power of the field $\hat{\phi}$ is defined as

$$P_\phi(\mathbf{x}) \equiv \lim_{T\to\infty} \frac{1}{T} \int_{-T/2}^{T/2} dt \, \hat{\phi}^2(t, \mathbf{x}) = \int_{-\infty}^{\infty} \frac{d\omega}{2\pi} S_\phi(\omega, \mathbf{x}) \tag{3.38}$$

[3]Note that in Section 3.1 we used $\mathbf{v}_0$ to denote the particle dark matter velocity asymptotically far away from the source. We omit the subscript here to ease the notation.

and the power spectral density is

$$S_\phi(\omega, \mathbf{x}) \equiv \lim_{T\to\infty} \frac{|\hat{\phi}(\omega, \mathbf{x})|^2}{T} \,, \tag{3.39}$$

with the Fourier component of the field obtained via

$$\hat{\phi}(\omega, \mathbf{x}) \equiv \int_{-\infty}^{\infty} dt\; e^{i\omega t} \hat{\phi}(t, \mathbf{x}) \,. \tag{3.40}$$

Since ϕ is a random field, both P_ϕ and S_ϕ have to be understood as random fields.

We can compute the ensemble averages of the quantities defined above. It is evident that $\langle P_\phi \rangle = \phi_0^2(1+\delta)$, manifesting the important relation between the power and the density contrast.

Instead, the ensemble average of the power spectral density requires a bit more effort. The ensemble average of the Fourier component of the field reads

$$\begin{aligned} \langle |\hat{\phi}(\omega, \mathbf{x})|^2 \rangle &= \phi_0^2 \int d^3v\, f(\mathbf{v}) |\psi_{\mathbf{v}}(\mathbf{x})|^2 \int_{-\infty}^{\infty} dt\, dt'\, e^{i\omega(t-t')} \cos[\omega_{\mathbf{v}}(t-t')] \\ &= \pi\phi^2 T \int d^3v\, f(\mathbf{v}) |\psi_{\mathbf{v}}(\mathbf{x})|^2 [\delta(\omega-\omega_{\mathbf{v}}) + \delta(\omega+\omega_{\mathbf{v}})] \\ &= \frac{2\pi T \phi_0^2}{mv} \bar{f}(v, \mathbf{x})\Big|_{v=\sqrt{2(\omega/m-1)}} \,. \end{aligned} \tag{3.41}$$

We have used $[\delta(\omega)]^2 = \delta(\omega)\delta(0) = \delta(\omega)T/(2\pi)$ and $\omega_{\mathbf{v}} = m + m\mathbf{v}^2/2$. The result is multiplied by a factor of two, summing positive and negative frequency contributions. We have defined the function

$$\bar{f}(v, \mathbf{x}) \equiv v^2 \int d\Omega_{\hat{v}}\, f(\mathbf{v}) |\psi_{\mathbf{v}}(\mathbf{x})|^2 \,. \tag{3.42}$$

This $\bar{f}(v, \mathbf{x})$ might be interpreted as the speed distribution of wave dark matter including the gravitational focusing effect (due to which it acquires a spatial dependence). From the result of Eq. (3.41) the power spectral density is trivially found

$$\langle S_\phi(\omega, \mathbf{x}) \rangle = \frac{2\pi\phi_0^2}{mv} \bar{f}(v, \mathbf{x})\Big|_{v=\sqrt{2(\omega/m-1)}} \,. \tag{3.43}$$

So far, we have focused on the variance of the field itself. However, some of axion and axion-like DM searches are based on interactions derived by the operator $\mathcal{L} \supset \partial_\mu\phi\bar{\psi}\gamma^\mu\gamma_5\psi$, see Section 2.7 for more details[4]. In such cases, the signal power as well as the power spectrum would depend on the variance of the gradient of the field. The variance of the gradient can be obtained in the same way as explained above. Introducing a detector sensitivity axis $\hat{n}$, we have

$$\langle |\hat{n}\cdot\nabla\phi|^2 \rangle = \phi_0^2 \int d^3v\, f(\mathbf{v}) |\hat{n}\cdot\nabla\psi_{\mathbf{v}}(\mathbf{x})|^2 \,. \tag{3.44}$$

[4]For instance, CASPEr [169,316], atomic magnetometers [311,312], and an oscillating neutron electric dipole moment experiment [165].

The ensemble average of the power spectral density can be obtained as

$$\left\langle S_{\nabla\phi}(\omega,\mathbf{x})\right\rangle = \frac{2\pi\phi_0^2}{mv}\left[v^2\int d\Omega_{\hat{v}}\, f(\mathbf{v})|\hat{n}\cdot\nabla\psi_{\mathbf{v}}(\mathbf{x})|^2\right]_{v=\sqrt{2(\omega/m-1)}}. \tag{3.45}$$

While we have mainly focused on computing variances at the same location (because we are interested in the single detector's response), it is straightforward to compute correlations of fields at different locations with the same formalism. Such correlations contain additional information on wave dark matter phase at different locations, which can be used to extract further information, such as the directionality of the dark matter velocity distribution, and the angular distribution of potential dark matter substructures, from a network of wave dark matter detectors [332, 333].

3.3 Discussions

In this Section, we discuss the wave features that appear in the gravitational focusing phenomenon. In particular, we study two limits: the monochromatic limit in Section 3.3.1, in which the wave features appear clearly as they are not masked by the velocity dispersion and the semi-classical, or particle, limit, in which the wave and particle description match (see Section 3.3.3). The full treatment of wave DM with non-negligible velocity dispersion is investigated in Section 3.3.2. The reader that is not interested in this in-depth discussions can already dive into the application of gravitational focusing of dark matter structures in the solar system in Section 3.4.

3.3.1 Monochromatic limit

In order to understand the distinct wave effects in the gravitational response of wave dark matter, we investigate the monochromatic limit. In this scenario, the velocity distribution is a Dirac delta function $f(\mathbf{v}) = \delta^{(3)}(\mathbf{v}-\mathbf{v}_{\rm dm})$, which assumes a narrow flux of dark matter particles with velocity $\mathbf{v} = \mathbf{v}_{\rm dm}$. This limit is valuable as it allows us to observe wave effects that are not obscured by a significant dark matter velocity dispersion. Despite being a theoretical construct, the monochromatic limit is useful in practical applications, as it accurately describes the behavior of very cold dark matter components with $v_{\rm dm}/\sigma \gg 1$, such as stream dark matter, as we will see in Section 3.4.4.

Under the monochromatic limit assumption, the velocity integral in Eq. (3.35) collapses to

$$\begin{aligned} 1+\delta(\mathbf{x}) &= |\psi_{\mathbf{v}}(\mathbf{x})|^2 \\ &= \frac{2\pi\beta}{1-e^{-2\pi\beta}}\left|{}_1F_1[i\beta,1,imvr(1-\hat{v}\cdot\hat{x})]\right|^2 \end{aligned} \tag{3.46}$$

Here $\beta = \alpha_G/v$ with v being the speed of dark matter far away from the source. Since the maximum value of the hypergeometric function squared is unity, the magnitude of the focusing is determined by the Sommerfeld enhancement factor. The hypergeometric function is responsible for the oscillation pattern.

Wave features

Figure 3.4 displays the density contrast for focused particle dark matter. The velocity of the dark matter is chosen to be $\mathbf{v} = \mathbf{v}_{\rm dm} = (-240, 0, 0)$ km/s, and the mass is varied as $m = 10^{-15}$, 10^{-14}, 10^{-13} eV. As the parameter $\alpha_G = GMm$ increases with increasing mass, so does β, which increases the prefactor in Eq. (3.46) and enhances the density contrast near the origin. Unlike the particle case, the density contrast does not diverge at the origin but instead saturates to a constant value $\delta \approx |\psi_{\mathbf{v}}(0)|^2 - 1$ for sufficiently small r. Moreover, since wave effects depend on the de Broglie wavelength $\lambda_{\rm dB}$, increasing the mass reduces the wavelength, leading to the distinct interference patterns we see in the various panels.

To better understand the wave properties in the density wake, we examine Figure 3.5. We plot the density contrast in the direction $\mu = 0$, normalized with respect to the central value, i.e., $\delta|_{\mu=0}/\delta(0)$, as a function of two parameters: $r/\bar{r}$ and $2\pi\bar{r}/\lambda_{\rm dB}$, where $\lambda_{\rm dB} = 2\pi/mv$ with v being the dark matter velocity far from the source M. The black line corresponds to $m\tilde{v}(r)r = 1$, where $\tilde{v} = \sqrt{v^2 + 2GM/r}$ is the *total* velocity. From this velocity, we can define the real, or effective de Broglie wavelength $\tilde{\lambda}_{\rm dB} = 2\pi/(m\tilde{v})$, so that the condition $m\tilde{v}r = 1$ corresponds to $\tilde{\lambda}_{\rm dB}/r = 2\pi$.

We observe that the density contrast approaches a saturation value of $\delta(0)$ for sufficiently small r, i.e., when $m\tilde{v}(r)r \lesssim 1$. However, for $m\tilde{v}(r)r \gtrsim 1$, the wave density contrast oscillates rapidly. When $m\tilde{v}(r)r \gg 1$, the density contrast is suppressed. It is important to note that the decay pattern is similar to that of particle dark matter, and this is the essence of the particle limit, which we discuss further in Section 3.3.3.

Comparison to particle dark matter

We can take advantage of the simplicity of the monochromatic limit to gain some insight regarding the comparison between wave and particle dark matter density contrasts. In the right panel of Figure 3.6, we plot the ratio of the density contrast averaged over the solid angle for wave and particle dark matter. Since we are in the monochromatic limit, the approximation in Eq. (3.15) becomes $1 + \delta_{\rm avg,\,p} = \sqrt{1 + v_e^2/v^2}$. We observe that for $m\tilde{v}(r)r \gtrsim 1$ the averaged density contrast for the wave dark matter becomes increasingly similar to the particle result. Instead, for $m\tilde{v}(r)r \lesssim 1$ the averaged density contrast is suppressed.

We can evince the suppression factor from Figure 3.7. In this plot we show again the ratio between the density contrasts averaged over the solid angle for wave and particle dark matter. However, in this figure we fix the ratio $r/\bar{r}$ to different values and we vary $m\tilde{v}r$. We observe that for $m\tilde{v}r < 1$ the wave dark matter result is suppressed with respect to the particle result by a factor $\delta_{\rm avg,\,w}/\delta_{\rm avg,\,p} \propto \pi m\tilde{v}r$. We understand that the angle-averaged wave density contrast in the monochromatic case goes as

$$1 + \delta_{\rm avg,\,w} \approx \pi \times \frac{2\pi r}{\tilde{\lambda}_{\rm dB}} \sqrt{1 + \frac{v_e^2}{v^2}}\,. \tag{3.47}$$

Remarkably, the ratio $\delta_{\rm avg,\,w}/\delta_{\rm avg,\,p}$ does not depend substantially on $r/\bar{r}$.

Summing up, in Figures 3.5, 3.6 and 3.7 we observe that a key parameter controlling the wave dark matter density contrast is the relative size of the de Broglie

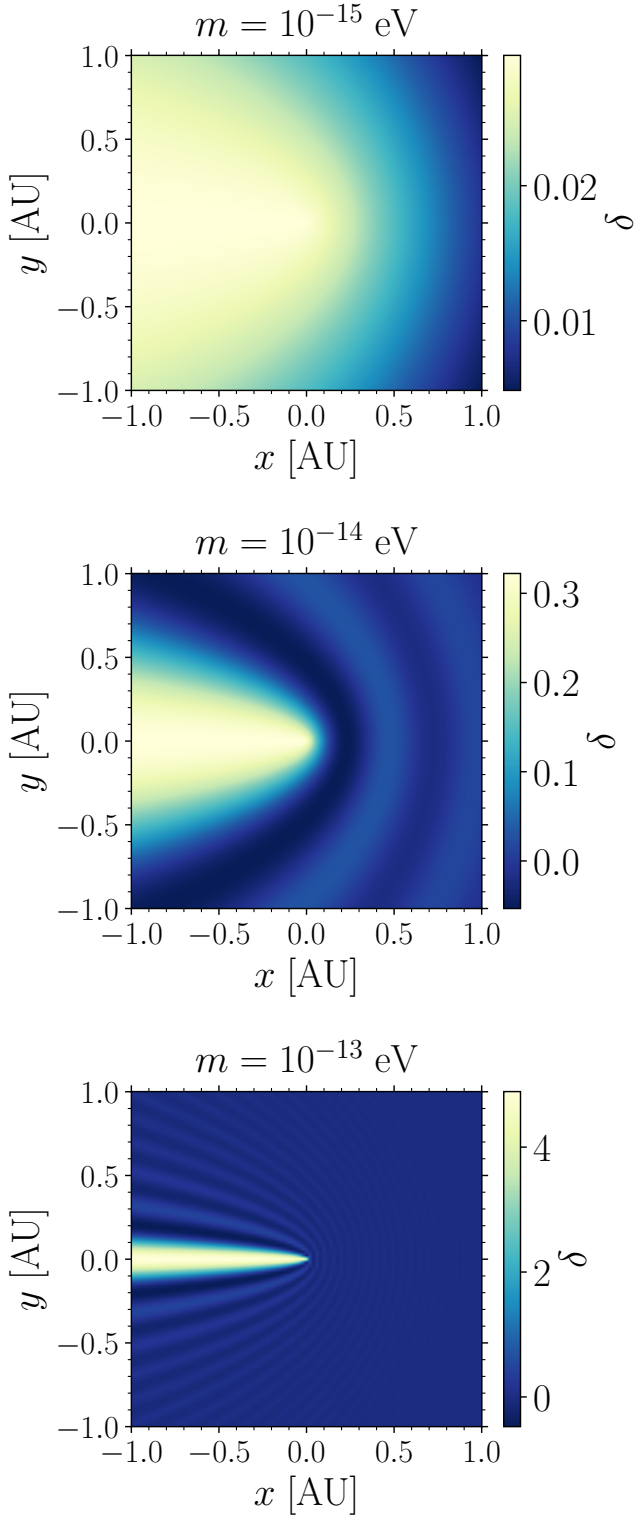

FIGURE 3.4: The density contrast for the wave dark matter in the monochromatic limit, i.e. with vanishing velocity dispersion. We choose $\mathbf{v} = \mathbf{v}_{\rm dm} = (-240, 0, 0)$ km/sec and $m = 10^{-15}$, 10^{-14}, 10^{-13} eV. The source mass is chosen to be the solar mass.

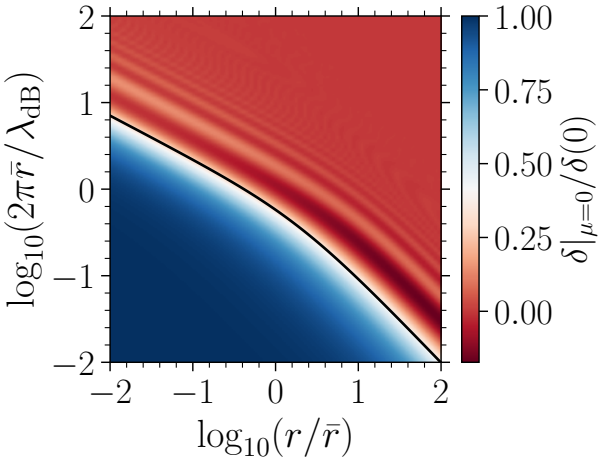

FIGURE 3.5: The density contrast in the orthogonal direction $\mu = \hat{x} \cdot \hat{v} = 0$ normalized to the value at the origin as a function of parameters $r/\bar{r}$ and $2\pi\bar{r}/\lambda_{\rm dB}$. A constant density contrast is observed for small radii satisfying $m\tilde{v}(r)r < 1$. The black line corresponds to radii for which $m\tilde{v}r = 1$.

wavelength computed with the total velocity $\tilde{\lambda}_{\rm dB}$ and the distance from the source r. For $m\tilde{v}r \gtrsim 1$ the response of wave dark matter to the gravitational potential is similar to the one of particle dark matter, albeit some oscillations, while for $m\tilde{v}r \lesssim 1$, wave features appear. In particular we observe suppression of the density contrast at scales smaller than the de Broglie wavelength. The limit $m\tilde{v}r \gg 1$ is the limit at which the wave dark matter approaches to particle dark matter. This will be the subject of Section 3.3.3.

3.3.2 Dispersed wave dark matter

The monochromatic results of Section 3.3.1 clearly show the role of de Broglie wavelength in distinguishing the wave and the particle case. We now consider the density contrast of wave dark matter with velocities distributed according to the Maxwell-Boltzmann distribution with mean $\mathbf{v}_{\rm dm}$ and dispersion σ, Eq. (3.7), to compare the wave dark matter with particle dark matter on an equal and more general footing.

To compare with particle dark matter, we consider again the density contrast along the downstream $\delta_{\rm ds}$

$$1 + \delta_{\rm ds}(r) = \int d^3v\, f(\mathbf{v}) |\psi_{\mathbf{v}}(r, \mu = 1)|^2 \tag{3.48}$$

and the wake field averaged over the solid angle $\delta_{\rm avg}$

$$1 + \delta_{\rm avg}(r) = \int d^3v\, f(\mathbf{v}) \int \frac{d\mu}{2}\, |\psi_{\mathbf{v}}(r, \mu)|^2 \,. \tag{3.49}$$

We calculate these quantities for various values of $r/\bar{r}$ while fixing $v_{\rm dm}/\sigma$, similar to what we did for the particle case in Figure 3.3. The results for the downstream density (left) and the density contrast averaged over angles (right) are presented in Figure 3.8. Similar to the monochromatic case, the particle-to-wave transition occurs

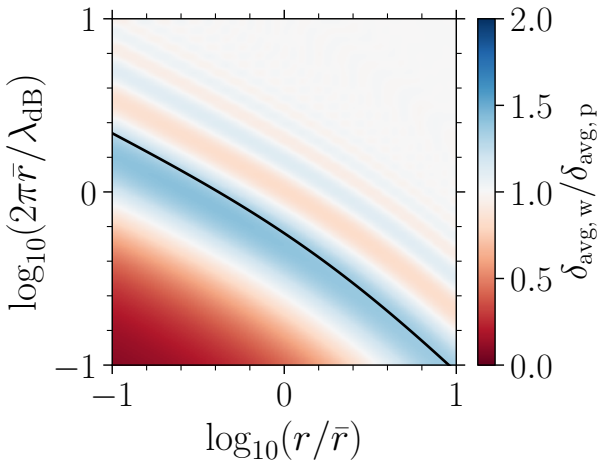

FIGURE 3.6: The ratio between the density contrast averaged over the solid angle for wave and particle dark matter in the monochromatic limit as a function of parameters $r/\bar{r}$ and $2\pi\bar{r}/\lambda_{\rm dB}$. For large radii, $m\tilde{v}r > 1$, the averaged density contrast for wave dark matter approaches that of the particle dark matter. The solid black line represents $m\tilde{v}r = 1$. Around this line, the wave result shows an enhancement with respect to the particle case.

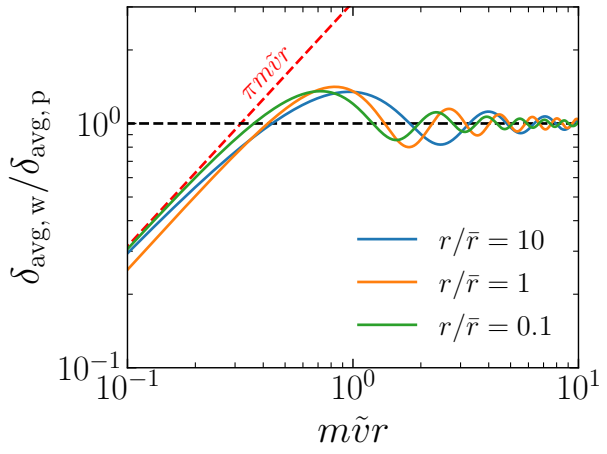

FIGURE 3.7: We present the ratio of density contrast averaged over the solid angle in the monochromatic case for wave and particle dark matter as a function of $m\tilde{v}r$. Different solid lines correspond to different values of $r/\bar{r}$. All of them approach to the classical particle result for $m\tilde{v}r \gg 1$. For $m\tilde{v}r < 1$, instead, the averaged wave density contrast is suppressed with respect to the particle case.

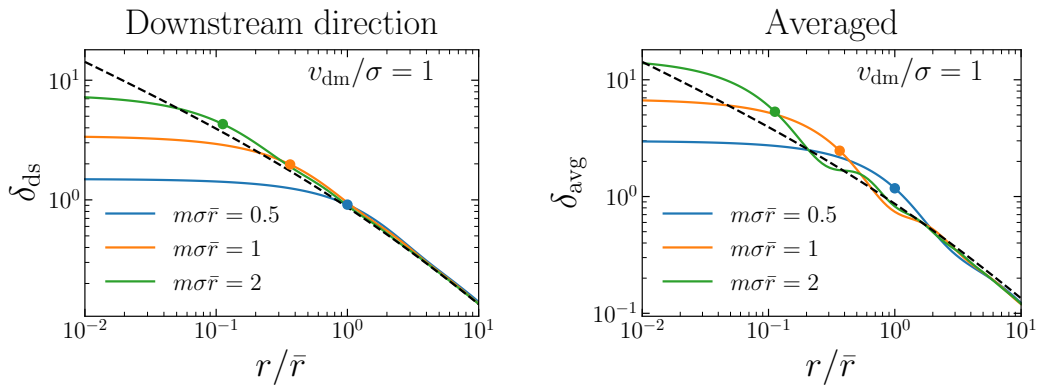

FIGURE 3.8: The density contrast along the downstream direction Eq. (3.48) (**left**) and averaged on the solid angle Eq. (3.49) (**right**) as a function of $r/\bar{r}$ with non negligible velocity dispersion. In both plots we choose $v_{\rm dm}/\sigma = 1$; each color represents different values of $m\sigma\bar{r}$; the circles represent the point where $m\tilde{v}(r)r = 1$; the black dashed line is the exact result of particle dark matter, obtained with Eq. (3.4).

when $m\tilde{v}(r)r = 1$, i.e., at the position of the dot(s) shown in the figure. However, since we are now analyzing a dispersed dark matter medium, we must adjust the definition of the total speed to incorporate the contribution from the velocity dispersion.

$$\tilde{v}(r) \equiv \sqrt{v_{\rm dm}^2 + \sigma^2 + v_e^2(r)}\,. \tag{3.50}$$

Given the above definition, the transition happens at $m\tilde{v}(r)r \simeq 1$, which can be solved to find the value of $r/\bar{r}$ for each choice of $m\sigma\bar{r}$ and $v_{\rm dm}/\sigma$. In the figure, the black dashed line represents the (exact) result of particle dark matter, while colored lines represent the result of wave dark matter with $m\sigma\bar{r} = 0.5$ (blue), 1 (orange), 2 (green).

Notice that, for $m\tilde{v}r \lesssim 1$, the wave contrast saturates to

$$1 + \delta(0) = \int d^3v\, f(\mathbf{v})|\psi_{\mathbf{v}}(0)|^2 = \langle|\psi_{\mathbf{v}}(0)|^2\rangle \approx \frac{2\pi\,\langle\beta\rangle}{1 - e^{-2\pi\langle\beta\rangle}} \tag{3.51}$$

with

$$\langle\beta\rangle = \frac{\alpha_G}{v_{\rm dm}}\,\mathrm{erf}\left[\frac{v_{\rm dm}}{2\sigma}\right]\,. \tag{3.52}$$

For $m\tilde{v}r \gtrsim 1$, the wave result converges to the particle dark matter result.

3.3.3 Semi-classical limit

In Sections 3.3.1 and 3.3.2 we have demonstrated that the wave outcome approaches the classical particle dark matter result if the condition

$$m\tilde{v}(r)r \gg 1 \tag{3.53}$$

is satisfied, and an appropriate value for the total velocity $\tilde{v}$ is chosen. This limit arises when the size of the system is significantly larger than the de Broglie wavelength of the wave dark matter, necessitating a match between the wave and particle descriptions. In this Section, we briefly explain why both results converge in this limit, reintroducing the reduced Planck constant $\hbar$ for clarity.

WKB limit of the Schrödinger equation

Let us discuss the semi-classical limit in the Schrödinger equation. We write the Schrödinger equation once more

$$i\hbar\partial_t\psi_{\mathbf{k}} = \left(\frac{-\hbar^2}{2m}\nabla^2 + V\right)\psi_{\mathbf{k}} \,. \tag{3.54}$$

Here V is a generic (external) potential, for example $V = m\Phi$, if Φ is the gravitational potential. The wavefunction $\psi_{\mathbf{k}}$ is characterized by the continuous quantum number $\mathbf{k} = m\mathbf{v}$, the wavenumber of the plane wave far away from the source of mass M. If we substitute $\psi_{\mathbf{k}}(t,\mathbf{x}) \to e^{-iE_{\mathbf{k}}t}\psi_{\mathbf{k}}(\mathbf{x})$, with $E_{\mathbf{k}} = \mathbf{k}^2/2m$ the energy eigenvalue, the Schrödinger equation becomes

$$\left[\nabla^2 + \frac{2m(E_{\mathbf{k}} - V)}{\hbar^2}\right]\psi_{\mathbf{k}} = 0 \,. \tag{3.55}$$

We can perform a Legendre expansion of the wave function

$$\psi_{\mathbf{k}}(\mathbf{x}) = \frac{1}{r}\sum_{\ell=0}^{\infty}\chi_{k\ell}(r)P_\ell(\cos\theta) \,, \tag{3.56}$$

where $\cos\theta = \hat{x}\cdot\hat{k}$. Substituting the expansion, we obtain the Schrödinger equation for the radial wave function $\chi_{k\ell}$,

$$\chi''_{k\ell} + \frac{2m(E - V_\ell)}{\hbar^2}\chi_{k\ell} = 0 \tag{3.57}$$

where the prime denotes the derivative with respect to r and the potential V_ℓ is defined as

$$V_\ell(r) \equiv V(r) + \frac{\hbar^2}{2m}\frac{\ell(\ell+1)}{r^2} \,. \tag{3.58}$$

Following [325], we seek for a solution of the form

$$\chi_{k\ell}(r) = e^{i\sigma/\hbar} = \exp\left[\frac{i}{\hbar}\sum_n \hbar^n \sigma_\ell^{(n)}\right] \,. \tag{3.59}$$

The Schrödinger equation becomes

$$\sigma'^2 - i\hbar\sigma'' = 2m(E - V_\ell) \,. \tag{3.60}$$

By solving the equation order by order in $\hbar$, we find the first solutions to be

$$\sigma_\ell^{(0)}(r) = \int^r dr' \sqrt{2m(E - V_\ell)} \equiv \int^r dr'\, p_\ell(r') \,, \tag{3.61}$$

$$\sigma_\ell^{(1)}(r) = \frac{i}{2} \log p_\ell(r) \,. \tag{3.62}$$

Notice we have defined $p_\ell(r) = \sqrt{2m[E - V_\ell(r)]}$, which is the radial momentum in a central $1/r$-potential in classical mechanics.

This semi-classical solution throught the WKB approximation of the Schrödinger equation is valid as long as

$$\left| \frac{k p_\ell'}{p_\ell^2} \right| \ll 1 \Longleftrightarrow \frac{d}{dr} \frac{\hbar}{p_\ell} \ll 1 \,. \tag{3.63}$$

Naively speaking, this condition is approximately $\hbar/(p_\ell r) \sim \lambda_{\rm dB}/r \ll 1$, indicating that the semi-classical limit is valid only when the size of the system is much greater than the de Broglie wavelength. More specifically, if we define the radial force

$$F_\ell = p_\ell' = \frac{1}{2mr^3}[(mv_e r)^2 - 2\hbar^2 \ell(\ell+1)] \,, \tag{3.64}$$

then the condition in Eq. (3.63) becomes

$$\frac{\hbar m}{p_\ell^3} |F_\ell| \ll 1 \,. \tag{3.65}$$

For a given set of parameters, the dominant contribution in the series expansion of the wave function arises at $\ell \sim m\tilde{v}r$, where $\tilde{v}$ is the total velocity $\tilde{v}(r) = \sqrt{v^2 + v_e^2(r)}$. Since $m\tilde{v}r > mv_e r$, we see that

$$\frac{\hbar m}{p_\ell^3} |F_\ell| \approx \frac{\hbar}{p_\ell^3 r^3} (m\tilde{v}r)^2 \approx \frac{\hbar}{m\tilde{v}r} \ll 1 \tag{3.66}$$

Therefore the semi-classical, or WKB, approximation is valid as long as

$$m\tilde{v}r \gg \hbar \,. \tag{3.67}$$

From Schrödinger to Boltzmann

The concept of particle dark matter focusing centers on the phase space distribution modified by the source's gravitational potential. In Section 3.1, we have observed that Liouville's theorem guarantees that the total phase space volume remains constant, while the particles undergo acceleration, which leads to a distinct density in velocity space. Therefore, to investigate the limit in which the results for particle and wave dark matter converge, we require a quantity similar to the classical phase space distribution and that converges to it under appropriate conditions.

The quantum mechanical analog of the phase space distribution is given by the quasi-probability distribution introduced by Wigner [334]

$$f_{\rm W}(t, \mathbf{x}, \mathbf{p}) = \int d^3y\, e^{i\mathbf{p}\cdot\mathbf{y}/\hbar} \int d^3v\, f(\mathbf{v}) \psi_{\mathbf{v}}^\star(t, \mathbf{x} + \mathbf{y}/2) \psi_{\mathbf{v}}(t, \mathbf{x} - \mathbf{y}/2) \,. \tag{3.68}$$

Remarkably, this function, when integrated over momenta, reproduces the variance of the field

$$\int \frac{d^3p}{(2\pi)^3} f_W(t,\mathbf{x},\mathbf{p}) = \int d^3v\, f(\mathbf{v}) |\psi_{\mathbf{v}}(\mathbf{x})|^2 = \langle \phi^2 \rangle \ . \tag{3.69}$$

Therefore the Wigner function can be used to compute expectation values of operators.

Let us study the time evolution of the Wigner function. We take the time derivative of Eq. (3.68)

$$\begin{aligned} \partial_t f_W &= \int d^3y\, e^{i\mathbf{p}\cdot\mathbf{y}/\hbar} \int d^3v\, f(\mathbf{v}) \\ &\quad \left[\partial_t \psi^\star_{\mathbf{v}}(t,\mathbf{x}+\mathbf{y}/2)\psi_{\mathbf{v}}(t,\mathbf{x}-\mathbf{y}/2) + \psi^\star_{\mathbf{v}}(t,\mathbf{x}+\mathbf{y}/2)\partial_t\psi_{\mathbf{v}}(t,\mathbf{x}-\mathbf{y}/2) \right] . \end{aligned} \tag{3.70}$$

We can exploit the Schrödinger equation Eq. (3.54) to express the time derivatives of the wave function.

$$\begin{aligned} \partial_t f_W &= \int d^3y\, e^{i\mathbf{p}\cdot\mathbf{y}/\hbar} \int d^3v\, f(\mathbf{v}) \\ &\quad \Big\{ -\frac{\hbar}{2im} \left[\psi_{\mathbf{v}}(\mathbf{x}-\mathbf{y}/2)\nabla^2_{\mathbf{x}}\psi^\star_{\mathbf{v}}(\mathbf{x}+\mathbf{y}/2) - \psi^\star_{\mathbf{v}}(\mathbf{x}+\mathbf{y}/2)\nabla^2_{\mathbf{x}}\psi_{\mathbf{v}}(\mathbf{x}-\mathbf{y}/2) \right] \\ &\quad -\frac{i}{\hbar} \left[V(\mathbf{x}+\mathbf{y}/2) - V(\mathbf{x}-\mathbf{y}/2) \right] \psi^\star_{\mathbf{v}}(\mathbf{x}+\mathbf{y}/2)\psi_{\mathbf{v}}(\mathbf{x}-\mathbf{y}/2) \Big\} \\ &= \partial_t f_W^{(T)} + \partial_t f_W^{(V)} \ . \end{aligned} \tag{3.71}$$

We split the result in two terms, a "kinetic" term $f_W^{(T)}$ and a "potential" term $f_W^{(V)}$. We exploit $\nabla_{\mathbf{x}}\, \psi(\mathbf{x}\pm\mathbf{y}/2) \ = \ \pm\, 2\nabla_{\mathbf{y}}\psi(\mathbf{x}\pm\mathbf{y}/2)$ and integrate by parts, to obtain

$$\partial_t f_W^{(T)} = -\frac{\mathbf{p}}{m}\cdot\nabla_{\mathbf{x}} f_W(t,\mathbf{x},\mathbf{p}) \ . \tag{3.72}$$

For the second term, we assume that V can be expanded in a power series in $\mathbf{x}$ and write

$$V(\mathbf{x}+\mathbf{y}/2) - V(\mathbf{x}-\mathbf{y}/2) = \sum_{s=0} \frac{1}{2^{2s}(2s+1)!} \frac{\partial^{2s+1}}{\partial \mathbf{x}^{2s+1}} V(\mathbf{x}) y^{2s+1} \ . \tag{3.73}$$

We are then able to rewrite this factor exploiting the term $e^{i\mathbf{p}\cdot\mathbf{y}/\hbar}$ in the integral, to exchange $\mathbf{y} \to i\hbar\nabla_{\mathbf{p}}$ and resum the series. We finally obtain

$$\partial_t f_W + \mathbf{v}\cdot\nabla_{\mathbf{x}} f_W + \frac{i}{\hbar}\left[V\left(\mathbf{x}+\frac{i\hbar}{2}\nabla_p\right) - V\left(\mathbf{x}-\frac{i\hbar}{2}\nabla_p\right)\right] f_W = 0 \ . \tag{3.74}$$

If all derivatives of V higher than the second order are zero, as for a free particle, a constant force, and a harmonic oscillator, last term becomes $-[\nabla_{\mathbf{x}} V]\nabla_{\mathbf{p}} f_W$.

More generally, we see that the leading term in the semi-classical limit in Eq. (3.74) is identical to the Boltzmann (or Liouville) equation

$$\partial_t f_W + \mathbf{v}\cdot\nabla_{\mathbf{x}} f_W - (\nabla_{\mathbf{x}} V)\nabla_{\mathbf{p}} f_W = 0 \ . \tag{3.75}$$

This equation can also be solved in linear perturbation theory, giving, as a result for the density contrast, (assuming $v_e < \sigma$) the one in Eq. (3.10).

From this discussion, we can conclude that the wave and particle dark matter results should converge in the limit $\hbar \to 0$. This semi-classical limit is identical to the one obtained from the semi-classical limit of the Schrödinger equation: $m\tilde{v}r \gg \hbar$, see indeed Eq. (3.67).

3.4 Dark Matter in the solar system

Equipped with the formalism developed in Section 3.2 to describe gravitational focusing of wave dark matter, we apply our previous discussion to dark matter structures in the solar system. We work in the Galactic coordinate system where the origin of coordinates is at the location of the Sun. Each component of (X, Y, Z) in the rectangular Cartesian coordinate system points towards the Galactic center, the direction of Galactic rotation, and the Galactic north pole, respectively. We provide a detailed description of the Earth and a dark matter detector's position in Galactic coordinates in Appendix B. We will now clarify the relationship between the observables in the detector rest frame and those in the Galactic frame.

Observables in detector rest frame and galactic coordinate frame

The Galactic coordinate system is utilized as the natural rest frame of the dark matter halo, and gravitational focusing effects can be isolated in these coordinates. It is worth noting how observables, such as the density contrast and spectrum, change in the detector's rest frame of terrestrial experiments with respect to the Galactic frame.

Regarding the density contrast, it remains constant. Denoting x for the Galactic coordinate and x' for the detector's proper coordinate, the density contrast is defined from the two-point function of the scalar field $\langle \hat{\phi}^2(x) \rangle$. As this quantity is a scalar under general coordinate transformations, it remains the same in both frames:

$$\langle \hat{\phi}^2(x) \rangle = \langle \hat{\phi}'^2(x') \rangle \ . \tag{3.76}$$

Note that, as previously found in Section 3.2.2, the density contrast is related to the total power of the signal. Therefore, the density contrast is directly related to the total power of the signal measured in detectors on Earth.

However, the spectrum requires a more careful discussion. The frequency ω is associated with the coordinate time t of the Galactic frame. The Fourier transform of the field in the Galactic frame and in the detector frame are defined, respectively:

$$\hat{\phi}(\omega, \mathbf{x}) = \int dt \, e^{i\omega t} \hat{\phi}(x) \ , \qquad \hat{\phi}'(\omega', \mathbf{x}') = \int dt' \, e^{i\omega' t'} \hat{\phi}(x') \ . \tag{3.77}$$

If the detector is an inertial observer moving at a constant velocity with respect to the Galactic frame, the proper coordinate can be related to the Galactic coordinate as $x' = \Lambda x$, with the appropriate Lorentz transformation Λ. In this case, it can be shown that the same expression for the spectrum, Eq (3.43), can be used in the detector frame by replacing the velocity in the distribution with the velocity $v = |\mathbf{k}|/m$ observed in the detector frame, $k \to \Lambda^{-1} k$. Therefore, the spectrum in the detector's

rest frame can be calculated from the spectrum in the Galactic frame by applying the appropriate Lorentz transformation.

The discussion above, however, becomes complicated by the orbital motion of the Earth, as a detector on Earth is not a constant-velocity, inertial observer. Therefore, replacing $k \to \Lambda^{-1}k$ to obtain the spectrum in the detector frame is only valid if the data time series is shorter than the Earth's orbital time scale. Attempting to Fourier-transform the signal over a longer time scale introduces side-bands in the frequency space. This is due to the frequency modulation induced by the Earth's orbital motion and wave function oscillations. Additionally, for experiments sensitive to the gradient, the Earth's rotation further modulates the signal's amplitude, creating side-bands in the spectrum. As a result, frequency space analysis becomes even more complicated [215].

Using the Galactic coordinate system, we calculate the density contrast and the dark matter spectrum at Earth's location during various times of the year. We examine various dark matter substructures with distinct kinematic properties, and for the velocity distribution, we utilize the Maxwell-Boltzmann distribution (Eq. (3.7)) for the majority of them. This distribution is characterized by the mean velocity $\langle \mathbf{v} \rangle = \mathbf{v}_{\rm dm}$ and the one-dimensional velocity dispersion σ.

3.4.1 Halo dark matter

We begin with the relaxed halo dark matter component. In the Galactic coordinate, the halo dark matter can be represented by the standard halo model with a mean velocity in the Galactic coordinate [51, 335]

$$\mathbf{v}_{\rm dm} = -\mathbf{v}_\odot = -(11, 241, 7)\ \text{km/sec} \tag{3.78}$$

and velocity dispersion

$$\sigma = \frac{v_c(R_\odot)}{\sqrt{2}} = 162\ \text{km/sec}\,, \tag{3.79}$$

where $v_c(R_\odot) = 229$ km/sec is the circular velocity of Milky Way at the position of the Sun [51].

In Figure 3.9, we show the density contrast of wave dark matter (colored lines) at the position of the Earth throughout the year of 2021 for different values of the $m\tilde{v}r$ parameter, that is $2\pi r/\tilde{\lambda}_{\rm dB}$; since the velocity distribution and the orbit of the Earth around the Sun is fixed, this amounts to change $\tilde{\lambda}_{\rm dB}$, or just the wave dark matter mass m. We express this mass, for shortness of notation, as multiples of $m_{15} = 10^{-15}$ eV. Since $v_e(r_\oplus) \simeq 42$ km/sec is much smaller than both σ and $v_{\rm dm}$, we expect that the overall amplitude of density contrast is $\delta \sim v_e^2/2\sigma^2 \sim 0.03$, at least for the particle dark matter, which is confirmed by the black dashed line in the figure. The maximum of the density contrast takes place around March 1st since this is when $\mu = \hat{x}_\oplus \cdot \hat{v}_{\rm dm}$ takes the largest value over a year. This pattern can be seen also from the wave dark matter density contrast with varying degree of annual modulation strength. We observe that the density contrast flattens for small masses $m\tilde{v}r \lesssim 1$, as $\tilde{\lambda}_{\rm dB}$ becomes larger than the AU. Instead, for $m\tilde{v}r \gg 1$, the result can be approximated as that of

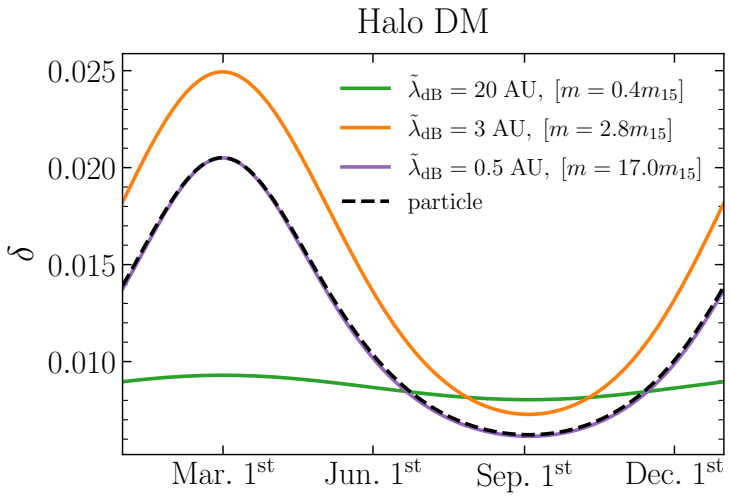

FIGURE 3.9: Density contrast for halo dark matter at the position of the Earth during year 2021. The black dashed line is for the particle dark matter, while each colored line represents the wave dark matter result for $\tilde{\lambda}_{\rm dB} =$ 20, 3, 0.5 AU, respectively. Corresponding wave DM mass with respect to $m_{15} = 10^{-15}$ eV is also shown. The density contrast flattens for $m\tilde{v}r \lesssim 1$, while it approaches the particle dark matter result for $m\tilde{v}r \gtrsim 1$. Around $m\tilde{v}r \sim 1$, the wave density contrast becomes $\sim$ 25 % larger than that of particle dark matter.

particle dark matter. We also observe that the wave density contrast is enhanced by $\sim$ 25 % compared to the particle at $m\tilde{v}r \sim 1$.

In Figure 3.10, we show the modification of the speed distribution for the wave dark matter. More specifically, we plot

$$\Delta\bar{f}(v, \mathbf{x}) = v^2 \int d\Omega_{\hat{v}}\, f(\mathbf{v})(|\psi_{\mathbf{v}}(\mathbf{x})|^2 - 1)\,, \tag{3.80}$$

that is the difference between the speed distribution with and without the gravitational focusing. For the figures, we choose to show March 1st and September 1st. As it is clear from the plots, the effect of gravitational focusing is prominent in the low velocity tail, as the naive estimate in Section 3.1 suggests: the peak of the speed distribution without focusing is located at much larger velocities >300 km/sec ; we plot it, reduced by a factor of 100 for the visual comparison, as a dotted black line. Each colored line represents wave dark matter for different values of $m\tilde{v}r$, or the wave dark matter mass, with the same choices made in Figure 3.9. The black dashed line is the modification of the speed distribution in case of particle dark matter. The difference between particle and wave dark matter is still visible even for $\tilde{\lambda}_{\rm dB} = 0.5$ AU, while the density contrast modulations are almost impossible to distinguish: in particular, on September 1st we see several oscillations in the spectrum.

In Figure 3.11, we show the daily modulation of the field gradient from the halo dark matter component calculated with Eq. (3.44). As a benchmark we consider a detector located in Hamburg, Germany (54°N, 10°E) with sensitivity axis pointing towards the east direction on March 1st, 2021. We use the same benchmark choices

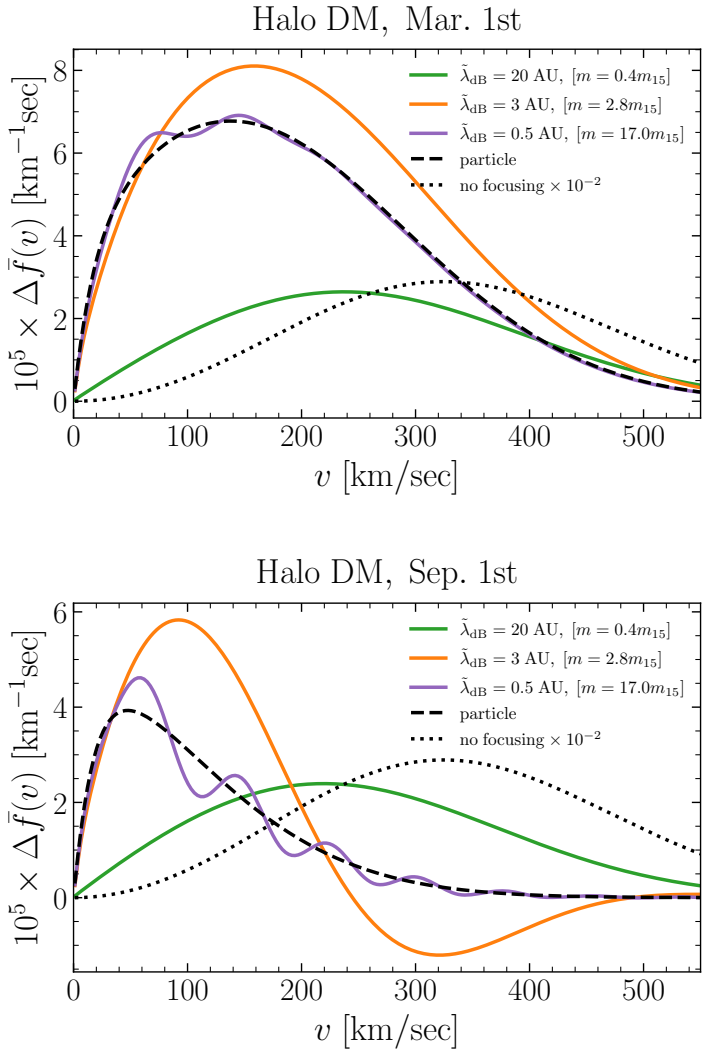

FIGURE 3.10: **Top**: the difference of speed distribution with and without the gravitational focusing on March 1st, 2021. **Bottom**: same as left panel but on September 1st, 2021. Each colored line represents $\tilde{\lambda}_{\rm dB} = 0.5,\ 3,\ 20$ AU as in Figure 3.9. The black dashed line is the same result for the particle dark matter, and the black dotted line is the rescaled speed distribution without gravitational focusing.

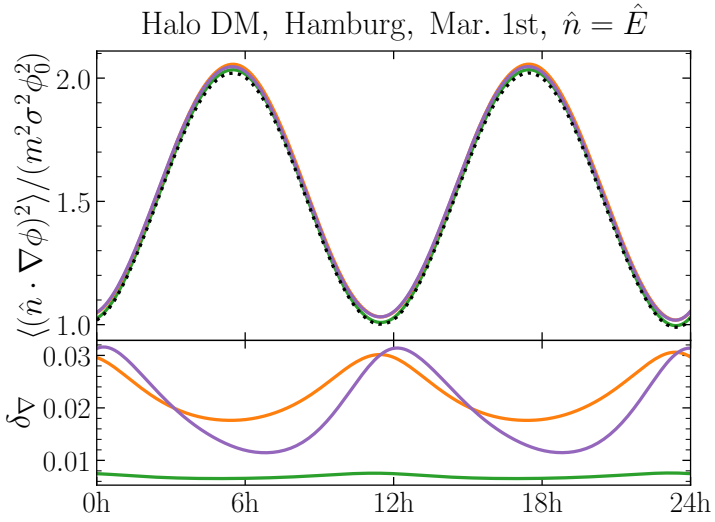

FIGURE 3.11: Daily modulation of the variance of the field gradient projected on the sensitivity axis of a detector located in Hamburg, Germany and pointing in the east direction for halo dark matter on March 1st, 2021. Colored lines are the results with gravitational focusing for different values of $\tilde{\lambda}_{\rm dB}$ as in Figure 3.9. The black dotted line represents the asymptotic result far away from the solar system. The contrast of the focused result with respect to the unfocused one (asymptotic) is shown in the bottom panel.

for $m\tilde{v}r$ as in Figure 3.9. The dotted black line shows the result with no focusing, asymptotically far away from the solar system. In the bottom panels we show the contrast δ_∇ between the focused lines and the asymptotic value far away from the solar system. Explicitly

$$\delta_\nabla = \frac{\langle|\hat{n}\cdot\nabla\phi|^2\rangle}{m^2\phi_0^2[(\hat{n}\cdot\mathbf{v}_{\rm dm})^2+\sigma^2]} - 1\,. \tag{3.81}$$

The magnitude of the contrast is comparable to the density contrast, signaling the effect is of order $\mathcal{O}(v_e^2/\sigma^2)$.

3.4.2 Gaia sausage

We consider a dark matter substructure with anisotropic velocity distribution. Such a dark matter substructure is motivated by the observation of a stellar population with an anisotropic velocity distribution, referred to as Gaia-Sausage or Gaia-Enceladus [56, 57]. It is inferred that this stellar component originates from a relatively recent merger with a luminous satellite galaxy of mass $M > 10^{10} M_\odot$. It is naturally expected that not only stars but also dark matter is accreted onto the Milky Way from the same event, contributing to the local density. Some studies [58, 59] have shown that the kinematic properties of accreted stars and dark matter are similar and it could constitute $\mathcal{O}(10\%)$ of local dark matter.

Our analysis involves examining how the sausage-component dark matter reacts to the solar gravitational potential. Due to the anisotropic nature of the velocity

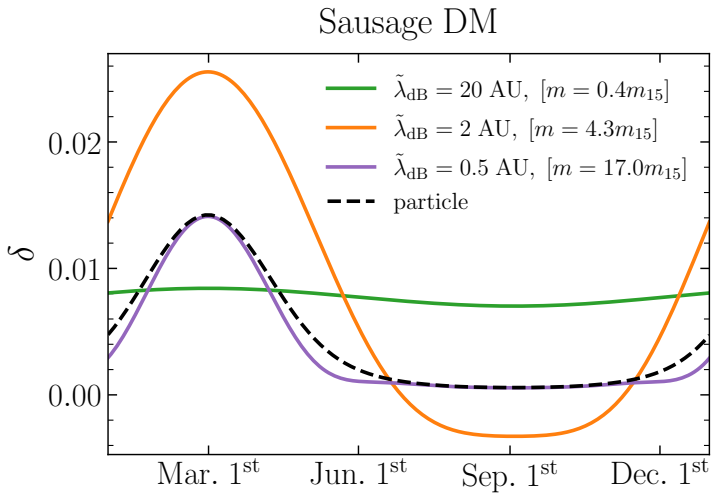

FIGURE 3.12: Same as Figure 3.9 but for sausage dark matter component. Around $\tilde{\lambda}_{\rm dB} = 2$ AU, corresponding to $m\tilde{v}r = 3$, the wave dark matter contrast can be almost a factor two larger than the particle density contrast. We also observe a slight underdensity around fall.

distribution of dark matter, we employ a three-dimensional Gaussian

$$f(\mathbf{v}) = \frac{1}{(2\pi)^{3/2}\sqrt{\det\Sigma}} \exp\left[-\frac{1}{2}(\mathbf{v}-\mathbf{v}_{\rm dm})\cdot\Sigma^{-1}(\mathbf{v}-\mathbf{v}_{\rm dm})\right], \tag{3.82}$$

where Σ is the covariance matrix. We parameterize the sausage component with $v_{\rm dm} = -\mathbf{v}_\odot$ and [56, 143, 336]

$$\sigma_r = 256\ \text{km/sec}, \qquad \sigma_\theta = \sigma_\phi = 81\ \text{km/sec}\,. \tag{3.83}$$

with $\Sigma = \text{diag}(\sigma_r^2, \sigma_\theta^2, \sigma_\phi^2)$. The covariance matrix reflects the high velocity anisotropy of this substructure.

The density contrast for the sausage dark matter component is depicted in Figure 3.12. We observe a comparable pattern to the halo dark matter example. Despite the highly anisotropic velocity distribution, the overall amplitude remains alike to the halo dark matter component. Additionally, a small underdensity is noticeable during the fall.

3.4.3 Dark disk

We now consider a disk-shaped dark matter substructure. This type of substructure is motivated by the existence of a thick stellar disk in our own galaxy. Several scenarios have been proposed to explain the vertical structure of the stellar disk, such as the accretion of stars from satellite galaxies [337] or the heating of stars in a pre-existing thin disk through merger events [338, 339]. It has been suggested that such merger events could naturally lead to the formation of a thick dark disk as the accreted dark matter is dragged to the disk plane through dynamical friction [64]. The resulting dark matter disk co-rotates with the Galactic disk but has a slightly smaller circular

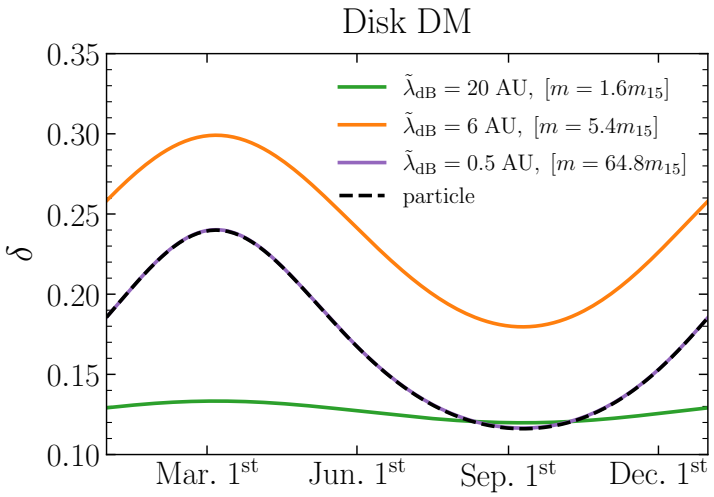

FIGURE 3.13: Same as Figures 3.9 and 3.12, but for the disk dark matter component. The density contrast's amplitude is greater than previous dark matter structures due to the small mean velocity and dispersion. We choose a different benchmark point $\tilde{\lambda}_{\rm dB} = 6$ AU with respect to the above figures, since this is the choice that maximizes the density contrast on Earth.

velocity of $\Delta v = 50$ km/sec. While it is still unclear whether the aforementioned merger scenario can fully explain the evolution of the stellar disk (see the review in [340] and references therein), it is still worthwhile to investigate the response of such a dark matter component to the gravitational potential of the Sun.

To study the dark disk, we parameterize its mean velocity and velocity dispersion as follows:

$$\mathbf{v}_{\rm dm} = (0, -50, 0)\ \text{km/sec} \qquad \text{and} \qquad \sigma = 50\ \text{km/sec}\,. \tag{3.84}$$

Although we refer to this component as the "dark disk," this structure has the potential to serve as a substructure for any cold dark matter with a low mean velocity. In Figure 3.13, the density contrast for the dark disk is displayed. The pattern of the density contrast is comparable to earlier instances, see Figures 3.9 and 3.12 but with a greater amplitude because of the reduced velocity and dispersion. In this specific scenario, the dark matter disk can be focused, resulting in a density approximately 30 % greater near Earth's orbital path than asymptotically further away from the Sun.

In Figure 3.14 we show the daily modulation of the variance of the dark disk in Hamburg on March 1st, 2021 and its contrast with the asymptotic result far away from the Solar system. Compared to Figure 3.11, we have an order-of-magnitude-larger contrast, that again agrees with the estimate $\delta \sim \delta_\nabla \sim v_\oplus^2/\sigma^2$ since σ^2 is an order-of-magnitude smaller than in the halo case. An interesting effect due to gravitational focusing that is particularly evident in the disk case, because of the smaller velocities, is the modification of the position of the peaks in the daily modulation. The change in the direction of the total dark matter velocity vector due to the gravitational potential of the Sun results in a velocity component acquired by the dark

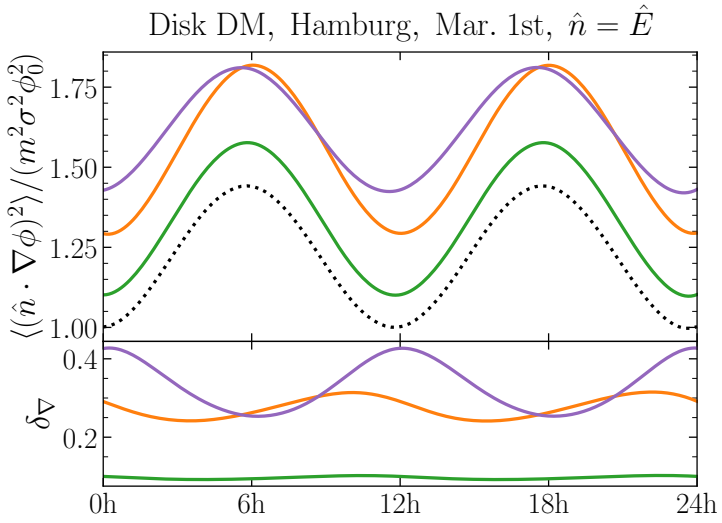

FIGURE 3.14: Same as Figure 3.11 but for the disk dark matter component. The different colored lines correspond to the values of $\tilde{\lambda}_{\rm dB}$ chosen for Figure 3.13. Since the focusing effect is stronger, the feature of peak-shifting is visible in this case. See the main text for more details.

matter, which affects the time when the peak value is reached.

3.4.4 Streams

As a last example, we examine dark matter streams, which share a kinematic structure similar to that of stellar streams. Stellar streams are coherent substructures of stars, both spatially and kinematically. If these stellar streams originated from dwarf galaxies, the presence of associated dark matter streams with similar kinematic properties is highly probable [58]. In the Milky Way's rest frame, these streams typically exhibit large streaming velocities with small velocity dispersions. Over the past few decades, numerous streams and substructures have been observed in the inner halo, providing valuable insights into the nature of dark matter. A comprehensive review of stellar streams and substructures in the Milky Way can be found in [63].

To study the gravitational response of fast-moving cold objects like streams, we consider the following mean speed and dispersion

$$v_{\rm dm} = 400\ {\rm km/sec}, \qquad \sigma = 30\ {\rm km/sec}\ . \tag{3.85}$$

Note that here the direction of the stream velocity can be diverse, so this value of the mean speed is purely an assumption: the average speed of the stream dark matter in the rest frame of the Sun might be much smaller than this, e.g. when the stream is *prograde*, i.e. dark matter moves roughly in the same direction as the Sun. However, in such cases, the kinematic properties of the stream would be very similar to the ones of the dark disk component we studied in the previous section and so would be the gravitational focusing of such substructure. Therefore, focusing on *retrograde*-like streams, i.e. when the dark matter velocity is in roughly the opposite direction to the Sun's velocity, we consider two different inclination angles of the stream velocity $\mathbf{v}_{\rm dm}$ with respect to the ecliptic plane, $\theta_{\rm dm} = 0,\ \pi/6$.

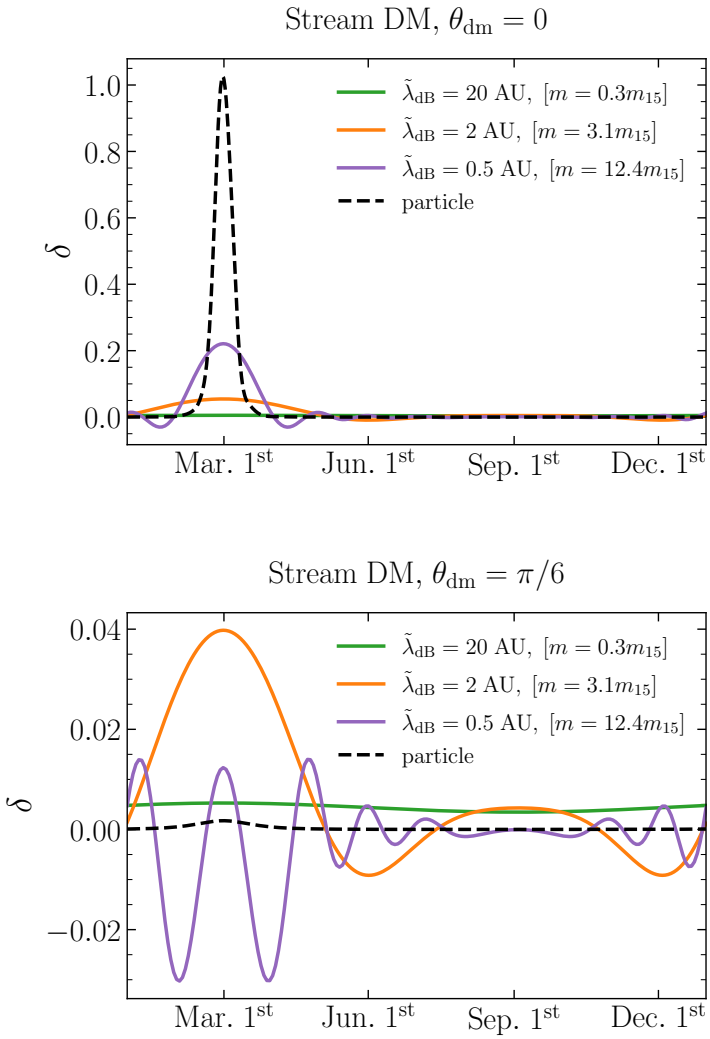

FIGURE 3.15: **Top**: the density contrast of the stream wave dark matter for a vanishing inclination angle $\theta_{\rm dm} = 0$. The density contrast is highly concentrated near March 1st, owing to the disparity between the mean velocity and the dispersion. Even with a wave dark matter contrast of approximately 0.5 AU (which corresponds to an $m\tilde{v}r$ of around 10), the resulting contrast is still quite different from the particle dark matter result. For further details, see the main text. **Bottom**: the density contrast of the stream wave dark matter for an inclination angle of $\theta_{\rm dm} = \pi/6$. Despite the stream having a non-vanishing velocity dispersion, the oscillations of the wave function are not entirely erased. As a result, this example yields a much faster oscillation of density contrast, as particularly evident for small values of $\tilde{\lambda}_{\rm dB}$.

Figure 3.15 illustrates the density contrast of dark matter streams for two different inclination angles. For the case of an inclination angle of $\theta_{\rm dm} = 0$, we observe noteworthy differences between particle dark matter and wave dark matter. Even for an $m\tilde{v}r$ of 10, the wave contrast is much wider than the particle contrast in the time-axis. While we have argued that the wave dark matter contrast approaches the particle contrast for $m\tilde{v}r$ greater than or equal to unity, this is based on quantities such as $\delta_{\rm avg}$ that are averaged over the solid angle. Furthermore, we have observed in Section 3.1 that for both particle and wave dark matter, there exists an angular scale $\Delta\mu \sim \delta_{\rm avg}/\delta_{\rm ds}$ over which the density contrast takes a non-vanishing value. For particle dark matter, this scale is typically $\Delta\mu \sim \sigma^2/v_{\rm dm}^2$ if $v_e \ll \sigma, v_{\rm dm}$ due to the non-zero velocity dispersion, whereas for wave dark matter, it is

$$\Delta\mu \sim \max\left[\frac{1}{m\tilde{v}r}, \frac{\sigma^2}{v_{\rm dm}^2}\right], \tag{3.86}$$

owing to the de Broglie wavelength suppressing structures on scales smaller than $\tilde{\lambda}_{\rm dm}$. In the stream component under consideration, there exists a large disparity between $v_{\rm dm}$ and σ, which means that the particle density contrast is non-vanishing for only a relatively short period of time in a year, i.e., $\Delta t \sim \sigma^2/v_{\rm dm}^2 \sim 2$ days. For wave dark matter, with an $m\tilde{v}r$ of 10, the angular spread $\Delta\mu$ is still controlled by $(m\tilde{v}r)^{-1}$ rather than $\sigma^2/v_{\rm dm}^2$. Therefore, the wave contrast in Figure 3.15 is much less temporally (or spatially) localized than the particle contrast: it is localized on a month timescale instead of a day timescale.

The same phenomenon can also be observed in the case of $\theta_{\rm dm} = \pi/6$. Here, the density contrast for particle dark matter approaches zero, because it is very localized on the ecliptic plane, while for wave dark matter, being more spatially spread, it remains non-zero at a few percent level. Another interesting aspect is that the density contrast pattern over a year shows faster oscillations compared to other substructures. This can be attributed to the small velocity dispersion, where it behaves more like a monochromatic wave, allowing the characteristic oscillation patterns to survive even after mixing with waves of different wavenumbers.

3.5 Summary and conclusions

In this Chapter, we have explored the gravitational response of wave dark matter to a central Newtonian potential and compared it to that of particle dark matter. We began with a brief review of the gravitational response of particle dark matter in Section 3.1, and then, in Section 3.2, we developed a simple formalism for investigating wave dark matter in the presence of a gravitational potential due to an astrophysical object of mass M.

Specifically, we considered a spinless bosonic field that is minimally coupled to gravity, and expanded the dark matter field in terms of creation and annihilation operators with a mode function, as is typical in the canonical formulation of quantum field theories. By solving the Schrödinger equation, in Section 3.2.1 we determined the response of each wave mode. Equipped with the formalism developed in Section 2.3, this approach allowed us to examine both the gravitational response and

the stochastic nature of wave dark matter. The main result of Section 3.2 is Eq. (3.35) that provides the overdensity contrast around the massive object due to the focusing of wave dark matter. The wave nature appears as a factor $|\psi_{\mathbf{k}}|^2$ obtained from the eigenfunction solution Eq. (3.24) of the Schrödinger equation, weighted by the velocity distribution of wave dark matter asymptotically away from the massive body.

Comparing particle and wave dark matter, in Section 3.3.2 we found interesting similarities and differences between the two. The monochromatic result, explored in Section 3.3.1 indicates that the wave nature of dark matter becomes apparent only when $m\tilde{v}r \lesssim 1$, whereas for $m\tilde{v}r \gg 1$, it closely approximates the result of particle dark matter. A characteristic feature of wave dark matter is the presence of an additional scale, the de Broglie wavelength, which is given by $\tilde{\lambda}_{\rm dB} = m\tilde{v}r$. The spatial structure of the wave density contrast is smoothed over the scale of its de Broglie wavelength, which is a commonly observed feature in the study of wave dark matter.

In Section 3.4, we have utilized the formalism to study wave dark matter in substructures and halo dark matter in the solar system. To investigate the gravitational response of wave dark matter, we have considered different substructures based on recent astrometric data and theoretical models explaining the stellar substructures in the Milky Way. By varying the mean velocity and velocity dispersion, we have observed the clear manifestation of wave characteristics in all of the examples provided. For $m\tilde{v}r \gg 1$, the wave response is nearly identical to that of particle dark matter, whereas for $m\tilde{v}r \ll 1$, the wave result becomes independent on the Earth's location. Remarkably, for $m\tilde{v}r \sim 1$, we have found that the wave density contrast can be at most twice that of particle dark matter. Moreover, when dealing with streams with low velocity dispersion, the angular distribution of the density contrast may still differ from that of particle density contrast.

Although the gravitational focusing effects are sub-leading in many of the cases we have examined, they could provide significant insights into local dark matter structures upon the detection of dark matter.

Chapter 4

Adiabatic Compression

In this Chapter, we consider another deformation of the phase space of dark matter via gravitational interaction. The adiabatic growth of a massive black hole at the center of a halo could compress the surrounding dark matter halo, leading to a steeper dark matter inner density profile. This phenomenon is called adiabatic compression. Since the dark matter density is greatly enhanced, indirect detection signals for dark matter coupled to standard model states are compelling, as studied for particle dark matter in [99]. The adiabatic compression of wave dark matter leads to a much denser halo similar to particle dark matter in the semi-classical limit. However, the compressed wave halo differs from that of the particle halo near the center, and the central profile depends on dark matter and the central black hole mass. We also examine whether the soliton and the low angular momentum modes can survive over the astrophysical time scale without being absorbed by the black hole.

This Chapter is divided into two parts. In the first part, Section 4.1, we review how the particle halo responds to the adiabatic change of the system. We begin with a general understanding of the compression phenomenon in Section 4.1.1, then we examine the phase space distribution of a power law density profile (4.1.2) and investigate how this distribution evolves as a result of the adiabatic change of the system. We also check the cosmologically viability of the initial halo in Section 4.1.3, which is assumed to host a growing black hole at high redshift. Finally, in Section 4.1.4, we compute the density profile after the adiabatic change of the system taking also into account the black hole horizon.

The second part of the Chapter, Section 4.2, investigates the compression of a wave dark matter halo. We describe the construction of such a halo and its relaxation timescale which leads to a NFW-like profile at large radii and a solitonic core in the center (Sections 4.2.1, 4.2.2). We then decompose the wave halo into eigenmodes in Section 4.2.3 and provide a semi-analytical understanding of the compression process in Section 4.2.4. We then study the absorption of the low angular momentum modes by the central black hole (Section 4.2.5), which leads to a peculiar broken power law density profile. Finally, in Section 4.2.6, we check the relaxation time scale for the compressed halo and obtain important constraints on the consistency of the above mentioned density profile. We conclude in Section 4.3.

The Chapter follows the first part of [107], but it is substantially expanded with more details, discussions and plots.

4.1 Formation of a particle dark matter spike

In this Section, we review the formation of a dark matter spike in the center of a dark matter halo through adiabatic compression. This occurs when the gravitational potential of a massive baryonic object at the center of the system changes slowly compared to the crossing time scale of the dark matter particles. The gravity of the central baryonic object gradually dominates the gravitational potential at smaller scales, inducing a contraction on the surrounding dark matter. For example, adiabatic compression may occur when a black hole forms and grows adiabatically at the center of the system or when a gas cloud sinks to the center of the system through dissipative effects.

Let us introduce this process exploiting conservation laws. We want to understand why the dark matter develops a steeper inner density profile. We follow the arguments in [341]. Let us assume the original inner density profile of the dark matter to be a simple power law $\rho_{\rm i} \propto r_i^{-\gamma}$. This is the case, e.g. for the NFW halo profile, introduced in Section 1.2.2. It is natural to assume that also the final dark matter density profile will be a power law profile, but with a different index, $\rho_{\rm f} \propto r_{\rm f}^{-\gamma_{\rm sp}}$. Then we assume that in the initial configuration the system is sustained by the dark matter self gravity, while in the final state a central black hole of mass $M_{\rm bh}$ has grown enough to dominate the gravitational potential. The dark matter angular momentum has to be conserved. Assuming the dark matter follows circular orbits with velocity v_c, we have

$$\begin{aligned} v_c(r_{\rm i})r_{\rm i} = v_c(r_{\rm f})r_{\rm f} \quad &\Longleftrightarrow \quad M_{\rm dm}(r_{\rm i})r_{\rm i} = M_{\rm bh}r_{\rm f} \\ &\Longleftrightarrow \quad r_{\rm i}^{4-\gamma} \propto r_{\rm f} \end{aligned} \tag{4.1}$$

we have used $v_c(r_{\rm i}) = \sqrt{GM_{\rm dm}(r_{\rm i})/r_{\rm i}}$ and $v_c(r_{\rm f}) = \sqrt{GM_{\rm bh}/r_{\rm f}}$ with $M_{\rm dm}(r_{\rm i}) \propto \rho_{\rm i} r_{\rm i}^3 \propto r_{\rm i}^{3-\gamma}$ the dark matter mass enclosed in the sphere of radius $r_{\rm i}$. Next, we impose the conservation of the dark matter mass, so

$$M_{\rm dm}(r_{\rm i}) = M_{\rm dm}(r_{\rm f}) \quad \Longleftrightarrow \quad r_{\rm i}^{3-\gamma} \propto r_f^{3-\gamma_{\rm sp}} \tag{4.2}$$

Comparing the two equations above, we see that $4-\gamma = (3-\gamma)/(3-\gamma_{\rm sp})$. This gives us

$$\gamma_{\rm sp} = \frac{9-2\gamma}{4-\gamma}\,. \tag{4.3}$$

We see, that for a common dark matter halo, say with $0 \leq \gamma \leq 2$, $\gamma_{\rm sp} \in [2.25, 2.5]$: the final inner density profile is substantially steeper. In particular, for the NFW-like profile, $\gamma = 1$, we have $\gamma_{\rm sp} = 7/3$.

4.1.1 General procedure

Let us be more quantitative and general. The dark matter system is described by the phase space distribution $f(t, \mathbf{x}, \mathbf{v})$, which denotes the number of dark matter particles in the unit phase space volume. Assuming that the dark matter is collisionless, the distribution function satisfies the collisionless Boltzmann equation, $df/dt = 0$.

The adiabatic change of the gravitational potential due to the growth of a central black hole does not modify the phase space distribution and the integral of motion, but alters the shape of the phase space volume. This implies that the number of particles in the velocity space can change, leading to a different density profile. The dark matter density profile is given by the velocity-space integral of the phase space distribution

$$\rho(\mathbf{x}) = \int d^3v \, f(\mathbf{x}, \mathbf{v}) \, . \tag{4.4}$$

For a steady-state solution, the distribution function depends on the phase space coordinate only through the integrals of motion, i.e. a function of phase space variables, $I(\mathbf{x}, \mathbf{v})$, that satisfies $dI/dt = 0$. In a spherical system, the integrals of motion are the energy and angular momentum. We denote these quantities, per unit mass, respectively with $(E, \mathbf{L})$. Assuming a spherically symmetric halo, we can rewrite the density profile integral of Eq. (4.4) as

$$\rho(r) = \int_{\Phi}^{0} dE \int_{L_{\min}}^{L_{\max}} dL \, \frac{4\pi L}{r^2 v_r} f(E, L) \, . \tag{4.5}$$

We further assumed that the phase space distribution depends only on E and $L = |\mathbf{L}|$. Here

$$v_r = \sqrt{2[E - \Phi(r)] - \frac{L^2}{r^2}} \tag{4.6}$$

is the radial velocity. We have denoted with $\Phi(r)$ the gravitational potential, with $\Phi \to 0$ for $r \to \infty$. The upper bound on the energy integral denotes that we are considering only particles gravitationally bound to the system. The maximum value for L is the one for which v_r is vanishing, while the minimum value is either zero (radial orbit) or some lower-cutoff, imposed by the boundary conditions of the system, e.g. because of the presence of the black hole.

If the phase space distribution is *ergodic*, i.e. depends only on energy, the Eq. (4.5) simplifies to

$$\rho(r) = 4\pi \int_{\Phi(r)}^{0} dE \, f(E) \sqrt{2[E - \Phi(r)]} \, . \tag{4.7}$$

The above equation, Eq. (4.7), can be inverted. If the phase space distribution depends only on the energy E, the phase space distribution for a density profile $\rho(r)$ is given by the Eddington's formula [42]

$$f(E) = \frac{1}{2\sqrt{2}\pi^2} \frac{d}{dE} \left[\int_{E}^{0} d\Phi \frac{d\rho/d\Phi}{\sqrt{\Phi - E}} \right] . \tag{4.8}$$

Note that there is no guarantee that the $f(E)$ from the formula above is positive definite. However, a density profile like in Eq. (4.7) can arise from an ergodic distribution if and only if $f(E) \geq 0$.

Suppose now that the system changes slowly from $t = t_{\rm i}$ to $t = t_{\rm f}$, i.e. the Hamiltonian of the system changes on a time scale longer than the crossing time scale but

shorter than the halo relaxation time scale. During this slow evolution, called *adiabatic*, invariants such as the angular momentum L and the radial action

$$J_r = \frac{1}{2\pi} \oint dr\, v_r \tag{4.9}$$

are conserved. Using the conservation of the phase space distribution, we can write

$$f(E_\mathrm{f}, L_\mathrm{f}) = f(E_\mathrm{i}(E_\mathrm{f}, L_\mathrm{f}), L_\mathrm{i})\ . \tag{4.10}$$

Since the angular momentum is an adiabatic invariant, $L_\mathrm{i} = L_\mathrm{f}$. The relation between the final energy and the initial energy $E_\mathrm{i} = E_\mathrm{i}(E_\mathrm{f}, L_\mathrm{f})$ is found from the conservation of the radial action

$$J_{r,\mathrm{f}}(E_\mathrm{f}, L_\mathrm{f}) = J_{r,\mathrm{i}}(E_\mathrm{i}, L_\mathrm{i})\ . \tag{4.11}$$

Notice that, despite the initial distribution being ergodic, independent on L_i, the final distribution function depends on angular momentum, causing a mild velocity anisotropy of the compressed dark matter halo [342]. Once the phase space distribution as a function of final energy and angular momentum is known, we can integrate to find the final density profile

$$\rho_\mathrm{f}(r) = \int_{\Phi_\mathrm{f}(r)}^{0} dE_\mathrm{f} \int dL_\mathrm{f}\, \frac{4\pi L_\mathrm{f}}{r^2 v_r(E_\mathrm{f}, L_\mathrm{f})} f(E_\mathrm{i}(E_\mathrm{f}, L_\mathrm{f}), L_\mathrm{f})\ . \tag{4.12}$$

This procedure is general, under the specified assumptions.

4.1.2 Power law density profile

We apply the above recipe to find the density profile for an initial power-law profile

$$\rho_\mathrm{i}(r) = \rho_s \left(\frac{r_s}{r}\right)^\gamma \tag{4.13}$$

with $0 < \gamma < 2$. Let us assume a central Schwarzschild black hole of mass M_bh has formed and grown via adiabatic processes. We have already found, through a naive application of dark matter mass conservation and angular momentum conservation for circular orbits, that the final density profile is given by a power law with index γ_sp, given by Eq. (4.3). In Appendix D, we apply the general procedure outlined in the previous Section to the power-law profile of the inner NFW halo Eq. (D.1). What we find is the spike density profile

$$\rho_\mathrm{f} \;=\; \rho_s \left(\frac{r_s}{r}\right)^{\gamma_\mathrm{s}} \left[\frac{\Phi_s}{\Phi_\mathrm{f}(r_s)}\right]^{-\frac{3-\gamma}{4-\gamma}} \frac{\Gamma(\beta)}{\Gamma(\beta - 3/2)} \left[\frac{2B\left(\frac{3}{2}, \frac{1}{2-\gamma}\right)}{\pi(2-\gamma)}\right]^{\frac{6-\gamma}{4-\gamma}} I(\gamma) \tag{4.14}$$

Here $I(\gamma)$ an integral that evaluates numerically to $I(\gamma) \in [0.5, 0.7]$ for $0 \leq \gamma \leq 2$ and $L_\mathrm{min} = 0$,

$$\Phi_s = \frac{4\pi G \rho_s r_s^2}{(2-\gamma)(3-\gamma)} \tag{4.15}$$

and $B(z_1, z_2)$ is the beta function, or Euler integral of the first kind.

Once the density profile $\rho_{\rm f}(r)$ is known, we can derive an ergodic distribution $f(E_{\rm f})$ from it via the the Eddington inversion formula. The calculation is simplified by the fact that the final potential is simply $\Phi_{\rm f} = -GM_{\rm bh}/r$. The result is

$$\boxed{f(E_{\rm f}) = \frac{\rho_{\rm f}(r)}{[-2\pi\Phi_{\rm f}(r)]^{3/2}} \frac{\Gamma(\gamma_{\rm sp}+1)}{\Gamma(\gamma_{\rm sp}-1/2)} \left(\frac{\Phi_{\rm f}(r)}{E_{\rm f}}\right)^{3/2-\gamma_{\rm sp}}} \,. \tag{4.16}$$

This will be the form we use in the explicit calculations of quantities in the compressed halo, and proves to be a good approximation to the much more complicated formula that we show in Appendix D. An example proving the goodness of the ergodic approximation is given in Appendix E, where the dynamical friction force on an object is computed with the full distribution and with the ergodic one, and the differences prove to be at percent level.

Spike size and parameterization

We want a simple parameterization for the spike density profile and we want to make manifest the dependence of the spike parameters on the initial halo parameters r_s, ρ_s, γ and the black hole mass.

Up to which radius does the spike extend? In the derivation above, the key assumption is that the central black hole dominates the gravitational potential, so that we can ignore the dark matter self-gravity. This is valid approximately up to a radius r_h, defined as the radius at which the total dark enclosed dark matter mass of the spike equals twice the mass of the black hole [342]

$$M_{\rm dm}(r < r_h) = 2M_{\rm bh} \,. \tag{4.17}$$

We re-parameterize the density profile as a simple power law $\rho_{\rm f}(r) = \rho_\star \, (r_\star/r)^{\gamma_{\rm sp}}$. The condition in Eq. (4.17), assuming the spike extends up until r_h, is then

$$r_h = r_\star \left[\frac{(3-\gamma_{\rm sp})M_{\rm bh}}{2\pi\rho_\star r_\star^3}\right]^{\frac{1}{3-\gamma_{\rm sp}}} \,. \tag{4.18}$$

However, since the self-gravity becomes important surely for $r < r_h$, it is a stretch to think that the spike extends up until that value. If we compute the value of r/r_h for which $\rho_{\rm f} = \rho_{\rm i}$ we obtain, depending on the choice of γ, a value of order few percent. Careful numerical computations [342] find that the spike extends up to $r_{\rm sp} \simeq 0.2\, r_h$, where then it converges to the initial power law profile $\rho_{\rm i}(r)$.

Because of that, we parameterize

$$\rho_{\rm f}(r) = \rho_{\rm sp} \left(\frac{r_{\rm sp}}{r}\right)^{\gamma_{\rm sp}} \,. \tag{4.19}$$

with $\rho_{\rm sp} = \rho_{\rm i}(r_{\rm sp}) = \rho_s (r_s/r_{\rm sp})^\gamma$. The condition $M_{\rm dm}(r < r_{\rm sp}/0.2) = 2M_{\rm bh}$ can be rewritten to find $r_{\rm sp}$

$$r_{\rm sp} = \left[\frac{0.2^{3-\gamma_{\rm sp}}(3-\gamma_{\rm sp})M_{\rm bh}}{2\pi\rho_{\rm sp}}\right]^{1/3} \,. \tag{4.20}$$

Substituting the expression for $\rho_{\rm sp}$, we arrive to an expression for $r_{\rm sp}$ as function of the black hole mass and the initial halo parameters γ, r_s, ρ_s

$$r_{\rm sp} = r_s \left[\frac{0.2^{3-\gamma_{\rm sp}} (3-\gamma_{\rm sp}) M_{\rm bh}}{2\pi \rho_s r_s^3} \right]^{\frac{1}{3-\gamma}} . \tag{4.21}$$

This equation, together with the one for $\gamma_{\rm sp}$, fully determines the spike profile once the initial halo and the black hole mass are specified.

Black hole absorption

The presence of a central black hole is a boundary condition we have to take into account. In particular, dark matter matter particles with angular momentum smaller than $L \sim 2R_S$, with $R_S = 2GM_{\rm bh}$ the Schwarzschild radius, get absorbed. This causes a sudden depletion of the spike profile around the Schwarzschild radius. We take this into account by imposing a lower cutoff in the angular momentum $L_{\rm min} = 2R_S$

$$\rho_{\rm f}(r) \approx \int dE_{\rm f} \int_{2R_S} dL_{\rm f} \, \frac{4\pi L_{\rm f}}{r^2 v_r} f(E_{\rm f}) \tag{4.22}$$

and computing the density profile using the ergodic spike distribution Eq. (4.16). Assuming $r \gg 2R_S$, we obtain

$$\boxed{\rho_{\rm f}(r) \approx \rho_{\rm sp} \left(\frac{r_{\rm sp}}{r} \right)^{\gamma_{\rm sp}} \left(1 - \frac{2R_S}{r} \right)^{\gamma_{\rm sp}} ,} \tag{4.23}$$

that amounts to the multiplication of the spike profile by a factor $(1 - 2R_S/r)^{\gamma_{\rm sp}}$. This approximate profile matches to relativistic results in Sadeghian et al. [343] with an error less than 20% over all radii.

4.1.3 Cosmological viability of the initial halo

It is important to assess the cosmological viability of the adiabatic compression scenario. In this Section we discuss the plausible cosmological setup, in ΛCDM cosmology, under which adiabatic compression can take place. The adiabatic compression of a dark matter halo is motivated by the presence of a supermassive black hole of sufficient size in the center of the system. One case of interest is the compression of halos at high redshift, which is motivated by the observation of black holes of unclear origin at redshift $z > 6$. One of the explanations of the existence of such black holes is the formation of an intermediate mass black hole $M_{\rm bh} \sim 10^3 \, M_\odot$ at the center of a dark matter halo at very high redshift $z \gtrsim 10$ [344].

In the investigation of the adiabatic compression we take a slightly modified version of the Navarro-Frenk-White (NFW) density profile discussed in Section 1.2.2 as the initial profile:

$$\rho_{\rm i}(r) = \frac{\rho_s}{(r/r_s)^\gamma (1 + r/r_s)^{3-\gamma}} , \tag{4.24}$$

NFW is recovered for $\gamma = 1$.

It is important to understand which is the phenomenologically viable halo parameter space for this particular choice. An important parameter in the description of halos is the *halo concentration* c. Depending on the definition of the halo mass, either through the virialization radius $r_{\rm vir}$ or r_{200} as in Eq. (1.29) and Eq. (1.30), one has $c_{\rm vir} = r_{\rm vir}/r_s$ or $c_{200} = r_{200}/r_s$. The characteristic overdensity can be found from the concentration parameters exploiting the equations defining the halo mass ($M_{\rm vir}$ or M_{200}) in Eq. (1.29) and Eq. (1.30).

$$\begin{aligned} \delta_{\rm ch} &= \frac{\Delta_{\rm vir}\Omega_{\rm m}c_{\rm vir}^3}{3}\left[\log(1+c_{\rm vir}) - \frac{c_{\rm vir}}{1+c_{\rm vir}}\right]^{-1} \\ &= \frac{\Delta_{200}c_{200}^3}{3}\left[\log(1+c_{200}) - \frac{c_{200}}{1+c_{200}}\right]^{-1}. \end{aligned} \tag{4.25}$$

It is clear that we can now find ρ_s and r_s once c and the size or mass of halo are specified. The NFW halo is specified by fixing both the halo mass and the concentration parameter (M, c). However, these two parameters are correlated and the halo concentration has a non-trivial dependence on the redshift at which the halo forms. Understanding these relations is crucial to find which values of the scale radius and density are characteristic of an halo of mass M formed at redshift z and then which are the parameters of a NFW profile, that is likely to host a black hole and undergo adiabatic compression.

To investigate the M vs c relation and the dependence on redshift we refer to the model of Diemer and Joyce [345]. With their semianalytical treatment, we are able to find the concentration parameter c_{200} as a function of the halo mass M_{200} for given redshift $z \in [0, 20]$. Diemer and Joyce claim that the model is able to reproduce accurately the small concentration observed in simulations for the halos at very high redshift $z \sim 30$. Once the concentration parameter is known, it is trivial to find the scale radius r_s and ρ_s as function of M_{200} and z.

We show the findings in Figure 4.1. The different panels show the concentration c_{200}, the scale factor r_s and the scale density ρ_s as function of the halo mass M_{200} for different redshifts. The dots indicate the values of the mass when the peak height ν, defined in Eq. (1.42) is 3, 5 or 7. We stop drawing lines for masses higher than the one for which $\nu = 7$, considering higher values to be too unlikely.

4.1.4 A concrete example

We are now able to choose in a consistent way our benchmarks for the initial halo that undergoes adiabatic compression at high redshift. For example we can choose a halo formed at $z = 20$ with mass $M_{200} = 10^6\ M_\odot$. This choice corresponds to peak height $\nu \sim 3$, so the halo is quite rare. According to the used model of [345], we have a concentration of $c_{200} \simeq 2.7$ as one can read off Figure 4.1. This brings $r_s \simeq 55$ pc, $\rho_s \simeq 0.8\ M_\odot/{\rm pc}^3$ and $r_{200} \simeq 150$ pc. This benchmark halo is similar to the one considered by Eda et al. [103], with the differences probably due to a different model for the concentration parameter.

Having motivated the viability of the benchmark, we present the initial NFW-like density profile in Figure 4.2, with the parameters fixed by the benchmark used

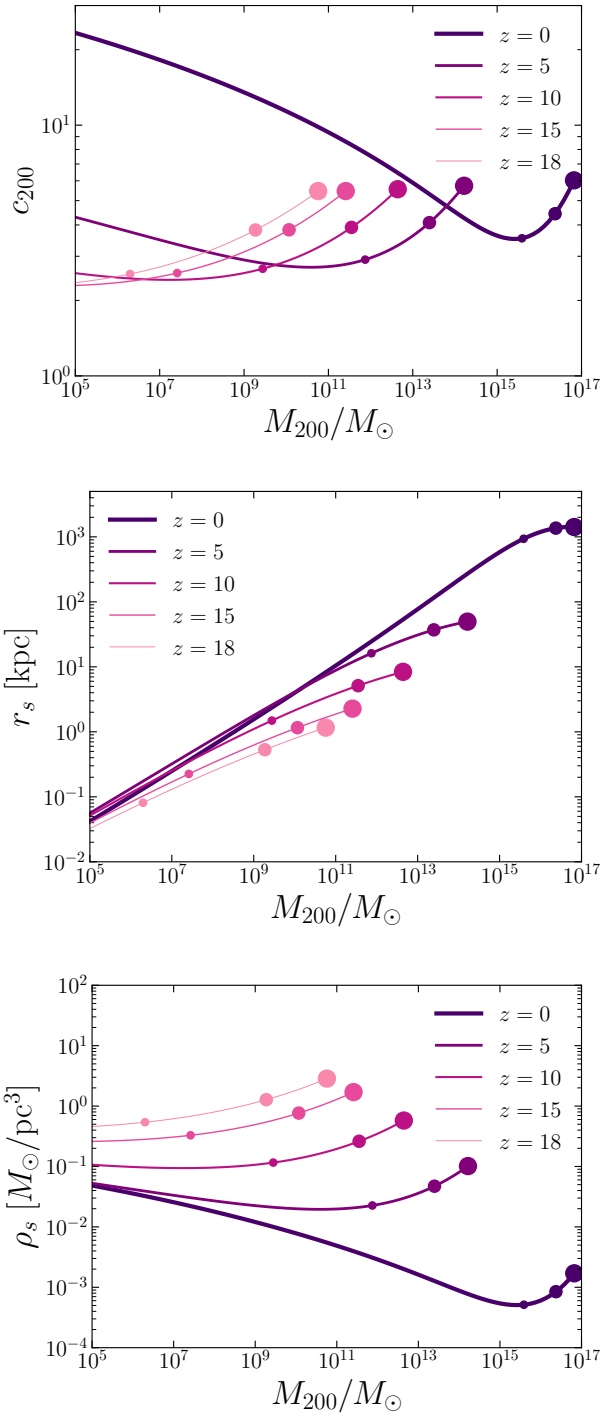

FIGURE 4.1: The concentration c_{200} (**top**), the scale factor r_s (**middle**) and the scale density ρ_s (**bottom**) as functions of the halo mass M_{200} for different redshifts, from $z = 0$ to $z = 18$. The dots increasing in size mark the values of the mass when the peak height ν, defined in Eq. (1.42), is 3, 5 or 7.

z	$M_{\rm vir}\ [M_\odot]$	r_s [pc]	$\rho_s\ [M_\odot/{\rm pc}^3]$	γ
20	10^6	23.1	5.3	1

TABLE 4.1: Reference benchmark for a NFW halo hosting a black hole, before compression, used in [103].

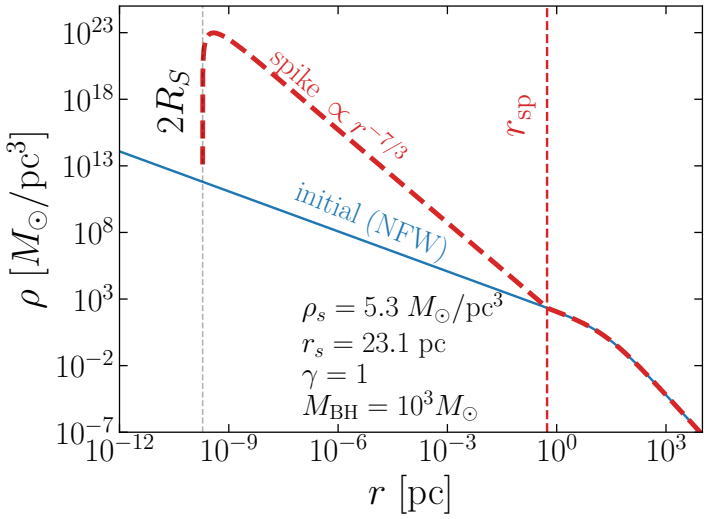

FIGURE 4.2: The initial NFW density profile (blue) for the benchmark in [103] and the formed spike (red, dashed) due to a central black hole of mass $10^3\ M_\odot$. The initial halo parameters are in the benchmark of Table 4.1.

by Eda et. al. [103] to study intermediate-mass-ratio inspirals in dark matter spikes: $r_s = 23.1$ pc and $\rho_s = 5.3\ M_\odot/{\rm pc}^3$ for a halo formed at $z = 20$ of mass $M_{\rm vir} = 10^6\ M_\odot$ (see Table 4.1). From now on this will be our reference benchmark for halos which then undergo compression.

We specialize to the NFW profile with $\gamma = 1$. We also show the final dark matter spike profile from the adiabatic compression due to a central black hole of mass $M_{\rm bh} = 10^3\ M_\odot$. The final resulting profile is

$$\rho(r) = \begin{cases} \rho_{\rm sp}(r_{\rm sp}/r)^{\gamma_{\rm sp}} & r < r_{\rm sp} \\ \rho_{\rm i}(r) & r > r_{\rm sp} \end{cases} \tag{4.26}$$

The presence of the black hole horizon results in a depletion of the density around $r \sim 2R_S$ because of the factor we introduced to take into account the absorption of the particles with low angular momentum. At radius $r_{\rm sp} \simeq 0.54$ pc, obtained from Eq. (4.21), the spike transitions to the initial NFW profile $\rho_{\rm f} \approx \rho_{\rm i}$. The shown profile assumes a vanishing dark matter interaction with the visible matter. In case of a non-negligible interaction, the dark matter can decay into standard model particle and the spike gets cored [99].

4.2 Compression of a wave dark matter halo

In this Section, we explore how wave dark matter halos react to the adiabatic change in the gravitational potential. We have observed that the adiabatic invariants are conserved, and there is a relationship between the initial and final phase space distribution, as shown in Eq. (4.10).

To apply these observations to wave halos, we begin by discussing the initial profile of the wave dark matter halo and how it can be described as a superposition of eigenmodes. We then discuss its possible relaxation over short time scales. The occupation numbers of the eigenmodes are the quantum analog of the phase space distribution in the particle limit. We then utilize the Schrödinger equation and the adiabatic theorem to demonstrate that the response of wave dark matter is comparable to that of particle dark matter in the semi-classical limit. However, as we move closer to the center of the compressed wave halo, we cannot rely on the semi-classical approximation anymore. In this region, there may be a distinctive core with a profile similar to the ground state solution of a hydrogen-like atom. The survival of this core over cosmological times depends on the type of dark matter and the mass of the central black hole, which we will discuss shortly.

As it will be further explained in Chapter 5, a compressed wave halo could be detected through the observation of gravitational waves produced by inspirals of compact objects orbiting a black hole that was responsible for the adiabatic compression. For this reason, we will have in mind, throughout this Section, a benchmark point characterized by:

- Central black hole masses of $M_{\rm bh} \sim 10^3 - 10^5\ M_\odot$. The value of $M_{\rm bh}$ determines the radius of the innermost stable circular orbit $r_{\rm ISCO} = 6GM_{\rm bh}$ around the black hole and also the distance between the black hole and the inspiralling compact object five years (the observation time for a gravitational wave detector like LISA [110]) before the coalescence, dubbed $r_{\rm 5yr}$. They are given by

$$r_{\rm ISCO} \simeq 3\times 10^{-9}\ {\rm pc}\left(\frac{M_{\rm bh}}{10^4\ M_\odot}\right), \tag{4.27}$$

$$r_{\rm 5yr} \simeq 3\times 10^{-8}\ {\rm pc}\left(\frac{M_{\rm bh}}{10^4\ M_\odot}\right)^{1/2}. \tag{4.28}$$

  The proof for the second formula will be obtained rigorously in Section 5.3.

- Wave dark matter masses such as that the gravitational Bohr radius $a = (GM_{\rm bh}m^2)^{-1}$ happens to be smaller than $r_{\rm 5yr}$ for the wave nature to impact the compressed density profile but not completely deplete it (the reason for this is explained in Section 4.2.5 and it is due to the survival of the ground state in presence of the black hole). This implies, from $a \lesssim r_{\rm 5yr}$

$$m \gtrsim \sqrt{\frac{1}{GM_{\rm bh}r_{\rm 5yr}}} \simeq 10^{-15}\ {\rm eV}\left(\frac{M_{\rm bh}}{10^4\ M_\odot}\right)^{-1/2}\left(\frac{r_{\rm 5yr}}{3\times 10^{-8}\ {\rm pc}}\right)^{-1/2}. \tag{4.29}$$

Once the wave dark matter mass and the black hole mass are specified, one can map an initial wave halo into the compressed one. The phenomenologically relevant region of the compressed density profile will be $r \in [r_{\rm ISCO}, r_{\rm 5yr}]$.

4.2.1 Construction of a wave dark matter halo

We have seen that over distances that are large compared to the de Broglie wavelength, wave dark matter behaves similarly to the standard collisionless cold dark matter. In particular this is the case for dark matter structure on galactic scales such as halos. Numerical simulations [29,108,219,220,346,347] found a characteristic soliton, i.e. a cored stable self-gravitating structure at the center of wave dark matter halo, surrounded by a Navarro-Frenk-White (NFW) outer profile. This profile is characteristic for collision-less cold dark matter, as seen in Section 1.2.2.

We assume that the wave halo is given by

$$\rho(r) = \begin{cases} \rho_{\rm sol}(r) & r < r_{\rm t} \\ \rho_{\rm i}(r) & r \geq r_{\rm t} \end{cases} \tag{4.30}$$

where $\rho_{\rm sol}(r)$ is the core profile and ρ_i some unspecified NFW-like profile as in Eq. (4.24). The transition happens at a radius $r_{\rm t}$ that can be found numerically. The soliton is characterized by a core mass M_c and a density profile given by [29,108]

$$M_c = 6\times 10^9\, M_\odot \left(\frac{10^{-23}\,{\rm eV}}{m}\right)^2 \left(\frac{\rm kpc}{r_c}\right), \tag{4.31}$$

$$\rho_{\rm sol}(r) = \frac{2\, M_\odot/{\rm pc}^3}{[1+0.091(r/r_c)^2]^8} \left(\frac{\rm kpc}{r_c}\right)^4 \left(\frac{10^{-23}\,{\rm eV}}{m}\right)^2. \tag{4.32}$$

The core mass is the mass enclosed within the core radius r_c, that is the radius at which the soliton density drops by a factor of 2, i.e. $\rho_{\rm sol}(r_c) = \rho_{\rm sol}(0)/2$. The total soliton mass M is related to the core mass as $M_c = 0.24M$. These expressions come from the ground state solutions of the SP system that we have outlined in Section 2.5.1.

We have seen that the SP system scaling symmetry is such that the properties of the soliton are fixed once one parameter, e.g. the core radius r_c is specified. We determine this quantity as

$$r_c = \frac{c_r}{m v_c(r_c)}. \tag{4.33}$$

Here v_c is the circular velocity and $c_r \sim O(1)$ some constant. This implicit equation fixes the core radius to the typical wavelength of dark matter, similarly to the procedure in [167]. The core radius connects the property of the host halo to the soliton radius. The easiest way to see this is by rewriting the expression as $r_c = c_r/(GM_{\rm dm}(< r_c)m^2)$. Imposing the core radius relation Eq. (4.33) is equivalent to say that the soliton mass is determined by the enclosed mass of halo within the typical wavelength of dark matter.

z	$M_{\rm vir}\,[M_\odot]$	r_s [kpc]	$\rho_s\,[M_\odot/{\rm kpc}^3]$	γ
0	10^{10}	10	10^6	1

TABLE 4.2: Reference benchmark for a wave (fuzzy) dark matter halo, used in [109] to study a eigenmode construction of a wave halo.

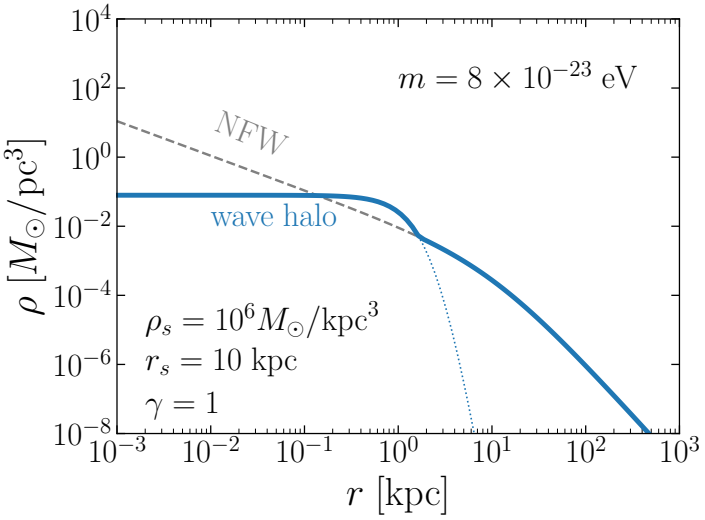

FIGURE 4.3: A (fuzzy) wave dark matter halo for $m = 8 \times 10^{-23}$ eV (solid blue). We see the soliton core $\rho_{\rm sol}(r)$ (blue dotted line) embedded in a NFW halo (dashed gray) with parameters of the benchmark in Table 4.2.

In Figure 4.3 we show an example of a wave halo for ultra-light wave dark matter in the fuzzy ballpark, $m \sim 8 \times 10^{-23}$ eV. The parameters correspond to a benchmark chosen in [109] to describe the construction of a fuzzy dark matter halo (see Table 4.2). The soliton core is embedded in a large halo with $r_{\rm vir}$ of several tens of kpc.

In Section 2.5.1 we found another relation to fix the core radius from the halo mass, Eq. (2.98), $r_c \sim 1/(m v_{\rm vir})$. Comparing to Eq. (4.33), the sole contrast is the replacement of the circular velocity with the virial velocity of the halo. This relation has been debated: see [348] for a recent review and also for the discussion on the validity of soliton-host halo relation for larger particle mass. This dissimilarity is insignificant provided that the size of the halo is roughly equivalent to the average dark matter wavelength. Indeed for the small mass considered in Figure 4.3, the two methods of Eq. (2.98) and Eq. (4.33) give $r_c \sim 0.78$ kpc and $r_c \sim 0.91$ kpc respectively. Alternatively, if the core radius is not much smaller than the scale radius of the halo, the circular velocity at the core radius is analogous to the virial velocity. This is evident in most numerical simulations [29, 108, 220, 347].

A complication arises when the wavelength of dark matter is much smaller than the system's size. In this situation, the wave dark matter enters the inner part of the halo, and utilizing the conventional soliton-host halo relation Eq. (2.98) naively may underestimate the soliton's size, as well as considerably overestimate the soliton's mass [228].

We visualize the huge difference in the two prescription in Figure 4.4. In this case

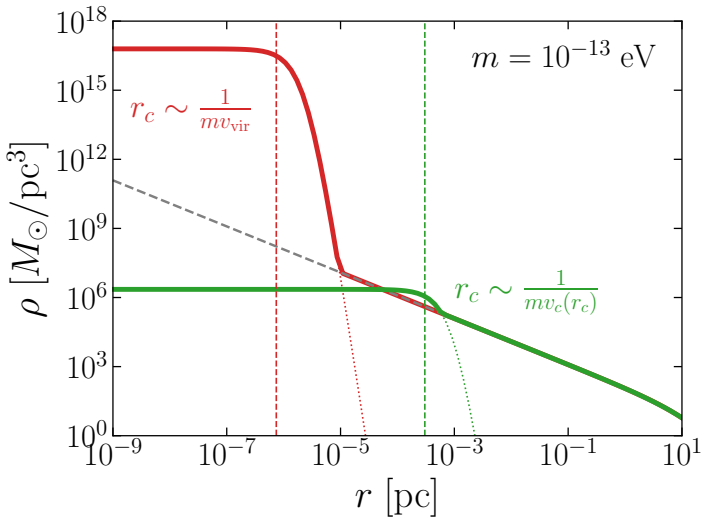

FIGURE 4.4: Comparison of the wave dark matter halos obtained for a large mass $m = 10^{-13}$ eV using the prescription of Eq. (2.98) (red) and the one of Eq. (4.33) (green) to determine the core radius r_c. We consider the same outer NFW-like halo of the pre-compression benchmark in Table 4.1. We see that the Eq. (2.98) predicts a core radius which is considerably underestimated, leading to a nonphysical core density.

we choose $m = 10^{-13}$ eV and the benchmark shown in Table 4.1, that is the one of a halo which can undergo adiabatic compression if a growing black hole is present in the center. Unlike the one involving the virial velocity, the relation Eq. (4.33) provides a gradual progression from an NFW-like profile to a cored profile when the radius is approximately equal to the wavelength of dark matter.

As we will examine a wide range of wave dark matter masses, such as values up to $m \sim 10^{-13}$ eV, we use the core radius prescription in Eq. (4.33) for our analysis.

4.2.2 Relaxation of the wave halo

We have seen that the self-gravitating wave DM halo has a similar density profile to the particle dark matter halo, except for the presence of a central soliton. Due to small-scale fluctuations in the density, modeled by quasiparticles, the wave halo can relax much faster than the particle halo. This can further change the density profile. In Section 2.5.2, we estimated the relaxation timescale for fuzzy dark matter and we have concluded that the relaxation is relevant up to scales of the kpc, which indeed is similar to the core radius (see Figure 4.3). Due to the strong dependence on r, i.e. $t_{\rm relax} \propto r^4 v_{\rm vir} \propto r^4 r_{\rm vir}$, the relaxation time for external shells is too large to be relevant.

What happens for larger values of the wave dark matter mass? In particular, we would like to check whether the benchmark in Table 4.1 and the halo shown in the green line of Figure 4.4 are consistent with the relaxation time at the relevant scales. Indeed this is the NFW-like benchmark halo we will consider for compression. A quick estimate in Section 2.5.2 gave a very short relaxation time.

Let us check this estimate carefully. The relaxation timescale is [42, 46, 349]

$$t_{\rm relax} \equiv \frac{1}{3}\frac{v^2}{D[(\Delta v_\parallel)^2]} \,. \tag{4.34}$$

For wave dark matter, the diffusion coefficient is given by [46] (see Appendix C.2 for the proof)

$$D[(\Delta v_\parallel)^2](v) = \frac{32\pi^2 G^2 m_{\rm eff}\log\Lambda}{3}\left[\frac{1}{v^3}\int_0^v dv' v'^4 f_{\rm eff}(v') + \int_v^\infty dv'\, v' f_{\rm eff}(v')\right] . \tag{4.35}$$

Here the effective mass and velocity distribution are defined from the dark matter velocity distribution as

$$m_{\rm eff} \equiv \frac{(2\pi)^3}{m^3}\frac{\int d^3v\, f^2(v)}{\int d^3v\, f(v)} \,, \tag{4.36}$$

$$f_{\rm eff} \equiv f^2(v)\frac{\int d^3v\, f(v)}{\int d^3v\, f^2(v)} \,. \tag{4.37}$$

The Coulomb logarithm is given by $\log\Lambda = \log(mrv)$. We have assumed an isotropic velocity distribution, i.e. function only of v or of energy E. We are interested in the wave halo density profile at radii $r > r_c$ but $r \ll r_s$. This is because we know that at larger radii the relaxation timescale would be considerably longer. Therefore, a suitable choice of the distribution would be ergodic one found from the profile $\rho(r) = \rho_s(r_s/r)$ in the low energy limit, i.e. Eq. (D.6). Changing variable to velocity, $E = v^2/2 + \Phi_{\rm i}(r)$,

$$f(v) \approx \frac{\rho_s}{(2\pi\Phi_s)^{3/2}}\frac{\Gamma(\beta)}{\Gamma(\beta-3/2)}\left[\frac{1}{2}\frac{v^2}{\Phi_s} + \left(\frac{r}{r_s}\right)^{2-\gamma}\right]^{-\beta} . \tag{4.38}$$

If we specify $\gamma = 1$ ($\beta = 5/2$).

$$f(v) \approx \frac{3\sqrt{\pi}}{4}\frac{\rho_s}{(2\pi\Phi_s)^{3/2}}\left[\frac{1}{2}\frac{v^2}{\Phi_s} + \frac{r}{r_s}\right]^{-5/2} . \tag{4.39}$$

Here $\Phi_s = 2\pi G\rho_s r_s^2$.

To understand which velocity we should exploit in Eq. (4.34), we can take a look at the velocity distribution in the inner part of the halo. In Figure 4.5, we show the speed distribution in Eq. (4.39) for the parameters of the pre-compression benchmark in Table 4.1 at radius $r = 10^{-5} r_c$. We evince that the circular velocity, shown as a solid line, is more representative of the velocity of the particles at low radii than the dispersion σ, defined as

$$\sigma^2 = \frac{1}{3}\frac{\int_0^{v_e} d^3v\, v^2 f(v)}{\int_0^{v_e} d^3v f(v)} \,. \tag{4.40}$$

The dispersion appears to be determined by a small number of very fast particles. Therefore, if we consider the circular velocity, we can interpret $t_{\rm relax}$ as the timescale

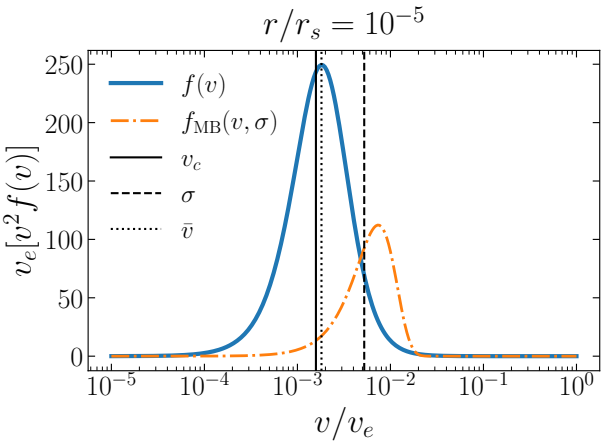

FIGURE 4.5: The normalized speed distribution in Eq. (4.39) (solid blue line), compared to the Maxwell-Boltzmann distribution with standard deviation equal to the σ of Eq. (4.39). We fix $r = 10^{-5} r_s$. We consider the same outer NFW-like halo of the pre-compression benchmark in Table 4.1. The vertical lines show how the circular velocity v_c is more representative of the velocity of the particles than the dispersion σ, being closer to the median $\bar{v}$.

at which half of the particles at such radius are relaxed through gravitational interaction, while if we use $v = \sqrt{3}\sigma$, it becomes the time scale at which almost all of kinetic energy at such radius is relaxed through gravitational interaction.

We show the result of the computation in Figure 4.6 for the benchmark halo in Table 4.1 and $m = 10^{-13}$ eV. As predicted, the relaxation time using the velocity dispersion is considerably larger (three orders of magnitude) than the one computed with the circular or median velocity. This is because it takes much longer to relax the high velocity tail of the speed distribution than the average one. At scales comparable to the de Broglie wavelength computed with the typical velocity of particles (v_c or $\bar{v}$), the relaxation time scales for these fast particles is of the order of the Gyr. This signals that the wave halo must have formed a soliton at scales $r < 10^{-3}$ pc exactly as we found with our prediction Eq. (4.33). The relaxation time sharply increases, as $\propto r^{4.3}$, for larger radii, so that outer dark matter shells undergo relaxation in a much longer time.

4.2.3 Eigenmode decomposition

Having discussed the density profile of wave dark matter, we consider an effective description of wave dark matter halo with eigenmode decomposition, following previous works by Lin et al [93] and Yavets et al [109]. The occupation number for each eigenmode plays a similar role as the phase space distribution in the particle halo.

Spherical solutions of the SP system

We describe the wave dark matter field as outlined in Section 2.4. We perform the non-relativistic expansion of Eq. (2.62) and we obtain from the Einstein equations coupled to the Klein-Gordon equation on small-scales the Schrödinger-Poisson (SP)

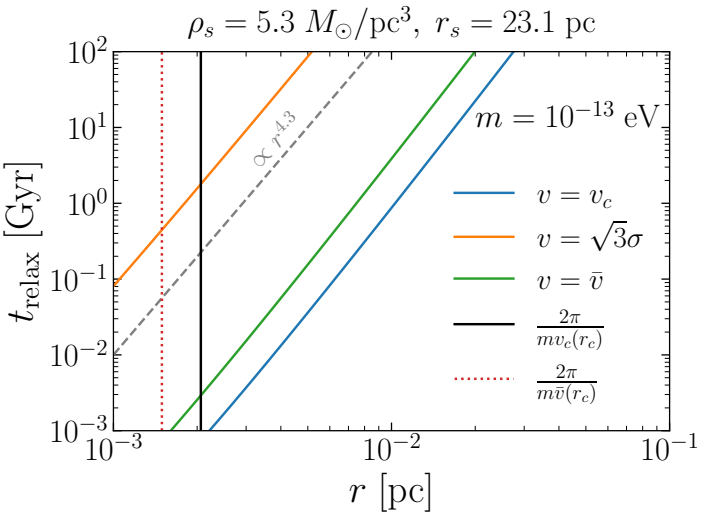

FIGURE 4.6: The relaxation time scale in Eq. (4.34) computed with different choices of the velocity: circular (blue), rms (orange) and median (green). We consider the same outer NFW-like halo of the pre-compression benchmark in Table 4.1. The vertical lines show the de Broglie wavelength computed with the circular velocity (solid black) and the median $\bar{v}$ (dotted red). The relaxation time scales as $\propto r^{4.3}$,as shown by the dashed gray line.

system for self-gravitating wave dark matter

$$\begin{aligned} i\partial_t\psi &= \left[-\frac{\nabla^2}{2ma^2} + m\Phi\right]\psi\,, \\ \nabla^2\Phi &= 4\pi G m|\psi|^2\,. \end{aligned} \tag{4.41}$$

The wavefunction is normalized as $\int d^3x\ |\psi(t,\mathbf{x})|^2 = 1$. We model the wave dark matter halo as a superposition of eigenmodes of the SP system

$$\langle\rho\rangle = \bar{\rho} = m\sum_i f_i|\psi_i(t,\mathbf{x})|^2\,, \tag{4.42}$$

where f_i is the occupation number of each mode ψ_i and the angle bracket is the ensemble average defined in Eq. (2.56). To find the eigenmodes, we assume a time-independent gravitational potential Φ_t obtained from the Poisson equation $\nabla^2\Phi_t = 4\pi G\rho_t$, where ρ_t is an initial target profile, given by the soliton and the NFW-like profile, that is the profile in Eq. (4.30). Then the eigenmodes can be found by solving the time-independent Schrödinger equation for each mode

$$\left[\nabla^2 - 2m^2(\Phi_t - E_i)\right]\psi_i(\mathbf{x}) = 0\,, \tag{4.43}$$

where E_i is the energy eigenvalue divided by the particle mass. We find the occupation number for each mode f_i such that $\bar{\rho} \approx \rho_t$. Practically, this is achieved by minimizing a cost function of the form [109]

$$D(\rho_t,\bar{\rho}) = \frac{1}{r}\int_0^r dr'\,\frac{(\rho_t-\bar{\rho})^2}{\rho_t^2}\,. \tag{4.44}$$

To find a self-consistent profile, we iterate the above fitting procedure several times by updating the target density profile and gravitational potential until the density profile converges.

This construction is qualitatively identical to the particle halo construction with phase space distribution. In the particle halo, we assume that the dark matter particles are distributed according to the phase space distribution, $f(\mathbf{x}, \mathbf{v})$, where each trajectory evolves according to the Hamiltonian of the system, which is constructed with the mean potential of the system Φ. The density profile $\rho = \int d^3v\ f(\mathbf{x}, \mathbf{v})$ should then satisfy the Poisson equation, $\nabla^2\Phi = 4\pi G\rho$, for self-consistency. In the wave halo, we follow the same procedure, with the additional step of solving the Schrödinger equation to find the eigenfunctions.

Since we consider a spherically symmetric system, it is more convenient to decompose the wavefunction into a radial wavefunction and spherical harmonics,

$$\psi_i = \psi_{n\ell m_\ell}(\mathbf{x}) = R_{n\ell}(r)Y_\ell^{m_\ell}(\theta,\phi) = \frac{1}{r}\chi_{n\ell}(r)Y_\ell^{m_\ell}(\theta,\phi)\ . \tag{4.45}$$

The radial wave function satisfies

$$\chi''_{n\ell} + \left[2m^2(E_{n\ell} - \Phi_{\rm t}) - \frac{\ell(\ell+1)}{r^2}\right]\chi_{n\ell} = 0\ . \tag{4.46}$$

The mean density is then given by

$$\bar{\rho}(r) = \frac{m}{4\pi r^2}\sum_{n\ell}(2\ell+1)f_{n\ell}|\chi_{n\ell}|^2\ , \tag{4.47}$$

where we assume that the occupation number does not depend on the magnetic quantum number as we consider a spherically symmetric system.

Wave-particle correspondence

For the following discussion, it is useful to see how the above wave dark matter construction Eq. (4.47) compares to the particle dark matter one Eq. (4.5). The correspondence between particle and wave halo becomes clearer in the semi-classical limit [109] (see also Section 3.3.3). We can approximate the discrete sum in Eq. (4.47) with a continuous integral as

$$\bar{\rho} = \int dE \int dL\ \frac{4\pi L}{v_r r^2}\left[\frac{m^4}{(2\pi)^3}f_{n\ell}\right]\left(\frac{\pi}{m}\frac{dn}{dE}\right)(v_r|\chi_{n\ell}|^2)\ , \tag{4.48}$$

where dn/dE is the density of the states. In the semi-classical limit $mvr \gg \hbar$ (notice we reintroduced the reduced Planck constant for now), the WKB approximation can be used to find a radial wavefunction as

$$\chi_{n\ell}(r) = \frac{c_\pm}{\sqrt{mv_r(r)}}\exp\left[\pm\frac{im}{\hbar}\int^r dr' v_r(r')\right]\ . \tag{4.49}$$

While for unbound particles the above two solutions represent left- and right-moving particles, in bound systems the WKB solution is subject to boundary conditions

which fix the coefficients $c_\pm$. We find [350]

$$\chi^-_{n\ell} = \frac{\mathcal{N}_{n\ell}}{\sqrt{m v_r}} \cos\left[\frac{m}{\hbar}\int_{r_{\rm min}}^{r} dr' v_r(r') - \frac{\pi}{4}\right], \tag{4.50}$$

$$\chi^+_{n\ell} = \frac{\mathcal{N}_{n\ell}}{\sqrt{m v_r}} \cos\left[\frac{m}{\hbar}\int_{r}^{r_{\rm max}} dr' v_r(r') - \frac{\pi}{4}\right], \tag{4.51}$$

where $r_{\rm min}$ and $r_{\rm max}$ are solutions to $v_r(r) = 0$. The normalization constant is found from $\int d^3x\, |\psi|^2 = 1$. The two solutions must be identical $\chi^+_{n\ell} = \chi^-_{n\ell}$.

$$|\mathcal{N}_{n\ell}|^2 = \left| \oint \frac{dr}{m v_r(r)} \cos^2\left[\frac{m}{\hbar}\int_{r_{\rm min}}^{r} dr' v_r(r') - \frac{\pi}{2}\right]\right| \approx \left| \oint \frac{dr}{2 m v_r(r)}\right|^{-1}, \tag{4.52}$$

where we have assumed the wave function to be non-vanishing only in the $r \in [r_{\rm min}, r_{\rm max}]$ classical region and the cosine squared term to average to $1/2$ because of the fast oscillations. From the $\chi^+_{n\ell} = \chi^-_{n\ell}$ condition, we arrive to the semi-classical Bohr-Sommerfeld quantization, for $\ell \neq 0$

$$\pi\left(n + \frac{1}{2}\right) = m \oint dr\, v_r(r) = 2\pi m J_r\,. \tag{4.53}$$

We see that the right-hand side is proportional to the radial action J_r. We compute the density of states from the quantization condition

$$\frac{dn}{dE} = \frac{m}{\pi}\oint \frac{dr}{v_r} \approx \frac{2m^2}{\pi |\mathcal{N}_{n\ell}|^2}\,. \tag{4.54}$$

We substitute this expression in Eq. (4.48) and we find

$$\bar{\rho} = \int dE \int dL \frac{4\pi L}{r^2 v_r}\left[\frac{m^4}{(2\pi)^3} f_{n\ell}\right]. \tag{4.55}$$

Therefore, the correspondence between the occupation number and classical phase space distribution is found as [109]

$$f(E) \approx \frac{m^4}{(2\pi)^3} f_{n\ell}\,, \tag{4.56}$$

allowing us to interpret the occupation number as a phase space distribution in the semi-classical limit.

In Figure 4.7, we show the density profile constructed according to the method described above, as well as the occupation number. As an example, we consider as target profile an initial soliton and NFW profile (gray line) with parameters from Table 4.2 and fuzzy particle mass $m = 8 \times 10^{-23}$ eV. Next, we derive the gravitational potential by using the target density profile. Then, we solve the Schrödinger equation and determine a set of occupation numbers for each mode that can best replicate the initial profile. To achieve this, we group the energy eigenvalues and assign the same occupation number to the modes that share the same energy bin. We repeat this process three times to ensure that the halo is self-consistent. The final halo, which is formed by the superposition of eigenmodes, is represented by a red

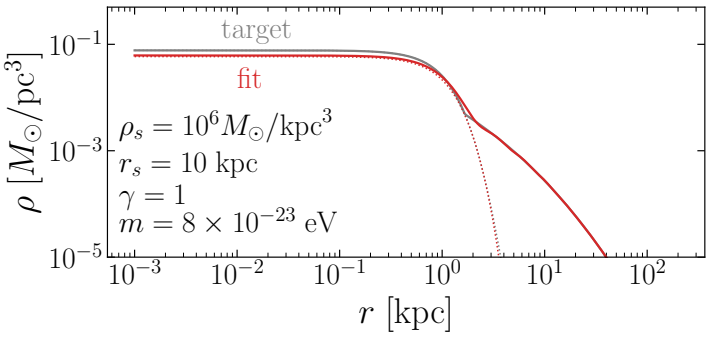

FIGURE 4.7: The initial and wave halo profile for the benchmark in Table 4.2 and $m = 8 \times 10^{-23}$ eV. The initial target profile is given by Eq. (4.30) (gray). The red solid line is the density profile obtained by fitting the occupation numbers such that $\bar{\rho} \approx \rho_t$.

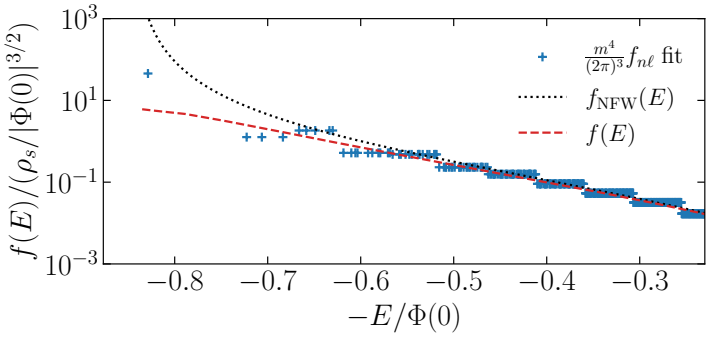

FIGURE 4.8: The normalized occupation number in the halo considered in Figure 4.7. The dotted line is the phase space distribution of NFW profile obtained from ρ_{NFW} Eq. (4.24) via the Eddington's formula, the dashed line is the phase space distribution of target density profile obtained by the Eddington inversion formula $f(E)$, and the crosses are the corresponding occupation numbers for wave halo $f_{n\ell}[m^4/(2\pi)^3]$ obtained from the fit.

line. The corresponding occupation number is shown in Figure 4.8. As expected, the occupation number $f_{n\ell}[m^4/(2\pi)^3]$ closely follows the classical phase space distribution $f(E)$ except for the ground state. The ground state occupation number is simply given by $f_0 \simeq M_{\mathrm{sol}}/m$ with the total soliton mass M_{sol}.

4.2.4 Wave dark matter spike

We are now ready to consider the adiabatic change of the system. Suppose that the initial Hamiltonian $H_i = H(t_i)$ adiabatically changes to $H_f = H(t_f)$, as in the particle case. According to the adiabatic theorem, an eigenstate of the Hamiltonian at an initial time t_i remains as an instantaneous eigenstate of the Hamiltonian as the system evolves. If the initial density profile is given by

$$\bar{\rho}_i = m \sum_j f_j |\psi_j^{(i)}(r)|^2 \,, \tag{4.57}$$

where $\psi_j^{(\mathrm{i})}$ is the eigenmode of the initial Hamiltonian H_i, the final density profile is given by

$$\bar{\rho}_\mathrm{f} = m\sum_j f_j|\psi_j^{(\mathrm{f})}(r)|^2 = \frac{m}{4\pi r^2}\sum_{n\ell}(2\ell+1)f_{n\ell}|\chi_{n\ell}^{(\mathrm{f})}(r)|^2\,, \tag{4.58}$$

with the eigenmode $\psi_j^{(\mathrm{f})} = \chi_{n\ell}^{(\mathrm{f})}Y_\ell^{m_\ell}/r$ of the final Hamiltonian H_f. The occupation number remains the same $f_{n'\ell'} = f_{n\ell}$. We denote with primes the quantum numbers after the compression.

To see how this compressed wave halo compares to the compressed particle halo, we consider the semi-classical limit $mvr \gg 1$. In this limit, the initial wave dark matter density profile is approximated as in Eq. (4.55) with $f_{n\ell}[m^4/(2\pi)^3] \approx f(E,L)$ and $L^2 = \ell(\ell+1)/m^2$. Since the eigenstate stays in the same eigenstate during the adiabatic evolution, the quantum number before and after the adiabatic evolution is the same: $n = n'$ and $\ell = \ell'$. The conservation of quantum numbers is translated into the conservation of classical adiabatic invariants. For instance, the condition $\ell' = \ell$ leads to $L_\mathrm{f} = L_\mathrm{i} = L$, while the condition $n' = n$ leads to

$$\oint dr\, v_r^{(\mathrm{i})}(r) = \oint dr\, v_r^{(\mathrm{f})}(r)\,, \tag{4.59}$$

from the semi-classical Bohr-Sommerfeld quantization condition Eq. (4.53). Given the definition of the radial action in Eq. (4.9), this condition is identical to the conservation of the radial action $J_r^{(\mathrm{i})}(E_\mathrm{i}, L_\mathrm{i}) = J_r^{(\mathrm{f})}(E_\mathrm{f}, L_\mathrm{f})$, which we use to derive $E_\mathrm{i} = E_\mathrm{i}(E_\mathrm{f}, L_\mathrm{f})$ for the compression of the particle halo, as explained in Section 4.1.1. From these arguments, we see that the adiabatic compression proceeds in the same way as in the particle case, as long as the semi-classical approximation is valid, i.e. at sufficiently large distances.

The semi-classical approximation becomes unreliable when considering small values of r. At these radii, the profile is primarily influenced by modes with low angular momentum, particularly the ground state solution. If we assume that the ground state is the primary contributor to the central profile, then the core profile before adiabatic compression can be described as follows

$$\rho_\mathrm{sol}^{(\mathrm{i})} = mf_0|\psi_0^{(\mathrm{i})}(r)|^2 = M_\mathrm{sol}|\psi_0^{(\mathrm{i})}(r)|^2\,, \tag{4.60}$$

where $\psi_0^{(\mathrm{i})}$ is the ground state wave function of the initial system H_0 and $f_0 = M_\mathrm{sol}/m$ is the ground state occupation number. The above form is a simple reparameterization of the soliton profile $\rho_\mathrm{sol}(r)$ Eq. (4.32). Being the occupation number conserved, the final core profile is

$$\rho_\mathrm{sol}^{(\mathrm{f})} = mf_0|\psi_0^{(\mathrm{f})}(r)|^2 = M_\mathrm{sol}|\psi_0^{(\mathrm{f})}(r)|^2 \tag{4.61}$$

We have to determine $\psi_0^{(\mathrm{f})}$, the ground state of the final Hamiltonian H_f. If the central black hole of mass M_bh dominates the gravitational potential of the final system, the

Hamiltonian $H_{\rm f}$ can be approximated as

$$H_{\rm f} \approx \frac{p^2}{2m} - \frac{GM_{\rm bh}}{r} \,, \tag{4.62}$$

and, therefore, the ground state wave function is given by the ground state wave function of the hydrogen atom

$$\psi_0^{(\rm f)}(r) \approx \frac{e^{-r/a}}{\sqrt{\pi} a^{3/2}} \,, \tag{4.63}$$

with a the gravitational Bohr radius

$$a \equiv \frac{1}{GM_{\rm bh} m^2} \,. \tag{4.64}$$

The final compressed wave dark matter halo consists of the central soliton and the outer particle-like cuspy profile

$$\rho_{\rm f} = \begin{cases} \rho_{\rm sol}^{(\rm f)}(r) & r < r_{\rm t} \\ \rho_{\rm sp}(r_{\rm sp}/r)^{\gamma_{\rm sp}} & r_{\rm t} < r < r_{\rm sp} \end{cases} \,, \tag{4.65}$$

where $r_{\rm t}$ is defined such that $\rho_{\rm sp}(r_{\rm sp}/r_{\rm t})^{\gamma_{\rm sp}} = \rho_{\rm sol}^{(\rm f)}(r_{\rm t})$. The profile for $r > r_{\rm t}$ is the same as the compressed particle halo, $\rho_{\rm sp}(r_{\rm sp}/r)^{\gamma_{\rm sp}}$, which is valid up to $r \sim r_{\rm sp}$, after which it converges to the uncompressed profile. In summary, the central part is replaced by the soliton and the outer part is the same as compressed particle dark matter halo.

In the top panel of Figure 4.9, we present the compressed wave halo obtained by solving the final Hamiltonian's, $H_{\rm f}$, Schrödinger equation, using the occupation numbers determined in the previous section. We choose $M_{\rm bh} = 3 \times 10^9 \, M_\odot$ for illustration purposes. The resulting compressed profile is displayed as a blue solid line, featuring a central core and an outer spike profile similar to the compressed particle halo. The central density profile corresponds to the ground state wave function of hydrogen. Moreover, we compare this numerical result to the analytical profile presented in Eq. (2.62), represented by a red dashed line, which agrees with the numerical outcome. To ensure the compressed halo's self-consistency, we iterate the process three times.

4.2.5 Survival of the core

If a massive black hole is at the center of the halo, it may swallow the low angular momentum modes over an astrophysical timescale. It is exactly the reason why the particle halo density profile sharply drops at $r = 2R_S$ (see Figure 4.2).

The absorption of wave modes by the central black hole can occur in a similar manner, with the survival of a particular mode dependent on both the central black hole mass and the wave dark matter mass. To study this phenomenon, we consider the Schwarzschild black hole for simplicity. Although the system is analogous to the hydrogen atom in the non-relativistic regime, the energy eigenvalue acquires an imaginary component due to the boundary condition at the black hole horizon [351].

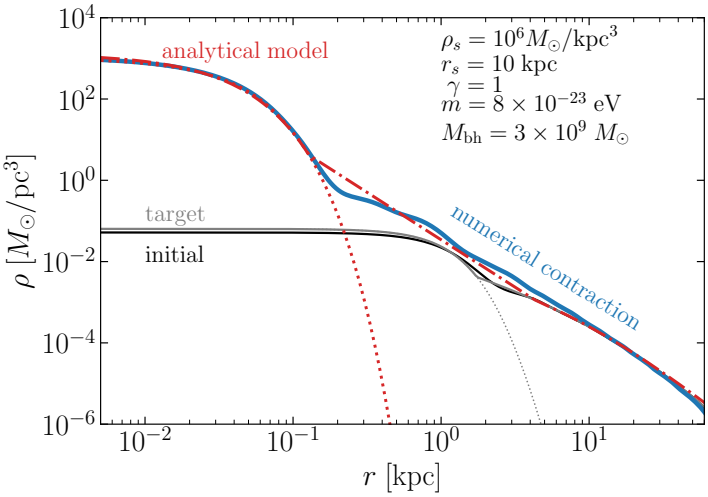

FIGURE 4.9: The initial and compressed wave halo profile with parameters given in Table 4.2 and for $m = 8 \times 10^{-23}$ eV. The black solid line is the red line in Figure 4.7, the initial profile obtained from the eigenmode decomposition, the gray line is the target profile. The blue line is the compressed wave halo, which consists of the central solitonic core and outer spike profile that is similar to the particle dark matter halo. For this, we assume an adiabatic formation of the central black hole of mass $M_{\rm bh} = 3 \times 10^9 M_\odot$. The red dot-dashed line is the analytical model in Eq. (4.65) which is in a good agreement with the numerical result of the contraction.

The imaginary part of the energy eigenvalue is interpreted as a decay rate and is given by

$$\Gamma_{n\ell} \approx m\alpha_G^{4\ell+5} \frac{2^{4\ell+3}(n+\ell)!}{n^{2\ell+4}(n-\ell-1)!} \left[\frac{\ell!}{(2\ell)(2\ell+1)!}\right]^2 \prod_{k=1}^{\ell}[k^2 + (4\alpha_G)^2]\,, \tag{4.66}$$

where we take the Schwarzschild limit of the result obtained in the Kerr geometry [351,352]. Here $\alpha_G = GM_{\rm bh}m$ is the fine structure constant of the gravitational atom. Including the possible decay of modes into the black hole, i.e. the wavefunction finite lifetime, the wave dark matter halo density at a given age $t_{\rm halo}$ is

$$\boxed{\bar{\rho}(r) = \frac{m}{4\pi r^2} \sum_{n\ell} (2\ell+1) |\chi_{n\ell}(r)|^2 e^{-2\Gamma_{n\ell} t_{\rm halo}}\,.} \tag{4.67}$$

Compared to the previous wave dark matter profile, we have an additional exponential decay factor due to the absorption. The above estimation assumes that the central black hole dominates the dynamics of the system. We only consider such cases in this work. The decay of the central soliton given by Eq. (4.66) agrees with full numerical simulations [101].

The decay rate of the ground state scales as $\Gamma \propto m\alpha_G^5$. For the example shown in Figure 4.9, the gravitational fine structure constant is $\alpha_G \sim 2 \times 10^{-3}$ and the decay rate is $\Gamma_{00} \sim (10^3 \mathrm{Gyr})^{-1}$; the solitonic core of the compressed wave halo survives over the age of the universe in this case. Note, however, that whether the soliton and low angular momentum modes can survive over the age of the halo crucially

depends on $\alpha_G = GM_{\rm bh}m$. For larger wave dark matter masses and smaller black hole masses, α_G can get of order unity and the decay rate increases sharply. This is the case of the intermediate-mass ratio inspirals to be discussed in Chapter 5 where low angular momentum modes, not only the soliton, are indeed unstable over the age of the halo as the central black hole absorbs them. The decay of wave modes leads to a distinctive compressed wave halo compared to the one studied above. In particular, it can be described with a broken power-law profile, which will be discussed below.

To illustrate the density profile in the case where the low angular momentum modes get absorbed by the black hole, let us consider the wave dark matter mass around $m \sim 10^{-14}$ eV and a black hole mass of $M_{\rm bh} = 10^4\ M_\odot$. The Bohr radius in this case is $a = (GM_{\rm bh}m^2)^{-1} \sim 10^{-8}$pc, roughly Earth-Moon distance, and, as we will see in Chapter 5 the separation between such a black hole an a compact solar-mass companion object five years before coalescence. In this case, the gravitational fine structure constant is

$$\alpha_G \simeq 0.74 \times \left(\frac{M_{\rm bh}}{10^4\ M_\odot}\right)\left(\frac{m}{10^{-14}}\right)\,, \tag{4.68}$$

while the decay rate of the ground state is given by Eq. (4.66) by $\Gamma \simeq 300$ Hz: the ground state decays and cannot survive over the Gyr time scale and the central black hole swallows the whole soliton in a short time scale. This conclusion holds for the parameter ranges which will be of our interest: the mass of the central black hole being $M_{\rm bh} \sim 10^3 - 10^5\ M_\odot$ and the Bohr radius being $a \sim 10^{-9} - 10^{-8}$ pc, again in the ballpark of the distance between the objects in an intermediate mass ratio inspiral several years before coalescence [1].

The most straightforward way to compute the density profile including the decay, is to use Eq. (4.67), which is shown in Figure 4.10. We choose the initial halo benchmark of Table 4.1 compressed with a black hole of mass $M_{\rm bh} = 10^4\ M_\odot$ and we vary the Bohr radius $a \in [10^{-12}, 10^{-9}]$ pc, corresponding to wave dark matter masses $m \in [3\times10^{-13}, 10^{-14}]$ eV. As one can see, the core is absent and the inner part of density profile behaves as a power-law profile of $\rho \propto r^{2\ell_c}$ where the critical angular momentum ℓ_c is defined such that

$$2\max_n \Gamma_{n\ell_c} t_{\rm halo} = 1\,. \tag{4.69}$$

The modes with ℓ_c are the modes with the lowest angular momentum that survive over the age of the halo. Note that, for very small Bohr radii a, the profile converges to the particle one, shown as a thick gray dot-dashed line, (because this implies larger masses and the semi-classical limit kicks in). Due to the particle-wave correspondence, at large radii the density profile has to converge to $\rho \propto r^{-\gamma_{\rm sp}}$, therefore the resulting profile has a broken power law, with a smooth interpolation between the two regimes characterized by a smaller $\rho \propto r^{\ell_c}$ slope and a shallow peak.

For a later numerical purpose, being the Riemann sum in Eq. (4.67) computationally slow, we provide a simple analytical expression for the density profile. Since low angular momentum modes are absorbed, and the density profile begins to have

[1] For further on the response of ultralight dark matter soliton to external perturbations see [353,354]

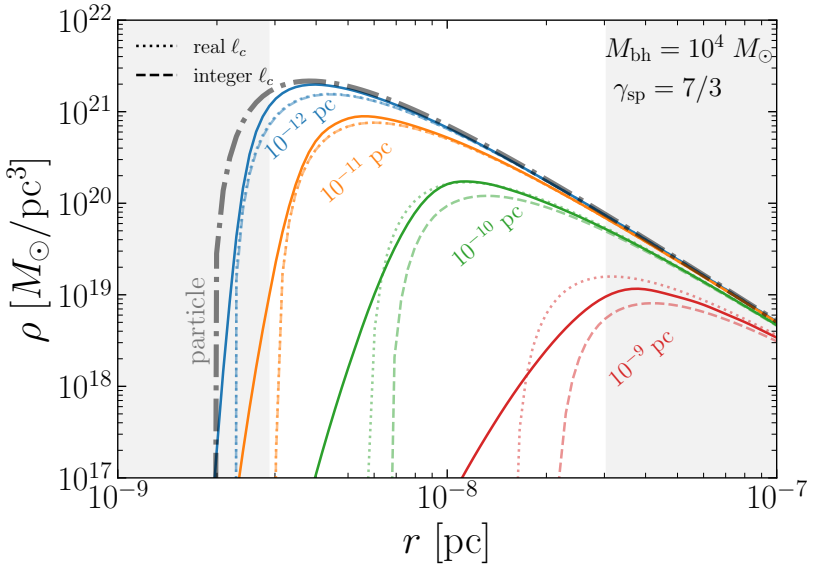

FIGURE 4.10: The density profile of a compressed wave halo. The soliton, as well as other low angular momentum modes, are absorbed by the central black hole, leading to a broken power-law profile. At large radii, the profile behaves as $\rho \propto r^{-\gamma_{\rm sp}}$, while at small radii, it behaves as $\rho \propto r^{2\ell_c}$, with ℓ_c given by the solution of Eq. (4.69). The gray dot-dashed line is the profile of particle dark matter halo Eq. (4.23). Colored lines show the compressed wave halo profiles for different values of the Bohr radius $a = 1/(GM_{\rm bh}m^2)$. The dashed lines are the analytical approximations given in Eq. (4.71) with integer $\lfloor \ell_c \rfloor$, while dotted lines consider a real ℓ_c. We fix $M_{\rm bh} = 10^4\ M_\odot$ and we use the spike parameters derived from the halo in Table 4.1. The gray shaded areas show radii smaller than the innermost stable circular orbit (ISCO) for a binary with masses $M_{\rm bh}$ and $M_\odot$ and radii larger than the distance between these two objects five years before mergers. We will see in Chapter 5 that the physically interesting region is in the unshaded area.

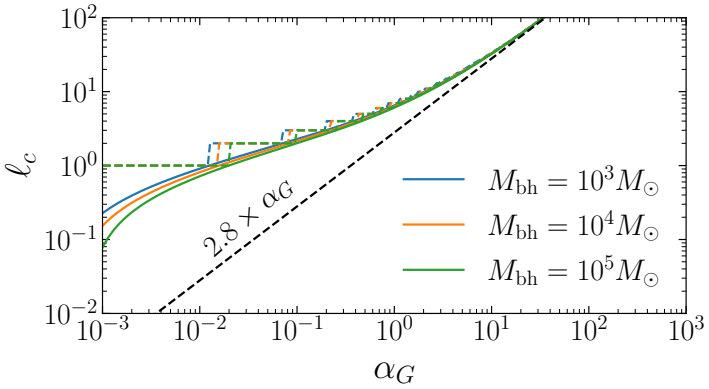

FIGURE 4.11: The critical angular momentum above which the mode can survive cosmological time $t_{\rm halo} = 10\,{\rm Gyr}$ for different back hole masses. The lines show the solutions of Eq. (4.69) with ℓ_c real (solid) and $\lfloor \ell_c \rfloor$ (dashed). We also see that $\ell_c \gtrsim 2.8\alpha_G$.

non-vanishing value at $r \gg a$, taking the continuum limit is a good approximation in most cases. We approximate the discrete sum in Eq. (4.67) to the continuous integral

$$\bar{\rho} \approx \int dE \int_{L_c} dL \frac{4\pi L}{r^2 v_r} f(E)\,. \tag{4.70}$$

where we have taken $m^4/(2\pi)^3 f_{n\ell} \to f(E)$ and put a low angular momentum cutoff $L_c = a\ell_c(\ell_c+1)/2$, where ℓ_c is the solution of Eq. (4.69) where we fix $n = \max(\ell+1, \frac{1}{3}\sqrt{(\ell+1)(\ell+2)(2\ell+3)})$, which is an approximate value maximizing the decay rate for a given angular momentum ℓ. The value of ℓ_c is shown in Figure 4.11 for different choice of the black hole mass and as a function of α_G. The value of ℓ_c can either be rounded to integer or taken as a real number. The momentum cutoff gets rid of all the modes which have a short lifetime. A useful expression for $f(E)$ is given by the spike distribution in Eq. (4.16) and it is the same distribution we used to compute the particle spike profile, with a cutoff given by $2R_S$, instead. Therefore a simple substitution $R_S \to L_c/2 = R_c/2$ in Eq. (4.23), with $R_c = a\ell_c(\ell_c+1)$ gives

$$\boxed{\bar{\rho} \approx \rho_{\rm sp}\left(\frac{r_{\rm sp}}{r}\right)^{\gamma_{\rm sp}}\left(1-\frac{R_c}{2r}\right)^{\gamma_{\rm sp}}\,.} \tag{4.71}$$

This approximation reliably reproduces the profile from the discrete summation for $\ell_c \gg 1$. As one can see in Figure 4.10, a subtlety arises when we choose to take ℓ_c as a real number or the integer part $\lfloor \ell_c \rfloor$ if ℓ_c is not large enough. This difference however is not crucial for the description of the profile.

One can check if the relevant modes are safely non-relativistic. The energy (over mass) of the modes is $E = -\alpha_G^2/(2n^2)$. If $|E| < 1$, the mode is non-relativistic. This happens if $n > \alpha_G/\sqrt{2}$. The minimum value of n is $\ell_c + 1$ so it is sufficient to prove that $\ell_c > \alpha_G/\sqrt{2} - 1$. Actually, as one can see from Figure 4.11, $\ell_c \gtrsim 2.8\alpha_G$, so the modes are non-relativistic.

4.2.6 Relaxation of the compressed wave halo

In Section 4.2.2, we studied the relaxation of the wave halo to the ground state and we checked that a soliton forms at radius r_c. During the adiabatic compression, the density profile of the dark matter on the smallest scales changes considerably. Gravitational interaction among wave dark matter can modify the compressed halo profile over time through the relaxation process. In particular, this process replenishes the lower angular momentum modes which are absorbed by the black hole, being the relaxation most efficient at small radii. It is therefore important to check if the relaxation takes place in the system that we considered in the previous section.

We can estimate the relaxation time scale in the wave halo by considering the gravitational interaction between quasiparticles [33]. These quasiparticles have a size equal to the wavelength of dark matter and a mass equivalent to the total mass enclosed within the de Broglie volume. The timescale for relaxation in the wave halo can be estimated as the time taken for quasiparticles to exchange kinetic energy by an order of magnitude. This is referred to as the relaxation timescale and can be approximated as [42, 349]

$$t_{\rm relax} = \left.\frac{v^2}{3D[(\Delta v_\parallel)^2]}\right|_{v=\sqrt{3}\sigma} . \tag{4.72}$$

We are considering the compressed halo, so we compute the velocity dispersion and the diffusion coefficient using the analytical distribution in Eq. (4.16). This distribution is a reliable approximation for both the particle and the wave case. We find

$$\sigma^2 = \frac{1}{3\rho}\int d^3v\, v^2 f(v) = \frac{1}{3}\frac{\int_\Phi^0 dE[2(E-\Phi)]^{3/2} f(E)}{\int_\Phi^0 dE[2(E-\Phi)]^{1/2} f(E)} = \frac{v_c^2}{1+\gamma_{\rm sp}} . \tag{4.73}$$

we used $v = \sqrt{2[E-\Phi]}$ and $f(E) \propto (\Phi/E)^{3/2-\gamma_{\rm sp}}$. Here $v_c^2 = GM_{\rm bh}/r$ is the circular velocity. An equivalent form of the diffusion coefficient for the wave dark matter, with respect to Eq. (4.35), is [47, 355]

$$\begin{aligned} D[(\Delta v_\parallel)^2] &= \frac{32\pi^2 G^2 \log\Lambda}{3}\frac{(2\pi)^3}{m^3} \\ &\quad\times\left[\frac{1}{v^3}\int_\Phi^{\frac{v^2}{2}+\Phi} dE\,[2(E-\Phi)]^{3/2} f^2(E) + \int_{\frac{v^2}{2}+\Phi}^0 dE\, f^2(E)\right] \\ &= \frac{32\pi^2 G^2 \log\Lambda}{3}\frac{\rho^2(r)}{m^3 v_c^4}\left[\frac{\Gamma(\gamma_{\rm sp}+1)}{\Gamma(\gamma_{\rm sp}-1/2)}\right]^2 \mathcal{I}(v/v_c, \gamma_{\rm sp}) , \end{aligned} \tag{4.74}$$

where $\log\Lambda \simeq \log(m\sigma r)$ is the Coulomb logarithm and $\mathcal{I}$ is defined as

$$\mathcal{I}(x,\gamma_{\rm sp}) = \frac{1}{x^3}\int_{1-\frac{x^2}{2}}^1 d\epsilon\, \frac{[2(1-\epsilon)]^{3/2}}{\epsilon^{3-2\gamma_{\rm sp}}} + \int_0^{1-\frac{x^2}{2}} \frac{d\epsilon}{\epsilon^{3-2\gamma_{\rm sp}}} . \tag{4.75}$$

With this diffusion coefficient, the relaxation time reads

$$t_{\rm relax} = \frac{m^3\sigma^6}{G^2\rho^2\log\Lambda}\left\{\frac{3}{32\pi^2}\left[\frac{\Gamma(\gamma_{\rm sp}-1/2)}{\Gamma(\gamma_{\rm sp}+1)}\right]^2 \frac{(\gamma_{\rm sp}+1)^2}{\mathcal{I}(\sqrt{3/(1+\gamma_{\rm sp})},\gamma_{\rm sp})}\right\} . \tag{4.76}$$

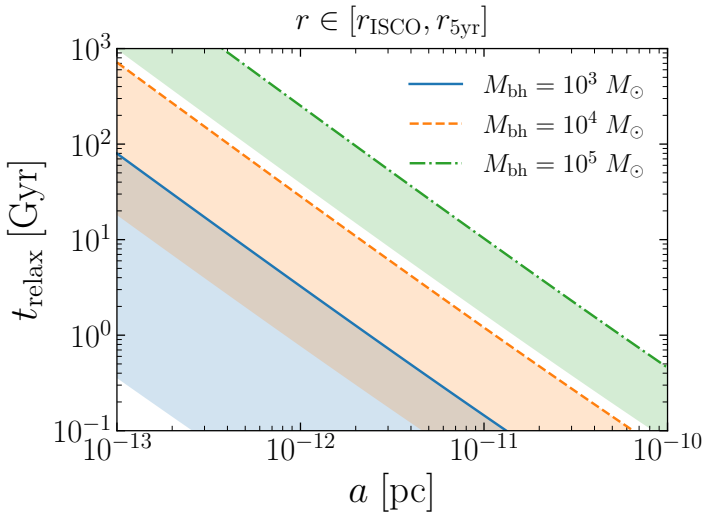

FIGURE 4.12: The relaxation time scale between $r_{\rm ISCO}$ and $r_{\rm 5yr}$ for three different values of the black hole mass. As we increase the mass of the central black hole, the relaxation time scale generally increases. If the relaxation time scale is significantly smaller than Gyr time scale, it is expected that the wave halo profile is further suppressed as the low angular momentum will be replenished through the relaxation process. The colored bands show the interval between $r_{\rm ISCO}$ (lower bound) and $r_{\rm 5yr}$ (upper bound and line).

The quantity in the square brackets has a mild dependence on $\gamma_{\rm sp}$: it takes values $[0.070, 0.075]$ for $\gamma_{\rm sp} \in [2.25, 3.00]$. Notice that $\rho(r)$ depends on the mass of the black hole, since $\rho_{\rm sp}$ and $r_{\rm sp}$ do.

Let us have a physical intuition of this timescale. We saw in Section 2.5.2 that for a self-gravitating system, like the initial halo, $t_{\rm relax} \sim 0.1\, r/v \times M_{\rm dm}(<r)/m_{\rm eff}$, with $M_{\rm dm}(<r)$ the enclosed mass in r and $m_{\rm eff} = \rho(\lambda_{\rm dB}/2)^3$ the mass of the quasiparticle. The relaxation time is proportional to v^4 and in the compressed halo this quantity is increased by a factor of $(M_{\rm bh}/M_{\rm dm}(<r))^{1/2}$. Therefore we expect

$$t_{\rm relax}^{\rm compressed} \sim 0.1 \frac{r}{v} \times \frac{M_{\rm dm}(<r)}{m_{\rm eff}} \times \left(\frac{M_{\rm bh}}{M_{\rm dm}(<r)}\right)^2 \tag{4.77}$$

and this confirms the result we obtained in the careful computation.

After the relaxation time scale, wave modes have exchanged energy by an order-one factor, replenishing low angular momentum modes that are subsequently absorbed by the central black hole, suppressing the wave halo density further.

As we anticipated in the previous Section and in the introduction of Section 4.2, we are mostly interested in the density profile in a specific range of radii, for reasons we will explore in Chapter 5. Considering a compact object of mass $\sim M_\odot$ orbiting the black hole $M_{\rm bh}$, we are interested in the region $r \in [r_{\rm ISCO}, r_{\rm 5yr}]$, corresponding to the distances between the innermost stable circular orbit $r_{\rm ISCO} = 6GM_{\rm bh}$ and the separation at 5 years before coalescence Eq. (4.28).

We compute the relaxation time scales for $r \in [r_{\rm ISCO}, r_{\rm 5yr}]$ as a function of the Bohr radius, for $M_{\rm bh} = 10^3,\ 10^4,\ 10^5\ M_\odot$ and show the results in Figure. 4.12. For $M_{\rm bh} = 10^3 M_\odot$, the relaxation timescale becomes smaller than the Gyr scale for $a \gtrsim$

10^{-11} pc ($m \gtrsim 2 \times 10^{-13}$ eV). In such cases, the wave halo is subject to relaxation at scales smaller than $r_{5\mathrm{yr}}$ and hence the density profile is further suppressed from what we discussed in the previous section. To correctly model the density profile, one needs to investigate the dynamical evolution of the wave modes due to gravitational interactions, which is beyond the scope of this work. We also compute the relaxation time scale for the other black hole masses. As the mass of central black hole increases, the relaxation time scale also increases at a given Bohr radius. In the Figure, we see that the relaxation time scale for these two benchmark scenarios can be Gyr time scale even for $a > 10^{-11}$ pc. Since the relaxation time scale is comparable to t_{halo}, we expect that the wave profile is given approximately by Eq. (4.67) and does not significantly change over the age of halo.

4.3 Summary and conclusions

This Chapter explored the response of wave dark matter to the adiabatic growth of a black hole. The first Section focuses on the formation of a spike from the inner part of a halo, while also checking the cosmological viability of the initial halo. Details on the computation of the density profile are in Appendix D.

Next, in Section 4.2, we consider a benchmark halo where the wave nature of dark matter is relevant, constructing the halo using the self-gravitating SP system. The resulting wave halo profile exhibits a solitonic core at the center that transitions smoothly to a NFW-like outer halo. The correct soliton-host halo relation is found to determine the soliton core radius based on the typical de Broglie wavelength of the dark matter particle. However, the wave nature of the halo can lead to gravitational cooling effects, so it is important to check that the wave halo forms a solitonic core in the age of the halo timescale without fully relaxing to the ground state.

The discussion then moves to finding the compressed wave profile. The compressed wave halo possesses a solitonic core near the central region, which may or may not be absorbed by the black hole depending on the system. Two examples are presented, one where the central soliton survives over the astrophysical timescale, and another where it does not. If the soliton and other low angular momentum modes are absorbed, the wave density profile exhibits a broken-power law that follows the typical spike profile at large radii. The main result of the Chapter is Eq. (4.71), which provides a simple but accurate formula to describe the compressed wave dark matter halo, being Eq. (4.67) the exact result.

It is also crucial to check the relaxation timescale of the compressed halo to ensure that the above-mentioned compressed wave halo profile is stable. Low angular momentum eigenmodes, i.e., the inner part of the halo, may decay to modes with shorter lifetimes and be absorbed by the black hole. We find that the profile in Eq. (4.67) is valid for black hole masses $M_{\mathrm{bh}} > 10^3\ M_\odot$ and Bohr radii $a \gtrsim 10^{-11}$ pc.

We have previously stated that the wave dark matter spike profile can be investigated via the inspiral of a solar-mass compact object around the central black hole. The inspiral process can be detected via gravitational wave emission and can be sensitive to the wave nature of dark matter. In Chapter 5, we will examine this astrophysical scenario as a way to probe the inner part of a compressed wave dark matter halo.

Chapter 5

Intermediate-Mass-Ratio Inspirals

In this Chapter, we consider a concrete astrophysical application of the adiabatic compression scenario discussed in detail in Chapter 4. The adiabatic growth of a black hole in the center of a halo causes the concentration of the mass density of the dark matter towards the central region.

This compression of the dark matter profile has been previously studied in the literature. Due to the enhanced mass density, celestial objects orbiting inside the adiabatically compressed halo experience larger dynamical friction and it has been suggested that it could cause the gravitational wave signals from a binary system to lose coherence, as discussed e.g. in [102–105,356,357]. This effect could potentially be observed by future gravitational wave detectors like the Laser Interferometer Space Antenna (LISA) [110, 358]. It might also be used to test interactions between dark matter and standard model particles [359,360]. Interestingly, indirect evidence of the dark matter spikes has been recently reported from the observations of anomalously fast orbital decays of companion stars near black holes [361].

We explore the possibility of using an intermediate-mass ratio inspiral (IMRI) scenario, where a solar-mass compact object m_2 inspirals towards an intermediate-mass black hole $m_1 \sim 10^3 - 10^5\ M_\odot$ at the center of the halo. We investigate if the gravitational wave observations from such an inspiral could provide information about the wave dark matter halo surrounding the black hole.

The outline of the Chapter is the following. In Section 5.1, we introduce the topic of intermediate mass black holes. Section 5.2 is dedicated to the detailed study of the intermediate-mass-ratio inspirals in a dark matter halo: we summarize the properties of the density profiles in the wave and particle case and we describe energy loss contributions to the evolution of the system, i.e. the gravitational wave emission and dynamical friction. Next, in Section 5.2.1, we take into account the backreaction due to the injection of energy into the compressed halo by the companion's inspiral. The next subsections comment on the approximations exploited to write such a formula: we discuss the choice of impact parameters in the Coulomb logarithm appearing in the expression for the dynamical friction and we motivate why quasiparticle effects and accretion by the companion object are negligible.

Section 5.3 is dedicated to the description of the gravitational wave radiation emitted by such a binary. We find that the phase is particularly sensitive to the presence of dark matter and its nature, producing a dephasing with respect to the waveform in absence of dark matter or with a different dark matter model.

We specify the dephasing intuition with a proper statistical analysis in Section 5.4. We perform a likelihood analysis in order to understand which information can be extracted about the system via the observation of gravitational waves with the LISA detector. We also discuss the cases in which we can distinguish the wave nature of dark matter. We conclude in Section 5.5.

Most of the content of the Chapter is adapted form the second part of [107] and expanded with further details and plots when needed, such as in Sections 5.2.1 and 5.2.2.

5.1 Intermediate Mass Black Holes

Before we dive into the scenario of a IMRI in a dark matter halo, we briefly review the origin of intermediate mass black holes.

In recent years, the possibility of intermediate mass black holes (IMBHs) has gained increasing support both theoretically and observationally, challenging the previous assumption of a mass gap between stellar black holes (about $1 - 100\ M_\odot$) and supermassive black holes (SMBHs, about $10^6 - 10^9\ M_\odot$). The formation of IMBHs as SMBH "seeds" at high redshift is attractive due to the difficulty of creating a SMBH in less than a Gyr, as observed in high redshift [362–364] quasars. While a stellar-mass black hole would need to accrete at the Eddington limit for its entire lifetime to achieve such mass, a more massive IMBH seed would provide a head start for black hole growth, allowing them to reach supermassive sizes more quickly. Some observations have identified potential candidates in the IMBH mass range ($10^2 - 10^5\ M_\odot$). Indeed, if seed formation is truly a high-redshift event that occurs in small halos, due to the hierarchical structure formation of ΛCDM, some of these small halos will remain small throughout their lifetimes and exist in the local universe as dwarf galaxies. Some recent works have found evidence for SMBHs in dwarf galaxies and some of them have masses diving into the IMBH range [365–367].

There are several proposed theories to explain the origin of SMBH seeds: the candidates include (i) remnants of Population III stars ($10^2 - 10^3\ M_\odot$) that formed at redshifts between 15 and 30 [368], (ii) direct collapse black holes from a molecular cloud ($10^4 - 10^6\ M_\odot$) that formed at redshifts between 10 and 20 [369], and (iii) runaway collision of objects in dense star clusters ($\sim 10^3\ M_\odot$) that formed at either high or low redshifts [370]. Only the first two cases are relevant for the adiabatic compression scenario. Each of these models for SMBH seed formation also has different predicted efficiencies. Population III stars, for instance, are expected to be widespread in the early universe, forming in every galaxy during its initial epochs of star formation. On the other hand, direct collapse black holes are anticipated to be less common, as they require a specific set of circumstances in order to develop. See [344] for a complete review on IMBHs. The underlying astrophysical origin of the IMBH has an impact on the dark matter halo which is most likely to host such IMBH and then undergo adiabatic compression, as we have seen in Section 4.1.3.

If the estimation of the number of IMBHs in the local universe is characterized by some uncertainties, the estimate of the number of IMRIs in the universe or in the Milky Way is an ever more complex task that requires detailed knowledge of the

astrophysical processes that give rise to these events. The difficulty is due to the fact that it is not clear how a IMRI would form, i.e. how likely is the encounter between a IMBH and a compact object and the mechanisms leading to the energy loss necessary to form a bound system. Several authors have estimated the rate at which stellar remnants are captured by a IMBH, with results between $\sim 10^{-6} - 10^{-8}$ yr^{-1} for a $\sim 10^6\ M_\odot$ black hole [371–374]. When combined with the uncertainty in the number density IMBHs, the net predicted number of detections that LISA will make spans three orders of magnitude, from a few to a few thousand events per year. If these events do occur, they will result in an extremely strong gravitational wave signal, that can easily be detected. We refer to [375] for an extensive review on IMRIs.

5.2 IMRI in a Dark Matter Halo

Let us present the system under consideration. We gather the useful information about adiabatic contraction from Chapter 4.

We investigate an initial (outer) NFW-like profile. The halo's density profile is given by the expression

$$\rho_{\rm i} = \frac{\rho_s}{(r/r_s)^\gamma (1 + r/r_s)^{3-\gamma}}\ , \tag{5.1}$$

where r_s, ρ_s, and $\gamma = 1$ are the parameters listed in Table 4.1. This halo formed at $z = 20$ with a virial mass of $M_{\rm vir} = 10^6\ M_\odot$, as discussed in Eda et al [103]. Our investigation focuses on the scenario where an intermediate-mass black hole with a mass of $m_1 = 10^3 - 10^5\ M_\odot$ forms at the center of the halo through the collapse of Population III stars [368] or a direct collapse of a gas cloud [369]. This formation process results in the compression of the surrounding dark matter halo, as explained in the previous Chapter. Such intermediate-mass black holes could potentially serve as seeds for supermassive black holes that are observed at high redshifts [362–364].

It is worth noting that the compressed halo may be compromised by off-center formation, merger events, and DM-star interactions [341, 376, 377]. A more detailed discussion on this topic and an estimate of the number of compressed halos without major merger events can be found in [378, 379]. Since the radius of gravitational influence of such intermediate black holes is much smaller than r_s, the adiabatic compression takes place mainly in the inner part of the halo, where the density profile can be approximated by a single power-law

$$\rho_{\rm i} \approx \rho_s \left(\frac{r_s}{r}\right)^\gamma\ . \tag{5.2}$$

The construction of an initial wave halo is discussed in Section 4.2.1, but it is not relevant to the following discussion.

After the adiabatic compression, a dark matter spike has formed. For the particle halo and the wave halo we consider the density profiles, for $r < r_{\rm sp}$

$$\rho_{\rm f}^{\rm p}(r) \approx \rho_{\rm sp}\left(\frac{r_{\rm sp}}{r}\right)^{\gamma_{\rm sp}}\left(1-\frac{2R_S}{r}\right)^{\gamma_{\rm sp}}, \tag{5.3}$$

$$\rho_{\rm f}^{\rm w}(r) \approx \rho_{\rm sp}\left(\frac{r_{\rm sp}}{r}\right)^{\gamma_{\rm sp}}\left(1-\frac{R_c}{2r}\right)^{\gamma_{\rm sp}}, \tag{5.4}$$

with $R_S = 2Gm_1$ and $R_c = a\ell_c(\ell_c+1)$, ℓ_c taken as a real number from the solution of Eq. (4.69) with fixed $n = \max(\ell+1, \frac{1}{3}\sqrt{(\ell+1)(\ell+2)(2\ell+3)})$, $a = 1/GM_{\rm bh}m^2$ the Bohr radius. These profiles have been motivated in Section 4.1.2 and 4.2.4 respectively. Albeit not exact, the wave profile is a good approximation to study the IMRI. In any case the huge astrophysical uncertainties in the spike density parameters make up for any factor of 2 differences in the assumed density profile. The spike parameters as function of the initial halo parameters are given by

$$\gamma_{\rm sp} = \frac{9-2\gamma}{4-\gamma}, \tag{5.5}$$

$$r_{\rm sp} = r_s\left[\frac{(3-\gamma_{\rm sp})0.2^{3-\gamma_{\rm sp}}m_1}{2\pi\rho_s r_s^2}\right]^{\frac{1}{3-\gamma}}, \tag{5.6}$$

$$\rho_{\rm sp} = \rho_s\left[\frac{2\pi\rho_s r_s^3}{(3-\gamma_{\rm sp})0.2^{3-\gamma_{\rm sp}}m_1}\right]^{\frac{\gamma}{3-\gamma}}. \tag{5.7}$$

The last two equations can be easily derived from $\rho_{\rm sp} = \rho_{\rm i}(r_{\rm sp})$ and $r_{\rm sp} = [(3-\gamma_{\rm sp})0.2^{3-\gamma_{\rm sp}}m_1/(2\pi\rho_{\rm sp})]^{1/3}$.

Consider now the inspiral between the central intermediate-mass black hole and a solar-mass compact object in a quasi-circular orbit within the compressed wave halo. The quasi-circular assumption is a good assumption in IMRI embedded in a dark matter spike [357]. The change of the orbital energy of the companion object given by

$$\boxed{\frac{dE_o}{dt} = -\left(\frac{dE_{\rm GW}}{dt}+\frac{dE_{\rm DF}}{dt}\right).} \tag{5.8}$$

This is the master equation describing the evolution of the system due to gravitational wave emission and dynamical friction exerted by the dark matter halo. Here

$$E_o = -\frac{Gm_1m_2}{2r} \tag{5.9}$$

is the orbital energy of the companion object, with r the distance between the objects. The first term of Eq. (5.8), $dE_{\rm GW}/dt$ represents the energy loss due to gravitational wave emission and it is given as [380]

$$\frac{dE_{\rm GW}}{dt} = \frac{32}{5G}(GM_c\pi f_{\rm GW})^{10/3}, \tag{5.10}$$

where the chirp mass $M_c = \mu^{3/5}M^{2/5}$ with the reduced mass $\mu = m_1m_2/(m_1+m_2)$ and the total mass $M = m_1+m_2$. The gravitational wave frequency is related to the

orbital frequency $f_o = v_c/(2\pi r)$ via

$$f_{\rm GW} = 2f_o = \frac{1}{\pi}\sqrt{\frac{GM}{r^3}}\,. \tag{5.11}$$

The second term $dE_{\rm DF}/dt$ is due to the friction induced by the dark matter halo, called dynamical friction and it is the contribution we are mostly interested in. The dynamical friction energy loss can be written as

$$\boxed{\frac{dE_{\rm DF}}{dt} \approx \frac{4\pi(Gm_2)^2\rho_{\rm f}(<v)}{v}C(v)\,,} \tag{5.12}$$

where $v = \sqrt{GM/r}$ is the circular velocity of the companion object and

$$\rho_{\rm f}(<v) = 4\pi\int_0^v dv' v'^2 f(v') \simeq 0.6\times\rho_{\rm f}(r)\,, \tag{5.13}$$

is the mass density of dark matter particles whose velocity is smaller than v. The numerical factor $\simeq 0.6$ depends on the spike power-law index $\gamma_{\rm sp}$. We study the origin and the underlying approximations more carefully in Appendix E.

The microscopic nature of dark matter affects both the density profile $\rho_{\rm f}(r)$ and the Coulomb logarithm factor $C(v)$. Therefore, it is this dynamical friction energy loss that can potentially allow us to probe the nature of dark matter. We are interested in how the dynamical friction changes the waveform of gravitational waves during five years of inspiral before the coalescence.

We compute the explicit form of the Coulomb logarithm factor $C(v)$ in Appendix E exploiting the approximation for which the C factor is assumed constant. Note that we evaluate C in the circular velocity, assuming that the velocity dispersion is negligible with respect to v, as it is the case since $\sigma^2 = v^2/(1+\gamma_{\rm sp}) < v$.

For the particle dark matter one finds [33, 42]

$$C_{\rm p}(v) = \frac{1+\Lambda}{\Lambda}\log\left[1+\Lambda+\sqrt{\Lambda(\Lambda+2)}\right] - \sqrt{1+\frac{2}{\Lambda}}\,. \tag{5.14}$$

The parameter Λ is given by

$$\Lambda = \frac{b_{\rm max}}{b_{90}} = \frac{v^2 r}{Gm_2}\,. \tag{5.15}$$

here $b_{\rm max}$ is the maximum impact parameter in the dark particle-object collision and $b_{90} = Gm_2/v^2$ is the impact parameter at which the encounter results in 90° deflection of the trajectory. In the limit $\Lambda \gg 1$, the above expression reproduces $C_{\rm p} \approx \log\Lambda$.

For the wave dark matter the Coulomb-logarithm factor becomes [33]

$$C_{\rm w}(kr) \approx {\rm cin}(2kr) - 1 + \frac{\sin(2kr)}{2kr}\,, \tag{5.16}$$

where $k = mv = 2\pi/\lambda_{\rm dB}$ is the wavenumber of dark matter. The cosine integral is defined as ${\rm cin}(z) = \int_0^z dt\,(1-\cos t)/t$. This expression is valid as long as the de

Broglie wavelength is larger than the b_{90}, so that the wave interference effects set a scale for the minimum impact parameter, in formulae, $b_{90}/\lambda_{\rm dB} \ll 1$. Since $r_{\rm 5yr}$, the orbital separation 5 years before coalesce is the largest radius we are interested in,

$$\frac{b_{90}}{\lambda_{\rm dB}} \sim \frac{Gm_2 m}{v} \sim 0.003 \left(\frac{m}{10^{-13}\,{\rm eV}}\right)\left(\frac{m_2}{M_\odot}\right)\left(\frac{10^4\,M_\odot}{m_1}\right)^{1/2}\left(\frac{r_{\rm 5yr}}{10^{-8}\,{\rm pc}}\right)^{1/2} . \quad (5.17)$$

We see that $b_{90}/\lambda_{\rm dB} \ll 1$ is always satisfied in our parameter space of interest. In the limit of large distances from the Bohr radius, $kr = \sqrt{r/a} \gg 1$, we have a Coulomb log-like expression $C_{\rm w} \sim \log 2kr$.

5.2.1 Backreaction

The orbit of the companion decays more rapidly as a consequence of dynamical friction. Consequently, the companion transfers energy into the halo, and when this energy is comparable to the gravitational binding energy, it could alter the density profile of the halo. The impact of this backreaction on the halo was first studied by Kavanagh et al [104] through numerical solutions of the kinetic equation. The study showed that when the mass ratio $q = m_2/m_1$ is on the order of 10^{-4} or larger, the injected energy on the dark matter spike becomes significant and greatly reduces the importance of dynamical friction. In this discussion we will refer to particle dark matter, as the implications for wave dark matter are the same.

To account for the backreaction effect without solving numerically the kinetic equation, a model was proposed as follows: if the energy loss through dynamical friction is greater than the gravitational binding energy of the halo at the radial position r where the companion object is located, the dark matter particles are heated, leading to a decrease in dark matter density and effectively stopping dynamical friction. Based on this, it is assumed that the maximum amount of energy that can be dissipated from the companion is limited by the kinetic energy stored in a halo shell of thickness Δr at r, which is approximately half of the corresponding gravitational binding energy. The maximum energy loss is then given by $\min(\Delta E_{\rm DF}, \Delta U/2)$, where ΔU is the gravitational binding energy of the halo shell

$$\Delta U = -\frac{-G[m_1 + M_{\rm dm}(<r)]}{r} \times 4\pi r^2 \Delta r\,, \quad (5.18)$$

with $M_{\rm dm}(<r) = 4\pi \int_0^r dr'\, r'^2 \rho(r')$ the enclosed mass. In other words, we replace the dynamical friction energy loss in Eq. (5.8) with

$$\frac{dE_{\rm DF}}{dt} \longrightarrow \frac{dE'_{\rm DF}}{dt} = \min\left(\frac{dE_{\rm DF}}{dt}, \frac{1}{2}\frac{dU}{dt}\right) \approx \frac{1}{1/\dot{E}_{\rm DF} + 2/\dot{U}}\,, \quad (5.19)$$

where the second expression represents the practical implementation of the model in our numerical analysis. The factor of two is due to the fact that we assume virialization, i.e. that half of the dark matter binding energy is sufficient kinetic energy to

evaporate the respective shell. Eq. (5.8) becomes

$$\frac{dE_o}{dt} = \frac{1}{2U'}\Big[- \dot{E}_{\rm DF}(E_o' + U') - \dot{E}_{\rm GW}U' + \sqrt{[\dot{E}_{\rm GW}U' + \dot{E}_{\rm DF}(E_o' + U')]^2 - 4\dot{E}_{\rm GW}U'\dot{E}_{\rm DF}E_o'}\Big] \tag{5.20}$$

with primes denoting $' \equiv d/dr$. We call this prescription the *improved shell model*.

We can observe the impact of the improved shell model prescription on the relative importance of the dynamical friction with respect to the gravitational wave emission energy loss and the binding energy. In the top panel of Figure 5.1 we show the ratio of the dynamical friction energy loss and half the binding energy of particle the dark matter shell for the three values of $m_1 = 10^3,\ 10^4,\ 10^5\ M_\odot$, keeping $m_2 = M_\odot$. The thick lines are for the improved shell model prescription, while thin lines without treating the backreaction. We only show lines in the range $r_{\rm ISCO}$ to $r_{\rm 5yr}$ for each case. We see that in the case in which the black hole is lightest the dynamical friction, as it is, is several orders of magnitude larger than the binding energy. Our model avoids that. For larger values m_1, this is less of an issue.

In the bottom panel of Figure 5.1, we show the ratio of the gravitational wave and dynamical friction energy loss to understand the importance of the two contributions of Eq. (5.8) at different radii. In every case, the gravitational wave emission dominates over the dynamical friction by several orders of magnitude. Without a proper treatment of backreaction, we would have a dominating dynamical friction for $r \sim r_{\rm 5yr}$ in the $m_1 = 10^3\ M_\odot$ case.

5.2.2 Discussions

In what follows, we discuss the limits of applicability of Eq. (5.8) and Eq. (5.12) and other possible effects that could potentially complicate the description of the system. The discussion about impact parameters and backreaction regard both particle and wave dark matter in the same way so we discuss the effect for particle dark matter only. Instead, the quasiparticle contribution and accretion are peculiar in the wave case. The reader not interested in these subtleties can already skip to Section 5.3.

Impact parameters and dynamical friction

Let us comment on the use of the classical Chandrasekhar [229–231] formula for the dynamical friction, Eq. (5.12). In the case of particle dark matter, $C \sim \log \frac{b_{\rm max}}{b_{\rm min}}$: this factor regularizes the infrared and ultraviolet logarithmic divergences due to the long-range nature of gravity. We explain the choices for the maximum and minimum impact parameters. $b_{\rm max} \approx \min(r, R)$ is intuitively determined by the fact that the system has a finite size R and for a central system of orbital size r, the encounters with $b \in [r, R]$ average to zero [46]. Instead, the UV cutoff $b_{\rm min} \approx \max(b_{90}, d)$ is determined by the maximum momentum exchange, corresponding to a 90 degree deflection of the trajectory $b_{90} = Gm_2/v^2$ or the finite size d of the scatterer m_2.

For the wave dark matter, the same arguments can be applied, with the de Broglie wavelength entering the expression of the Coulomb logarithm [33] as the smallest

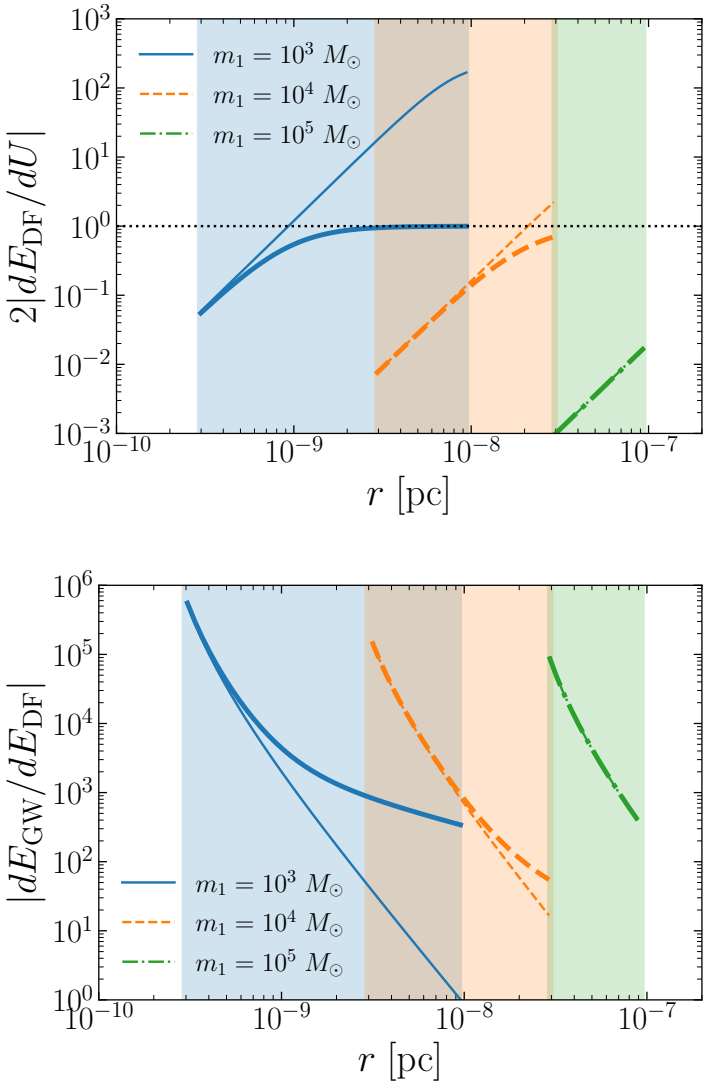

FIGURE 5.1: **Top**: the ratio of the dynamical friction energy loss in the dark matter shell and the gravitational binding energy of the same shell as a function of the $m_1 - m_2$ distance r. The thick lines take into account the backreaction according to the improved shell model, the thin lines do not. **Bottom**: same as above, but we show the ratio of the energy loss via gravitational wave emission and the dynamical friction. In both panels, a particle dark matter halo is assumed and the only parameter varying is the central black hole mass m_1, $m_2 = M_\odot$, $\rho_{\rm sp}$ and $r_{\rm sp}$ are found from this value. The bands show the radii between the ISCO and the distance between the objects 5 years before coalescence.

scale at which the dark matter responds to the test mass. Indeed, in the limit $b_{90} \ll \lambda_{\rm dB}$, we can use Eq. (5.16), which, in the limit $kr = \sqrt{r/a} \gg 1$, gives $C_{\rm w} \sim \log r/\lambda_{\rm dB}$, consistently with $b_{\rm max} = r$ and $b_{\rm min} = \lambda_{\rm dB}$. We notice that for our binary inspiral study we are always in the regime where $C_{\rm w} \sim \log r/\lambda_{\rm dB}$: the dark matter spike forms only for $r > R_c = a\ell_c(\ell_c + 1)$, because modes with $\ell < \ell_c$, that dominate at radii smaller than R_c, get absorbed in the black hole on a timescale less than 10 Gyr.

One has to bear in mind that the Chandrasekhar formula is strictly valid for an object traveling in an infinite homogeneous medium. However, it was found that the Chandrasekhar formula works well also in inhomogeneous medium [381, 382] up to a factor of two. We will therefore stick for its simplicity and reliability to this formula for the computation of dynamical friction.

A common approach in galactic astrophysics is to use the Coulomb logarithm, as a fitting parameter. This was done in [104], where various N-body simulations of the IMRI in a dark matter spike were performed, finding a dynamical friction roughly half of the one predicted by the Chandrasekhar formula. The authors explained this fact exploiting as $b_{\rm max}$ the radius of gravitational influence of m_2, which is smaller than r, i.e. $b_{\rm max} = \sqrt{m_2/m_1}r < r$. This choice, in the particle case, suppresses C by a factor of 2. However, it is not clear whether the smaller dynamical friction is due to a smaller maximum impact parameter or, rather, some other effects such as the self-gravity of the response to the wake caused by the orbiting object [381].

We show in Figure 5.2 that the results of [104] can be equally well fit by the following formula

$$\log \Lambda = \frac{1}{2} \log \frac{r}{\sqrt{b_{90}^2 + \epsilon^2}} \,, \tag{5.21}$$

with ϵ the softening length used in the N-body simulation, whereas in [104]

$$\log \Lambda = \log \frac{\sqrt{m_2/m_1}r}{\sqrt{b_{90}^2 + \epsilon^2/4}} \tag{5.22}$$

was used. Therefore, in our analysis, we stick to $b_{\rm max} = r$, in both particle and wave cases.

Backreaction: comparison with Kavanagh et al

Our model of backreaction reproduces the numerical result obtained by Kavanagh et al [104], as shown in Figure 5.3. To compare with the result of [104], we compute the number-of-cycles difference in the particle dark matter halo. This quantity measures effectively the phase difference in the gravitational waves emitted by the system assuming the presence of a particle dark matter halo or neglecting it, see Section 5.3. The number-of-cycles is defined as

$$N(f) = \int_f^{f_{\rm ISCO}} df' \, [(f'/\dot{f}')_{\rm p} - (f'/\dot{f}')_{\rm v}] \,. \tag{5.23}$$

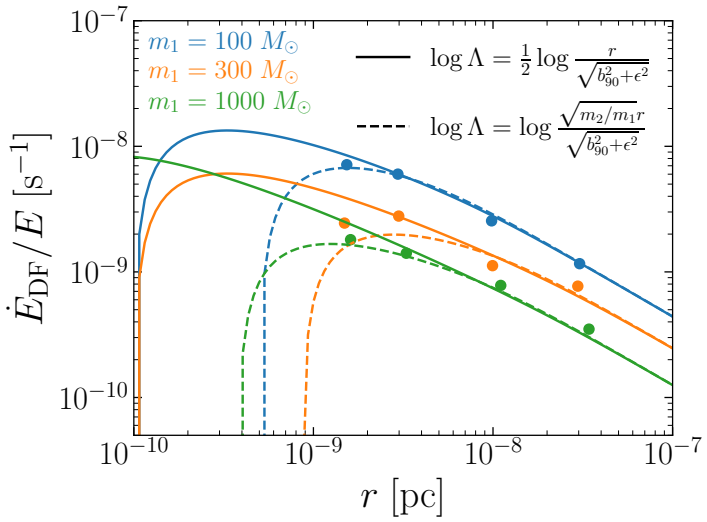

FIGURE 5.2: The dynamical friction energy loss normalized to orbital energy. The dots are the results from the N-body simulations in [104]. The solid lines are for our prescription of the Coulomb log times a factor of $1/2$ and the dashed lines are obtained with the prescription used in [104]. Different colors are for different values of m_1, all below the actual range of interest in our work.

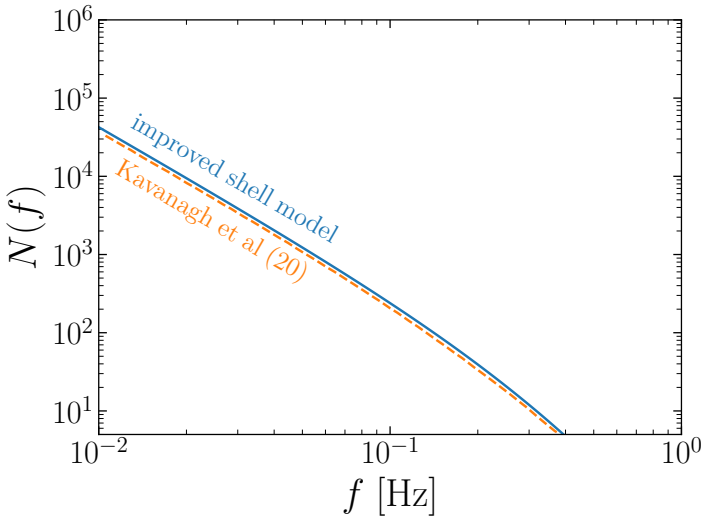

FIGURE 5.3: The difference in the number-of-cycles $N(f)$ between the cases with and without a particle dark matter halo, computed from the ISCO. The solid line is obtained from our analytical modeling (improved shell model) described in the main text, while the dashed line is the numerical result taken from [104]. For this figure, we choose $m_1 = 1400\ M_\odot$, $m_2 = 1.4\ M_\odot$, $\gamma_{\rm sp} = 7/3$ and $\rho_{\rm sp} = 226\ M_\odot/{\rm pc}^3$.

and corresponds to the gravitational wave phase difference $(\Phi_{\rm p} - \Phi_{\rm v})/(2\pi)$ as in Eq. (5.48). In the formula, f is the gravitational wave frequency, related to the separation r via Eq. (5.11). The change in frequency $\dot{f} = df/dt$ can be found trivially from

$$\frac{dr}{dt} = -\frac{r}{E_o}\frac{dE_o}{dt} \,. \tag{5.24}$$

with dE_o/dt given by Eq. (5.20). The subscripts "p" and "v" in Eq. (5.23) denote the evolution of gravitational wave frequencies with and without a particle dark matter halo, i.e. where Eq. (5.20) contains the friction term and the DM binding energy or just the gravitational wave energy loss factor, respectively.

Quasiparticle contributions and heating

Granular structures, which represent fluctuations of the gravitational potential, have been observed in numerical simulations of fuzzy dark matter [29]. These fluctuations of the wave dark matter halo can be described as quasiparticles with a size of the order of their de Broglie wavelength and a mass given by the mass enclosed within the de Broglie volume [33,46]. The kinetic energy imparted to stellar objects by these quasiparticles can be non-negligible, depending on their mass. As we shall see, we can have an additional contribution to dynamical friction, i.e. a cooling effect, for which quasiparticles absorb the energy of the compact object and also a stochastic heating of the orbiting body. Both effects can affect the orbital evolution of companion object and, therefore, potentially alter the gravitational wave emission of the binary system.

Let us compute the impact of the quasiparticles on the inspiral. We neglect the gravitational wave emission and focus on the compact object orbiting in the wave dark matter halo. The energy change of the compact object in the wave limit is given by the energy diffusion coefficient [46]

$$\frac{dE}{dt} = D[\Delta E] \,. \tag{5.25}$$

As shown in Appendix C.2, the energy diffusion coefficient is given by

$$D[\Delta E] = m_2 \left(v D[\Delta v_{\parallel}] + \frac{1}{2} D[(\Delta v)^2] \right) \,. \tag{5.26}$$

Adapting Eq. (C.69) and considering $m \ll m_2, m_{\rm eff}$, for wave dark matter, we have [46,47,355]

$$v D[\Delta v_{\parallel}] = -\frac{16\pi^2 G^2}{v} \log\Lambda \int_0^v dv'\, v'^2 \left[m_2 f(v') + m_{\rm eff} f_{\rm eff}(v') \right] \,, \tag{5.27}$$

and

$$\frac{1}{2} D[(\Delta v)^2] = 16\pi^2 G^2 m_{\rm eff} \log\Lambda \left\{ \int_0^v dv'\, \frac{v'^2}{v} f_{\rm eff}(v) + \int_v^\infty dv'\, v' f_{\rm eff}(v) \right\} \tag{5.28}$$

While the first term has negative sign, signaling it is the cooling term, i.e. dynamical friction, the second term is positive, hence is the heating term. In both terms we consider the ergodic spike distribution found from the Eddington formula from the simple spike profile Eq. (4.16), changing variables to velocity, $E = v'^2/2 + \Phi_{\rm f} = v^2/2 - v_e^2/2$, where $v_e^2 = 2Gm_1/r$ is the escape velocity from the central black hole,

$$f(v) = \frac{\rho_{\rm f}(r)}{[\pi v_e^2]^{3/2}} \frac{\Gamma(\gamma_{\rm sp}+1)}{\Gamma(\gamma_{\rm sp}-1/2)} \left[1-(v/v_e)^2\right]^{\gamma_{\rm sp}-3/2} . \tag{5.29}$$

and $m_{\rm eff}$ and $f_{\rm eff}$ are defined in Eq. (C.46) and Eq. (C.45).

Let us consider the first contribution $vD[\Delta v_{\parallel}]$. It consists of a term proportional to the compact object mass and a term proportional to the effective mass. Given that f and $f_{\rm eff}$ are of the same order, the importance of the second term, which we neglected in Eq. (5.12), is given by the ratio $m_{\rm eff}/m_2$. If $m_{\rm eff} \ll m_2$, then Eq. (5.27) reproduces Eq. (5.12) (except for some caveats about the C factor, see Appendix E). To see whether this approximation is justified, we have to compute $m_{\rm eff}$.

$$\begin{aligned} m_{\rm eff} &= \frac{(2\pi)^3}{m^3} \frac{\int_0^{v_e} dv'\, v'^2 f^2(v')}{\int_0^{v_e} dv'\, v'^2 f(v')} \\ &= \rho_{\rm f}(r) \left[\frac{\sqrt{2\pi}}{mv(r)}\right]^3 \left[\frac{\Gamma(\gamma_{\rm sp}+1)}{\Gamma(\gamma_{\rm sp}-1/2)}\right]^2 \frac{\Gamma(2\gamma_{\rm sp}-2)}{\Gamma(2\gamma_{\rm sp}-1/2)} . \end{aligned} \tag{5.30}$$

Note that, except the order-one factors depending on $\gamma_{\rm sp}$, the effective mass is approximately given by the dark matter mass in the de Broglie volume, with v the circular velocity around m_1. As it is clear from the expression, the quasiparticle mass increases as r decreases because both $\rho_{\rm f}$ and v increase, indicating that the quasiparticle mass would be the largest at the smallest radius we probe. This would naturally be the innermost stable circular orbit, $r_{\rm ISCO}$ but we check for $r = R_c = a\ell_c(\ell_c+1)$ which is the value for which the dark matter density profile gets suppressed because of the central black hole absorption. In Figure 5.4, we compute the mass of quasiparticle at the radius R_c. We see that the quasiparticle mass is always much smaller than m_2, therefore the quantum term in Eq. (5.27) is negligible and Eq. (5.12) is justified.

Now we come back to Eq. (5.28), the second term in the diffusion coefficient for the energy and which provides us stochastic heating of the companion object by the wave dark matter medium. The relative importance of this term with respect to the cooling term is again proportional to $m_{\rm eff}/m_2$ which we just proved to be very small on the scales and benchmarks of interest. We conclude that the stochastic heating is negligible for our discussion.

Accretion

Assuming a constant companion mass m_2 may not hold true in the case of a black hole companion, as it can potentially accrete mass from the surrounding dark matter halo. This can have significant effects on both the dynamical friction, $dE_{\rm DF}/dt \propto m_2^2$, and the gravitational wave emission, $dE_{\rm GW}/dt \propto m_2^2$. The rate at which the mass is

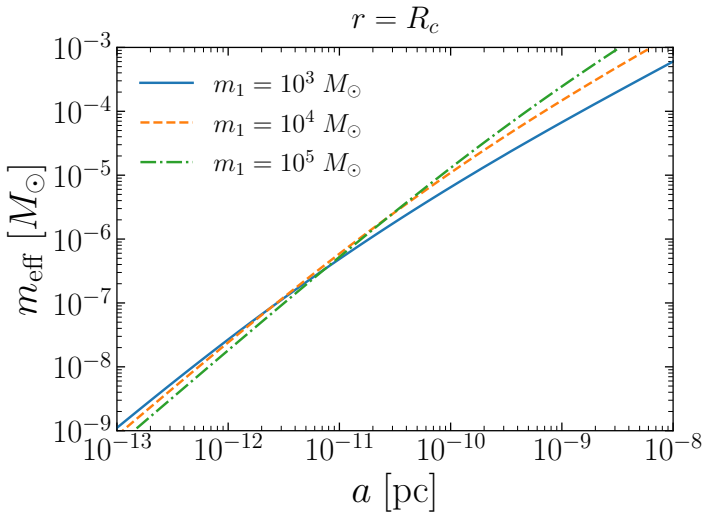

FIGURE 5.4: The effective mass of quasiparticles for each benchmark choice of the black hole mass. For all range of the gravitational Bohr radius, the effective mass is several orders of magnitude smaller than the companion mass.

accreted is given by

$$\frac{dm_2}{dt} = \rho_{\rm f}(\sigma_{\rm abs} v)\ , \tag{5.31}$$

where the absorption cross section $\sigma_{\rm abs}$ has been computed by Unruh [383]:

$$\begin{aligned} \sigma_{\rm abs} &= 16\pi (G m_2)^2 |\psi_v(0)|^2 = 16\pi (G m_2)^2 \left(\frac{2\pi\beta}{1-e^{-2\pi\beta}}\right) \\ &= 16\pi (G m_2)^2 \times \begin{cases} 1 & 2\pi\beta \lesssim 1 \\ 2\pi\beta & 2\pi\beta \gtrsim 1 \end{cases} . \end{aligned} \tag{5.32}$$

Here $|\psi_v(0)|^2$ is the wavefunction at the position of the companion object, i.e. the Sommerfeld enhancement factor of Eq. (3.29). Here $\beta = G m_2 m / v$, so the behavior depends on the velocity v, whether it is larger or smaller than the critical value $v_{\rm cr}$

$$v_{\rm cr} = 0.004 \times \left(\frac{m_2}{M_\odot}\right) \left(\frac{m}{10^{-13}\ {\rm eV}}\right) . \tag{5.33}$$

The circular velocity for $r < r_{\rm 5yr}$ is larger than the critical value for all the central black hole masses $m_1 > 10^3\ M_\odot$, therefore we are always in the regime for which

$$\frac{dm_2}{dt} \approx 16\pi (G m_2)^2 \rho_{\rm f}(r)\ . \tag{5.34}$$

The total value of the accreted dark matter mass will depend on the inspiralling pattern: since the density drastically increases as the companion gets closer to the central black hole, the crucial information to estimate the total accretion is dr/dt, which is given taking into account the gravitational wave and dynamical friction energy losses through Eq. (5.8), i.e. $dE_o/dt = -E_o/r \times dr/dt$. We therefore need

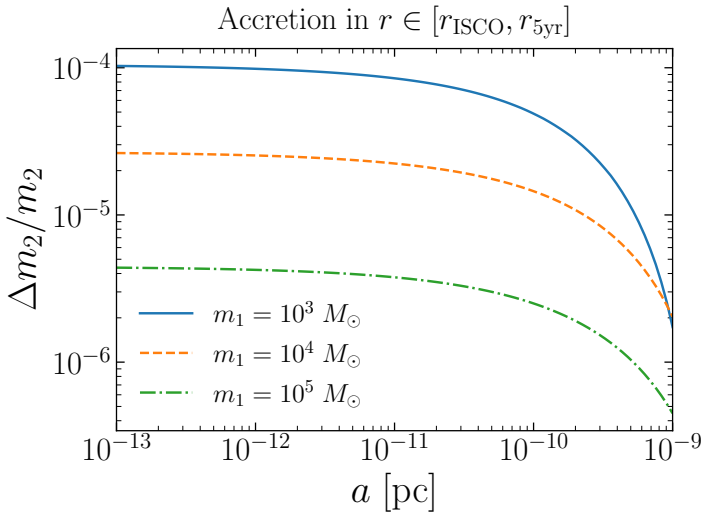

FIGURE 5.5: The accreted wave dark matter mass by the companion object m_2 in the inspiral between the distance 5 years before coalescence $r_{\rm 5yr}$ and the innermost stable circular orbit $r_{\rm ISCO}$ if it is a black hole. We see that for the parameter space under consideration, the accreted mass is safely several orders of magnitude smaller than m_2 .

to check numerically if $\Delta m_2/m_2 \ll 1$ over five years before the coalescence. We compute

$$\Delta m_2 = \int_{r_{\rm 5yr}}^{r_{\rm ISCO}} dr \frac{dm_2}{dt} \left[\frac{dr}{dt}\right]^{-1} . \tag{5.35}$$

We find that $\Delta m_2/m_2 \sim \mathcal{O}(10^{-4})$ in the parameter space under consideration, as shown in Figure 5.5. More detailed analyses can be found in [384, 385], where the dynamical friction and the accretion effect are derived in a consistent framework.

5.3 Dephasing of Gravitational Waves

In this Section, we investigate how the dynamical friction from the compressed halo affects the waveform of the emitted gravitational waves (GW).

We refer to Appendix F for the explicit computation of the waveform. The detector output without noise is $h(f) = F_+ h_+(f) + F_\times h_\times(f)$, where $F_{+,\times}$ are the detector pattern functions and $h_{+,\times}$ are the strains for each polarization state. For simplicity, we consider the strain averaged over the sky position, polarization, and inclination angle. We then obtain [386]

$$h(f) = \sqrt{\frac{4}{5}} A(f) e^{i\Psi(f)} , \tag{5.36}$$

with amplitude and strain given by

$$A(f) = \frac{2}{D_L}\frac{(GM_c)^{5/3}(\pi f)^{2/3}}{\dot{f}^{1/2}}\,, \tag{5.37}$$

$$\Psi(f) = 2\pi[t_0 + t(f)] - \Phi_0 - \Phi(f)\,, \tag{5.38}$$

where D_L is the luminosity distance of the event, t_0 and Φ_0 are some reference time and constant phase factor, and

$$t(f) = \int^f df'\,(1/\dot{f}')\,, \tag{5.39}$$

$$\Phi(f) = 2\pi\int^f df'\,(f'/\dot{f}')\,. \tag{5.40}$$

The phase Φ here is the key quantity to study the contribution due to dynamical friction, as it enters the time evolution of the GW frequency, which depends on the energy loss formula Eq. (5.8), that contains the dark-matter-dependent dynamical friction contribution Eq. (5.12).

Vacuum

If there is no dark matter, $\dot{E}_o = -\dot{E}_{\rm GW}$ and we obtain the compact expression

$$\left.\frac{\dot{f}}{f}\right|_{\rm v} = \frac{96}{5}(GM_c)^{5/3}(\pi f)^{8/3}\,, \tag{5.41}$$

from which we can obtain the time and phase referred to coalescence (t_0, Φ_0):

$$t_{\rm v}(f) = -\frac{5}{8\pi f}(8\pi G M_c f)^{-5/3}\,, \tag{5.42}$$

$$\Phi_{\rm v}(f) = -2(8\pi G M_c f)^{-5/3}\,. \tag{5.43}$$

Since the energy loss via gravitational wave emission largely dominates the dynamics of the system, the time to coalescence will not depend strongly on the dark matter profile around the black hole. Thanks to this, we can find a formula for the orbital distance five years before the coalescence $r_{5\rm yr}$.

We first find the frequency $f_{5\rm yr}$ of the GW emitted when m_1 and m_2 are separated by the distance $r_{5\rm yr}$; assuming $f(t_0) \gg f_{5\rm yr}$, we get

$$f_{5\rm yr} \approx \frac{1}{8\pi G M_c}\left(\frac{GM_c}{\rm yr}\right)^{3/8} \tag{5.44}$$

and using Eq. (5.11),

$$r_{5\rm yr} \approx 4{\rm yr}^{1/4}(GM)^{1/3}(GM_c)^{5/12} \tag{5.45}$$

$$\simeq 3\times 10^{-8}\,{\rm pc}\left(\frac{m_2}{M_\odot}\right)^{1/4}\left(\frac{m_1}{10^4\,M_\odot}\right)^{1/2}\,, \tag{5.46}$$

where in the last line we assume $m_1 \gg m_2$. We see that as long as the hierarchy between m_1 and m_2 is huge, the 5 years distance depends only weakly on both m_1

and m_2. Using Eq. (5.11), we deduce that the above values of $r_{5\mathrm{yr}}$ corresponds to the GW frequency

$$f_{5\mathrm{yr}} = \frac{1}{\pi}\sqrt{\frac{GM}{r_{5\mathrm{yr}}^3}} \simeq 0.01\ \mathrm{Hz}\left(\frac{m_1}{10^4\ M_\odot}\right)^{-1/4}\left(\frac{m_2}{M_\odot}\right)^{-3/4}. \tag{5.47}$$

The weak dependence of $f_{5\mathrm{yr}}$ on m_1 and m_2 in the case $m_1 \gg m_2$, that is characteristic of the IMRIs, has very important consequences.

Remember that the dynamical friction is most important, compared to the GW emission energy loss only when the sources are further away (see the bottom panel of Figure 5.1 for a comparison of the GW and friction contributions): this implies that the frequency band close to $f_{5\mathrm{yr}}$ is the most sensitive to the presence and the nature of dark matter. This frequency being around 0.01 Hz makes LISA [110] the ideal detector to target this effect in IMRIs; future detectors, sensitive to higher frequency GW such as the Einstein Telescope [380] will be able to detect the final phase of the coalescence and the merger, which are by many orders of magnitude dominated by energy loss via the GW emission, which is an in-vacuum effect, not due to the DM compressed halo. On the other hand, detectors sensitive to slightly lower frequencies, in the milli-Hz could be relevant for inspirals with $m_1 \gg 10^5 M_\odot$, but they would imply a much longer observation time. We will focus on the case of LISA for simplicity.

Dark matter

Since the dynamical friction modifies the gravitational wave frequency evolution through Eq (5.8), it affects the waveform by changing the amplitude $A(f)$ and, most importantly, the phase $\Psi(f)$.

The effect on the amplitude $A(f)$ is found to be small. When considering the inspiral's evolution several years before coalescence, as shown in the bottom panel of Figure 5.1, we have demonstrated that the orbital energy loss from dynamical friction is less significant than the energy loss due to gravitational wave emission. This means that the frequency evolution $\dot{f}/f$ is dominated by the gravitational wave emission, and thus, the gravitational wave energy loss dominates $A(f)$ at leading order. The role of dynamical friction in determining $A(f)$ is therefore sub-leading.

However, the phase can be considerably altered by dynamical friction as it accumulates over time. To illustrate this, we compute the phase difference between the gravitational waves from the black hole binary with and without the dynamical friction from the compressed halo

$$\Phi - \Phi_{\mathrm{v}} = 2\pi \int_f^{f_{\mathrm{ISCO}}} df' \left[(f'/\dot{f}') - (f'/\dot{f}')_{\mathrm{v}}\right], \tag{5.48}$$

where $(f/\dot{f})_{\mathrm{v}}$ is the gravitational wave frequency evolution without the dynamical friction, i.e. Eq. (5.41). The phase difference, or dephasing, for the particle halo and wave halo with respect to the vacuum case is presented in the top panel of Figure 5.6. It is observed that the phase difference can accumulate over several years to become much larger than unity by many orders of magnitude.

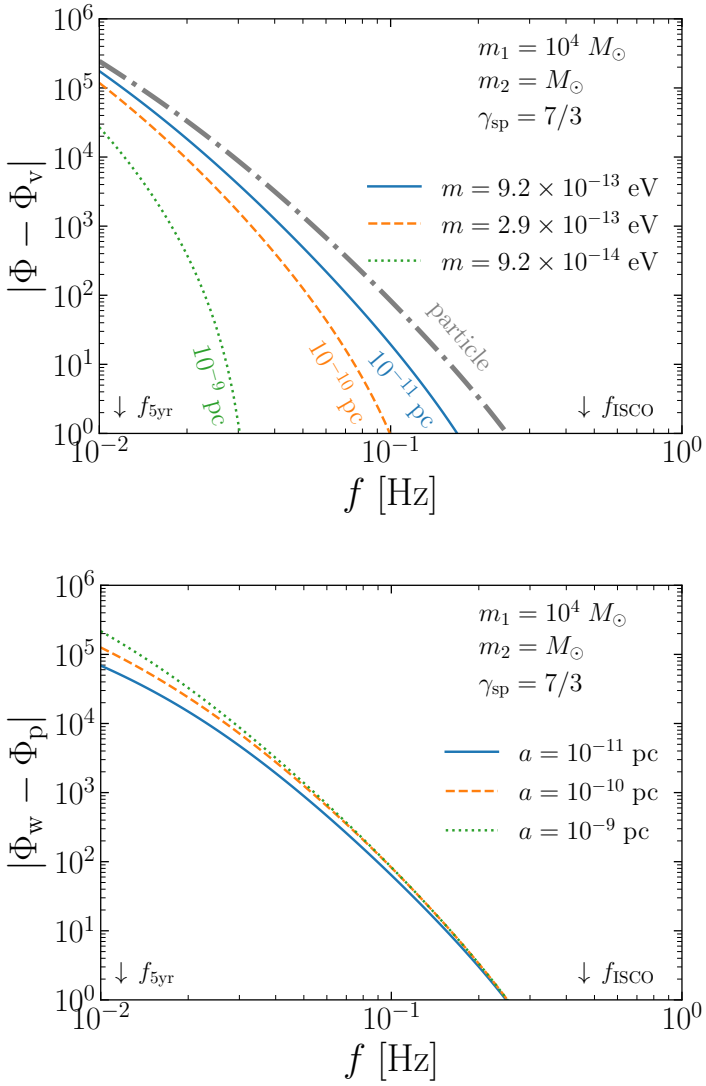

FIGURE 5.6: **Top**: the dephasing of gravitational waves emitted by the IMRI in a compressed dark matter halo with respect to those without compressed halo. The gray thick line represent the result from the particle dark matter halo. The blue solid, orange dashed, and green dotted lines are the results from wave halos with the Bohr radii $a = 10^{-11}, 10^{-10}, 10^{-9}$ pc, respectively. We also show the particle mass for each line. **Bottom**: the phase difference of gravitational waves emitted by the IMRI embedded in a wave dark matter spike and in a particle dark matter halo. The color and linestyle code is the same in both figures. Here $f_{\rm 5yr}$ denotes the frequency of gravitational waves five years before the coalescence.

In the bottom panel of Figure 5.6, we demonstrate the phase difference between gravitational waves from the wave halo and the particle halo

$$\Phi_{\rm w} - \Phi_{\rm p} = 2\pi \int_f^{f_{\rm ISCO}} df' \left[(f'/\dot{f}')_{\rm w} - (f'/\dot{f}')_{\rm p} \right] . \tag{5.49}$$

The selected Bohr radii lead to a significant phase difference, primarily due to the variations in the density profile and Coulomb logarithm factor as in Eq. 5.12.

5.4 Statistical analysis

Two natural questions arise: (i) does the phase difference in the emitted gravitational waves that we studied in the previous Section allow us to reconstruct the compressed wave halo parameters, such as the Bohr radius or the wave dark matter mass? (ii) are we able to distinguish the wave dark matter spike from the particle dark matter compressed halo? To answer these questions, we need to perform a proper statistical analysis by means of a matched filtering technique with the sensitivity of LISA [110].

5.4.1 Parameter estimation

Let us start from the first question, by performing a parameter estimation, to understand up to which confidence level we can detect a wave dark matter spike and reconstruct the parameters of the binary and the halo.

There are 5 parameters of interest related to the system:

$$\theta = \{M_c, q, \rho_6, \gamma_{\rm sp}, a\} , \tag{5.50}$$

where $M_c = (m_1 m_2)^{3/5}/(m_1+m_2)^{1/5}$ is the chirp mass, $q = m_2/m_1$ is the mass ratio, $\gamma_{\rm sp}$ is the power law index of the compressed halo profile and a is the gravitational Bohr radius. Instead of $\rho_{\rm sp}$, we use the density at $r_6 = 10^{-6}$ pc and $\rho_6 = \rho_{\rm sp}(r_{\rm sp}/r_6)^{\gamma_{\rm sp}}$ following [105]. There are three more parameters in the waveform $\theta_c = \{D_L, t_0, \Phi_0\}$, called *extrinsic parameters*, but for the parameter estimation we maximize the likelihood with respect to these parameters in order to reduce the computational cost.

The detector output is $d(t) = h(t) + n(t)$ where $h(t)$ is the gravitational wave strain, see Eq. (5.36), and $n(t)$ is the Gaussian detector noise. Under the Gaussian noise assumption, the likelihood function is

$$\mathcal{L}(\theta, \theta_c) = \mathcal{N} \exp\left[-\frac{1}{2}(d-h|d-h) \right] , \tag{5.51}$$

where $\mathcal{N}$ is the normalization constant. The inner product $(a|b)$ is defined as

$$(a|b) = {\rm Re} \int_{-\infty}^{\infty} df \frac{a^\star(f) b(f)}{\frac{1}{2} S_n(f)} . \tag{5.52}$$

	M_c [$M_\odot$]	q	ρ_6 [$10^{15} M_\odot/\mathrm{pc}^3$]	$\gamma_{\rm sp}$	a [pc]	D_L [Mpc]
$\theta_{\rm true}$	39.8	10^{-4}	25	7/3	10^{-11}	203

TABLE 5.1: Benchmark values for the wave dark matter spike for the parameter estimation.

Here $S_n(f)$ is the noise power spectral density defined as

$$\langle n^\star(f') n(f) \rangle = \frac{1}{2} \delta(f - f') S_n(f) \,. \tag{5.53}$$

For the LISA sensitivity, we use the $S_n(f)$ provided in Robson et al [386].

We maximize the likelihood $\mathcal{L}(\theta, \theta_c)$ over the extrinsic parameters θ_c. The maximization over D_L can be done analytically. We obtain

$$\mathcal{L}(\theta, t_0, \Phi_0) = \exp\left[\frac{(d|h)^2}{2(h|h)}\right] . \tag{5.54}$$

Notice that the signal to noise ratio

$$\mathrm{SNR} = \sqrt{(h|h)} \tag{5.55}$$

is independent on t_0 and Φ_0 since these quantities only appear in the phase Ψ of $h(f)$. Therefore we need to maximize $(d|h)$ only. For Φ_0 it is enough to replace the real part selection in the definition of the inner product with an absolute value because the phase maximizing the scalar product will be the one such that the projection to the real axis is exactly the absolute value of the complex number. Instead, for t_0, since $(d|h)$ is an inverse Fourier transform as a function of t_0, we can just maximize over t_0 effectively taking the maximum value. After these steps, the log-likelihood becomes [387]

$$\log \mathcal{L} = \frac{2 \max_{t_0} \left| \int_0^\infty df \, e^{2\pi i f t_0} h^\star(f) d(f) / S_n(f) \right|^2}{\int_0^\infty df \, |h(f)|^2 / S_n(f)} \,. \tag{5.56}$$

Here the waveform should be understood as $h(f;\theta) = h(f;\theta)|_{\Phi_0=0,\, t_0=0}$. The quantity in the numerator is indeed the maximum of the Fourier transform of $h^\star d / S_n$.

For the parameter estimation, we inject the signal according to the compressed wave dark matter halo, while ignoring the detector noise, i.e. we set $d = h(\theta_{\rm true})$ with $\theta_{\rm true}$ given by the benchmark values in Table 5.1. In terms of black hole masses, the chosen $\theta_{\rm true}$ corresponds to $m_1 = 10^4\ M_\odot$ and $m_2 = M_\odot$. The density ρ_6 is obtained from the benchmark halo in Eq. (5.1) with parameters given in Table 4.1 and $m_1 = 10^4\ M_\odot$. We assume that LISA measures the last five years of inspiral before the coalescence. Therefore we impose a lower bound on the frequency integration in the log-likelihood Eq. (5.56) $f_{\rm lower} = f_{\rm 5yr}$. The upper bound is chosen to be $f_{\rm upper} = \min(1\ \mathrm{Hz}, f_{\rm ISCO})$, with $f_{\rm ISCO}$ the frequency of the gravitational wave at the innermost stable circular orbit $r_{\rm ISCO} = 6 G m_1$. For the numerical sampling of the posterior distribution, we use the publicly available nested sampler `dynesty` [388]. The benchmark in Table 5.1 has D_L chosen such that the signal-to-noise ratio is SNR $\simeq 15$.

Figure 5.7 displays the 1D and 2D marginalized posterior distribution of the wave dark halo in the benchmark scenario. The 1D marginalized distribution of certain parameters such as the chirp mass (M_c), mass ratio (q), and Bohr radius (a) exhibit resolved peaks near the true value with relatively small errors. However, the posterior distribution for this scenario does not provide strong information on the other two parameters, ρ_6 and $\gamma_{\rm sp}$. We also observe strong degeneracy among parameters, such as between ρ_6 and $\gamma_{\rm sp}$, and between ρ_6 and $\log_{10} q$. These parametric degeneracies can be understood looking at the form of the density profile in the dynamical friction term.

From this likelihood analysis and Figure 5.7, we see that the compressed wave halo chosen as a benchmark can be successfully reconstructed with five years of gravitational wave observations before the coalescence. The value of the wave dark matter mass that corresponds to the gravitational Bohr radius of $a = 10^{-11}$pc is $m \simeq 10^{-13}$ eV. The implication is that we are able to both detect the wave dark matter spike and also have a strong, and model-independent, hint on the value of the wave dark matter mass from the gravitational waves emitted by the IMRI.

5.4.2 Distinguishing the wave spike from the particle spike

We move on to answering the second question quantitatively. For which regions of the parameter space we can successfully distinguish the wave dark matter spike from the particle one? The qualitative answer can be guessed from the behavior of the wave spike density profile varying the Bohr radius, see Figure 4.10. If the Bohr radius is too small the density profile of the wave and the particle are very similar so the only difference between the two scenario is the Coulomb log factor C. On the other hand, if the Bohr radius is larger, the density profile is suppressed and the effect of dynamical friction might be not enough to even detect the spike.

The quantitative answer relies on a Bayesian analysis. We compute the Bayes factor to see if the gravitational waves from wave halo can be distinguished from those of a particle halo. The Bayes factor is defined as

$$B(d) = \frac{Z_{\rm w}(d)}{Z_{\rm p}(d)} \,, \tag{5.57}$$

where the evidence Z_i is given by

$$Z_i = \int d\theta \mathcal{L}_i(\theta)\pi_i(\theta) \,, \tag{5.58}$$

and $i = {\rm w}, {\rm p}$, representing the wave and the particle spike models, respectively. Here $\pi_i(\theta)$ is the prior on the parameters. Since we are integrating over the parameters, the choice of this prior is crucial.

To compute the evidence, we inject the signal according to a wave dark matter halo, and compute the evidence with the wave halo model and also with the particle halo model. For the Bayes factor computation, we choose three benchmarks, labeled B1, B2 and B3 and shown in Table 5.2.

B1 corresponds to $m_1 = 1400\ M_\odot$ and $m_2 = 1.4 M_\odot$, as in [105], while B3 corresponds to $m_1 = 10^5\ M_\odot$ and $m_2 = M_\odot$. B2 is the same as the one considered for

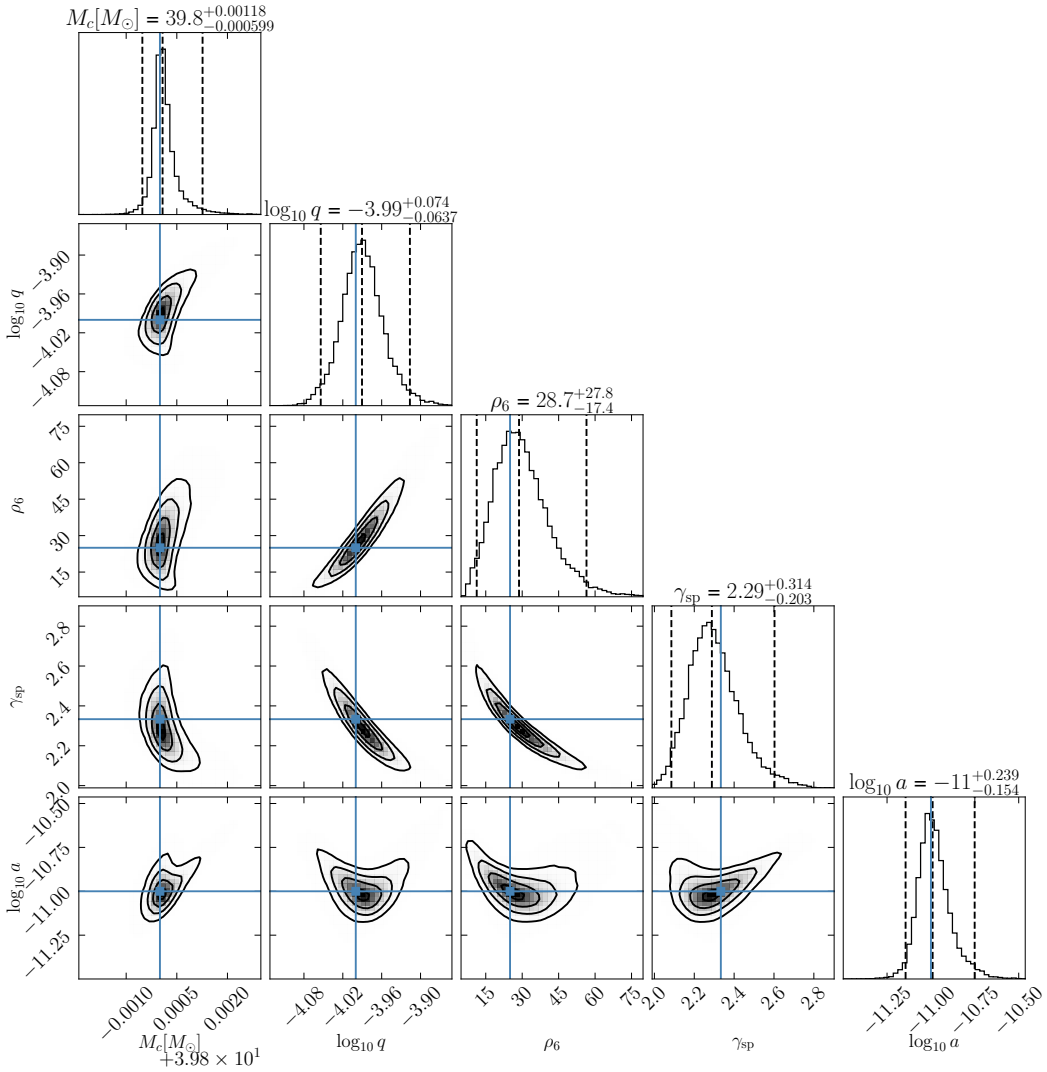

FIGURE 5.7: Posterior distribution for an IMRI within the compressed wave halo. The signal-to-noise ratio is SNR $\simeq$ 15. The numbers quoted in the panel titles of the corner plot on the top of the 1D histograms represents 2.5% and 97.5% quantiles; the contours in the 2D histograms represent 0.5, 1, 1.5, 2σ levels. The compressed wave halo can be successfully reconstructed with five years of gravitational wave observations before the coalescence. The value of the wave dark matter mass that corresponds to $a = 10^{-11}$pc is $m \simeq 10^{-13}$ eV.

	M_c [$M_\odot$]	q	ρ_6 [$10^{15} M_\odot/\mathrm{pc}^3$]	$\gamma_{\rm sp}$	D_L [Mpc]
B1	22.2	10^{-3}	6.8	7/3	83
B2	39.8	10^{-4}	25	7/3	203
B3	100	10^{-5}	120	7/3	750

TABLE 5.2: Benchmark scenarios for the evidence computation.

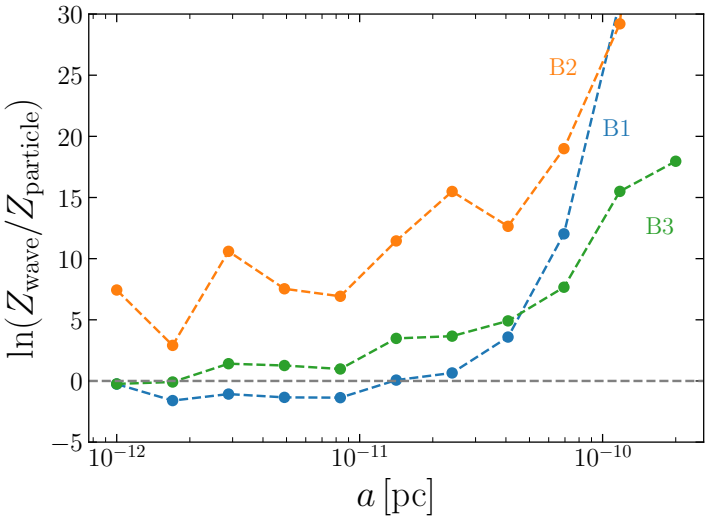

FIGURE 5.8: The difference of the log-evidence between the wave and the particle halo models, when the input is generated according to a black hole binary in a compressed wave dark matter halo. We consider the benchmark scenarios listed in Table 5.2.

the parameter estimation, see Table 5.1. We do not set a value for the Bohr radius for each benchmark because we scan $a \in [10^{-12}, 2\times10^{-10}]$ pc, as it is what determines the difference between particle and wave density profile. For all the benchmarks we set the prior range as $M_c/M_\odot = M_{c,\rm true}/M_\odot \pm 10^{-2}$, $\log_{10} q = \log_{10} q_{\rm true} \pm 0.5$, $\gamma_{\rm sp} \in [2.25, 2.5]$ and $\log_{10}(a/\text{pc}) \in [-13, -9]$. For ρ_6 we choose $\rho_6/(10^{15} M_\odot/\text{pc}^3) \in [0, 20]$, $[0, 100]$, $[0, 500]$ for B1, B2, B3, respectively. Notice that all our models include the vacuum case, for which $\rho_6 = 0$.

The Bayes factor is shown in Figure 5.8. In all cases, if the Bohr radius is sufficiently small, the log-Bayes factor approaches zero. This means that even though the data is generated according to the wave model, the particle halo can still fit the data. This is because, as expected, the wave density profile becomes similar to that of the particle halo for small Bohr radius. Although there will always be some difference due to the Coulomb logarithm, it is not significant enough to distinguish between the wave and particle halos. However, as the gravitational Bohr radius increases, the log-Bayes factor increases as well, indicating a preference for the wave model over the particle model. Specifically, for B2, the log-Bayes factor reaches values of around $\mathcal{O}(1)$ at relatively small Bohr radius, roughly few $\times\, 10^{-12}$ pc. This suggests that the most promising physics scenarios for identifying the wave nature of dark matter from gravitational wave observations occur at benchmark values similar to those of B2. This is important, because the fact that the log-Bayes factor increases at large values of a, and so the wave spike becomes distinguishable from the particle one, can be due to the fact that the density profile is more and more suppressed, and then similar to vacuum. Therefore, a large log-Bayes factor may not be directly associated with a prominent detection of a wave spike halo. For B2 instead, the log-Bayes factor is large enough also at relatively small Bohr radii and as we saw in the parameter estimation Section, the wave spike can be distinguished from the vacuum at 2σ (see Figure 5.7 for the reconstruction of the ρ_6 and a parameters).

5.5 Summary and conclusions

After the discussion about the adiabatic compression of wave dark matter in Chapter 4, we explored an exciting astrophysical application involving the detection of gravitational waves from intermediate mass-ratio inspirals.

After reviewing the present knowledge about intermediate mass black holes and binaries in Section 5.1, we studied the intermediate mass ratio inspiral of a binary embedded in a compressed dark matter halo. In the presence of compressed wave dark matter, the inspiral experiences energy loss through dynamical friction. This is an additional dissipation effect with respect to the sole energy loss via GW emission, as shown in Eq. (5.8).

We study in detail this effect in Section 5.2 with the aid of the additional material in Appendix E. We arrived to a simple description of dynamical friction by means of Eq. (5.12) that encodes the nature of dark matter through the density profile, studied in Section 4.2 and the C factor, carefully detailed in Appendix E. By analyzing the density and Coulomb logarithm factor in the dynamical friction term, we found that the companion object experiences a distinctive drag force from the wave halo, compared to what it would experience in a particle halo.

It is important to notice that, for the cases under consideration, the feedback of the inspiral on the compressed dark matter halo, both in the particle and wave case, has to be taken into account. In Section 5.2.1 we use a simple analytical model based on an upper bound on the dynamical friction imposed by the realistic condition that dynamical friction is bounded from above by the gravitational binding energy of the halo, since particle excited by the inspirals cannot contribute to the drag forc.

The simple formula of Eq. (5.8), with the backreaction prescription, needs further discussions. First of all, Eq. (5.8) neglects some effects which can be relevant in different regimes, such as cooling and heating by the granules, or quasiparticles, that characterize wave dark matter with large de Broglie wavelengths. We carefully check that these effects are negligible in the cases under consideration and that the dynamical friction Eq. (5.12) is the dominant contribution that depends on the nature of dark matter. Another possible phenomenon that can occur during the IMRI inside a dark matter halo and spoil the simple description via Eq. (5.8), is the accretion of dark matter by the companion object in the case it is a black hole: we check that accretion is not relevant in the parameter space under examination.

In Section 5.3, with details in Appendix F, we derived the waveform of the gravitational waves emitted by the IMRI and we studied the dephasing of gravitational wave signals which tells us how the wave dark matter spike can be detected through observations. In Section 5.4, we performed a likelihood analysis with matched filtering technique in order to understand how much information about the binary and the dark matter we can extract via the observation of gravitational waves. We demonstrated that the wave halo can be reconstructed through future LISA mission observations, for certain benchmark values, and can be distinguished from the particle halo. This presents an intriguing opportunity to explore the microscopic nature of dark matter.

While we focused on the wave halo in this study, it would be worthwhile to investigate other types of particle dark matter, such as self-interacting dark matter or

degenerate fermionic dark matter, which can form cored profiles and predict unique Coulomb logarithm factors for dynamical friction. Such studies could potentially reveal new insights into the properties of dark matter and its behavior in astrophysical systems.

Conclusion and Outlook

From the phenomenological point of view, the idea that dark matter exhibits wave features on astrophysical scales is intriguing [21,33]. A significant portion of the dark matter mass spectrum is populated by light bosons with a macroscopic, and perhaps even astronomical-sized, de Broglie wavelength and large occupation numbers in phase space. As a result, dark matter exhibits wave properties such as interference effects, oscillation patterns, granularity, and order-one density fluctuations that can potentially be observed in astrophysical systems through the gravitational interaction, which is currently the only known interaction between visible and dark matter.

In cases where dark matter does not interact with standard model particles via any other means than gravity, wave signatures could offer valuable information on the mass of these elusive particles. Astrophysical observations play a critical role in the study of wave dark matter due to (i) the enormous range of length scales involved, which allows us to explore a wide range of particle masses, and (ii) the diversity of environmental settings in which the dark matter phase space distribution can be peculiarly distorted to produce an observational signature (e.g. higher density, higher or lower velocities, and dispersion). It is clear that investigating the wave-like properties of dark matter offers an exciting avenue for exploring the mysteries of the universe.

In this thesis, we investigated the phenomenology of dark matter based only on the minimal assumptions that it is constituted by ultra-light bosons with mass in the right ballpark to produce wave effects on the studied systems. In particular, we considered the behavior of wave dark matter under the gravitational influence of a massive body. We developed a formalism to describe the response of wave dark matter to an external gravitational potential, both in the solar system [106] and in the case of a self-gravitating dark matter halo undergoing adiabatic compression [107] due to the growth of a central black hole or the gravitational collapse of a large gas cloud. In the solar system, we predicted distortions in the local density and spectrum of wave dark matter, which could be of interest for direct detection. In the case of a compressed wave halo, we proposed an intriguing idea to gain some hints on the microscopic nature of dark matter. An intermediate mass ratio inspiral, i.e. a binary composed of a central black hole and a compact companion, can probe the inner part of a compressed wave halo, where the dark matter density is sufficiently high to exert a significant dynamical friction force on the inspiralling object. This dragging effect is dependent on the wave nature of dark matter. It could be detected by studying the gravitational waves emitted by the binary. In fact, we derived the dephasing with respect to the case in which a compressed halo is absent, or the dark matter lacks wave properties.

Below, we synthesize the main results of this work and we discuss possible future research directions.

Chapter 1 provided a comprehensive overview of dark matter, setting the stage for our investigations into its potential wave nature in Chapter 2. We briefly described several compelling particle physics models that predict the existence of ultralight bosons capable of exhibiting wave properties. An important feature of such candidates is their stochastic nature: in Section 2.3 we provide a formalism to describe the wave dark matter as a linear superposition of wave mode functions with complex amplitudes drawn from a known probability distribution. The knowledge of the density matrix and the high occupation number, which allowed to neglect the non-commutativity of the field, led us to a compact description of the wave dark matter field, exploited in concrete physical applications [106, 107].

While the complex coefficients describe the stochasticity of the field, the wave functions contain the response of the wave dark matter to gravity. In the next sections, we reviewed the interplay between the wave dark matter and gravity described via the Schrödinger-Poisson system [33] and discussed the main phenomenological consequences, such as the existence of a stable ground state, known as soliton, and the process of relaxation, or gravitational cooling [219, 389–391], which leads to the formation of a core in the center of dark matter halos, confirmed by numerical simulations [29, 108, 219, 346]. These concepts are the main theoretical background for this thesis. We concluded by summarizing observational constraints and the status of experimental searches of ultra-light dark matter.

In Chapter 3, we investigated the phenomenon of gravitational focusing i.e. the deformation of the dark matter distribution by the gravitational field of a massive object traveling inside the dark matter medium. In particular, gravity distorts the dark matter phase space leading to an overdensity tail behind the massive body. While already known in literature as the reason for the dynamical friction force on an object moving in a homogeneous medium of massive particles [229–231], this focusing effect was so far only studied for particle dark matter [68, 99] or in regimes in which the dark matter wavelength was negligible [213]. Therefore we studied for the first time the impact of the wave dark matter nature in the focusing effect, finding different features in both the overdensity field and the power spectrum. We also successfully retrieved the particle results in the large distance, or small de Broglie wavelength limit.

As an application, we focused on the local dark matter and the distortions caused by the Sun. We extended the analysis to any possible component of the local dark matter, including the virialized halo component as well as substructures such as the so-called Gaia sausage [56, 57], a dark disk component [64, 337–340], and dark streams [63]. Those are all well-motivated by the recent observation of specific kinematic features in the Milky Way stars [57, 63] under the reasonable assumption that the dark matter shares the same phase-space properties of these stars [58, 59]. The phenomenon of focusing is particularly relevant for "slow" dark matter particles and the wave features are most apparent in cold structures, where the small-wavelength oscillations are not "washed away" by a large velocity dispersion. Therefore, despite

constituting just a few percent or more of the local dark matter, some prograde dark matter streams could give us valuable information about the nature of the dark matter. It warrants further investigation to develop a map of all the dark matter substructures in the solar neighborhood to see which ones are the most promising for wave dark matter detection. Upon detection, the wave nature could prove crucial to develop a detailed map of local dark matter and a precious tool for Milky Way archaeology.

An important aid to detection could come from a network of wave dark matter detectors [332, 333]. Making can make use of the wave DM phase at different locations can provide information on the directionality of the dark matter and angular distribution of substructures. It would be therefore interesting to compute correlation of wave fields at different locations with the formalism developed in Chapter 3.

A necessary extension of the formalism would include effects due to the orbital motion of the observer on Earth. On timescales longer than the orbital period and the coherence timescale of wave dark matter, side-bands in the frequency space due to the frequency modulation induced by the orbital motion of Earth and the oscillations of the wave function would appear in the spectrum. Additionally, once the rotation of the Earth is included, the frequency space analysis for experiments sensitive to the gradient of the wave field can be much more complicated, as outlined in [215].

We investigated another instance of distortion of the distribution of dark matter in Chapter 4. Due to conservation laws, the inner part of a dark matter halo can be compressed to form a so-called "spike" if an adiabatically growing black hole or a collapsing molecular cloud is located in the center of the halo. This phenomenon has been studied in the literature for particle, WIMP-like dark matter [99] as the larger dark matter density would enhance the annihilation rate into SM states, e.g. gamma rays. For the first time in the literature, we extended the formalism to study the interplay between the adiabatic compression and the wave nature of dark matter. We constructed the wave halo as a superposition of eigenfunctions as in [93, 109] with appropriate occupation numbers to reproduce the profile observed in simulations [219, 389–391]. For the discussion, we focused on the ultralight end of the spectrum, considering fuzzy dark matter halos, but the scaling symmetry of the Schrödinger-Poisson system allowed us to consider larger masses under the appropriate scales. The soliton size in this case is determined by the typical wavelength of dark matter in the halo, as explained in Section 4.2.1: this prescription is different from the one of fuzzy dark matter halos [108], for which the typical de Broglie wavelength is of the same scale of the halo virial radius.

Due to the characteristic length scales of the system we considered, where an intermediate mass black hole is responsible for the compression of the halo, we had to take into account wave dark matter masses several orders of magnitude larger than the fuzzy dark matter case, i.e. $m \sim 10^{-13}$ eV. For these masses, the relaxation time scale at small radii is short enough so that we are sure a soliton has formed in the inner region of the halo. However, the lifetime of such low angular momentum states is much shorter than the age of the halo and they are absorbed by the central black hole. This led us to a peculiar density profile for the compressed wave dark

matter halo as a broken power law (see Figure 4.10), at small radii $\propto r^{2\ell_c}$ with ℓ_c the lowest angular momentum of the surviving states, and at large radii $\propto r^{-\gamma_{\rm sp}}$ as in the particle case.

Further investigation reveals that the compressed halo can relax in timescales less than the Gyr if, for a fixed black hole mass, the mass of the wave dark matter is small enough, as shown in Figure 4.12 for our benchmarks. This would replenish the low momentum states which would be absorbed into the black hole spoiling the profile discussed above. We therefore limit our analysis to the cases in which the inner part of the halo does not have the time to relax. It would be of interest to understand the relaxation process in presence of a central black hole swallowing the low angular momentum modes and to predict the resulting power law index of the steady configuration: this profile could have some important universal features and attractive phenomenological properties.

Another question of interest is how wave dark matter self-interactions would affect the adiabatic compression of a wave dark matter halo. For a suitable self-interaction cross section we expect a core at some radius as self-annihilations would forbid high densities. This scenarios are worth to be explored, specially in light of possible interesting phenomenological consequences.

A concrete astrophysical scenario in which a compressed wave dark matter halo can be observed is described in Chapter 5. The idea is simple and it was already explored for particle dark matter [102–105]: if a compact object orbits around the intermediate-mass black hole it can probe the inner part of the halo and we can get information on the dark matter environment through the emission of gravitational waves. These intermediate-mass-ratio inspirals (IMRIs) are one of the primary targets of the LISA [110] mission. Due to the high dark matter density, if the halo had been compressed, the orbiting object would experience a dragging force via dynamical friction which would leave a detectable imprint in the gravitational wave signal. Indeed, once the binary has been detected, in the scenarios under consideration, the predicted waveform would be out-of-phase from the no-dark matter scenario by several orders of magnitude. What is even more remarkable is that the dynamical friction force depends naturally on the dark matter model under assumption in two ways: (i) via the density profile, as we saw in Chapter 4, the wave profile is distinct from the particle one at sufficiently low masses and (ii) via the Coulomb logarithm which has to do with the range of impact parameters over which the encounters between the dark matter and the companion object contribute to the friction; the smallest scale is given by the de Broglie wavelength which replaces the maximum momentum transfer for a 90 degree collision.

Other contributions to the dynamical evolution of the system could come more directly from the wave nature of dark matter itself: order-one fluctuations in the density of the size of the de Broglie wavelength could exchange energy with the orbiting compact object. We checked that in the case under consideration these effects, such as stochasting heating and cooling via quasiparticles can be neglected as they are suppressed by the ratio of the quasiparticle mass over the companion mass. However, these effects can be relevant in other systems, e.g in the case we consider a more

massive central black hole. Another effect is the accretion of dark matter by the companion object in the case it is a black hole. We showed that this effect is negligible for sufficiently massive central black holes. Another problem that can arise if the central black hole is not massive enough, say less than $10^4 M_\odot$, is the feedback of the inspiral on the dark matter halo: the energy lost by the companion because of the dynamical friction is injected into the dark matter and these can be energetic enough to be excited to outer shells. Therefore we have to realistically impose that the dynamical friction energy loss is bounded from above by the gravitational binding energy of the dark matter.

It would be of interest to further verify our backreaction model with some N-body simulations of an IMRI in a dark matter halo. A computational approach could also shed some light on some ambiguities in the choice of the appropriate maximum impact parameter which is important for a correct modeling of the dynamical friction. A more challenging investigation would be to perform a simulation of wave dark matter in such a system.

Assuming our simple analytical model of the density profile and dynamical friction for the wave dark matter, we performed a proof of concept statistical analysis of the gravitational wave signal that a detector as LISA could be dealing with. We exploited the matched filtering technique and we constructed a likelihood function to perform a parameter estimation. We wanted to answer the simple question of how well we can reconstruct the parameters of the compressed halo and the wave dark matter mass, that we parameterized via the gravitational Bohr radius, and in which parameter space. The answer we obtained is shown in Figure 5.7: for a IMRI detected with signal-to-noise ratio 15 with five years of gravitational wave observation before its coalescence, a dark matter spike would be detected at the 2σ level and we would obtain a tight constrain on the gravitational Bohr radius for $a \sim 10^{-11}$ pc, corresponding to $m \sim 10^{-13}$ eV.

We showed that this specific benchmark represents the most promising scenario for identifying the nature of dark matter in this kind of systems through a Bayesian analysis. We computed the evidence of a wave halo against the evidence of a particle halo for data generated according to the wave model. We found out that our benchmark lies in a sweet spot where the wave compressed halo can be distinguished from the particle spike as well as being consistent with out assumptions on the wave profile and not being suppressed enough to be indistinguishable from the vacuum case.

While we concentrated our interest on the wave dark matter in this work, the analysis could be extended to other types of particle dark matter. Models involving self interactions, for instance, can form a core and possibly be distinguished from the non-interacting scenario. It would be interesting to extensively study the dark matter zoo to explore which differences can arise in the density profile and in the dynamical friction that can be hopefully observed through a detection of gravitational waves dephasing.

The prospect of uncovering the wave-like properties of dark matter through gravitational wave observation is an intriguing one, to say the least. With the impressive precision of laser interferometry employed by existing gravitational wave

detectors like LIGO [392], VIRGO [393], and KAGRA [394] as well as upcoming missions like LISA [110] and the Einstein Telescope [395], we now have unprecedented opportunities to investigate the wave-like behavior of dark matter across different scales. Moreover, the study of various astrophysical systems could provide crucial insights into the phenomenology of wave dark matter, offering valuable clues for experimental searches and setting important constraints on the mass of dark matter. The potential for discovering the wave-like properties of dark matter through gravitational wave observation is a tantalizing prospect that should be further investigated.

Appendix A

Scalar matter field and gravity

In this Appendix, we derive useful equations for the interaction of a scalar field with gravity. To be general and cover a variety of cases, we consider an expanding and perturbed universe. Explicitly, we treat the Friedmann-Robertson-Walker metric with scalar perturbations in the Newtonian gauge, that is

$$ds^2 = [1 + 2\Phi(t, \mathbf{x})]dt^2 - a^2(t)[1 - 2\Psi(t, \mathbf{x})]\delta_{ij}dx^i dx^j. \tag{A.1}$$

Here $a(t)$ is the scale factor, parameterizing the expansion of the universe and Φ, Ψ are the scalar perturbations. In this background, we consider a spinless bosonic dark matter particle with a mass m, minimally coupled to gravity, with action

$$S = \int d^4x \sqrt{-g} \left[\frac{M_{\rm pl}^2}{2} R + \mathcal{L}_\phi \right] , \tag{A.2}$$

where $M_{\rm pl} = (8\pi G)^{-1/2}$ is the reduced Planck mass and

$$\mathcal{L}_\phi = \frac{1}{2} g^{\mu\nu} (\partial_\mu \phi)(\partial_\nu \phi) - \frac{1}{2} m^2 \phi^2 , \tag{A.3}$$

is the Lagrangian for the free scalar field, which constitutes the only matter content of our theory under consideration.

In the following Sections, we derive the field equations, i.e. the Einstein equations for the above metric and the equation of motion for the scalar field. For each, we specify the cases and approximation of interest.

A.1 Einstein equations

The Einstein equations are derived varying the action in Eq. (A.2) with respect to the metric and imposing $\delta S = 0$

$$G_{\mu\nu} = R_{\mu\nu} - \frac{1}{2} g_{\mu\nu} R = 8\pi G T_{\mu\nu} . \tag{A.4}$$

Here $R_{\mu\nu}$ is the Ricci tensor, R is the Ricci scalar and $T_{\mu\nu}$ is th energy-momentum tensor for ϕ, which is obtained from the variation of the Lagrangian in Eq. (A.3)

$$T_{\mu\nu} \equiv g_{\mu\nu} \mathcal{L}_\phi - 2 \frac{\delta \mathcal{L}_\phi}{\delta g^{\mu\nu}} = (\partial_\mu \phi)(\partial_\nu \phi) - g_{\mu\nu} \mathcal{L}_\phi . \tag{A.5}$$

We are particularly interested in the 00 component and in the trace of the ij components of the Einstein equations

$$G_{00} = 8\pi G\rho\,, \tag{A.6}$$
$$\mathrm{Tr}[G_{ij}] = 8\pi G\,\mathrm{Tr}[T_{ij}]\,. \tag{A.7}$$

Let us write the left hand-sides of these equations explicitly

$$G_{00} = 3H^2\left(1-\frac{2}{H}\partial_0\Psi\right)+\frac{2}{a^2}\nabla^2\Psi\,, \tag{A.8}$$
$$\mathrm{Tr}[G_{ij}] = 2\partial_0^2\Psi+2\nabla^2(\Phi-\Psi) \tag{A.9}$$
$$-(6a\ddot{a}+3a^2H^2)[1-(\Phi+\Psi)]+2H\partial_0(\Phi+3\Psi)\,. \tag{A.10}$$

We compute the components of the energy momentum tensor explicitly

$$\rho = T_{00} = \frac{1}{2}\left[(\partial_0\phi)^2+\frac{1}{a^2}[1+2(\Phi+\Psi)](\nabla\phi)^2+[1+2\Phi]m^2\phi^2\right]\,, \tag{A.11}$$
$$T_{0i} = (\partial_0\phi)(\partial_i\phi)\,, \tag{A.12}$$
$$T_{ij} = (\partial_i\phi)(\partial_j\phi) \tag{A.13}$$
$$+\frac{1}{2}a^2\delta_{ij}\left[[1-2(\Phi+\Psi)](\partial_0\phi)^2-\frac{1}{a^2}(\nabla\phi)^2-[1-2\Psi]m^2\phi^2\right]\,.$$

We recognized $\rho = T_{00}$. Moreover, the trace of the spatial component is equal to three times the pressure

$$3a^2P = \mathrm{Tr}[T_{ij}] = \frac{3}{2}a^2\left[[1-2(\Phi+\Psi)](\partial_0\phi)^2-\frac{1}{3a^2}(\nabla\phi)^2-[1-2\Psi]m^2\phi^2\right]\,. \tag{A.14}$$

If we are interested in the first solutions for the perturbations, we can ignore the feedback of the gravity perturbation on the energy momentum tensor, so that

$$\rho = T_{00} = \frac{1}{2}\left[(\partial_0\phi)^2+\frac{1}{a^2}(\nabla\phi)^2+m^2\phi^2\right]\,, \tag{A.15}$$
$$T_{0i} = (\partial_0\phi)(\partial_i\phi)\,, \tag{A.16}$$
$$T_{ij} = (\partial_i\phi)(\partial_j\phi)+\frac{1}{2}a^2\delta_{ij}\left[(\partial_0\phi)^2-\frac{1}{a^2}(\nabla\phi)^2-m^2\phi^2\right]\,, \tag{A.17}$$
$$\mathrm{Tr}[T_{ij}] = \frac{3}{2}a^2\left[(\partial_0\phi)^2-\frac{1}{3a^2}(\nabla\phi)^2-m^2\phi^2\right]\,. \tag{A.18}$$

A.1.1 Unperturbed metric, cosmological scales

Specializing the Einstein equations derived above to the unperturbed case $\Phi,\Psi=0$,

$$G_{00} = 3H^2\,, \tag{A.19}$$
$$\mathrm{Tr}[G_{ij}] = -3(\dot{a}^2+2a\ddot{a})\,, \tag{A.20}$$

and equating to the energy momentum tensor, we recover the Friedmann equations for a flat universe

$$H^2 = \frac{8\pi G\rho}{3}\,, \tag{A.21}$$

$$\frac{\ddot{a}}{a} = -\frac{4\pi G}{3}(\rho + 3P)\,. \tag{A.22}$$

A.1.2 Time-independent perturbations

In case the perturbations are time-independent, the Einstein equations simplify considerably. We neglect the background component $\Phi = 0,\ \Psi = 0$, i.e. the Friedmann equations and focus on the perturbations $\delta G = G - G^{(0)}$

$$\delta G_{00} = \frac{2}{a^2}\nabla^2\Psi\,, \tag{A.23}$$

$$\mathrm{Tr}[\delta G_{ij}] = 2\nabla^2(\Phi - \Psi) + (6a\ddot{a} + 3a^2H^2)(\Phi + \Psi)\,. \tag{A.24}$$

Also the energy density and pressure are perturbed $\rho = \rho^{(0)} + \delta\rho,\ P = P^{(0)} + \delta P$ Equating to the energy-momentum tensor,

$$\nabla^2\Psi = 4\pi G a^2\delta\rho\,, \tag{A.25}$$

$$\nabla^2(\Phi - \Psi) = 12\pi G a^2 P\,. \tag{A.26}$$

The first equation is the cosmological version of the Poisson equation. The second equation imposes $\Phi = \Psi$ for pressureless matter ($P = 0$, not just $\delta P = 0$).

Now we take the small-scale limit of equations (A.25) and (A.26), setting the scale factor to 1. The equations simplify to

$$\nabla^2\Psi = 4\pi G\delta\rho\,, \tag{A.27}$$

$$\nabla^2(\Phi - \Psi) = 12\pi G P\,. \tag{A.28}$$

We recognize the Poisson equation in the usual form.

A.1.3 Non-relativistic field

This approximation regards the scalar field, hence the energy momentum tensor side of the Einstein equation. If we expand the field ϕ in plane waves, it is clear that every term $\partial_i\phi \sim mv_i\phi \ll m\phi$ will be suppressed by velocity $v_i \ll 1$. Moreover, since the energy of the field can be expanded as $\omega \sim m + mv^2/2$, $\partial_0\phi \sim m\phi + mv^2\phi \sim m\phi$. To be more quantitative, we expand the field in the following way

$$\phi(t,\mathbf{x}) = \frac{1}{\sqrt{2m}}\left[\psi(t,\mathbf{x})e^{-imt} + \psi^\star(t,\mathbf{x})e^{imt}\right]\,, \tag{A.29}$$

allowing for some non-plane wave dependence of the modes. Notice ψ has mass dimension 3/2. We assume that the modes satisfy $|\partial_0^2\psi| \ll |\partial_0\psi| \ll m|\psi|$ and $|\nabla\psi| \ll m|\psi|$. The components of the energy-momentum tensor become, at zero

order in the velocity,

$$\rho = T_{00} = m|\psi|^2 + \mathcal{O}(v^2)\,, \tag{A.30}$$
$$T_{0i} = \mathcal{O}(v)\,, \tag{A.31}$$
$$T_{ij} = \mathcal{O}(v^2)\,, \tag{A.32}$$
$$\mathrm{Tr}[T_{ij}] = \mathcal{O}(v^2)\,. \tag{A.33}$$

Therefore, in the case of time-independent perturbations, the Einstein equations for the perturbations read

$$\nabla^2\Psi = 4\pi G a^2 m|\psi|^2 + \mathcal{O}(v^2)\,, \tag{A.34}$$
$$\nabla^2(\Phi - \Psi) = \mathcal{O}(v^2)\,. \tag{A.35}$$

The second equation enforces $\Phi = \Psi$ at zero order in velocity.

A.2 Klein-Gordon equation

In this Section, we focus on the equation of motion for the scalar field, which, in general will be coupled to the Einstein equations. We write the Euler-Lagrange equations

$$\frac{\partial\mathcal{L}}{\partial\phi} = \frac{1}{\sqrt{-g}}\partial_\mu\left[\sqrt{-g}\frac{\partial\mathcal{L}}{\partial\partial_\mu\phi}\right]\,, \tag{A.36}$$

so the equation of motion, called Klein-Gordon equation, is given by

$$\frac{1}{\sqrt{-g}}\partial_\mu[g^{\mu\nu}\sqrt{-g}\,\partial_\nu\phi] + m^2\phi = 0\,. \tag{A.37}$$

Let us now compute explicitly the let hand side of Eq. (A.37) in order to simplify the equation of motion. Since our metric is diagonal, the left-hand side breaks into two terms, one for $\mu = \nu = 0$ and the other(s) for $\mu = \nu = i$. We compute them

$$\frac{1}{\sqrt{-g}}\partial_0[g^{00}\sqrt{-g}\,\partial_0\phi] = (1-2\Phi)\partial_0^2\phi + [3H(1-2\Phi) - \partial_0(\Phi+3\Psi)]\partial_0\phi \tag{A.38}$$
$$\frac{1}{\sqrt{-g}}\partial_i[g^{ii}\sqrt{-g}\,\partial_i\phi] = -\frac{1}{a^2}\left[(1+2\Psi)\nabla^2\phi + \nabla(\Phi-\Psi)\cdot\nabla\phi\right] \tag{A.39}$$

We divide all terms by $(1-2\Phi)$ and we sum them, obtaining

$$0 = \partial_0^2\phi + [3H - (1+2\Phi)\partial_0(\Phi+3\Psi)]\partial_0\phi + (1+2\Phi)m^2\phi - \frac{1}{a^2}\left[(1+2\Psi+2\Phi)\nabla^2\phi + (1+2\Phi)\nabla(\Phi-\Psi)\cdot\nabla\phi\right]\,. \tag{A.40}$$

This equation looks rather complicated, but it is the most general. In the following, we perform several approximation for the case of interests in this thesis.

A.2.1 Unperturbed metric

In the case of $\Phi, \Psi = 0$, we retrieve the classical Klein-Gordon equation in the expanding FRW universe.

$$\partial_0^2\phi + 3H\partial_0\phi - \left[\frac{\nabla^2}{a^2} - m^2\right]\phi = 0\,. \tag{A.41}$$

Under the further assumption of homogeneity of the field $\phi = \phi(t)$, the Laplacian term disappears. This is the equation that is used to track the evolution of the ϕ field over the history of the universe, i.e. under the effect of the Hubble friction.

A.2.2 Time-independent perturbations

It is a common to assume that the perturbations vary slowly in time or are time-independent. In this limit the Klein-Gordon equation simplifies to

$$\begin{aligned} 0 &= \partial_0^2\phi + 3H\partial_0\phi + (1+2\Phi)m^2\phi \\ &\quad -\frac{1}{a^2}\left[(1+2\Psi+2\Phi)\nabla^2\phi + (1+2\Phi)\nabla(\Phi-\Psi)\cdot\nabla\phi\right]. \end{aligned} \tag{A.42}$$

This form is still rather complicated and not of particular use.

A.2.3 Non-relativistic field

The Klein-Gordon equation heavily simplifies in the non-relativistic limit for the field, in particular when coupled to the Einstein equations. We consider indeed Eq. (A.34) and Eq. (A.35). Using that $\Phi = \Psi$ at v^2 order, we reach the coupled system

$$0 = \partial_0^2\phi + 3H\partial_0\phi + (1+2\Phi)m^2\phi - \frac{1}{a^2}(1+4\Phi)\nabla^2\phi\,, \tag{A.43}$$

$$\nabla^2\Phi = 4\pi G a^2\delta\rho\,. \tag{A.44}$$

We use the expansion in Eq. (A.29) and the same assumptions $|\partial_0^2\psi| \ll |\partial_0\psi| \ll m|\psi|$. We obtain obtain the so-called Schrödinger - Poisson (SP) system.

$$\begin{aligned} i\left[\partial_t\psi + \frac{3}{2}H\psi\right] &= \left[-\frac{\nabla^2}{2m} + m\Phi\right]\psi\,, \\ \nabla^2\Phi &= 4\pi G a^2 m|\psi|^2\,. \end{aligned} \tag{A.45}$$

Once the equations are coupled, it is clear that variations of the field are sourced by the gravitational field, that is will be proportional to Φ. This implies that the term in the Klein-Gordon equation $\Phi\nabla^2\phi$ is higher order and can be neglected.

The SP system can be further specified on small (galactic) scales, if we set the Hubble parameter to zero and the scale factor to unity.

$$\begin{aligned} i\partial_t\psi &= \left[-\frac{\nabla^2}{2m} + m\Phi\right]\psi\,, \\ \nabla^2\Phi &= 4\pi G m|\psi|^2\,. \end{aligned} \tag{A.46}$$

Appendix B

Galactic reference frame

In this Appendix, we provide the transformation matrices, coordinates and formulae to describe the motion of the Earth and the orientation of a terrestrial detector in the Galactic frame. The notation and conventions are mostly borrowed from [396].

B.1 Position of the Earth in galactic coordinates

In the Galactic frame, the orbital plane of the Earth is spanned by two vectors [396]:

$$\begin{aligned} \hat{\epsilon}_1 &= \begin{pmatrix} 0.993821 \\ 0.110992 \\ 0.000352 \end{pmatrix} + \begin{pmatrix} 0.001316 \\ -0.011851 \\ 0.021267 \end{pmatrix} T \,, \\ \hat{\epsilon}_2 &= \begin{pmatrix} -0.054876 \\ 0.494109 \\ -0.867666 \end{pmatrix} + \begin{pmatrix} 0.024232 \\ 0.002689 \\ -1.546 \times 10^{-6} \end{pmatrix} T \,. \end{aligned} \tag{B.1}$$

The time dependence in the vector is small. T is a parameter, called epoch of date that measures the (fractional) number of days n from a reference moment, chosen to be the January 1st 2000 at noon (J2000.0), normalized to the number of days in a Julian century

$$T = \frac{n}{36525} \,. \tag{B.2}$$

We can find the fractional number of days n from J2000.0 using the algorithm to convert a date (Y year, M month, D day), in the Gregorian calendar (the commonly used one) to the Julian day number (from J2000.0)

$$n = \left\lfloor \frac{1461}{4} \left(Y + 4800 + \frac{M-14}{12} \right) \right\rfloor + \left\lfloor \frac{367}{12} (12 - 11M) \right\rfloor \tag{B.3}$$

$$- \left\lfloor \frac{3}{400} \left(Y + 4900 + \frac{M-14}{12} \right) \right\rfloor + D - 32075 - n_0 \,, \tag{B.4}$$

where $n_0 = 2451545$ is the Julian day number at J2000.0.

The position of the Earth in the Galactic frame is then given by a linear combination of $\hat{\epsilon}_1$ and $\hat{\epsilon}_2$

$$\mathbf{x}_\oplus = r_\oplus (\hat{\epsilon}_1 \sin \ell_E(n) - \hat{\epsilon}_2 \cos \ell_E(n)) \,, \tag{B.5}$$

where $r_\oplus \sim 1$ a.u., ℓ_E is the time-dependent ecliptic longitude in the orbital plane [396]

$$\ell_E(n) = L(n) + 2e \sin g(n) + \frac{5}{4} e^2 \sin 2g(n) + \mathcal{O}(e^3) \,, \tag{B.6}$$

where $e = 0.01671$ is the Earth's orbit eccentricity and the mean longitude L and the mean anomaly g are given by [396]

$$L(n) = 280^\circ.460 + 0^\circ.98564736 \times n \,, \tag{B.7}$$

$$g(n) = 357^\circ.528 + 0^\circ.98560028 \times n \,. \tag{B.8}$$

B.2 The detector vector in galactic coordinates

We want to represent the detector orientation vector $\hat{d}$, originally expressed in terrestrial horizontal coordinates (in the basis given by zenith, east and north unit vectors), into galactic coordinates. We know how to relate the rectangular equatorial coordinates at J2000.0 to galactic coordinates, by means of a linear transformation

$$\mathbf{x}_{\rm gal} = \mathcal{M} \mathbf{x}_{\rm eq}({\rm J2000.0}) \,. \tag{B.9}$$

The components of the matrix $\mathcal{M}$ are given in [396]. We now need to relate the equatorial coordinates $(x, y, z)_{\rm eq}$ to horizontal coordinates $(x, y, z)_{\rm hor} = x_{\rm hor}\hat{z} + y_{\rm hor}\hat{e} + z_{\rm hor}\hat{n}$ with $(\hat{z}, \hat{e}, \hat{n})$ a set of unit vectors pointing to the zenith, the east and the north of the detector, respectively. The transformation matrix between the two reference frames is given by

$$\mathbf{x}_{\rm hor} = \mathcal{A}\mathcal{B}\mathbf{x}_{\rm eq} \,, \tag{B.10}$$

where the matrices $\mathcal{A}$ and $\mathcal{B}$ are given by

$$\mathcal{A} = \begin{pmatrix} \cos\phi_O & 0 & \sin\phi_O \\ 0 & 1 & 0 \\ -\sin\phi_O & 0 & \cos\phi_O \end{pmatrix} \,, \qquad \mathcal{B} = \begin{pmatrix} \cos\theta_L & \sin\theta_L & 0 \\ -\sin\theta_L & \cos\theta_L & 0 \\ 0 & 0 & 1 \end{pmatrix} \,. \tag{B.11}$$

Here ϕ_O is the observer latitude (53.55° N for Hamburg), θ_L is the local sidereal time which accounts for the daily rotation of the Earth and the observer longitude θ_O (9.99° E for Hamburg):

$$\theta_L = \theta_O + 280^\circ.46061837 + 360^\circ.98564736629n + 0^\circ.000387993T^2 - T^3/38710000 \,. \tag{B.12}$$

Therefore the transformation of coordinates for the detector vector in the galactic frame is given by

$$\hat{d}_{\rm gal} = \mathcal{M}\mathcal{B}^T\mathcal{A}^T\hat{d}_{\rm hor} \,. \tag{B.13}$$

Appendix C

Fokker-Planck equation

In this Appendix, we review the Fokker-Planck equation formalism for galactic dynamics. Parts of the discussion follows the Binney and Tremaine textbook [42], chapter 7 and Appendix L.

We study the distribution $f(\mathbf{x}, \mathbf{v}, t)$ of objects (e.g. stars) under the influence of a smooth potential $\Phi(\mathbf{x})$. The distribution obeys the collisionless Boltzmann equation $df/dt = 0$; this derivative is taken along the phase-space trajectory of a given object, and therefore the phase space distribution on this path is constant. This is the essence of the Liouville's theorem. In the presence of encounters the phase-space density around a star changes with time, at a rate determined by the collision operator $\Gamma[f]$, in formulae, $df/dt = \Gamma[f]$.

Let us compute Γ. We denote the phase-space coordinates as $\mathbf{u} = (\mathbf{x}, \mathbf{v})$. Let $\Psi(\mathbf{u}, \Delta\mathbf{u}) d^6(\Delta\mathbf{u}) \Delta t$ be the probability that a star with coordinates $\mathbf{u}$ is scattered to the volume $d^6(\Delta\mathbf{u})$ around $\mathbf{u} + \Delta\mathbf{u}$ during the timescale Δt. Note that this Ψ doesn't take into account the acceleration by the gravitational potential, which is already taken into account by the Liouville equation. Encounters can scatter the stars in $(+)$ and out $(-)$ the phase-space volume

$$\left.\frac{\partial f}{\partial t}\right|_{-} = -\int d^6(\Delta\mathbf{u}) \Psi(\mathbf{u}, \Delta\mathbf{u}) f(\mathbf{u}) \,, \tag{C.1}$$

$$\left.\frac{\partial f}{\partial t}\right|_{+} = +\int d^6(\Delta\mathbf{u}) \Psi(\mathbf{u} - \Delta\mathbf{u}, \Delta\mathbf{u}) f(\mathbf{u} - \Delta\mathbf{u}) \,. \tag{C.2}$$

The sum of this two terms is equal to the collision term. Therefore we obtain the so-called master equation.

$$\frac{df}{dt} = \int d^6(\Delta\mathbf{u}) \left[\Psi(\mathbf{u} - \Delta\mathbf{u}, \Delta\mathbf{u}) f(\mathbf{u} - \Delta\mathbf{u}) - \Psi(\mathbf{u}, \Delta\mathbf{u}) f(\mathbf{u})\right] \,. \tag{C.3}$$

An important fact about this equation is that it is not time-reversible, unlike the Liouville equation: a distribution that is localized near a single point in phase space spreads on a larger volume under the influence of the encounter operator. The irreversibility is based on the assumption that $\Psi(\mathbf{u}, \Delta u)$ and $f(\mathbf{u})$ are statistically independent so they can be multiplied. Physically, this is the assumption that field stars and the subject we are following are statistically independent.

The master equation can be simplified in the case of gravitational encounters, i.e. weak encounters. Consider a subject star embedded in a system of size R containing

N stars. Gravitational encounters induce mean-square changes in velocity [42]

$$\Delta v^2 \approx \frac{8v^2}{N} \log \frac{R}{b_{90}} \tag{C.4}$$

where b_{90} is the impact parameter for a 90° deflection. This formula tells us that equal decades of impact parameters contribute equally to the velocity perturbation. Therefore, most of the contribution will come from $b \gg b_{90}$, being $R/b_{90} \sim N \gg 1$ for the virial theorem. The fractional velocity change in an encounter $\delta v/v \sim b_{90}/b$, therefore we understand that most of the evolution of the phase space is due to weak encounters, for which $\delta v \ll v$.

From this observation, we can expand the first term of the master equation Eq. (C.3) in a Taylor series for small $|\Delta \mathbf{u}|$

$$\begin{aligned} \Psi(\mathbf{u}-\Delta\mathbf{u},\Delta\mathbf{u})f(\mathbf{u}-\Delta\mathbf{u}) &= \Psi(\mathbf{u},\Delta\mathbf{u})f(\mathbf{u}) \\ &\quad -\Delta u_i \frac{\partial}{\partial u_i}[\Psi(\mathbf{u},\Delta\mathbf{u})f(\mathbf{u})] \\ &\quad +\frac{1}{2}\Delta u_i \Delta u_j \frac{\partial^2}{\partial u_i \partial u_j}[\Psi(\mathbf{u},\Delta\mathbf{u})f(\mathbf{u})] + \mathcal{O}(\Delta\mathbf{u}^3)\,. \end{aligned} \tag{C.5}$$

The Fokker-Planck approximation consists of truncating the series at second order, obtaining the Fokker-Planck equation

$$\frac{df}{dt} = -\frac{\partial}{\partial u_i}\left\{D[\Delta u_i] f(\mathbf{u})\right\} + \frac{1}{2}\frac{\partial^2}{\partial u_i \partial u_j}\left\{D[\Delta u_i \Delta u_j] f(\mathbf{u})\right\}\,. \tag{C.6}$$

The quantities

$$D[\Delta u_i] \equiv \int d^6(\Delta\mathbf{u})\, \Psi(\mathbf{u},\Delta\mathbf{u})\Delta u_i\,, \tag{C.7}$$

$$D[\Delta u_i \Delta u_j] \equiv \int d^6(\Delta\mathbf{u})\, \Psi(\mathbf{u},\Delta\mathbf{u})\Delta u_i \Delta u_j\,. \tag{C.8}$$

are called *diffusion coefficients*, and they describe the rate at which stars diffuse through phase space due to scatterings. While the first-order coefficient $D[\Delta u_i]$ represents a steady drift contribution, the second-order coefficient $D[\Delta u_i \Delta u_j]$ sets the rate at which the subject star diffuses, i.e. performs a random walk in phase-space.

We can further simplify the Fokker-Planck equation. Again, since all decades in the impact parameter contribute equally to the scattering, most of the contribution is due to short-range, local encounters, i.e. for which $b \ll R$. This fact is in perfect agreement with the statistic independence of stars: close encounters are rare. other consequences follow: (i) since $b/v \ll R/v$, i.e. the encounter time is short with respect to the crossing time, the position of the interacting stars is not affected; (ii) during the encounter, the stars can be thought to follow a Keplerian hyperbolic trajectory, unaffected by the large-scale potential; (iii) the effects of encounters at $\mathbf{x}$ can be computed as if the stars were embedded in an infinite homogeneous medium in which f is everywhere equal to the $f(\mathbf{x})$. Then $\Psi(\mathbf{u},\Delta\mathbf{u})$ is zero unless $\Delta\mathbf{x} = 0$, and as a consequence, all the coefficients $D[\Delta x_i]$, $D[\Delta x_i \Delta x_j]$, $D[\Delta x_i \Delta v_j]$ vanish. The

only relevant diffusion coefficients will then be $D[\Delta v_i]$ and $D[\Delta v_i \Delta v_j]$, so the Fokker-Planck equation becomes

$$\frac{df}{dt} = -\frac{\partial}{\partial v_i}\left\{D[\Delta v_i] f(\mathbf{v})\right\} + \frac{1}{2}\frac{\partial^2}{\partial v_i \partial v_j}\left\{D[\Delta v_i \Delta v_j] f(\mathbf{v})\right\} \ . \tag{C.9}$$

We compute these coefficients in Section C.2, using the formalism we develop in what follows.

C.1 From Boltzmann to Fokker-Planck

In this Section, we show that the Fokker-Planck equation can be obtained from the Boltzmann equation for the phase space distribution of an object we label "1" undergoing gravitational scatterings with objects we label "2". This approach, introduced in [397], leads us to a formalism to deal with the case in which the occupation number in the phase space is high and cannot be neglected. This is indeed the wave dark matter scenario.

We consider the scattering

$$1(p_1) + 2(p_2) \to 1(p_1') + 2(p_2') \ . \tag{C.10}$$

We are interested in the evolution of objects 1, so we write the Boltzmann equation for its distribution f_1

$$\frac{df_1(p_1)}{dt} = \Gamma[f_1] \ . \tag{C.11}$$

The collision term is written as [398]

$$\Gamma[f_1] = \frac{1}{2E_1}\int d\Pi_2 d\Pi_1' d\Pi_2' \, (2\pi)^4 \delta^{(4)}(p_1 + p_2 - p_1' - p_2') |\mathcal{M}|^2 \tag{C.12}$$

$$\Big\{ f_1(p_1') f_2(p_2') [1 \pm f_1(p_1)][1 \pm f_2(p_2)]$$

$$- f_1(p_1) f_2(p_2) [1 \pm f_1(p_1')][1 \pm f_2(p_2')] \Big\} \ . \tag{C.13}$$

Here $d\Pi_i = [d^3 p_i/(2\pi)^3] g_i/(2E_i)$ is the Lorentz invariant phase-space with g_i the number of internal degrees of freedom of object i. The momentum distribution is normalized such that, when integrated over momenta, it gives the number density of 1-type objects

$$\int \frac{d^3 p}{(2\pi)^3} f_1(\mathbf{p}) = \frac{\rho_1}{m_1} \ . \tag{C.14}$$

The $\pm$ factors account for the quantum statistics of the objects, if they are particles. The matrix element averaged over all the degrees of freedom $|\mathcal{M}|^2$ mediates the gravitational interaction between the objects. We know that in the non-relativistic limit the gravitational potential and the Coulomb potential are identical upon the replacement of the fine structure constant α with $\alpha_G = G m_1 m_2$. Therefore the matrix

element for the weak gravitational encounters in the non-relativistic limit is

$$|\mathcal{M}|^2 = \frac{(16\pi\alpha_G)^2 m_1^2 m_2^2}{|\mathbf{q}|^4}\,, \tag{C.15}$$

where $\mathbf{q} = \mathbf{p}_1' - \mathbf{p}_1$ is the momentum transfer. This reproduces the central gravitational potential $V = -Gm_1m_2/r$.

C.1.1 Transition probability

We can rewrite the Boltzmann equation in a fashion similar to the master equation by defining a transition probability from $\mathbf{p}_1$ to $\mathbf{p}_2'$, we call it $W(\mathbf{p}_1, \mathbf{p}_1')$

$$\begin{aligned} W(\mathbf{p}_1, \mathbf{p}_1') &= \frac{1}{4E_1E_1'}\int d\Pi_2 d\Pi_2'\,(2\pi)^4\delta^{(4)}(p_1 + p_2 - p_1' - p_2') && \text{(C.16)}\\ &\quad \times|\mathcal{M}|^2 f_2(p_2)[1 \pm f_2(p_2')]\,. && \text{(C.17)} \end{aligned}$$

Notice that this probability can be split in two contributions, a classical and a wave one $W = W_{\rm cl} + W_{\rm w}$. In the first we keep only terms linear in f_2, in the second the quadratic ones, which are relevant only in case of high phase-space occupancy.

$$\begin{aligned} W_{\rm cl}(\mathbf{p}_1, \mathbf{p}_1') &= \frac{1}{4E_1E_1'}\int d\Pi_2 d\Pi_2'\,(2\pi)^4\delta^{(4)}(p_1 + p_2 - p_1' - p_2')|\mathcal{M}|^2 f_2(p_2)\,, && \text{(C.18)}\\ W_{\rm w}(\mathbf{p}_1, \mathbf{p}_1') &= \pm\frac{1}{4E_1E_1'}\int d\Pi_2 d\Pi_2'\,(2\pi)^4\delta^{(4)}(p_1 + p_2 - p_1' - p_2')|\mathcal{M}|^2 f_2(p_2)f_2(p_2')\,. \end{aligned}$$

For future usage, we want to simplify these expressions in the non-relativistic limit. We start from the classical contribution.

$$\begin{aligned} W_{\rm cl}(\mathbf{p}_1, \mathbf{q}) &\approx \frac{2\pi}{16m_1^2m_2^2}\int\frac{d^3p_2}{(2\pi)^3}\delta(q^0 - E_2 + E_2')|\mathcal{M}|^2 f_2(\mathbf{p}_2) && \text{(C.19)}\\ &= \frac{\pi}{8m_1^2m_2^2}\frac{1}{q}\int\frac{d^3p_2}{(2\pi)^3}\delta\left[\hat{q}\cdot\left(\frac{\mathbf{p}_1}{m_1} - \frac{\mathbf{p}_2}{m_2}\right) + \frac{\mathbf{q}}{2\mu}\right]|\mathcal{M}|^2 f_2(\mathbf{p}_2)\,, \end{aligned}$$

where we used the conservation of energy in the non-relativistic limit

$$\frac{q^2}{2} + \mathbf{q}\cdot\mathbf{p}_{\rm cm} = 0\,, \tag{C.20}$$

with $\mathbf{p}_{\rm cm} = \mu(\mathbf{p}_1/m_1 - \mathbf{p}_2/m_2)$ the center-of-mass momentum and $\mu = m_1m_2/(m_1 + m_2)$ the reduced mass. We expand the delta function for small $\mathbf{q}$ and obtain

$$\begin{aligned} W_{\rm cl}(\mathbf{p}_1, \mathbf{q}) &\approx \frac{\pi}{8m_1^2m_2^2}\frac{1}{q}\left(1 + \frac{m_1}{2\mu}\mathbf{q}\cdot\frac{\partial}{\partial\mathbf{p}_1}\right) && \text{(C.21)}\\ &\quad \times\int\frac{d^3p_2}{(2\pi)^3}\delta\left[\hat{q}\cdot\left(\frac{\mathbf{p}_1}{m_1} - \frac{\mathbf{p}_2}{m_2}\right)\right]|\mathcal{M}|^2 f_2(\mathbf{p}_2)\,. && \text{(C.22)} \end{aligned}$$

Now we do the same for the wave contribution

$$W_{\rm w}(\mathbf{p}_1,\mathbf{q}) \approx \frac{2\pi}{16m_1^2m_2^2}\int\frac{d^3p_2}{(2\pi)^3}\delta(q^0-E_2+E_2')|\mathcal{M}|^2 f_2(\mathbf{p}_2)f_2(\mathbf{p}_2')] \tag{C.23}$$

$$= \frac{\pi}{8m_1^2m_2^2}\frac{1}{q}\int\frac{d^3p_2}{(2\pi)^3}\delta\left[\hat{q}\cdot\left(\frac{\mathbf{p}_1}{m_1}-\frac{\mathbf{p}_2}{m_2}\right)+\frac{\mathbf{q}}{2\mu}\right]|\mathcal{M}|^2 f_2(\mathbf{p}_2)f_2(\mathbf{p}_2-\mathbf{q})\,.$$

We expand $f_2(\mathbf{p}_2-\mathbf{q})\approx f_2(\mathbf{p}_2)-\mathbf{q}\cdot\partial_{\mathbf{p}_2}f_2(\mathbf{p}_2)$, integrate by part and use

$$\frac{\partial}{\partial\mathbf{p}_2}\delta\left[\hat{q}\cdot\left(\frac{\mathbf{p}_1}{m_1}-\frac{\mathbf{p}_2}{m_2}\right)\right] = -\frac{m_1}{m_2}\frac{\partial}{\partial\mathbf{p}_1}\delta\left[\hat{q}\cdot\left(\frac{\mathbf{p}_1}{m_1}-\frac{\mathbf{p}_2}{m_2}\right)\right]\,. \tag{C.24}$$

We therefore get

$$W_{\rm w}(\mathbf{p}_1,\mathbf{q}) \approx \frac{\pi}{8m_1^2m_2^2}\frac{1}{q}\left(1+\frac{1}{2}\mathbf{q}\cdot\frac{\partial}{\partial\mathbf{p}_1}\right) \tag{C.25}$$

$$\times\int\frac{d^3p_2}{(2\pi)^3}\delta\left[\hat{q}\cdot\left(\frac{\mathbf{p}_1}{m_1}-\frac{\mathbf{p}_2}{m_2}\right)\right]|\mathcal{M}|^2 f_2^2(\mathbf{p}_2)\,. \tag{C.26}$$

C.1.2 Collision operator

We can write the collision operator as

$$\Gamma[f_1] = \int\frac{d^3p_1'}{(2\pi)^3}\Big\{W(\mathbf{p}_1',\mathbf{p}_1)f_1(\mathbf{p}_1')[1\pm f_1(\mathbf{p}_1)] \tag{C.27}$$

$$-W(\mathbf{p}_1,\mathbf{p}_1')f_1(\mathbf{p}_1)[1\pm f_1(\mathbf{p}_1')]\Big\}\,. \tag{C.28}$$

For practical reasons, we can decompose this result in a classical and a quantum (wave) contribution $\Gamma[f_1]=\Gamma_{\rm cl}[f_1]+\Gamma_{\rm w}[f_1]$

$$\Gamma_{\rm cl} = \int\frac{d^3p_1'}{(2\pi)^3}\Big\{W(\mathbf{p}_1',\mathbf{p}_1)f_1(\mathbf{p}_1')-W(\mathbf{p}_1,\mathbf{p}_1')f_1(\mathbf{p}_1)\Big\}\,, \tag{C.29}$$

$$\Gamma_{\rm w} = \pm\int\frac{d^3p_1'}{(2\pi)^3}[W(\mathbf{p}_1',\mathbf{p}_1)-W(\mathbf{p}_1,\mathbf{p}_1')]f_1(\mathbf{p}_1)f_1(\mathbf{p}_1')\,. \tag{C.30}$$

Under the Fokker-Planck approximation, the momentum transfer in the encounter is smaller than the momenta of the scatterers and the Boltzmann equation can be rewritten in the form of the Fokker-Planck equation. To show that, we multiply the Boltzmann equation by an arbitrary auxiliary function $s(\mathbf{p}_1)$ and integrate over the $\mathbf{p}_1$ momenta. We treat the classical and wave contribution independently

$$\int\frac{d^3p_1}{(2\pi)^3}s(\mathbf{p}_1)\Gamma_{\rm cl} = \int\frac{d^3p_1}{(2\pi)^3}\frac{d^3p_1'}{(2\pi)^3}s(\mathbf{p}_1)\Big\{W(\mathbf{p}_1',\mathbf{p}_1)f_1(\mathbf{p}_1')-W(\mathbf{p}_1,\mathbf{p}_1')f_1(\mathbf{p}_1)\Big\}$$

$$= \int\frac{d^3p_1}{(2\pi)^3}\frac{d^3p_1'}{(2\pi)^3}[s(\mathbf{p}_1')-s(\mathbf{p}_1)]W(\mathbf{p}_1,\mathbf{p}_1')f_1(\mathbf{p}_1) \tag{C.31}$$

We can Taylor expand the square brackets as $\mathbf{p}_1' = \mathbf{p}_1 + \mathbf{q}$:

$$s(\mathbf{p}_1') - s(\mathbf{p}_1) \approx q_i \frac{\partial h}{\partial p^i} + \frac{1}{2} q_i q_j \frac{\partial^2 h}{\partial p^i \partial p^j} \,. \tag{C.32}$$

Substituting, integrating by parts and rearranging, we get to

$$\Gamma_{\rm cl} \;=\; -\frac{\partial}{\partial p_1^i}[D_i f_1(\mathbf{p}_1)] + \frac{1}{2}\frac{\partial^2}{\partial p_1^i \partial p_1^j}[D_{ij} f_1(\mathbf{p}_1)] \,, \tag{C.33}$$

where we have introduced diffusion coefficients for momentum transfer

$$D_i(\mathbf{p}) \;=\; \int \frac{d^3p'}{(2\pi)^3}(\mathbf{p}' - \mathbf{p})_i W(\mathbf{p}, \mathbf{p}') \,, \tag{C.34}$$

$$D_{ij}(\mathbf{p}) \;=\; \int \frac{d^3p'}{(2\pi)^3}(\mathbf{p}' - \mathbf{p})_i (\mathbf{p}' - \mathbf{p})_j W(\mathbf{p}, \mathbf{p}') \,. \tag{C.35}$$

Notice that, if we assume $f_1^2 \ll 1$, then $\Gamma_{\rm cl}$ dominates and we obtain the Fokker-Planck equation for f_1:

$$\frac{df_1}{dt} = -\frac{\partial}{\partial p_1^i}[D_i(\mathbf{p}_1) f_1(\mathbf{p}_1)] + \frac{1}{2}\frac{\partial^2}{\partial p_1^i \partial p_1^j}[D_{ij}(\mathbf{p}_1) f_1(\mathbf{p}_1)] \,. \tag{C.36}$$

Let us consider the wave collision term

$$\begin{aligned}\int \frac{d^3p_1}{(2\pi)^3} s(\mathbf{p}_1)\Gamma_{\rm w} \;&=\; \pm \int \frac{d^3p_1}{(2\pi)^3}\frac{d^3p_1'}{(2\pi)^3} s(\mathbf{p}_1)[W(\mathbf{p}_1', \mathbf{p}_1) - W(\mathbf{p}_1, \mathbf{p}_1')] f_1(\mathbf{p}_1) f_1(\mathbf{p}_1') \\ &=\; \pm \int \frac{d^3p_1}{(2\pi)^3}\frac{d^3p_1'}{(2\pi)^3} [s(\mathbf{p}_1') - s(\mathbf{p}_1)] W(\mathbf{p}_1, \mathbf{p}_1') f_1(\mathbf{p}_1) f_1(\mathbf{p}_1') \,.\end{aligned}$$

We want to exploit the same diffusion coefficient defined above, so we expand f_1 at first order: $f_1(\mathbf{p}_1') \approx f_1(\mathbf{p}_1) + q_i \partial_{p_1^i} f_1(\mathbf{p}_1)$. Putting all the pieces together

$$\Gamma_{\rm w} = \mp \frac{\partial}{\partial p_1^i}[D_i f_1^2(\mathbf{p}_1)] \pm \frac{1}{2}\left\{ \frac{\partial^2}{\partial p_1^i \partial p_1^j}\left[D_{ij} f_1(\mathbf{p}_1{}^2)\right] - \frac{\partial}{\partial p_1^i}\left[D_{ij}\frac{\partial}{\partial p_1^j} f_1^2(\mathbf{p}_1)\right]\right\} . \tag{C.37}$$

Summing the classical and wave contributions, we obtain a non-linear version of the Fokker-Planck equation

$$\frac{df_1}{dt} = -\frac{\partial}{\partial p_1^i}\{D_i f_1[1 \pm f_1]\} + \frac{1}{2}\frac{\partial^2}{\partial p_1^i \partial p_1^j}\{D_{ij} f_1[1 \pm f_1]\} \mp \frac{1}{2}\frac{\partial}{\partial p_1^i}\left[D_{ij}\frac{\partial}{\partial p_1^j} f_1^2\right] . \tag{C.38}$$

C.2 Diffusion coefficients

The next step is to compute the diffusion coefficients defined in Eqs. (C.34) and (C.35) for our gravitational encounters, parameterized by the matrix element in Eq. (C.15), that depends only on $|\mathbf{q}|^{-4}$. We exploit the results for the transition probability in the non-relativistic limit.

C.2.1 First-order coefficient

We start from the drift coefficient. We compute the classical contribution

$$\begin{aligned} D_i^{\rm cl} &= \int \frac{d^3q}{(2\pi)^3} q_i W_{\rm cl}(\mathbf{p},\mathbf{q}) \\ &= \frac{\pi}{8m_1^2m_2^2}\int \frac{d^3q}{(2\pi)^3}\frac{q_i}{q}\left(1+\frac{m_1}{2\mu}\mathbf{q}\cdot\frac{\partial}{\partial \mathbf{p}_1}\right) \\ &\quad \times \int \frac{d^3p_2}{(2\pi)^3}\delta\left[\hat{q}\cdot\left(\frac{\mathbf{p}_1}{m_1}-\frac{\mathbf{p}_2}{m_2}\right)\right]|\mathcal{M}|^2 f_2(\mathbf{p}_2)\,. \end{aligned} \tag{C.39}$$

It is clear that the first term in the round brackets vanishes, because of the symmetry of the integrand under $\mathbf{q}\to-\mathbf{q}$. We will use multiple times the useful relation [46]

$$\frac{\partial}{\partial x_{j_1}}\cdots\frac{\partial}{\partial x_{j_\ell}}\int d\Omega_{\hat{k}}\hat{k}_{i_1}\ldots\hat{k}_{i_n}\delta(\hat{k}\cdot\mathbf{x}) = \frac{\partial}{\partial x_{i_1}}\cdots\frac{\partial}{\partial x_{i_n}}\int d\Omega_{\hat{k}}\hat{k}_{j_1}\ldots\hat{k}_{j_\ell}\Delta_{n-\ell}(\hat{k}\cdot\mathbf{x}) \tag{C.40}$$

with

$$\Delta_{n-\ell}(y) = \begin{cases} \dfrac{1}{2(n-\ell-1)!}\dfrac{y^{n-\ell}}{|\mathbf{y}|} & n>\ell \\ \dfrac{d^{n-\ell}}{dy^{n-\ell}}\delta(y) & n\le\ell \end{cases} \tag{C.41}$$

Therefore,

$$\begin{aligned} D_i^{\rm cl} &= \frac{\pi}{16m_1m_2^2\mu}\frac{\partial}{\partial p_1^j}\int\frac{d^3q}{(2\pi)^3}q\,\hat{q}_i\hat{q}_j|\mathcal{M}|^2\int\frac{d^3p_2}{(2\pi)^3}\delta\left[\hat{q}\cdot\left(\frac{\mathbf{p}_1}{m_1}-\frac{\mathbf{p}_2}{m_2}\right)\right]f_2 \\ &= \frac{\pi}{16m_1m_2^2\mu}\frac{\partial}{\partial p_1^i}\int\frac{d^3q}{(2\pi)^3}q|\mathcal{M}|^2\int\frac{d^3p_2}{(2\pi)^3}\delta\left[\hat{q}\cdot\left(\frac{\mathbf{p}_1}{m_1}-\frac{\mathbf{p}_2}{m_2}\right)\right]f_2 \\ &= \frac{\pi}{16m_1m_2^2\mu}\frac{\partial}{\partial p_1^i}\int\frac{d^3q}{(2\pi)^3}q|\mathcal{M}|^2\int\frac{d^3p_2}{(2\pi)^3}\frac{f_2(\mathbf{p}_2)}{\left|\frac{\mathbf{p}_1}{m_1}-\frac{\mathbf{p}_2}{m_2}\right|} \\ &= 4\pi G^2(m_1+m_2)m_1\log\Lambda\frac{\partial}{\partial v_1^i}\int d^3v_2\frac{f_2(\mathbf{v}_2)}{|\mathbf{v}_1-\mathbf{v}_2|}\,. \end{aligned} \tag{C.42}$$

We applied the above formula for $n=\ell=0$ to bring the i index outside of the integral. Notice we changed normalization for the distribution as a function of velocity, such that $f(\mathbf{v})=[m^4/(2\pi)^3]f(\mathbf{p})$ and

$$\int d^3v\, f(\mathbf{v}) = \rho\,. \tag{C.43}$$

The integral goes under the name of (first) Rosenbluth potential

$$h[f](\mathbf{v}) = \int d^3v'\frac{f(\mathbf{v}')}{|\mathbf{v}-\mathbf{v}'|}\,. \tag{C.44}$$

The wave contribution can be computed in a similar way. The only difference with respect to the classical one is $f_2(\mathbf{p})\to f_2^2(\mathbf{p}_2)=[(2\pi)^3/m_2^4]^2f_2^2(\mathbf{v}_2)$ and a factor

μ/m_1 overall, so:

$$D_i^{\mathrm{W}} = 4\pi G^2 m_1 \frac{(2\pi)^3}{m_2^3} \log\Lambda \frac{\partial}{\partial v_1^i} \int d^3v_2 \frac{f_2^2(\mathbf{v}_2)}{|\mathbf{v}_1 - \mathbf{v}_2|} .$$

We can rewrite this contribution in the same form as the classical one, once we introduce the following quantities

$$f_{\mathrm{eff}} = f_2^2 \frac{\int d^3v f_2}{\int d^3v\, f_2^2} , \tag{C.45}$$

$$m_{\mathrm{eff}} = \frac{(2\pi)^3}{m_2^3} \frac{\int d^3v\, f_2^2}{\int d^3v f_2} . \tag{C.46}$$

meaning $f_2^2 = m_{\mathrm{eff}} f_{\mathrm{eff}} [m_2^3/(2\pi)^3]$. We obtain

$$D_i^{\mathrm{W}} = 4\pi G^2 m_1 m_{\mathrm{eff}} \log\Lambda \frac{\partial}{\partial v_1^i} \int d^3v_2 \frac{f_{\mathrm{eff}}(\mathbf{v}_2)}{|\mathbf{v}_1 - \mathbf{v}_2|} .$$

So the total diffusion coefficient is

$$D_i = 4\pi G^2 m_1 \log\Lambda \frac{\partial}{\partial v_1^i} \left[(m_1 + m_2) h[f_2](\mathbf{v}_1) + m_{\mathrm{eff}} h[f_{\mathrm{eff}}](\mathbf{v}_1) \right] . \tag{C.47}$$

We can get a more explicit form for the Rosenbluth potential if we assume an isotropic distribution $f_s \equiv f_2(v)$. we have

$$\begin{aligned} h[f_2](v_1) &= 2\pi \int dv_2\, v_2^2 f_2(v_2) \int d\cos\theta \frac{1}{|\mathbf{v}_1 - \mathbf{v}_2|} \\ &= 2\pi \int dv_2\, v_2^2 f_2(v_2) \int d\cos\theta \sum_\ell \frac{\min(v_2, v_1)^\ell}{\max(v_2, v_1)^{\ell+1}} P_\ell(\cos\theta) \\ &= 4\pi \left[\int_0^{v_1} dv_2\, \frac{v_2^2}{v_1} f_2(v_2) + \int_{v_1}^{\infty} dv_2\, v_2 f_2(v_2) \right] , \end{aligned} \tag{C.48}$$

having used $\int_{-1}^{1} d\mu\, P_\ell(\mu) = 2\delta_{\ell 0}$. Note $\partial/\partial v^i = \partial v/\partial v^i \times \partial/\partial v = v^i/v \times \partial/\partial v$, so

$$D_i = \frac{v_1^i}{v_1} 4\pi G^2 m_1 m_{\mathrm{eff}} \log\Lambda \left[\frac{m_1 + m_2}{m_{\mathrm{eff}}} h'[f_2] + h'[f_{\mathrm{eff}}] \right] . \tag{C.49}$$

If we further assume $f_2 = f_{\mathrm{MB}}$

$$f_{\mathrm{MB}}(v;\sigma) = \frac{\rho}{(2\pi\sigma^2)^{3/2}} e^{-v^2/(2\sigma^2)} , \tag{C.50}$$

we have

$$h[f_{\mathrm{MB}}](\mathbf{v}_1) = \frac{\rho_2}{v_1} \mathrm{erf}(X_1) , \tag{C.51}$$

where $X_1 \equiv v_1/\sqrt{2\sigma^2}$. In the MB case $m_{\rm eff} = \pi^{3/2}\rho_2/(m_2^4\sigma^3)$ and $f_{\rm eff} = f_{\rm MB}(v, \sigma_{\rm eff})$ with $\sigma^2_{\rm eff} = \sigma^2/2$. To compute the derivative, we use

$$\frac{\partial}{\partial v^i}\frac{\mathrm{erf}(X)}{v} = \frac{v^i}{v}\frac{\partial}{\partial v}\frac{\mathrm{erf}(X)}{v} = -\frac{v^i}{v}\frac{G(X)}{\sigma^2}\,, \tag{C.52}$$

where

$$G(X) = \frac{1}{2X^2}\left[\mathrm{erf}(X) - \frac{2X}{\sqrt{\pi}}e^{-X^2}\right]. \tag{C.53}$$

We substitute the result and obtain

$$D_i = -\frac{v_1^i}{v_1}\frac{4\pi G^2\rho_2 m_1 m_{\rm eff}}{\sigma^2_{\rm eff}}\log\Lambda\left[\frac{m_1+m_2}{m_{\rm eff}}\frac{\sigma^2_{\rm eff}}{\sigma^2}G(X_1) + G(X_{\rm eff})\right]. \tag{C.54}$$

This expression reproduces the result in [46], except for a factor of m_1 in numerator, due to the fact that D_i is a diffusion coefficient for momentum and not velocity. Our formula automatically includes the dynamical friction contribution, as we will see.

C.2.2 Second-order coefficient

We now compute the second-order coefficient. We start from the classical contribution. The steps are the same for the computation of D_i.

$$\begin{aligned} D^{\rm cl}_{ij} &= \int \frac{d^3q}{(2\pi)^3} q_i q_j W_{\rm cl}(\mathbf{p},\mathbf{q}) \qquad\qquad (C.55)\\ &= \frac{\pi}{8m_1^2m_2^2}\int\frac{d^3q}{(2\pi)^3}\frac{q_iq_j}{q}\left(1+\frac{m_1}{2\mu}\mathbf{q}\cdot\frac{\partial}{\partial\mathbf{p}_1}\right)\\ &\qquad\times\int\frac{d^3p_2}{(2\pi)^3}\delta\left[\hat{q}\cdot\left(\frac{\mathbf{p}_1}{m_1}-\frac{\mathbf{p}_2}{m_2}\right)\right]|\mathcal{M}|^2 f_2(\mathbf{p}_2) \end{aligned}$$

In this case, the second term in the round brackets doesn't contribute because of the symmetry of the integrand. We follow the same steps as above, using Eq.(C.40) for $n=2,\ \ell=0$

$$\begin{aligned} D^{\rm cl}_{ij} &= \frac{\pi}{8m_1^2m_2^2}\int\frac{d^3q}{(2\pi)^3}q\,\hat{q}_i\hat{q}_j|\mathcal{M}|^2\int\frac{d^3p_2}{(2\pi)^3}\delta\left[\hat{q}\cdot\left(\frac{\mathbf{p}_1}{m_1}-\frac{\mathbf{p}_2}{m_2}\right)\right]f_2\\ &= \frac{\pi}{16m_2^2}\frac{\partial^2}{\partial p_1^i\partial p_1^j}\int\frac{d^3q}{(2\pi)^3}q|\mathcal{M}|^2\int\frac{d^3p_2}{(2\pi)^3}\left|\hat{q}\cdot\left(\frac{\mathbf{p}_1}{m_1}-\frac{\mathbf{p}_2}{m_2}\right)\right|f_2\\ &= \frac{\pi^2}{8m_2^2}\frac{\partial^2}{\partial p_1^i\partial p_1^j}\int\frac{dq}{(2\pi)^3}q^3|\mathcal{M}|^2\int\frac{d^3p_2}{(2\pi)^3}\left|\frac{\mathbf{p}_1}{m_1}-\frac{\mathbf{p}_2}{m_2}\right|f_2(\mathbf{p}_2)\\ &= 4\pi G^2m_1^2m_2\log\Lambda\frac{\partial^2}{\partial v_1^i\partial v_1^j}\int d^3v_2|\mathbf{v}_1-\mathbf{v}_2|f_2(\mathbf{v}_2)\,. \end{aligned}$$

The integral is the second Rosenbluth potential

$$g[f](\mathbf{v}) = \int d^3v'|\mathbf{v}-\mathbf{v}'|f(\mathbf{v}')\,. \tag{C.56}$$

We compute the wave contribution using $f_2(\mathbf{p}) \to f_2^2(\mathbf{p}_2) = [(2\pi)^3/m_2^4]^2 f_2^2(\mathbf{v}_2)$ and introducing $m_{\rm eff}$ and $f_{\rm eff}$

$$D_{ij}^{\rm w} = 4\pi G^2 m_1^2 m_{\rm eff} \log\Lambda \frac{\partial^2}{\partial v_1^i \partial v_1^j} \int d^3 v_2 |\mathbf{v}_1 - \mathbf{v}_2| f_{\rm eff}(\mathbf{v}_2) \,. \tag{C.57}$$

Therefore,

$$D_{ij} = 4\pi G^2 m_1^2 \log\Lambda \frac{\partial^2}{\partial v_1^i \partial v_1^j} \left[m_2 g[f_2](\mathbf{v}_1) + m_{\rm eff} g[f_{\rm eff}](\mathbf{v}_1) \right] . \tag{C.58}$$

We compute the Rosenbluth potential

$$\begin{aligned} g[f_2](v_1) &= 2\pi \int dv_2 \, v_2^2 f_2(v_2)) \int d\cos\theta \frac{v_1^2 + v_2^2 - 2v_1 v_2 \cos\theta}{|\mathbf{v}_1 - \mathbf{v}_2|} \\ &= 2\pi \int dv_2 \, v_2^2 f_2(v_2) \int d\cos\theta \sum_\ell \frac{\min(v_2, v_1)^\ell}{\max(v_2, v_1)^{\ell+1}} \\ &\quad \times P_\ell(\cos\theta)(v_1^2 + v_2^2 - 2v_1 v_2 \cos\theta) \\ &= 2\pi \int dv_2 \, v_2^2 f_2(v_2) \left[\frac{2(v_1^2 + v_2^2)}{\max(v_2, v1)} - \frac{4 v_1 v_2 \min(v_2, v_1)}{3 \max(v_2, v_1)^2} \right] \\ &= \frac{4\pi}{3} \left[\int_0^{v_1} dv_2 \, \left(3 v_1 v_2^2 + \frac{v_2^4}{v_1} \right) f_2(v_2) + \int_{v_1}^\infty dv_2 \, \left(v_1^2 v_2 + 3 v_2^3 \right) f_2(v_2) \right] . \end{aligned} \tag{C.59}$$

Now we have to take the derivatives of this potential. We use

$$\frac{\partial^2 g}{\partial v^i \partial v^j} = \frac{v^i v^j}{v^2} \left[g''(v) - \frac{g'(v)}{v} \right] + \delta_{ij} \frac{g'(v)}{v} \,, \tag{C.60}$$

from which

$$\begin{aligned} D_{ij} &= 4\pi G^2 m_1^2 m_{\rm eff} \log\Lambda \\ &\quad \times \left\{ \frac{m_2}{m_{\rm eff}} \left[\frac{v_1^i v_1^j}{v_1^2} \left[g''[f_2](v_1) - \frac{g'[f_2](v_1)}{v_1} \right] + \delta_{ij} \frac{g'[f_2](v_1)}{v_1} \right] \right. \\ &\quad \left. + \left[\frac{v_1^i v_1^j}{v_1^2} \left[g''[f_{\rm eff}](v_1) - \frac{g'[f_{\rm eff}](v_1)}{v_1} \right] + \delta_{ij} \frac{g'[f_{\rm eff}](v_1)}{v_1} \right] \right\} . \end{aligned} \tag{C.61}$$

Now we assume $f_2 = f_{\rm MB}$. We have

$$g[f_{\rm MB}](v_1) = \frac{\sqrt{2}\rho_2 \sigma}{X} \left[(1 + X^2) {\rm erf}(X) - X^2 G(X) \right] \tag{C.62}$$

and

$$\frac{g'}{v} = \frac{\rho_2}{\sqrt{2} X \sigma} ({\rm erf}(X) - G(X)) \,, \tag{C.63}$$

$$g'' = \frac{\sqrt{2}\rho_2}{X\sigma} G(X) \,, \tag{C.64}$$

so

$$\frac{\partial^2 g}{\partial v^i \partial v^j} = \frac{\rho_2}{\sqrt{2}\sigma}\left[\frac{X^i X^j}{X^3}[3G(X) - \mathrm{erf}(X)] + \delta_{ij}\frac{\mathrm{erf}(X) - G(X)}{X}\right], \tag{C.65}$$

from which

$$\begin{aligned} D_{ij} &= 4\pi G^2 m_1^2 m_{\rm eff} \log\Lambda \frac{\rho_2}{\sqrt{2}\sigma_{\rm eff}} \\ &\times\left\{\frac{m_2}{m_{\rm eff}}\frac{\sigma_{\rm eff}}{\sigma}\left[\frac{X^i X^j}{X^3}[3G(X) - \mathrm{erf}(X)] + \delta_{ij}\frac{\mathrm{erf}(X) - G(X)}{X}\right]\right. \\ &\left. + \left[\frac{X^i_{\rm eff} X^j_{\rm eff}}{X^3_{\rm eff}}[3G(X_{\rm eff}) - \mathrm{erf}(X_{\rm eff})] + \delta_{ij}\frac{\mathrm{erf}(X_{\rm eff}) - G(X_{\rm eff})}{X_{\rm eff}}\right]\right\}. \end{aligned} \tag{C.66}$$

C.2.3 Other diffusion coefficients

We can rewrite the diffusion coefficients in the form [42]

$$\frac{D_i}{m_1} = D[\Delta v_i] = \frac{v^i}{v} D[\Delta v_\parallel], \tag{C.67}$$

$$\begin{aligned} \frac{D_{ij}}{m_1^2} &= D[\Delta v_i \Delta v_j] \\ &= \frac{v^i v^j}{v^2}\left(D[(\Delta v_\parallel)^2] - \frac{1}{2}D[(\Delta v_\perp)^2]\right) + \frac{1}{2}\delta^{ij} D[(\Delta v_\perp)^2] \end{aligned} \tag{C.68}$$

We read off these projected coefficients:

$$D[\Delta v_\parallel] = -\frac{16\pi^2 G^2 m_{\rm eff}}{v_1^2}\log\Lambda \int_0^{v_1} dv\, v^2\left[\frac{m_1 + m_2}{m_{\rm eff}} f_2(v) + f_{\rm eff}(v)\right], \tag{C.69}$$

$$\begin{aligned} D[(\Delta v_\parallel)^2] &= \frac{32\pi^2 G^2 m_{\rm eff}}{3}\log\Lambda\left\{\int_0^{v_1} dv\, \frac{v^4}{v_1^3}\left[\frac{m_2}{m_{\rm eff}} f_2(v) + f_{\rm eff}(v)\right]\right. \\ &\left. + \int_{v_1}^{\infty} dv\, v\left[\frac{m_2}{m_{\rm eff}} f_2(v) + f_{\rm eff}(v)\right]\right\}, \end{aligned} \tag{C.70}$$

$$\begin{aligned} D[(\Delta v_\perp)^2] &= \frac{32\pi^2 G^2 m_{\rm eff}}{3}\log\Lambda \\ &\times\left\{\int_0^{v_1} dv\, \left(\frac{3v^2}{v_1} - \frac{v^4}{v_1^3}\right)\left[\frac{m_2}{m_{\rm eff}} f_2(v) + f_{\rm eff}(v)\right]\right. \\ &\left. + 2\int_{v_1}^{\infty} dv\, v\left[\frac{m_2}{m_{\rm eff}} f_2(v) + f_{\rm eff}(v)\right]\right\}. \end{aligned} \tag{C.71}$$

Notice that $D[\Delta v_\parallel]$ depends only on the total number density of objects of mass m_2 traveling slower than the subject mass m_1.

In case of Maxwell-Boltzmann distributions,

$$D[\Delta v_\parallel] = -\frac{4\pi G^2 \rho_2 m_{\rm eff}}{\sigma_{\rm eff}^2} \log\Lambda \left[\frac{m_1+m_2}{m_{\rm eff}} \frac{\sigma_{\rm eff}^2}{\sigma^2} G(X_1) + G(X_{\rm eff}) \right], \quad \text{(C.72)}$$

$$D[(\Delta v_\parallel)^2] = \frac{4\sqrt{2}\pi G^2 \rho_2 m_{\rm eff}}{\sigma_{\rm eff}} \log\Lambda \left[\frac{m_2}{m_{\rm eff}} \frac{\sigma_{\rm eff}}{\sigma} \frac{G(X)}{X} + \frac{G(X_{\rm eff})}{X_{\rm eff}} \right], \quad \text{(C.73)}$$

$$D[(\Delta v_\perp)^2] = \frac{4\sqrt{2}\pi G^2 \rho_2 m_{\rm eff}}{\sigma_{\rm eff}} \log\Lambda \times \left[\frac{m_2}{m_{\rm eff}} \frac{\sigma_{\rm eff}}{\sigma} \frac{{\rm erf}(X) - G(X)}{X} + \frac{{\rm erf}(X_{\rm eff}) - G(X_{\rm eff})}{X_{\rm eff}} \right]. \quad \text{(C.74)}$$

These expressions reproduce the results of [46].

Based on the velocity diffusion coefficients, we can compute other diffusion coefficients. In particular, we are interested in the diffusion coefficients for kinetic energy, as this is intimately connected to the dynamical friction.

The change in kinetic energy per unit mass is given by

$$\Delta E = \frac{1}{2}(\mathbf{v}+\Delta\mathbf{v})^2 - \frac{1}{2}\mathbf{v}^2 = \mathbf{v}\cdot\Delta\mathbf{v} + \frac{1}{2}(\Delta\mathbf{v})^2 \,. \quad \text{(C.75)}$$

The energy diffusion coefficients are

$$D[\Delta E] = vD[\Delta v_\parallel] + \frac{1}{2}D[(\Delta v_\parallel)^2] + \frac{1}{2}D[(\Delta v_\perp)^2] \,, \quad \text{(C.76)}$$

$$D[(\Delta E)^2] = v^2 D[(\Delta v_\parallel)^2] \,. \quad \text{(C.77)}$$

We finish by noticing the important relation between diffusion coefficients:

$$D[\Delta v_i] = \frac{1}{2}\frac{\partial}{\partial v^j} D[\Delta v_i \Delta v_j] \,. \quad \text{(C.78)}$$

This implies, given the expression of the diffusion coefficients in terms of the Rosenbluth potentials, that

$$\frac{D_{ii}}{m_1^2} = D[(\Delta v)^2] = 8\pi G^2 \log\Lambda \left[m_2 h[f_2](\mathbf{v}_1) + m_{\rm eff} h[f_{\rm eff}](\mathbf{v}_1) \right] \quad \text{(C.79)}$$

$$= 32\pi^2 G^2 m_{\rm eff} \log\Lambda \left\{ \int_0^{v_1} dv_2 \, \frac{v_2^2}{v_1} \left[\frac{m_2}{m_{\rm eff}} f_2(v_2) + f_{\rm eff}(v) \right] + \int_{v_1}^{\infty} dv_2 \, v_2 \left[\frac{m_2}{m_{\rm eff}} f_2(v_2) + f_{\rm eff}(v) \right] \right\},$$

which is of use in the computation of $D[\Delta E]$.

Appendix D

Adiabatic Compression of a power-law Dark Matter profile

We apply the procedure described in Section 4.1.1 to find the compressed density profile for an initial power-law profile

$$\rho_{\rm i}(r) = \rho_s \left(\frac{r_s}{r}\right)^{\gamma} \tag{D.1}$$

with $0 < \gamma < 2$. We assume a Schwarzschild black hole of mass $M_{\rm bh}$ grows adiabatically in the center of the halo.

We start by solving the Poisson equation $\nabla^2\Phi_{\rm i} = 4\pi G\rho_{\rm i}$ to find the initial gravitational potential. We use the Green function's method

$$\begin{aligned}
\Phi_{\rm i}(\mathbf{x}) - \Phi_{\rm i}(0) &= -G\int d^3x' \frac{\rho_{\rm i}(\mathbf{x}')}{|\mathbf{x}-\mathbf{x}'|} \\
&= -2\pi G \int_0^\infty dr'\, r'^2 \rho_{\rm i}(r') \int d\mu \sum_{\ell=0}^{\infty} \frac{\min(r,r')^\ell}{\max(r,r')^{\ell+1}} P_\ell(\mu) \\
&= -4\pi G \int_0^\infty dr'\, r'^2 \frac{\rho_{\rm i}(r')}{\max(r,r')} \\
&= \Phi_s \left(\frac{r}{r_s}\right)^{2-\gamma} ,
\end{aligned} \tag{D.2}$$

where

$$\Phi_s = \frac{4\pi G\rho_s r_s^2}{(2-\gamma)(3-\gamma)} . \tag{D.3}$$

Note that $\Phi_{\rm i}(0)$ is not determined, because it would be obtained from the condition that $\Phi_{\rm i}(\infty) = 0$, which is not the case because the potential difference would be infinite in our case. For the NFW case of Section 1.2.2, of which the potential constitutes the inner part, we would have $\Phi_{\rm i}(0) = -2\Phi_s$. We can easily find $\rho_{\rm i}(\Phi_{\rm i})$

$$\rho_{\rm i}(\Phi_{\rm i}) = \rho_s \left(\frac{\Phi_{\rm i} - \Phi_{\rm i}(0)}{\Phi_s}\right)^{\frac{\gamma}{\gamma-2}} \tag{D.4}$$

to exploit in the Eddington formula, from which we can obtain $f(E_\mathrm{i})$. The result is analytical,

$$f(E_\mathrm{i}) = \frac{\sqrt{\pi}\rho_s(\beta-3/2)}{2(2\pi\Phi_s)^{3/2}\beta}\left[-\frac{\Phi_s}{\Phi_\mathrm{i}(0)}\right]^\beta\left[\frac{\Phi_\mathrm{i}(0)}{E_\mathrm{i}}\right]^{3/2} \times\left[1+\frac{E_\mathrm{i}-\Phi_\mathrm{i}(0)}{\Phi_\mathrm{i}(0)}{}_2F_1\left(1,\beta-\frac{1}{2},-\frac{1}{2},\frac{E_\mathrm{i}}{\Phi_\mathrm{i}(0)}\right)\right], \tag{D.5}$$

having defined $\beta = (6-\gamma)/[2(2-\gamma)]$. This complicated expression is however interesting only for $E_\mathrm{i} \simeq \Phi_\mathrm{i}(0)$, because we want to investigate the behavior of the inner part of the halo. Therefore we expand in this limit. We obtain

$$f(E_\mathrm{i}) \approx \frac{\rho_s}{(2\pi\Phi_s)^{3/2}}\frac{\Gamma(\beta)}{\Gamma(\beta-3/2)}\left[\frac{\Phi_s}{E_\mathrm{i}-\Phi_\mathrm{i}(0)}\right]^\beta. \tag{D.6}$$

This reproduces the result in [99].

The next step is to compute the radial actions and solve Eq. (4.11) to find the relation $E_\mathrm{i}(E_\mathrm{f}, L_\mathrm{f})$. The final radial action is straightforward to find, thanks to the simple form of the final potential, $\Phi_\mathrm{f} = -GM_\mathrm{bh}/r$, where the black hole dominates

$$J_{r,\mathrm{f}}(E_\mathrm{f}, L_\mathrm{f}) = \frac{1}{\pi}\int_{r_\mathrm{min}}^{r_\mathrm{max}} dr\sqrt{2\left(E_\mathrm{f}+\frac{GM_\mathrm{bh}}{r}\right)-\frac{L_\mathrm{f}^2}{r^2}} = \frac{GM_\mathrm{bh}}{\sqrt{-2E_\mathrm{f}}} - L_\mathrm{f}\,. \tag{D.7}$$

The values of r_max and r_min are the zeroes of the integrand.

The initial radial action is, instead

$$J_{r,\mathrm{i}}(E_\mathrm{i}, L_\mathrm{i}) = \frac{1}{\pi}\int_{r_\mathrm{min}}^{r_\mathrm{max}} dr\sqrt{2(E_\mathrm{i}-\Phi_\mathrm{i}(0)-\Phi_s(r/r_s)^{2-\gamma})-L_\mathrm{i}^2/r^2}\,. \tag{D.8}$$

Unfortunately, an analytic expression for the radial action integral does not exist except in the extreme cases of a radial and a circular orbit. We can make use of these results and find an analytical approximation valid for any angular momentum. In the first case, $L_\mathrm{i} = 0$, the radial orbit, we find

$$J_r(E_\mathrm{i}, 0) = \frac{\sqrt{2\Phi_s r_s^2}}{\pi(2-\gamma)}\left(\frac{E_\mathrm{i}-\Phi_\mathrm{i}(0)}{\Phi_s}\right)^{\frac{4-\gamma}{2(2-\gamma)}} B\left(\frac{3}{2},\frac{1}{2-\gamma}\right). \tag{D.9}$$

Here $B(z_1, z_2)$ is the beta function, or Euler integral of the first kind. Equating this result to Eq. (D.7), with $L_\mathrm{f} = 0$, i.e. $J_{r,\mathrm{i}}(E_\mathrm{i}, 0) = J_{r,\mathrm{f}}(E_\mathrm{f}, 0)$ we obtain the following scalings

$$[E_\mathrm{i}-\Phi_\mathrm{i}(0)] \propto E_\mathrm{f}^{-\frac{2-\gamma}{4-\gamma}}. \tag{D.10}$$

Using this, we can already estimate the r-dependence of the final density profile

$$\rho_\mathrm{f}(r) \propto \int_\Phi^0 dE_\mathrm{f}\sqrt{2(E_\mathrm{f}-\Phi_\mathrm{f})}E_\mathrm{i}^{-\beta} \propto \int_{\Phi_\mathrm{f}}^0 dE_\mathrm{f}\sqrt{2(E_\mathrm{f}-\Phi_\mathrm{f})}[-E_\mathrm{f}]^{\frac{\beta(2-\gamma)}{4-\gamma}} \propto (-\Phi_\mathrm{f})^{\gamma_\mathrm{sp}}. \tag{D.11}$$

This result already confirms the rough estimate we did in the previous section, where

we found $\rho_f \propto r^{-\gamma_{sp}}$. Let us prove that the energy scaling also holds for purely circular orbits. If the orbit is circular the initial radial action vanishes, as v_r does. We exploit the conservation of momentum

$$L_i = \sqrt{GM_{dm}(r)r}\,, \tag{D.12}$$
$$L_f = \sqrt{GM_{bh}r}\,, \tag{D.13}$$

with $M_{dm}(r) = 4\pi \int_0^r dr'\, r'^2 \rho_i(r')$. We invert $E = v_c^2(r)/2 - \Phi(r)$ to find $r(E)$ and substitute in the expression for the angular momentum. We find

$$L_i = \frac{\sqrt{2\Phi_s r_s^2(2-\gamma)}}{(4-\gamma)^{\frac{4-\gamma}{2(2-\gamma)}}} \left(\frac{E-\Phi_i(0)}{\Phi_s}\right)^{\frac{4-\gamma}{2(2-\gamma)}}\,, \tag{D.14}$$
$$L_f = \frac{GM_{bh}}{\sqrt{-2E_f}}\,. \tag{D.15}$$

Imposing $L_i = L_f$, we find the same scaling relation Eq. (D.10). We can try to guess the form of the initial radial action designing an expression that reproduces the obtained result for the radial and circular orbits. We approximate as in [99]

$$J_{r,i}(E_i, L_i) \approx \frac{B\left(\frac{3}{2}, \frac{1}{2-\gamma}\right)}{\pi(2-\gamma)} \left\{ \sqrt{2\Phi_s r_s^2} \left(\frac{E-\Phi_i(0)}{\Phi_s}\right)^{\frac{4-\gamma}{2(2-\gamma)}} - L \left(\frac{4-\gamma}{2-\gamma}\right)^{\frac{1}{2}} \left(\frac{4-\gamma}{2}\right)^{\frac{1}{2-\gamma}} \right\}. \tag{D.16}$$

While the first term is just the radial action for purely radial orbits, the second term is designed to cancel the first in the circular orbit case. This form reproduces at the percent error the numerical integration in Eq. (D.8) in a large part of parameter space. We are finally able to find $E_i(E_f, L_f)$

$$\frac{E_i(E_f, L_f) - \Phi_i(0)}{\Phi_s} = \left[\frac{\pi(2-\gamma)}{\sqrt{2\Phi_s r_s^2} B\left(\frac{3}{2}, \frac{1}{2-\gamma}\right)}\right]^{\frac{2(2-\gamma)}{4-\gamma}} \left[\frac{GM_{bh}}{\sqrt{-2E_f}} - g(\gamma) L_f\right]^{\frac{2(2-\gamma)}{4-\gamma}}\,, \tag{D.17}$$

where we defined, to shorten the notation,

$$g(\gamma) = 1 - \frac{B\left(\frac{3}{2}, \frac{1}{2-\gamma}\right)}{\pi(2-\gamma)} \left(\frac{4-\gamma}{2-\gamma}\right)^{\frac{1}{2}} \left(\frac{4-\gamma}{2}\right)^{\frac{1}{2-\gamma}}\,. \tag{D.18}$$

We find the inner (low energy) compressed energy distribution

$$f(E_f, L_f) \approx \frac{\rho_s}{(2\pi\Phi_s)^{3/2}} \frac{\Gamma(\beta)}{\Gamma(\beta - 3/2)} \left[\frac{\pi(2-\gamma)}{\sqrt{2\Phi_s r_s^2} B\left(\frac{3}{2}, \frac{1}{2-\gamma}\right)}\right]^{-\frac{6-\gamma}{4-\gamma}} \times \left[\frac{GM_{bh}}{\sqrt{-2E_f}} - g(\gamma) L_f\right]^{-\frac{6-\gamma}{4-\gamma}}\,. \tag{D.19}$$

We compute the final density profile using Eq. (4.12). We change integration variables to $\epsilon = E/\Phi_{\rm f}(r)$, $\ell = L_{\rm f}/L_{\rm max}$, with $L_{\rm max} = r\sqrt{-2\Phi_{\rm f}}\sqrt{1-\epsilon}$. We obtain

$$\rho_{\rm f} \;=\; \rho_{\rm s}\left(\frac{r_{\rm s}}{r}\right)^{\gamma_{\rm s}}\left[\frac{\Phi_{\rm s}}{\Phi_{\rm f}(r_{\rm s})}\right]^{-\frac{3-\gamma}{4-\gamma}}\frac{\Gamma(\beta)}{\Gamma(\beta-3/2)}\left[\frac{2B\left(\frac{3}{2},\frac{1}{2-\gamma}\right)}{\pi(2-\gamma)}\right]^{\frac{6-\gamma}{4-\gamma}} I(\gamma)\,, \quad \text{(D.20)}$$

with

$$I(\gamma) = 2\pi^{-1/2}\int_0^1 d\epsilon \int_{\frac{L_{\rm min}}{L_{\rm max}}}^1 d\ell\;\ell\frac{\sqrt{1-\epsilon}}{\sqrt{1-\ell^2}}\left(\frac{1}{\sqrt{\epsilon}} - 2g(\gamma)\ell\sqrt{1-\epsilon}\right)^{-\frac{6-\gamma}{4-\gamma}}. \quad \text{(D.21)}$$

This integral evaluates numerically to $I(\gamma) \in [0.5, 0.7]$ for $0 \leq \gamma \leq 2$ and $L_{\rm min} = 0$. We found the expression for the spike density profile. Once the density profile $\rho_{\rm f}(r)$ is known, we can write a more compact version of the final phase space distribution

$$f(E_{\rm f}, L_{\rm f}) \approx \frac{\rho_{\rm f}(r)}{[-2\pi\Phi_{\rm f}(r)]^{3/2} I(\gamma)}\left[\sqrt{\frac{\Phi_{\rm f}(r)}{E_{\rm f}}} - g(\gamma)\sqrt{-\frac{2}{\Phi_{\rm f}(r)}\frac{L^2}{r^2}}\right]^{-\frac{6-\gamma}{4-\gamma}}. \quad \text{(D.22)}$$

An even better phase space distribution to be used in practical applications can be derived assuming the power-law density profile from scratch for the final halo, let us say $\rho_{\rm f} = \rho_{\rm sp}(r_{\rm sp}/r)^{\gamma_{\rm sp}}$. If we can neglect the dependence on angular momentum and are interested in an ergodic distribution, which proves to be a very good approximation (see Appendix E for an example), we can exploit the Eddington inversion formula and find $f(E_{\rm f})$. The calculation is simplified by the fact that the final potential is simply $\Phi_{\rm f} = -GM_{\rm bh}/r$. The result is

$$f(E_{\rm f}) = \frac{\rho_{\rm sp}(r_{\rm sp}/r)^{\gamma_{\rm sp}}}{[-2\pi\Phi_{\rm f}(r)]^{3/2}}\frac{\Gamma(\gamma_{\rm sp}+1)}{\Gamma(\gamma_{\rm sp}-1/2)}\left(\frac{\Phi_{\rm f}(r)}{E_{\rm f}}\right)^{3/2-\gamma_{\rm sp}}. \quad \text{(D.23)}$$

Appendix E

Dynamical friction

In this Appendix, we compute the dynamical friction force on a point-mass object, i.e. a test object moving through a dark matter medium. We present the classical result for particle dark matter and then we generalize it to the wave case.

We choose a coordinate system centered on the test object of mass M. The force acting on this object traveling through a dark matter medium with velocity $\mathbf{V}$ and density ρ is

$$\mathbf{F}_{\rm DF} = M\frac{d\mathbf{V}}{dt} = \int d^3x\, \rho(\mathbf{x})\nabla\Phi(\mathbf{x})\,, \tag{E.1}$$

where we call $\Phi = -GM/r$ the gravitational potential around the test object. Notice that if we decompose the density in a background plus a overdensity components, $\rho(\mathbf{x}) = \bar{\rho}[1+\delta(\mathbf{x})]$, thanks to the symmetry of the system, only the non-uniform part contributes to the dynamical friction. If we assume, without loss of generality, $\mathbf{v} = v\hat{z}$, we have

$$\mathbf{F}_{\rm DF} = \int d^3x\, \delta(\mathbf{x})\frac{\partial\Phi}{\partial z}\hat{z}\,. \tag{E.2}$$

The force is directed in the same direction as the dark matter "wind", $\mathbf{V}$.

It is convenient to parametrize the dynamical friction with the C coefficient [33]

$$C \equiv \frac{F_{\rm DF}}{F_{\rm rel}}\,, \tag{E.3}$$

where

$$F_{\rm rel} \equiv \frac{4\pi\bar{\rho}G^2M^2}{V^2}\,. \tag{E.4}$$

We will now compute the coefficient C in various cases of interest. Note that we are assuming a monochromatic dark matter medium. We will see how how to generalize our results in the case of a dispersed flux.

E.1 Particle dark matter

Let us consider a gas of dark particles. A convenient way to obtain the dynamical friction is to compute it as the surface integral of the fluid's momentum flux density

tensor $\Pi_{ij} = \rho v_i v_j$ which satisfies

$$\partial_t(\rho v_i) + \partial_j \Pi_{ij} + \rho \partial_i \Phi = 0 \,. \tag{E.5}$$

Note that $\mathbf{v}$ here is the dark matter velocity at position $\mathbf{x}$. The force explicitly reads, as we wrote above,

$$F^i_{\rm DF} = -\oint dS_j \Pi_{ji} = -\int d^3x\, \partial_j \Pi_{ji} = \int d^3x\, \rho \partial_i \Phi \,. \tag{E.6}$$

We can compute the dynamical friction in the z-direction via the momentum flux through a sphere of radius r centered in the position of M from hyperbolic Keplerian orbits that are parallel to the z-axis as $z \to \infty$:

$$\begin{aligned} C_{\rm p} &= \frac{F_{\rm DF}}{F_{\rm rel}} = -\frac{1}{F_{\rm rel}} \int d\Omega\, r^2 \rho(\mathbf{x})(\hat{x}\cdot\mathbf{v}) v_z \\ &= -\rho(r) \frac{V^2 r^2}{4\pi G^2 M^2 \bar{\rho}} \int_0^{2\pi} d\phi \int_{-1}^{1} d\mu\, \mu v v_z \end{aligned} \tag{E.7}$$

Here $\mu = \hat{x}\cdot\hat{v}$ and $v^2 = V^2 + 2GM/r$. We saw in Section 3.1 that the angle-averaged density profile around the test mass is $\rho(r) = \bar{\rho}\sqrt{1+\frac{2GM}{rV^2}}$. We use the formula from [69] to relate the velocity at $\mathbf{x}$ to the one at infinity $\mathbf{V}$:

$$\mathbf{V} = \frac{V^2\mathbf{v} + V(GM/r)\hat{x} - Vv^2\hat{v}\mu}{V^2 + (GM/r) - Vv\mu} \,. \tag{E.8}$$

We can obtain the expression for v_z projecting $\mathbf{V}$ on $\mathbf{v}/V$:

$$v_z = \frac{Vv^2 + v\mu(GM/r) - v^3\mu}{V^2 + (GM/r) - Vv\mu} \,. \tag{E.9}$$

Furthermore, we introduce the parameter

$$\Lambda = \frac{V^2 r}{GM} = \frac{r}{b_{90}} \,. \tag{E.10}$$

With this choice we solve the integral in Eq. (E.7), we obtain

$$C_{\rm p} = \frac{1+\Lambda}{\Lambda} \log\left[1 + \Lambda + \sqrt{\Lambda(2+\Lambda)}\right] - \sqrt{1+\frac{2}{\Lambda}} \,. \tag{E.11}$$

This expression, for $\Lambda \gg 1$, that is $r \gg b_{90}$, converges to $C_{\rm p} \approx \log 2\Lambda - 1 + \mathcal{O}(\Lambda)$.

E.2 Wave dark matter

We now consider wave dark matter with mass m. From Section 3.2, where we studied gravitational focusing, we know the solution of the Schrödinger equation with plane wave boundary conditions at infinity and a central potential $\Phi = -GM/r$. In the monochromatic case where all the dark matter particles have velocity $\mathbf{V} = V\hat{z}$,

the density profile is given by [106]

$$\rho(\mathbf{x}) = \bar{\rho}|\psi_{\mathbf{k}}(\mathbf{x})|^2 = \bar{\rho}|\psi_k(0)|^2\,|{}_1F_1[i\beta,1,ikr(1-z/r)]|^2 \tag{E.12}$$

where $\mathbf{k} = m\mathbf{V}$ and $\beta = GMm/V = 2\pi b_{90}/\lambda_{\rm dB}$ and

$$|\psi_k(0)|^2 = e^{\pi\beta}|\Gamma(1-i\beta)|^2 = \frac{2\pi\beta}{1-e^{-2\pi\beta}}\,. \tag{E.13}$$

The modulus of force is then

$$\begin{aligned} F_{\rm DF} &= 2\pi GM\bar{\rho}|\psi_k(0)|^2\int_0^r dr'\,r'^2\int_{-r'}^{r'}dz\frac{z}{r'^3}\,|{}_1F_1[i\beta,1,ikr(1-z/r)]|^2 \\ &= 2\pi GM\bar{\rho}|\psi_k(0)|^2\int_0^{2kr}dq\,|{}_1F_1(i\beta,1,iq)|^2\int_{q/2k}^{r}dr'\frac{1}{kr'}\left(1-\frac{q}{kr'}\right) \\ &= 2\pi GM\bar{\rho}|\psi_k(0)|^2\frac{1}{k}\int_0^{2kr}dq\,|{}_1F_1(i\beta,1,iq)|^2\left[\frac{q}{kr}-2-\log\frac{q}{2kr}\right] \\ &= \frac{4\pi G^2M^2\bar{\rho}}{V^2}C(\beta,kr)\,. \end{aligned} \tag{E.14}$$

The coefficient C is then given by

$$C(\beta,kr) = \frac{|\psi_k(0)|^2}{2\beta}\int_0^{2kr}dq\,|{}_1F_1(i\beta,1,iq)|^2\left[\frac{q}{kr}-2-\log\frac{q}{2kr}\right], \tag{E.15}$$

as in [33]. The expression and value of C factor will determine the behavior of dynamical friction. In general the integral in the above equation is difficult to compute, because of the hypergeometric function. However, we can rely on approximations.

In the $\beta \ll 1$ limit, i.e. when $b_{90} \ll \lambda_{\rm dB}$, $|\psi_k(0)|^2 \approx 1+\pi\beta$ and the hypergeometric function can be approximated as [33]

$${}_1F_1(i\beta,1,iq) \approx 1 - \beta\,\mathrm{si}(q) - i\beta\,\mathrm{cin}(q) + \mathcal{O}(\beta^2)\,, \tag{E.16}$$

where

$$\mathrm{si}(z) = \int_0^z dt\frac{\sin t}{t}\,, \qquad \mathrm{cin}(z) = \int_0^z dt\frac{1-\cos t}{t}\,. \tag{E.17}$$

At leading order in β, $|{}_1F_1(i\beta,1,iq)|^2 \approx 1-2\beta\,\mathrm{si}(q)$, therefore,

$$\begin{aligned} C(\beta\ll1,kr) &\approx -\int_0^{2kr}dq\left[\frac{q}{kr}-2-\log\frac{q}{2kr}\right]\int_0^q dt\,\frac{\sin t}{t} \\ &\approx -\int_0^{2kr}dt\,\frac{\sin t}{t}\int_0^t dq\left[\frac{q}{kr}-2-\log\frac{q}{2kr}\right] \\ &\approx -\int_0^{2kr}dt\left[\frac{t}{2kr}-1-\log\frac{t}{2kr}\right]. \end{aligned} \tag{E.18}$$

Solving this integral and using $\int_0^z dt\,\log t\sin t = (1-\cos z)\log z - \mathrm{cin}(z)$, we obtain

$$C(\beta\ll1,kr) \approx \mathrm{cin}(2kr) - 1 + \frac{\sin(2kr)}{2kr} + \mathcal{O}(\beta)\,. \tag{E.19}$$

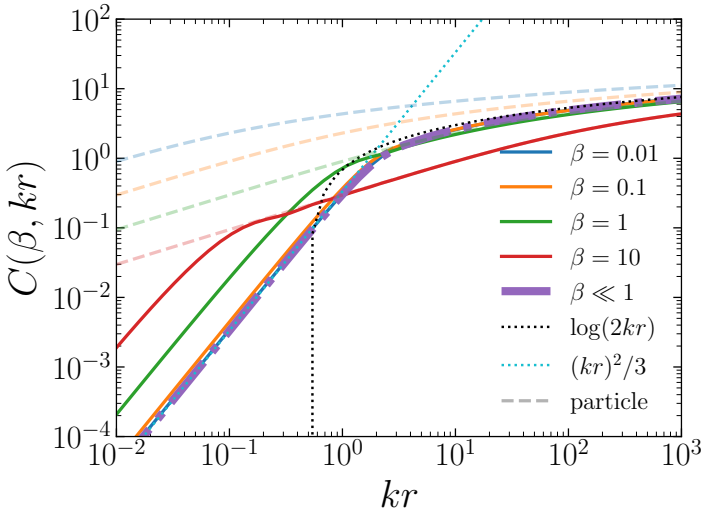

FIGURE E.1: Comparison of the exact dynamical friction coefficient $C(\beta, kr)$ with the various approximations. The dashed lines are for the particle result with $\Lambda = kr/\beta$.

For $kr \gg 1$, $C \approx \log(2kr)$, while for $kr \ll 1$, the Coulomb log is suppressed as $C \approx (kr)^2/3$.

If instead $b_{90} \gg \lambda_{\rm dB}$, the dark matter wavelength does not act as a cutoff for the Coulomb interaction as the largest momentum transfer and we are in the particle limit. We show in Figure E.1 the exact C factor for dynamical friction computed with Eq. (E.15) and compare to the various approximations and to the particle limit.

E.3 Dispersed dark matter medium

To obtain the dynamical friction in case of a dispersed dark matter medium, we need to convolute the dragging force for the monochromatic case with the velocity distribution of the particles. We can write

$$\mathbf{F}_{\rm DF} = F_{\rm rel} V^2 \int d^3v\, f(\mathbf{v}) \frac{(\mathbf{V}-\mathbf{v})}{|\mathbf{V}-\mathbf{v}|^3} C(|\mathbf{V}-\mathbf{v}|)\,, \tag{E.20}$$

which gives the monochromatic result, i.e. the definition of C, once $f(\mathbf{v}) = \delta^{(3)}(\mathbf{v})$. Notice here the distribution function is normalized as $\int d^3v\, f(\mathbf{v}) = 1$. Let us define the averaged C coefficient as

$$\langle C \rangle = V^2 \int d^3v\, f(\mathbf{v} + V\hat{z}) \frac{v_z}{v^3} C(v)\,, \tag{E.21}$$

so that the dynamical friction force can be rewritten as in the monochromatic case but with C replaced by $\langle C \rangle$.

Usually, in the computation of dynamical friction, the C coefficient is pulled out

of the integral, even if it is velocity dependent. We want to quantify the error associated to this approximation. If the distribution is isotropic and C is constant,

$$\begin{aligned} V^2 \int d^3v\, f(\mathbf{v}) \frac{(\mathbf{V}-\mathbf{v})}{|\mathbf{V}-\mathbf{v}|^3} C(|\mathbf{V}-\mathbf{v}|) &\approx -C\frac{\partial}{\partial \mathbf{V}} \int d^3v\, \frac{f(v)}{|\mathbf{v}-\mathbf{V}|} \\ &= -CV^2 \frac{\mathbf{V}}{V} h'[f](V) \\ &= 4\pi C \frac{\mathbf{V}}{V} \int_0^V d^3v\, v^2 f(v)\,. \end{aligned} \tag{E.22}$$

Note that this is the derivative of the Rosenbluth potential we computed in Section C.2. Therefore, under this approximation,

$$F_{\rm DF} = \frac{16\pi^2 G^2 \bar{\rho} M^2}{V^2} C \int_0^V d^3v\, v^2 f(v)\,. \tag{E.23}$$

This friction force corresponds to $F_{\rm DF} = MD[\Delta v_\parallel]$ (the minus sign due to the different frame convention) with $D[\Delta v_\parallel]$ in Eq. (C.69).

The comparison of the exact result and the constant C approximation shows a good agreement in the case of a Maxwell-Boltzmann distribution, as long as we compute C as the monochromatic C evaluated in the typical velocity of dark matter particles, e.g. $\bar{v} = \sqrt{V^2+\sigma^2}$, where σ is the velocity dispersion defined as the second moment of f. We will stick to this approximation from now on.

A second assumption is that the velocity distribution is isotropic. As we saw in Chapter 4 and Appendix D, this is not the case for adiabatically compressed dark matter halo. To check this approximation, we have to compare the first and last term of Eq. (E.22) with $C = 1$. The full spike velocity distribution, up to a normalization constant is given by

$$f(u,\mu) \propto \left[\frac{1}{\sqrt{1-u^2}} - 2u\sqrt{1-\mu^2}\left(1 - \frac{(4-\gamma)^{\frac{4-\gamma}{2(2-\gamma)}}}{2^{\frac{1}{2-\gamma}}\sqrt{2-\gamma}} \frac{B\left(\frac{3}{2}, \frac{1}{2-\gamma}\right)}{\pi(2-\gamma)}\right)\right]^{-\frac{6-\gamma}{4-\gamma}}, \tag{E.24}$$

as a function of $u = v/v_e$, the escape velocity (the dark matter is bound) and $\mu = \hat{v}\cdot\hat{V}$. The ergodic distribution is instead,

$$f(u) \propto (1-u^2)^{\frac{6-\gamma}{2(4-\gamma)}} = (1-u^2)^{\gamma_{\rm sp}-3/2}\,. \tag{E.25}$$

We normalize such that $\int_0^{v_e} d^3v\, f(\mathbf{v}) = 1$, so below f is intended as normalized. We obtain, for $\gamma = 1$ and $V = v_e/\sqrt{2}$,

$$\begin{aligned} &V^2 \hat{V} \int d^3v\, f(\mathbf{v}) \frac{(\mathbf{V}-\mathbf{v})}{|\mathbf{V}-\mathbf{v}|^3} = \\ &= V^2 \int_0^{v_e} dv\, v^2 \int d\phi \int d\mu \frac{V - v\cos\phi\sqrt{1-\mu^2}}{(v^2+V^2-2vV\cos\phi\sqrt{1-\mu^2})^{3/2}} f(v/v_e,\mu) \\ &\approx 0.5937 \end{aligned} \tag{E.26}$$

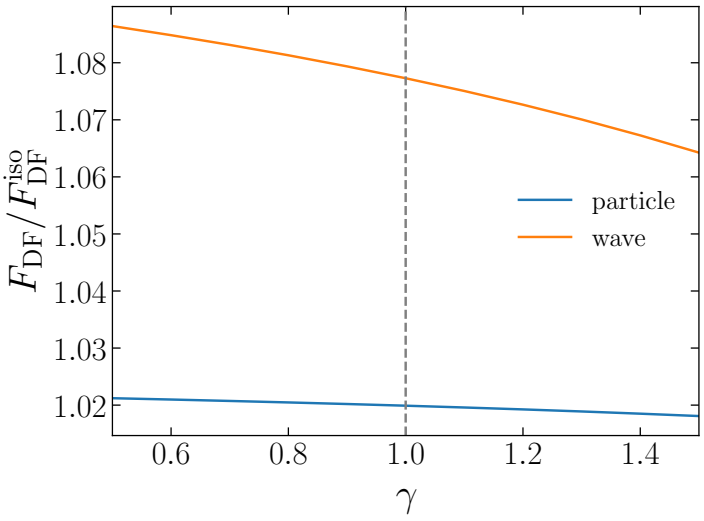

FIGURE E.2: The ratio between the dynamical friction force computed with the full distribution and under the ergodic assumption, for particle (blue) and wave (orange) dark matter. The error is about 2% and 8% for particle and wave, respectively. The vertical line $\gamma = 1$ is the reference value.

$$4\pi \int_0^V d^3v\, v^2 f(v/v_e) = \frac{\int_0^{1/\sqrt{2}} du\, u^2(1-u^2)^{\gamma_{\rm sp}-3/2}}{\int_0^1 du\, u^2(1-u^2)^{\gamma_{\rm sp}-3/2}} = \frac{B_{1/2}(3/2, \gamma_{\rm sp}-1/2)}{B(3/2,\gamma_{\rm sp}-1/2)} \approx 0.5821 \tag{E.27}$$

This is where the factor 0.6 comes from in Eq. (5.13). We see that the error is minimal. We can scan the error as a function of γ in the case of particle and wave dark matter. For the particle case, we compute, for $V = v_e/\sqrt{2}$ and as a function of γ,

$$\left.\frac{F_{\rm DF}}{F_{\rm DF}^{\rm iso}}\right|_{\rm p} = \frac{V^2 \int d^3v\, f(\mathbf{v}) \frac{(V-\mathbf{v}\cdot\hat{V})}{|\mathbf{V}-\mathbf{v}|^3}}{4\pi \int_0^V dv\, v^2 f(v)}\,. \tag{E.28}$$

For wave dark matter, the distribution gets replaced by $f_{\rm eff}$ and we have a factor of $m_{\rm eff}$ that replaces M in $F_{\rm rel}$. The "effective" quantities are defined in Eq. (C.45) and Eq. (C.46), respectively: they both depend on f, therefore on the ergodicity (isotropy) assumption. We compute

$$\left.\frac{F_{\rm DF}}{F_{\rm DF}^{\rm iso}}\right|_{\rm w} = \frac{m_{\rm eff}}{m_{\rm eff}^{\rm iso}}\frac{F_{\rm DF}}{F_{\rm DF}^{\rm iso}} = \frac{\int d^3v\, f^2(\mathbf{v})}{\int d^3v\, f^2(v)} \frac{V^2 \int d^3v\, f^2(\mathbf{v}) \frac{(V-\mathbf{v}\cdot\hat{V})}{|\mathbf{V}-\mathbf{v}|^3}}{4\pi \int_0^V dv\, v^2 f^2(v)}\,. \tag{E.29}$$

We show the results in Figure E.2. We see that for particle dark matter the error is roughly 2% over the values of γ of interest, while for wave dark matter is roughly 8%. This procedure can be generalized to arbitrary distributions to check the goodness of the ergodic approximation.

Appendix F

Gravitational Waves from a binary

In this Appendix, we show the derivation of the gravitational waveform exploited in Chapter 5 to study the dephasing of the gravitational wave signal caused by the dynamical friction exerted by the dark amter halo.

Let us consider the GW emission during the inspiral phase of the binary in a quasi-circular orbit, i.e. $\dot{f}_o \ll f_o^2$. The strain of the two GW polarizations emitted from the binary is [380]

$$h_+ = \frac{G}{D_L}(\ddot{\mathcal{M}}_{11} - \ddot{\mathcal{M}}_{22})\Big|_{t-D_L}, \tag{F.1}$$

$$h_\times = \frac{2G}{D_L}\ddot{\mathcal{M}}_{12}\Big|_{t-D_L}, \tag{F.2}$$

where $\mathcal{M}_{ij} = \int d^3x\, x_i x_j T^{00}$ are the quadrupole moment components and D_L is the luminosity distance between the observer and the binary. We introduce coordinates in the orbital (x, y) plane

$$x(t) = r(t)\sin[\Phi(t)/2], \qquad y(t) = r(t)\cos[\Phi(t)/2]\,, \tag{F.3}$$

where $\Phi_o(t) = \Phi(t)/2$ is the orbital phase, related to the GW frequency f via

$$\Phi(t) = \int^t dt'\, 2\pi f(t')\,. \tag{F.4}$$

We compute the waveform explicitly. In the center-of-mass frame $\mathcal{M}_{ij} = \mu x^i x^j$ has the explicit form

$$\mathcal{M}(t) = \frac{\mu r(t)^2}{2}\begin{pmatrix} 1-\cos\Phi(t) & \sin\Phi(t) & 0 \\ \sin\Phi(t) & 1+\cos\Phi(t) & 0 \\ 0 & 0 & 0 \end{pmatrix}. \tag{F.5}$$

When computing the time derivatives of $\mathcal{M}$, we can neglect terms of order $\dot{f} \ll f$ and $\dot{r} \ll rf$ or higher, thanks to the quasi-circular approximation. Taking into account the inclination ι, i.e. the angle between the observer's line of sight and the

normal to the orbital plane, we obtain

$$h_+(t) = \frac{4}{D_L}(GM_c)^{5/3}[\pi f(t)]^{2/3}\frac{1+\cos^2\iota}{2}\cos[\Phi(t)]\Big|_{t-D_L}, \tag{F.6}$$

$$h_\times(t) = \frac{4}{D_L}(GM_c)^{5/3}[\pi f(t)]^{2/3}\cos\iota\sin[\Phi(t)]\Big|_{t-D_L}. \tag{F.7}$$

However, we are interested in the strain in frequency space. Let us consider the $+$ polarization for now

$$h_+(f) = \frac{1}{2}\int dt\, a(t)\left[e^{2\pi i f t + i\Phi(t)} + e^{2\pi i f t - i\Phi(t)}\right], \tag{F.8}$$

where $a(t)$ contains all the factors except $\cos[\Phi(t)]$. The main time dependence is in the exponential factor, so we can use the saddle point approximation to extract the main contribution. If $t_\star$ is the point for which the phase is stationary, i.e. $2\pi f = \dot\Phi(t_\star)$. Notice that, given the definition of Φ, we have $\Phi(t_\star) = \Phi_0 + \Phi(f)$ and $t_\star = t_0 + t(f)$. We expand

$$\Phi(t) \approx \Phi(t_\star) + 2\pi f(t-t_\star) + \frac{1}{2}\ddot\Phi(t_\star)(t-t_\star)^2, \tag{F.9}$$

we drop the first exponential factor and write

$$\begin{aligned} h_+(f) &\approx \frac{1}{2}a(t_\star)e^{-i\Phi(t_\star)+2\pi f t_\star}\int dt\, e^{-\frac{i}{2}\ddot\Phi(t_\star)(t-t_\star)^2} \\ &= \frac{1}{2}a(t_\star)e^{-i\Phi(t_\star)+2\pi f t_\star - i\pi/4}\sqrt{\frac{2\pi}{\ddot\Phi(t_\star)}}. \end{aligned} \tag{F.10}$$

We therefore obtain

$$h_{+,\times}(f) = A_{+,\times}(f)e^{i\Psi_{+,\times}(f)}, \tag{F.11}$$

where the amplitudes are given by

$$A_+(f) = \frac{2}{D_L}\frac{1+\cos^2\iota}{2}\frac{(GM_c)^{5/3}(\pi f)^{2/3}}{\dot f^{1/2}}, \tag{F.12}$$

$$A_\times(f) = \frac{2}{D_L}\cos\iota\frac{(GM_c)^{5/3}(\pi f)^{2/3}}{\dot f^{1/2}}, \tag{F.13}$$

and the phases are

$$\Psi_+(f) = 2\pi[t_0 + t(f)] - \Phi_0 - \Phi(f) - \frac{\pi}{4}, \tag{F.14}$$

$$\Psi_\times(f) = 2\pi[t_0 + t(f)] - \Phi_0 - \Phi(f) + \frac{\pi}{4}. \tag{F.15}$$

Bibliography

[1] V.C. Rubin and W.K. Ford Jr, *Rotation of the andromeda nebula from a spectroscopic survey of emission regions*, *The Astrophysical Journal* **159** (1970) 379.

[2] K.C. Freeman, *On the disks of spiral and s0 galaxies*, *Astrophysical Journal, vol. 160, p. 811* **160** (1970) 811.

[3] J.P. Ostriker and P.J. Peebles, *A numerical study of the stability of flattened galaxies: or, can cold galaxies survive?*, *The Astrophysical Journal* **186** (1973) 467.

[4] F. Zwicky, *Die Rotverschiebung von extragalaktischen Nebeln*, *Helv. Phys. Acta* **6** (1933) 110.

[5] S. Smith, *The Mass of the Virgo Cluster*, *Astrophys. J.* **83** (1936) 23.

[6] A.H. Gonzalez, S. Sivanandam, A.I. Zabludoff and D. Zaritsky, *Galaxy Cluster Baryon Fractions Revisited*, *Astrophys. J.* **778** (2013) 14 [1309.3565].

[7] J.A. Tyson, G.P. Kochanski and I.P. Dell'Antonio, *Detailed mass map of CL0024+1654 from strong lensing*, *Astrophys. J. Lett.* **498** (1998) L107 [astro-ph/9801193].

[8] D. Clowe, M. Bradac, A.H. Gonzalez, M. Markevitch, S.W. Randall, C. Jones et al., *A direct empirical proof of the existence of dark matter*, *Astrophys. J. Lett.* **648** (2006) L109 [astro-ph/0608407].

[9] PLANCK collaboration, *Planck 2018 results. VI. Cosmological parameters*, *Astron. Astrophys.* **641** (2020) A6 [1807.06209].

[10] DES collaboration, *Dark Energy Survey Year 3 results: Cosmological constraints from galaxy clustering and weak lensing*, *Phys. Rev. D* **105** (2022) 023520 [2105.13549].

[11] M. Milgrom, *A modification of the newtonian dynamics as a possible alternative to the hidden mass hypothesis*, *Astrophysical Journal, Part 1 (ISSN 0004-637X), vol. 270, July 15, 1983, p. 365-370. Research supported by the US-Israel Binational Science Foundation.* **270** (1983) 365.

[12] J.D. Bekenstein, *Relativistic gravitation theory for the MOND paradigm*, *Phys. Rev. D* **70** (2004) 083509 [astro-ph/0403694].

[13] A. Aguirre, J. Schaye and E. Quataert, *Problems for modified newtonian dynamics in clusters and the lyα forest?*, *The Astrophysical Journal* **561** (2001) 550.

[14] A. Abramovici and Z. Vager, *Test of newton's second law at small accelerations*, *Physical review D* **34** (1986) 3240.

[15] J. Billard et al., *Direct detection of dark matter—APPEC committee report**, *Rept. Prog. Phys.* **85** (2022) 056201 [2104.07634].

[16] S. Tremaine and J.E. Gunn, *Dynamical Role of Light Neutral Leptons in Cosmology*, *Phys. Rev. Lett.* **42** (1979) 407.

[17] A. Boyarsky, O. Ruchayskiy and D. Iakubovskyi, *A Lower bound on the mass of Dark Matter particles*, *JCAP* **03** (2009) 005 [0808.3902].

[18] C. Di Paolo, F. Nesti and F.L. Villante, *Phase space mass bound for fermionic dark matter from dwarf spheroidal galaxies*, *Mon. Not. Roy. Astron. Soc.* **475** (2018) 5385 [1704.06644].

[19] D. Savchenko and A. Rudakovskyi, *New mass bound on fermionic dark matter from a combined analysis of classical dSphs*, *Mon. Not. Roy. Astron. Soc.* **487** (2019) 5711 [1903.01862].

[20] J. Alvey, N. Sabti, V. Tiki, D. Blas, K. Bondarenko, A. Boyarsky et al., *New Constraints on the Mass of Fermionic Dark Matter from Dwarf Spheroidal Galaxies*, 2010.03572.

[21] L. Hui, *Wave Dark Matter*, 2101.11735.

[22] M.S. Turner, *Coherent Scalar Field Oscillations in an Expanding Universe*, *Phys. Rev. D* **28** (1983) 1243.

[23] W.H. Press, B.S. Ryden and D.N. Spergel, *Single Mechanism for Generating Large Scale Structure and Providing Dark Missing Matter*, *Phys. Rev. Lett.* **64** (1990) 1084.

[24] S.-J. Sin, *Late time cosmological phase transition and galactic halo as Bose liquid*, *Phys. Rev. D* **50** (1994) 3650 [hep-ph/9205208].

[25] W. Hu, R. Barkana and A. Gruzinov, *Cold and fuzzy dark matter*, *Phys. Rev. Lett.* **85** (2000) 1158 [astro-ph/0003365].

[26] J. Goodman, *Repulsive dark matter*, *New Astron.* **5** (2000) 103 [astro-ph/0003018].

[27] P.J.E. Peebles, *Fluid dark matter*, *Astrophys. J. Lett.* **534** (2000) L127 [astro-ph/0002495].

[28] L. Amendola and R. Barbieri, *Dark matter from an ultra-light pseudo-Goldsone-boson*, *Phys. Lett. B* **642** (2006) 192 [hep-ph/0509257].

[29] H.-Y. Schive, T. Chiueh and T. Broadhurst, *Cosmic Structure as the Quantum Interference of a Coherent Dark Wave*, *Nature Phys.* **10** (2014) 496 [1406.6586].

[30] D.N. Spergel and P.J. Steinhardt, *Observational evidence for selfinteracting cold dark matter*, *Phys. Rev. Lett.* **84** (2000) 3760 [astro-ph/9909386].

[31] D.H. Weinberg, J.S. Bullock, F. Governato, R. Kuzio de Naray and A.H.G. Peter, *Cold dark matter: controversies on small scales*, *Proc. Nat. Acad. Sci.* **112** (2015) 12249 [1306.0913].

[32] M.G. Walker and A. Loeb, *Is the universe simpler than ΛCDM?*, *Contemp. Phys.* **55** (2014) 198 [1401.1146].

[33] L. Hui, J.P. Ostriker, S. Tremaine and E. Witten, *Ultralight scalars as cosmological dark matter*, *Phys. Rev. D* **95** (2017) 043541 [1610.08297].

[34] C. O'Hare, "cajohare/axionlimits: Axionlimits." https://cajohare.github.io/AxionLimits/, July, 2020. 10.5281/zenodo.3932430.

[35] A. Arvanitaki and S. Dubovsky, *Exploring the String Axiverse with Precision Black Hole Physics*, *Phys. Rev. D* **83** (2011) 044026 [1004.3558].

[36] R. Brito, V. Cardoso and P. Pani, *Black holes as particle detectors: evolution of superradiant instabilities*, *Class. Quant. Grav.* **32** (2015) 134001 [1411.0686].

[37] R. Brito, V. Cardoso and P. Pani, *Superradiance: New Frontiers in Black Hole Physics*, *Lect. Notes Phys.* **906** (2015) pp.1 [1501.06570].

[38] A. Arvanitaki, M. Baryakhtar, S. Dimopoulos, S. Dubovsky and R. Lasenby, *Black Hole Mergers and the QCD Axion at Advanced LIGO*, *Phys. Rev. D* **95** (2017) 043001 [1604.03958].

[39] R. Brito, S. Ghosh, E. Barausse, E. Berti, V. Cardoso, I. Dvorkin et al., *Gravitational wave searches for ultralight bosons with LIGO and LISA*, *Phys. Rev. D* **96** (2017) 064050 [1706.06311].

[40] A. Arvanitaki, J. Huang and K. Van Tilburg, *Searching for dilaton dark matter with atomic clocks*, *Phys. Rev. D* **91** (2015) 015015 [1405.2925].

[41] V. Cardoso, O.J.C. Dias, G.S. Hartnett, M. Middleton, P. Pani and J.E. Santos, *Constraining the mass of dark photons and axion-like particles through black-hole superradiance*, *JCAP* **03** (2018) 043 [1801.01420].

[42] J. Binney and S. Tremaine, *Galactic Dynamics: Second Edition* (2008).

[43] R. Ruffini and S. Bonazzola, *Systems of selfgravitating particles in general relativity and the concept of an equation of state*, *Phys. Rev.* **187** (1969) 1767.

[44] C. Uhlemann, M. Kopp and T. Haugg, *Schrödinger method as N-body double and UV completion of dust*, *Phys. Rev. D* **90** (2014) 023517 [1403.5567].

[45] M. Garny, T. Konstandin and H. Rubira, *The Schrödinger-Poisson method for Large-Scale Structure*, *JCAP* **04** (2020) 003 [1911.04505].

[46] B. Bar-Or, J.-B. Fouvry and S. Tremaine, *Relaxation in a Fuzzy Dark Matter Halo*, *Astrophys. J.* **871** (2019) 28 [1809.07673].

[47] B. Bar-Or, J.-B. Fouvry and S. Tremaine, *Relaxation in a Fuzzy Dark Matter Halo. II. Self-consistent Kinetic Equations*, *Astrophys. J.* **915** (2021) 27 [2010.10212].

[48] J. Bovy and S. Tremaine, *On the local dark matter density*, *The Astrophysical Journal* **756** (2012) 89.

[49] S. Sivertsson, H. Silverwood, J.I. Read, G. Bertone and P. Steger, *The localdark matter density from sdss-segue g-dwarfs*, *Monthly Notices of the Royal Astronomical Society* **478** (2018) 1677.

[50] C.F. McKee, A. Parravano and D.J. Hollenbach, *Stars, gas, and dark matter in the solar neighborhood*, *The Astrophysical Journal* **814** (2015) 13.

[51] A.-C. Eilers, D.W. Hogg, H.-W. Rix and M.K. Ness, *The circular velocity curve of the milky way from 5 to 25 kpc*, *The Astrophysical Journal* **871** (2019) 120.

[52] A.K. Drukier, K. Freese and D.N. Spergel, *Detecting Cold Dark Matter Candidates*, *Phys. Rev. D* **33** (1986) 3495.

[53] K. Freese, J.A. Frieman and A. Gould, *Signal Modulation in Cold Dark Matter Detection*, *Phys. Rev. D* **37** (1988) 3388.

[54] M. Vogelsberger, A. Helmi, V. Springel, S.D.M. White, J. Wang, C.S. Frenk et al., *Phase-space structure in the local dark matter distribution and its signature in direct detection experiments*, *Mon. Not. Roy. Astron. Soc.* **395** (2009) 797 [0812.0362].

[55] M. Kuhlen, N. Weiner, J. Diemand, P. Madau, B. Moore, D. Potter et al., *Dark Matter Direct Detection with Non-Maxwellian Velocity Structure*, *JCAP* **02** (2010) 030 [0912.2358].

[56] V. Belokurov, D. Erkal, N. Evans, S. Koposov and A. Deason, *Co-formation of the disc and the stellar halo*, *Monthly Notices of the Royal Astronomical Society* **478** (2018) 611.

[57] A. Helmi, C. Babusiaux, H.H. Koppelman, D. Massari, J. Veljanoski and A.G. Brown, *The merger that led to the formation of the milky way's inner stellar halo and thick disk*, *Nature* **563** (2018) 85.

[58] L. Necib, M. Lisanti, S. Garrison-Kimmel, A. Wetzel, R. Sanderson, P.F. Hopkins et al., *Under the Firelight: Stellar Tracers of the Local Dark Matter Velocity Distribution in the Milky Way*, 1810.12301.

[59] L. Necib, M. Lisanti and V. Belokurov, *Inferred Evidence For Dark Matter Kinematic Substructure with SDSS-Gaia*, 1807.02519.

[60] N.W. Evans, C.A.J. O'Hare and C. McCabe, *Refinement of the standard halo model for dark matter searches in light of the Gaia Sausage*, *Phys. Rev. D* **99** (2019) 023012 [1810.11468].

[61] C.A.J. O'Hare, C. McCabe, N.W. Evans, G. Myeong and V. Belokurov, *Dark matter hurricane: Measuring the S1 stream with dark matter detectors*, *Phys. Rev. D* **98** (2018) 103006 [1807.09004].

[62] C.A.J. O'Hare, N.W. Evans, C. McCabe, G. Myeong and V. Belokurov, *Velocity substructure from Gaia and direct searches for dark matter*, *Phys. Rev. D* **101** (2020) 023006 [1909.04684].

[63] A. Helmi, *Streams, substructures, and the early history of the milky way*, *Annual Review of Astronomy and Astrophysics* **58** (2020) 205.

[64] J. Read, G. Lake, O. Agertz and V.P. Debattista, *Thin, thick and dark discs in λcdm*, *Monthly Notices of the Royal Astronomical Society* **389** (2008) 1041.

[65] J. Danby and G. Camm, *Statistical dynamics and accretion*, *Monthly Notices of the Royal Astronomical Society* **117** (1957) 50.

[66] J. Danby and T. Bray, *Density of interstellar matter near a star*, *Astronomical Journal, Vol. 72, p. 219 (1967)* **72** (1967) 219.

[67] K. Griest, *Effect of the Sun's Gravity on the Distribution and Detection of Dark Matter Near the Earth*, *Phys. Rev. D* **37** (1988) 2703.

[68] P. Sikivie and S. Wick, *Solar wakes of dark matter flows*, *Phys. Rev. D* **66** (2002) 023504 [astro-ph/0203448].

[69] M.S. Alenazi and P. Gondolo, *Phase-space distribution of unbound dark matter near the Sun*, *Phys. Rev. D* **74** (2006) 083518 [astro-ph/0608390].

[70] S.K. Lee, M. Lisanti, A.H.G. Peter and B.R. Safdi, *Effect of Gravitational Focusing on Annual Modulation in Dark-Matter Direct-Detection Experiments*, *Phys. Rev. Lett.* **112** (2014) 011301 [1308.1953].

[71] ADMX collaboration, *A Search for Invisible Axion Dark Matter with the Axion Dark Matter Experiment*, *Phys. Rev. Lett.* **120** (2018) 151301 [1804.05750].

[72] ADMX collaboration, *Extended Search for the Invisible Axion with the Axion Dark Matter Experiment*, *Phys. Rev. Lett.* **124** (2020) 101303 [1910.08638].

[73] ADMX collaboration, *Search for "Invisible" Axion Dark Matter in the 3.3-4.2 μeV Mass Range*, 2110.06096.

[74] B.M. Brubaker et al., *First results from a microwave cavity axion search at 24 μeV*, *Phys. Rev. Lett.* **118** (2017) 061302 [1610.02580].

[75] HAYSTAC collaboration, *Results from phase 1 of the HAYSTAC microwave cavity axion experiment*, *Phys. Rev. D* **97** (2018) 092001 [1803.03690].

[76] Y. Kahn, B.R. Safdi and J. Thaler, *Broadband and Resonant Approaches to Axion Dark Matter Detection*, *Phys. Rev. Lett.* **117** (2016) 141801 [1602.01086].

[77] J.L. Ouellet et al., *First Results from ABRACADABRA-10 cm: A Search for Sub-μeV Axion Dark Matter*, *Phys. Rev. Lett.* **122** (2019) 121802 [1810.12257].

[78] S. Chaudhuri, K. Irwin, P.W. Graham and J. Mardon, *Optimal Impedance Matching and Quantum Limits of Electromagnetic Axion and Hidden-Photon Dark Matter Searches*, 1803.01627.

[79] CAPP collaboration, *First Results from an Axion Haloscope at CAPP around 10.7 μeV*, *Phys. Rev. Lett.* **126** (2021) 191802 [2012.10764].

[80] MADMAX WORKING GROUP collaboration, *Dielectric Haloscopes: A New Way to Detect Axion Dark Matter*, *Phys. Rev. Lett.* **118** (2017) 091801 [1611.05865].

[81] B.T. McAllister, G. Flower, J. Kruger, E.N. Ivanov, M. Goryachev, J. Bourhill et al., *The ORGAN Experiment: An axion haloscope above 15 GHz*, *Phys. Dark Univ.* **18** (2017) 67 [1706.00209].

[82] D. Alesini et al., *Galactic axions search with a superconducting resonant cavity*, *Phys. Rev. D* **99** (2019) 101101 [1903.06547].

[83] D. Alesini et al., *Search for invisible axion dark matter of mass $m_a = 43$ μeV with the QUAX–aγ experiment*, *Phys. Rev. D* **103** (2021) 102004 [2012.09498].

[84] D. Horns, J. Jaeckel, A. Lindner, A. Lobanov, J. Redondo and A. Ringwald, *Searching for WISPy Cold Dark Matter with a Dish Antenna*, *JCAP* **04** (2013) 016 [1212.2970].

[85] N. Crisosto, P. Sikivie, N.S. Sullivan, D.B. Tanner, J. Yang and G. Rybka, *ADMX SLIC: Results from a Superconducting LC Circuit Investigating Cold Axions*, *Phys. Rev. Lett.* **124** (2020) 241101 [1911.05772].

[86] A.V. Gramolin, D. Aybas, D. Johnson, J. Adam and A.O. Sushkov, *Search for axion-like dark matter with ferromagnets*, *Nature Phys.* **17** (2021) 79 [2003.03348].

[87] J.A. Devlin et al., *Constraints on the Coupling between Axionlike Dark Matter and Photons Using an Antiproton Superconducting Tuned Detection Circuit in a Cryogenic Penning Trap*, *Phys. Rev. Lett.* **126** (2021) 041301 [2101.11290].

[88] M. Baryakhtar, J. Huang and R. Lasenby, *Axion and hidden photon dark matter detection with multilayer optical haloscopes*, *Phys. Rev. D* **98** (2018) 035006 [1803.11455].

[89] A. Arvanitaki, S. Dimopoulos and K. Van Tilburg, *Resonant absorption of bosonic dark matter in molecules*, *Phys. Rev. X* **8** (2018) 041001 [1709.05354].

[90] C.A. Thomson, B.T. McAllister, M. Goryachev, E.N. Ivanov and M.E. Tobar, *Upconversion Loop Oscillator Axion Detection Experiment: A Precision Frequency Interferometric Axion Dark Matter Search with a Cylindrical Microwave Cavity*, *Phys. Rev. Lett.* **126** (2021) 081803 [1912.07751].

[91] A. Berlin, R.T. D'Agnolo, S.A.R. Ellis, C. Nantista, J. Neilson, P. Schuster et al., *Axion Dark Matter Detection by Superconducting Resonant Frequency Conversion*, *JHEP* **07** (2020) 088 [1912.11048].

[92] P. Sikivie, *Axion Dark Matter Detection using Atomic Transitions*, *Phys. Rev. Lett.* **113** (2014) 201301 [1409.2806].

[93] S.-C. Lin, H.-Y. Schive, S.-K. Wong and T. Chiueh, *Self-consistent construction of virialized wave dark matter halos*, *Phys. Rev. D* **97** (2018) 103523 [1801.02320].

[94] D. Antypas, O. Tretiak, A. Garcon, R. Ozeri, G. Perez and D. Budker, *Scalar dark matter in the radio-frequency band: atomic-spectroscopy search results*, *Phys. Rev. Lett.* **123** (2019) 141102 [1905.02968].

[95] I.G. Irastorza, *An introduction to axions and their detection*, *SciPost Phys. Lect. Notes* **45** (2022) 1 [2109.07376].

[96] D. Antypas et al., *New Horizons: Scalar and Vector Ultralight Dark Matter*, 2203.14915.

[97] C.B. Adams et al., *Axion Dark Matter*, in *Snowmass 2021*, 3, 2022 [2203.14923].

[98] PARTICLE DATA GROUP collaboration, *Review of Particle Physics*, *PTEP* **2022** (2022) 083C01.

[99] P. Gondolo and J. Silk, *Dark matter annihilation at the galactic center*, *Phys. Rev. Lett.* **83** (1999) 1719 [astro-ph/9906391].

[100] D. Horns, *TeV gamma-radiation from dark matter annihilation in the Galactic center*, *Phys. Lett. B* **607** (2005) 225 [astro-ph/0408192].

[101] V. Cardoso, T. Ikeda, R. Vicente and M. Zilhão, *Parasitic black holes: The swallowing of a fuzzy dark matter soliton*, *Phys. Rev. D* **106** (2022) L121302 [2207.09469].

[102] K. Eda, Y. Itoh, S. Kuroyanagi and J. Silk, *New Probe of Dark-Matter Properties: Gravitational Waves from an Intermediate-Mass Black Hole Embedded in a Dark-Matter Minispike*, *Phys. Rev. Lett.* **110** (2013) 221101 [1301.5971].

[103] K. Eda, Y. Itoh, S. Kuroyanagi and J. Silk, *Gravitational waves as a probe of dark matter minispikes*, *Phys. Rev. D* **91** (2015) 044045 [1408.3534].

[104] B.J. Kavanagh, D.A. Nichols, G. Bertone and D. Gaggero, *Detecting dark matter around black holes with gravitational waves: Effects of dark-matter dynamics on the gravitational waveform*, *Phys. Rev. D* **102** (2020) 083006 [2002.12811].

[105] A. Coogan, G. Bertone, D. Gaggero, B.J. Kavanagh and D.A. Nichols, *Measuring the dark matter environments of black hole binaries with gravitational waves*, *Phys. Rev. D* **105** (2022) 043009 [2108.04154].

[106] H. Kim and A. Lenoci, *Gravitational focusing of wave dark matter*, *Phys. Rev. D* **105** (2022) 063032 [2112.05718].

[107] H. Kim, A. Lenoci, I. Stomberg and X. Xue, *Adiabatically compressed wave dark matter halo and intermediate-mass-ratio inspirals*, *Phys. Rev. D* **107** (2023) 083005 [2212.07528].

[108] H.-Y. Schive, M.-H. Liao, T.-P. Woo, S.-K. Wong, T. Chiueh, T. Broadhurst et al., *Understanding the Core-Halo Relation of Quantum Wave Dark Matter from 3D Simulations*, *Phys. Rev. Lett.* **113** (2014) 261302 [1407.7762].

[109] T.D. Yavetz, X. Li and L. Hui, *Construction of wave dark matter halos: Numerical algorithm and analytical constraints*, *Phys. Rev. D* **105** (2022) 023512 [2109.06125].

[110] LISA collaboration, *Laser Interferometer Space Antenna*, 1702.00786.

[111] G. Bertone, D. Hooper and J. Silk, *Particle dark matter: Evidence, candidates and constraints*, *Phys. Rept.* **405** (2005) 279 [hep-ph/0404175].

[112] K. Freese, *Status of Dark Matter in the Universe*, *Int. J. Mod. Phys.* **1** (2017) 325 [1701.01840].

[113] M. Bauer and T. Plehn, *Yet Another Introduction to Dark Matter: The Particle Physics Approach*, vol. 959 of *Lecture Notes in Physics*, Springer (2019), 10.1007/978-3-030-16234-4, [1705.01987].

[114] A.M. Green, *Dark matter in astrophysics/cosmology*, *SciPost Phys. Lect. Notes* **37** (2022) 1 [2109.05854].

[115] K. Begeman, A. Broeils and R. Sanders, *Extended rotation curves of spiral galaxies: Dark haloes and modified dynamics*, *Monthly Notices of the Royal Astronomical Society* **249** (1991) 523.

[116] R.P. Olling and M.R. Merrifield, *Two measures of the shape of the dark halo of the milky way*, *Monthly Notices of the Royal Astronomical Society* **311** (2000) 361.

[117] F. Iocco, M. Pato and G. Bertone, *Evidence for dark matter in the inner Milky Way*, *Nature Phys.* **11** (2015) 245 [1502.03821].

[118] J. Sakstein and B. Jain, *Implications of the Neutron Star Merger GW170817 for Cosmological Scalar-Tensor Theories*, *Phys. Rev. Lett.* **119** (2017) 251303 [1710.05893].

[119] R. Massey, T. Kitching and J. Richard, *The dark matter of gravitational lensing*, *Rept. Prog. Phys.* **73** (2010) 086901 [1001.1739].

[120] S. Dodelson and F. Schmidt, *Modern Cosmology* (2020), 10.1016/C2017-0-01943-2.

[121] PLANCK collaboration, *Planck 2015 results. XIII. Cosmological parameters*, *Astron. Astrophys.* **594** (2016) A13 [1502.01589].

[122] B.D. Fields, P. Molaro and S. Sarkar, *Big-Bang Nucleosynthesis*, *Chin. Phys. C* **38** (2014) 339 [1412.1408].

[123] SUPERNOVA COSMOLOGY PROJECT collaboration, *Measurements of Ω and Λ from 42 high redshift supernovae*, *Astrophys. J.* **517** (1999) 565 [astro-ph/9812133].

[124] X. Wang, M. Tegmark, B. Jain and M. Zaldarriaga, *The Last stand before MAP: Cosmological parameters from lensing, CMB and galaxy clustering*, *Phys. Rev. D* **68** (2003) 123001 [astro-ph/0212417].

[125] WMAP collaboration, *First year Wilkinson Microwave Anisotropy Probe (WMAP) observations: The Angular power spectrum*, *Astrophys. J. Suppl.* **148** (2003) 135 [astro-ph/0302217].

[126] SDSS collaboration, *The 3-D power spectrum of galaxies from the SDSS*, *Astrophys. J.* **606** (2004) 702 [astro-ph/0310725].

[127] H. Hoekstra, H.K.C. Yee and M.D. Gladders, *Constraints on Omega(M) and Sigma(8) from weak lensing in RCS fields*, *Astrophys. J.* **577** (2002) 595 [astro-ph/0204295].

[128] N.Y. Gnedin and A.J.S. Hamilton, *Matter power spectrum from the Lyman-alpha forest: Myth or reality?*, *Mon. Not. Roy. Astron. Soc.* **334** (2002) 107 [astro-ph/0111194].

[129] R.A. Croft, D.H. Weinberg, M. Pettini, L. Hernquist and N. Katz, *The power spectrum of mass fluctuations measured from the lyα forest at redshift z= 2.5*, *The Astrophysical Journal* **520** (1999) 1.

[130] D.J. Eisenstein and W. Hu, *Baryonic features in the matter transfer function*, *Astrophys. J.* **496** (1998) 605 [astro-ph/9709112].

[131] D. Maniscalco, *La gerarchia dei vuoti nell'universo*, *Thesis Unipd* (2018) .

[132] G.L. Bryan and M.L. Norman, *Statistical properties of x-ray clusters: Analytic and numerical comparisons*, *Astrophys. J.* **495** (1998) 80 [astro-ph/9710107].

[133] W.H. Press and P. Schechter, *Formation of galaxies and clusters of galaxies by selfsimilar gravitational condensation*, *Astrophys. J.* **187** (1974) 425.

[134] J. Bond, S. Cole, G. Efstathiou and N. Kaiser, *Excursion set mass functions for hierarchical gaussian fluctuations*, *The Astrophysical Journal* **379** (1991) 440.

[135] J.F. Navarro, C.S. Frenk and S.D.M. White, *The Structure of cold dark matter halos*, *Astrophys. J.* **462** (1996) 563 [astro-ph/9508025].

[136] J.F. Navarro, C.S. Frenk and S.D.M. White, *A Universal density profile from hierarchical clustering*, *Astrophys. J.* **490** (1997) 493 [astro-ph/9611107].

[137] J.I. Read, *The Local Dark Matter Density*, *J. Phys. G* **41** (2014) 063101 [1404.1938].

[138] P.F. de Salas and A. Widmark, *Dark matter local density determination: recent observations and future prospects*, *Rept. Prog. Phys.* **84** (2021) 104901 [2012.11477].

[139] G. De Risi, T. Harko and F.S.N. Lobo, *Solar System constraints on local dark matter density*, *JCAP* **07** (2012) 047 [1206.2747].

[140] M. Reid, K. Menten, X. Zheng, A. Brunthaler, L. Moscadelli, Y. Xu et al., *Trigonometric parallaxes of massive star-forming regions. vi. galactic structure, fundamental parameters, and noncircular motions*, *The Astrophysical Journal* **700** (2009) 137.

[141] R. Abuter, A. Amorim, M. Bauböck, J. Berger, H. Bonnet, W. Brandner et al., *A geometric distance measurement to the galactic center black hole with 0.3% uncertainty*, *Astronomy & Astrophysics* **625** (2019) L10.

[142] G. Monari, B. Famaey, I. Carrillo, T. Piffl, M. Steinmetz, R.F. Wyse et al., *The escape speed curve of the galaxy obtained from gaia dr2 implies a heavy milky way*, *Astronomy & Astrophysics* **616** (2018) L9.

[143] G.C. Myeong, N.W. Evans, V. Belokurov, N.C. Amorisco and S. Koposov, *Halo Substructure in the SDSS-Gaia Catalogue : Streams and Clumps*, *Mon. Not. Roy. Astron. Soc.* **475** (2018) 1537 [1712.04071].

[144] H.H. Koppelman, A. Helmi, D. Massari, S. Roelenga and U. Bastian, *Characterization and history of the helmi streams with gaia dr2*, *Astronomy & Astrophysics* **625** (2019) A5.

[145] L. Necib, B. Ostdiek, M. Lisanti, T. Cohen, M. Freytsis, S. Garrison-Kimmel et al., *Evidence for a vast prograde stellar stream in the solar vicinity*, *Nature Astron.* **4** (2020) 1078 [1907.07190].

[146] S. Profumo, L. Giani and O.F. Piattella, *An introduction to particle dark matter*, *Universe* **5** (2019) .

[147] V. Iršič et al., *New Constraints on the free-streaming of warm dark matter from intermediate and small scale Lyman-α forest data*, *Phys. Rev. D* **96** (2017) 023522 [1702.01764].

[148] J.B. Muñoz and A. Loeb, *A small amount of mini-charged dark matter could cool the baryons in the early universe*, *Nature* **557** (2018) 684.

[149] T. Brinckmann, J. Zavala, D. Rapetti, S.H. Hansen and M. Vogelsberger, *The structure and assembly history of cluster-sized haloes in self-interacting dark matter*, *Mon. Not. Roy. Astron. Soc.* **474** (2018) 746 [1705.00623].

[150] M. Rocha, A.H.G. Peter, J.S. Bullock, M. Kaplinghat, S. Garrison-Kimmel, J. Onorbe et al., *Cosmological Simulations with Self-Interacting Dark Matter I: Constant Density Cores and Substructure*, *Mon. Not. Roy. Astron. Soc.* **430** (2013) 81 [1208.3025].

[151] B. Audren, J. Lesgourgues, G. Mangano, P.D. Serpico and T. Tram, *Strongest model-independent bound on the lifetime of Dark Matter*, *JCAP* **12** (2014) 028 [1407.2418].

[152] T.R. Slatyer and C.-L. Wu, *General Constraints on Dark Matter Decay from the Cosmic Microwave Background*, *Phys. Rev. D* **95** (2017) 023010 [1610.06933].

[153] D.J.E. Marsh, *Axion Cosmology*, *Phys. Rept.* **643** (2016) 1 [1510.07633].

[154] R.D. Peccei and H.R. Quinn, *CP Conservation in the Presence of Instantons*, *Phys. Rev. Lett.* **38** (1977) 1440.

[155] R.D. Peccei and H.R. Quinn, *Constraints Imposed by CP Conservation in the Presence of Instantons*, *Phys. Rev. D* **16** (1977) 1791.

[156] S. Weinberg, *A New Light Boson?*, *Phys. Rev. Lett.* **40** (1978) 223.

[157] F. Wilczek, *Problem of Strong P and T Invariance in the Presence of Instantons*, *Phys. Rev. Lett.* **40** (1978) 279.

[158] B. Holdom, *Two U(1)'s and Epsilon Charge Shifts*, *Phys. Lett. B* **166** (1986) 196.

[159] P. Fayet, *Extra U(1)'s and New Forces*, *Nucl. Phys. B* **347** (1990) 743.

[160] P. Fayet, *Effects of the Spin 1 Partner of the Goldstino (Gravitino) on Neutral Current Phenomenology*, *Phys. Lett. B* **95** (1980) 285.

[161] P. Fayet, *On the Search for a New Spin 1 Boson*, *Nucl. Phys. B* **187** (1981) 184.

[162] L.B. Okun, *LIMITS OF ELECTRODYNAMICS: PARAPHOTONS?*, *Sov. Phys. JETP* **56** (1982) 502.

[163] H. Georgi, P.H. Ginsparg and S.L. Glashow, *Photon Oscillations and the Cosmic Background Radiation*, *Nature* **306** (1983) 765.

[164] R.J. Crewther, P. Di Vecchia, G. Veneziano and E. Witten, *Chiral Estimate of the Electric Dipole Moment of the Neutron in Quantum Chromodynamics*, *Phys. Lett. B* **88** (1979) 123.

[165] C. Abel et al., *Search for Axionlike Dark Matter through Nuclear Spin Precession in Electric and Magnetic Fields*, *Phys. Rev. X* **7** (2017) 041034 [1708.06367].

[166] C. Vafa and E. Witten, *Parity Conservation in QCD*, *Phys. Rev. Lett.* **53** (1984) 535.

[167] D.J.E. Marsh and A.-R. Pop, *Axion dark matter, solitons and the cusp–core problem*, *Mon. Not. Roy. Astron. Soc.* **451** (2015) 2479 [1502.03456].

[168] E.W. Kolb and M.S. Turner, *The Early Universe*, vol. 69 (1990), 10.1201/9780429492860.

[169] P.W. Graham and S. Rajendran, *New Observables for Direct Detection of Axion Dark Matter*, *Phys. Rev. D* **88** (2013) 035023 [1306.6088].

[170] P. Svrcek and E. Witten, *Axions In String Theory*, *JHEP* **06** (2006) 051 [hep-th/0605206].

[171] A. Arvanitaki, S. Dimopoulos, S. Dubovsky, N. Kaloper and J. March-Russell, *String Axiverse*, *Phys. Rev. D* **81** (2010) 123530 [0905.4720].

[172] B.S. Acharya, K. Bobkov and P. Kumar, *An M Theory Solution to the Strong CP Problem and Constraints on the Axiverse*, *JHEP* **11** (2010) 105 [1004.5138].

[173] M. Cicoli, M. Goodsell and A. Ringwald, *The type IIB string axiverse and its low-energy phenomenology*, *JHEP* **10** (2012) 146 [1206.0819].

[174] P.W. Graham, D.E. Kaplan and S. Rajendran, *Cosmological Relaxation of the Electroweak Scale*, *Phys. Rev. Lett.* **115** (2015) 221801 [1504.07551].

[175] A. Arvanitaki, S. Dimopoulos, V. Gorbenko, J. Huang and K. Van Tilburg, *A small weak scale from a small cosmological constant*, *JHEP* **05** (2017) 071 [1609.06320].

[176] A. Banerjee, H. Kim and G. Perez, *Coherent relaxion dark matter*, *Phys. Rev. D* **100** (2019) 115026 [1810.01889].

[177] A. Banerjee, H. Kim, O. Matsedonskyi, G. Perez and M.S. Safronova, *Probing the Relaxed Relaxion at the Luminosity and Precision Frontiers*, *JHEP* **07** (2020) 153 [2004.02899].

[178] N. Arkani-Hamed, R. Tito D'agnolo and H.D. Kim, *Weak scale as a trigger*, *Phys. Rev. D* **104** (2021) 095014 [2012.04652].

[179] R. Tito D'Agnolo and D. Teresi, *Sliding Naturalness*, 2106.04591.

[180] R. Tito D'Agnolo and D. Teresi, *Sliding Naturalness: Cosmological Selection of the Weak Scale*, 2109.13249.

[181] A. Chatrchyan and G. Servant, *Relaxion Dark Matter from Stochastic Misalignment*, 2211.15694.

[182] A. Chatrchyan and G. Servant, *The Stochastic Relaxion*, 2210.01148.

[183] M. Fabbrichesi, E. Gabrielli and G. Lanfranchi, *The Dark Photon*, 2005.01515.

[184] H. Ruegg and M. Ruiz-Altaba, *The Stueckelberg field*, *Int. J. Mod. Phys. A* **19** (2004) 3265 [hep-th/0304245].

[185] A.E. Nelson and J. Scholtz, *Dark Light, Dark Matter and the Misalignment Mechanism*, *Phys. Rev. D* **84** (2011) 103501 [1105.2812].

[186] P. Arias, D. Cadamuro, M. Goodsell, J. Jaeckel, J. Redondo and A. Ringwald, *WISPy Cold Dark Matter*, *JCAP* **06** (2012) 013 [1201.5902].

[187] P.W. Graham, J. Mardon and S. Rajendran, *Vector Dark Matter from Inflationary Fluctuations*, *Phys. Rev. D* **93** (2016) 103520 [1504.02102].

[188] Y. Nakai, R. Namba and Z. Wang, *Light Dark Photon Dark Matter from Inflation*, *JHEP* **12** (2020) 170 [2004.10743].

[189] J.A. Dror, K. Harigaya and V. Narayan, *Parametric Resonance Production of Ultralight Vector Dark Matter*, *Phys. Rev. D* **99** (2019) 035036 [1810.07195].

[190] P. Agrawal, N. Kitajima, M. Reece, T. Sekiguchi and F. Takahashi, *Relic Abundance of Dark Photon Dark Matter*, *Phys. Lett. B* **801** (2020) 135136 [1810.07188].

[191] R.T. Co, A. Pierce, Z. Zhang and Y. Zhao, *Dark Photon Dark Matter Produced by Axion Oscillations*, *Phys. Rev. D* **99** (2019) 075002 [1810.07196].

[192] R.T. Co, K. Harigaya and A. Pierce, *Gravitational waves and dark photon dark matter from axion rotations*, *JHEP* **12** (2021) 099 [2104.02077].

[193] M. Bastero-Gil, J. Santiago, L. Ubaldi and R. Vega-Morales, *Vector dark matter production at the end of inflation*, *JCAP* **04** (2019) 015 [1810.07208].

[194] A.J. Long and L.-T. Wang, *Dark Photon Dark Matter from a Network of Cosmic Strings*, *Phys. Rev. D* **99** (2019) 063529 [1901.03312].

[195] J. Preskill, M.B. Wise and F. Wilczek, *Cosmology of the Invisible Axion*, *Phys. Lett. B* **120** (1983) 127.

[196] L.F. Abbott and P. Sikivie, *A Cosmological Bound on the Invisible Axion*, *Phys. Lett. B* **120** (1983) 133.

[197] M. Dine, W. Fischler and M. Srednicki, *A Simple Solution to the Strong CP Problem with a Harmless Axion*, *Phys. Lett. B* **104** (1981) 199.

[198] M. Dine and W. Fischler, *The Not So Harmless Axion*, *Phys. Lett. B* **120** (1983) 137.

[199] R.T. Co, L.J. Hall and K. Harigaya, *Axion Kinetic Misalignment Mechanism*, *Phys. Rev. Lett.* **124** (2020) 251802 [1910.14152].

[200] C.-F. Chang and Y. Cui, *New Perspectives on Axion Misalignment Mechanism*, *Phys. Rev. D* **102** (2020) 015003 [1911.11885].

[201] N. Fonseca, E. Morgante, R. Sato and G. Servant, *Relaxion Fluctuations (Self-stopping Relaxion) and Overview of Relaxion Stopping Mechanisms*, *JHEP* **05** (2020) 080 [1911.08473].

[202] N. Fonseca, E. Morgante, R. Sato and G. Servant, *Axion fragmentation*, *JHEP* **04** (2020) 010 [1911.08472].

[203] C. Eröncel, R. Sato, G. Servant and P. Sørensen, *ALP dark matter from kinetic fragmentation: opening up the parameter window*, *JCAP* **10** (2022) 053 [2206.14259].

[204] A. Chatrchyan, C. Eröncel, M. Koschnitzke and G. Servant, *ALP dark matter with non-periodic potentials: parametric resonance, halo formation and gravitational signatures*, 2305.03756.

[205] T. Hiramatsu, M. Kawasaki, K. Saikawa and T. Sekiguchi, *Production of dark matter axions from collapse of string-wall systems*, *Phys. Rev. D* **85** (2012) 105020 [1202.5851].

[206] M. Kawasaki, K. Saikawa and T. Sekiguchi, *Axion dark matter from topological defects*, *Phys. Rev. D* **91** (2015) 065014 [1412.0789].

[207] M. Gorghetto and G. Villadoro, *Topological Susceptibility and QCD Axion Mass: QED and NNLO corrections*, *JHEP* **03** (2019) 033 [1812.01008].

[208] M. Gorghetto, E. Hardy and G. Villadoro, *More axions from strings*, *SciPost Phys.* **10** (2021) 050 [2007.04990].

[209] R. Loudon, *The quantum theory of light*, OUP Oxford (2000).

[210] R.J. Glauber, *Coherent and incoherent states of the radiation field*, *Phys. Rev.* **131** (1963) 2766.

[211] E.C.G. Sudarshan, *Equivalence of semiclassical and quantum mechanical descriptions of statistical light beams*, *Phys. Rev. Lett.* **10** (1963) 277.

[212] A. Derevianko, *Detecting dark-matter waves with a network of precision-measurement tools*, *Phys. Rev. A* **97** (2018) 042506 [1605.09717].

[213] J.W. Foster, N.L. Rodd and B.R. Safdi, *Revealing the Dark Matter Halo with Axion Direct Detection*, *Phys. Rev. D* **97** (2018) 123006 [1711.10489].

[214] G.P. Centers et al., *Stochastic fluctuations of bosonic dark matter*, 1905.13650.

[215] M. Lisanti, M. Moschella and W. Terrano, *Stochastic properties of ultralight scalar field gradients*, *Phys. Rev. D* **104** (2021) 055037 [2107.10260].

[216] A.V. Gramolin, A. Wickenbrock, D. Aybas, H. Bekker, D. Budker, G.P. Centers et al., *Spectral signatures of axionlike dark matter*, *Phys. Rev. D* **105** (2022) 035029 [2107.11948].

[217] E. Madelung, *Quantum theory in hydrodynamical form*, *z. Phys* **40** (1927) 322.

[218] R. Feynman, R. Leighton and M. Sands, *The feynman lectures on physics addison-wesley, Reading, Ma* **1** (1963) 1.

[219] B. Schwabe, J.C. Niemeyer and J.F. Engels, *Simulations of solitonic core mergers in ultralight axion dark matter cosmologies*, *Phys. Rev. D* **94** (2016) 043513 [1606.05151].

[220] P. Mocz, M. Vogelsberger, V.H. Robles, J. Zavala, M. Boylan-Kolchin, A. Fialkov et al., *Galaxy formation with BECDM – I. Turbulence and relaxation of idealized haloes*, *Mon. Not. Roy. Astron. Soc.* **471** (2017) 4559 [1705.05845].

[221] M. Kamionkowski and A.R. Liddle, *The Dearth of halo dwarf galaxies: Is there power on short scales?*, *Phys. Rev. Lett.* **84** (2000) 4525 [astro-ph/9911103].

[222] N. Bar, K. Blum, J. Eby and R. Sato, *Ultralight dark matter in disk galaxies*, *Phys. Rev. D* **99** (2019) 103020 [1903.03402].

[223] P.-H. Chavanis, *Mass-radius relation of Newtonian self-gravitating Bose-Einstein condensates with short-range interactions: I. Analytical results*, *Phys. Rev. D* **84** (2011) 043531 [1103.2050].

[224] P.H. Chavanis and L. Delfini, *Mass-radius relation of Newtonian self-gravitating Bose-Einstein condensates with short-range interactions: II. Numerical results*, *Phys. Rev. D* **84** (2011) 043532 [1103.2054].

[225] R. RUFFINI and S. BONAZZOLA, *Systems of self-gravitating particles in general relativity and the concept of an equation of state*, *Phys. Rev.* **187** (1969) 1767.

[226] N. Bar, D. Blas, K. Blum and S. Sibiryakov, *Galactic rotation curves versus ultralight dark matter: Implications of the soliton-host halo relation*, *Phys. Rev. D* **98** (2018) 083027 [1805.00122].

[227] N. Bar, K. Blum and C. Sun, *Galactic rotation curves versus ultralight dark matter: A systematic comparison with SPARC data*, *Phys. Rev. D* **105** (2022) 083015 [2111.03070].

[228] N. Bar, K. Blum, T. Lacroix and P. Panci, *Looking for ultralight dark matter near supermassive black holes*, *JCAP* **07** (2019) 045 [1905.11745].

[229] S. Chandrasekhar, *Dynamical friction. i. general considerations: the coefficient of dynamical friction*, *Astrophysical Journal* **97** (1943) 255.

[230] S. Chandrasekhar, *Dynamical friction. ii. the rate of escape of stars from clusters and the evidence for the operation of dynamical friction*, *Astrophysical journal* **97** (1943) 263.

[231] S. Chandrasekhar, *Dynamical friction. iii. a more exact theory of the rate of escape of stars from clusters*, *Astrophysical Journal* **98** (1943) 54.

[232] X. Du, B. Schwabe, J.C. Niemeyer and D. Bürger, *Tidal disruption of fuzzy dark matter subhalo cores*, *Phys. Rev. D* **97** (2018) 063507 [1801.04864].

[233] L. Lancaster, C. Giovanetti, P. Mocz, Y. Kahn, M. Lisanti and D.N. Spergel, *Dynamical Friction in a Fuzzy Dark Matter Universe*, *JCAP* **01** (2020) 001 [1909.06381].

[234] SIMONS OBSERVATORY collaboration, *The Simons Observatory: Science goals and forecasts*, *JCAP* **02** (2019) 056 [1808.07445].

[235] CMB-S4 collaboration, *CMB-S4 Science Book, First Edition*, 1610.02743.

[236] N. Sehgal et al., *CMB-HD: An Ultra-Deep, High-Resolution Millimeter-Wave Survey Over Half the Sky*, 1906.10134.

[237] G.S. Farren, D. Grin, A.H. Jaffe, R. Hložek and D.J.E. Marsh, *Ultralight axions and the kinetic Sunyaev-Zel'dovich effect*, *Phys. Rev. D* **105** (2022) 063513 [2109.13268].

[238] S. Lee, G.-C. Liu and K.-W. Ng, *Cosmic Birefringence Fluctuations and Cosmic Microwave Background B-mode Polarization*, *Phys. Lett. B* **746** (2015) 406 [1403.5585].

[239] G. Sigl and P. Trivedi, *Axion-like Dark Matter Constraints from CMB Birefringence*, 1811.07873.

[240] S. Mukherjee, R. Khatri and B.D. Wandelt, *Polarized anisotropic spectral distortions of the CMB: Galactic and extragalactic constraints on photon-axion conversion*, *JCAP* **04** (2018) 045 [1801.09701].

[241] S. Mukherjee, R. Khatri and B.D. Wandelt, *Constraints on non-resonant photon-axion conversion from the Planck satellite data*, *JCAP* **06** (2019) 031 [1811.11177].

[242] M.A. Fedderke, P.W. Graham and S. Rajendran, *Axion Dark Matter Detection with CMB Polarization*, *Phys. Rev. D* **100** (2019) 015040 [1903.02666].

[243] K.K. Rogers and H.V. Peiris, *Strong Bound on Canonical Ultralight Axion Dark Matter from the Lyman-Alpha Forest*, *Phys. Rev. Lett.* **126** (2021) 071302 [2007.12705].

[244] E. Armengaud, N. Palanque-Delabrouille, C. Yèche, D.J.E. Marsh and J. Baur, *Constraining the mass of light bosonic dark matter using SDSS Lyman-α forest*, *Mon. Not. Roy. Astron. Soc.* **471** (2017) 4606 [1703.09126].

[245] T. Kobayashi, R. Murgia, A. De Simone, V. Iršič and M. Viel, *Lyman-α constraints on ultralight scalar dark matter: Implications for the early and late universe*, *Phys. Rev. D* **96** (2017) 123514 [1708.00015].

[246] L.B. Newburgh et al., *HIRAX: A Probe of Dark Energy and Radio Transients*, *Proc. SPIE Int. Soc. Opt. Eng.* **9906** (2016) 99065X [1607.02059].

[247] A. Weltman et al., *Fundamental physics with the Square Kilometre Array*, *Publ. Astron. Soc. Austral.* **37** (2020) e002 [1810.02680].

[248] J.B. Bauer, D.J.E. Marsh, R. Hložek, H. Padmanabhan and A. Laguë, *Intensity Mapping as a Probe of Axion Dark Matter*, *Mon. Not. Roy. Astron. Soc.* **500** (2020) 3162 [2003.09655].

[249] HERA collaboration, *HERA Phase I Limits on the Cosmic 21 cm Signal: Constraints on Astrophysics and Cosmology during the Epoch of Reionization*, *Astrophys. J.* **924** (2022) 51 [2108.07282].

[250] S.C. Hotinli, D.J.E. Marsh and M. Kamionkowski, *Probing ultralight axions with the 21-cm signal during cosmic dawn*, *Phys. Rev. D* **106** (2022) 043529 [2112.06943].

[251] B. Bozek, D.J.E. Marsh, J. Silk and R.F.G. Wyse, *Galaxy UV-luminosity function and reionization constraints on axion dark matter*, *Mon. Not. Roy. Astron. Soc.* **450** (2015) 209 [1409.3544].

[252] DES collaboration, *Milky Way Satellite Census. III. Constraints on Dark Matter Properties from Observations of Milky Way Satellite Galaxies*, *Phys. Rev. Lett.* **126** (2021) 091101 [2008.00022].

[253] J.-W. Hsueh, W. Enzi, S. Vegetti, M. Auger, C.D. Fassnacht, G. Despali et al., *SHARP – VII. New constraints on the dark matter free-streaming properties and substructure abundance from gravitationally lensed quasars*, *Mon. Not. Roy. Astron. Soc.* **492** (2020) 3047 [1905.04182].

[254] D. Gilman, S. Birrer, A. Nierenberg, T. Treu, X. Du and A. Benson, *Warm dark matter chills out: constraints on the halo mass function and the free-streaming length of dark matter with eight quadruple-image strong gravitational lenses*, *Mon. Not. Roy. Astron. Soc.* **491** (2020) 6077 [1908.06983].

[255] K. Schutz, *Subhalo mass function and ultralight bosonic dark matter*, *Phys. Rev. D* **101** (2020) 123026 [2001.05503].

[256] A. Khmelnitsky and V. Rubakov, *Pulsar timing signal from ultralight scalar dark matter*, *JCAP* **02** (2014) 019 [1309.5888].

[257] R. Kato and J. Soda, *Search for ultralight scalar dark matter with NANOGrav pulsar timing arrays*, *JCAP* **09** (2020) 036 [1904.09143].

[258] N.K. Porayko et al., *Parkes Pulsar Timing Array constraints on ultralight scalar-field dark matter*, *Phys. Rev. D* **98** (2018) 102002 [1810.03227].

[259] NANOGrav collaboration, *The NANOGrav 12.5 yr Data Set: Search for an Isotropic Stochastic Gravitational-wave Background*, *Astrophys. J. Lett.* **905** (2020) L34 [2009.04496].

[260] NANOGrav collaboration, *The NANOGrav 12.5 yr Data Set: Observations and Narrowband Timing of 47 Millisecond Pulsars*, *Astrophys. J. Suppl.* **252** (2021) 4 [2005.06490].

[261] NANOGrav collaboration, *The NANOGrav 12.5 yr Data Set: Wideband Timing of 47 Millisecond Pulsars*, *Astrophys. J. Suppl.* **252** (2021) 5 [2005.06495].

[262] S. Sun, X.-Y. Yang and Y.-L. Zhang, *Pulsar timing residual induced by wideband ultralight dark matter with spin 0,1,2*, *Phys. Rev. D* **106** (2022) 066006 [2112.15593].

[263] D.J.E. Marsh and J.C. Niemeyer, *Strong Constraints on Fuzzy Dark Matter from Ultrafaint Dwarf Galaxy Eridanus II*, *Phys. Rev. Lett.* **123** (2019) 051103 [1810.08543].

[264] J.A. Dror, R. Laha and T. Opferkuch, *Probing muonic forces with neutron star binaries*, *Phys. Rev. D* **102** (2020) 023005 [1909.12845].

[265] T. Kumar Poddar, S. Mohanty and S. Jana, *Constraints on long range force from perihelion precession of planets in a gauged $L_e - L_{\mu,\tau}$ scenario*, *Eur. Phys. J. C* **81** (2021) 286 [2002.02935].

[266] J.A. Grifols and E. Masso, *Constraints on Finite Range Baryonic and Leptonic Forces From Stellar Evolution*, *Phys. Lett. B* **173** (1986) 237.

[267] S. Hoffmann, *Paraphotons and Axions: Similarities in Stellar Emission and Detection*, *Phys. Lett. B* **193** (1987) 117.

[268] J.A. Grifols, E. Masso and S. Peris, *Energy Loss From the Sun and RED Giants: Bounds on Short Range Baryonic and Leptonic Forces*, *Mod. Phys. Lett. A* **4** (1989) 311.

[269] G.G. Raffelt, *Stars as laboratories for fundamental physics: The astrophysics of neutrinos, axions, and other weakly interacting particles*, University of Chicago press (1996).

[270] J. Redondo and G. Raffelt, *Solar constraints on hidden photons re-visited*, *JCAP* **08** (2013) 034 [1305.2920].

[271] H. An, M. Pospelov and J. Pradler, *New stellar constraints on dark photons*, *Phys. Lett. B* **725** (2013) 190 [1302.3884].

[272] E. Hardy and R. Lasenby, *Stellar cooling bounds on new light particles: plasma mixing effects*, *JHEP* **02** (2017) 033 [1611.05852].

[273] A. Caputo, G. Raffelt and E. Vitagliano, *Muonic boson limits: Supernova redux*, *Phys. Rev. D* **105** (2022) 035022 [2109.03244].

[274] N. Dalal and A. Kravtsov, *Excluding fuzzy dark matter with sizes and stellar kinematics of ultrafaint dwarf galaxies*, *Phys. Rev. D* **106** (2022) 063517 [2203.05750].

[275] M.A. Fedderke, P.W. Graham, D.F.J. Kimball and S. Kalia, *Earth as a transducer for dark-photon dark-matter detection*, *Phys. Rev. D* **104** (2021) 075023 [2106.00022].

[276] M.A. Fedderke, P.W. Graham, D.F. Jackson Kimball and S. Kalia, *Search for dark-photon dark matter in the SuperMAG geomagnetic field dataset*, *Phys. Rev. D* **104** (2021) 095032 [2108.08852].

[277] A. Arza, M.A. Fedderke, P.W. Graham, D.F.J. Kimball and S. Kalia, *Earth as a transducer for axion dark-matter detection*, *Phys. Rev. D* **105** (2022) 095007 [2112.09620].

[278] H. Liu, B.D. Elwood, M. Evans and J. Thaler, *Searching for Axion Dark Matter with Birefringent Cavities*, *Phys. Rev. D* **100** (2019) 023548 [1809.01656].

[279] M. Lawson, A.J. Millar, M. Pancaldi, E. Vitagliano and F. Wilczek, *Tunable axion plasma haloscopes*, *Phys. Rev. Lett.* **123** (2019) 141802 [1904.11872].

[280] G.B. Gelmini, A.J. Millar, V. Takhistov and E. Vitagliano, *Probing dark photons with plasma haloscopes*, *Phys. Rev. D* **102** (2020) 043003 [2006.06836].

[281] J.B. Pendry, A. Holden, D. Robbins and W. Stewart, *Low frequency plasmons in thin-wire structures*, *Journal of Physics: Condensed Matter* **10** (1998) 4785.

[282] M. Wooten, A. Droster, A. Kenany, D. Sun, S.M. Lewis and K. van Bibber, *Exploration of Wire Array Metamaterials for the Plasma Axion Haloscope*, 2203.13945.

[283] P. Sikivie, N. Sullivan and D.B. Tanner, *Proposal for Axion Dark Matter Detection Using an LC Circuit*, *Phys. Rev. Lett.* **112** (2014) 131301 [1310.8545].

[284] S. Chaudhuri, P.W. Graham, K. Irwin, J. Mardon, S. Rajendran and Y. Zhao, *Radio for hidden-photon dark matter detection*, *Phys. Rev. D* **92** (2015) 075012 [1411.7382].

[285] M. Silva-Feaver et al., *Design Overview of DM Radio Pathfinder Experiment*, *IEEE Trans. Appl. Supercond.* **27** (2017) 1400204 [1610.09344].

[286] DMRADIO collaboration, *Projected sensitivity of DMRadio-m3: A search for the QCD axion below 1 μeV*, *Phys. Rev. D* **106** (2022) 103008 [2204.13781].

[287] C.P. Salemi et al., *Search for Low-Mass Axion Dark Matter with ABRACADABRA-10 cm*, *Phys. Rev. Lett.* **127** (2021) 081801 [2102.06722].

[288] B.T. McAllister, M. Goryachev, J. Bourhill, E.N. Ivanov and M.E. Tobar, *Broadband Axion Dark Matter Haloscopes via Electric Sensing*, 1803.07755.

[289] A. Berlin, R.T. D'Agnolo, S.A.R. Ellis and K. Zhou, *Heterodyne broadband detection of axion dark matter*, *Phys. Rev. D* **104** (2021) L111701 [2007.15656].

[290] R. Lasenby, *Microwave cavity searches for low-frequency axion dark matter*, *Phys. Rev. D* **102** (2020) 015008 [1912.11056].

[291] Y.V. Stadnik and V.V. Flambaum, *Searching for dark matter and variation of fundamental constants with laser and maser interferometry*, *Phys. Rev. Lett.* **114** (2015) 161301 [1412.7801].

[292] Y.V. Stadnik and V.V. Flambaum, *Enhanced effects of variation of the fundamental constants in laser interferometers and application to dark matter detection*, *Phys. Rev. A* **93** (2016) 063630 [1511.00447].

[293] S.M. Brewer, J.-S. Chen, A.M. Hankin, E.R. Clements, C.-w. Chou, D.J. Wineland et al., *Al+ 27 quantum-logic clock with a systematic uncertainty below 10- 18*, *Physical review letters* **123** (2019) 033201.

[294] A.D. Ludlow, M.M. Boyd, J. Ye, E. Peik and P.O. Schmidt, *Optical atomic clocks*, *Reviews of Modern Physics* **87** (2015) 637.

[295] K. Van Tilburg, N. Leefer, L. Bougas and D. Budker, *Search for ultralight scalar dark matter with atomic spectroscopy*, *Phys. Rev. Lett.* **115** (2015) 011802 [1503.06886].

[296] A. Hees, J. Guéna, M. Abgrall, S. Bize and P. Wolf, *Searching for an oscillating massive scalar field as a dark matter candidate using atomic hyperfine frequency comparisons*, *Phys. Rev. Lett.* **117** (2016) 061301 [1604.08514].

[297] K. Beloy et al., *Frequency Ratio Measurements with 18-digit Accuracy Using a Network of Optical Clocks*, 2005.14694.

[298] C.J. Kennedy, E. Oelker, J.M. Robinson, T. Bothwell, D. Kedar, W.R. Milner et al., *Precision Metrology Meets Cosmology: Improved Constraints on Ultralight Dark Matter from Atom-Cavity Frequency Comparisons*, *Phys. Rev. Lett.* **125** (2020) 201302 [2008.08773].

[299] M. Abe, P. Adamson, M. Borcean, D. Bortoletto, K. Bridges, S.P. Carman et al., *Matter-wave atomic gradiometer interferometric sensor (magis-100)*, *Quantum Science and Technology* **6** (2021) 044003.

[300] A.A. Geraci, C. Bradley, D. Gao, J. Weinstein and A. Derevianko, *Searching for Ultralight Dark Matter with Optical Cavities*, *Phys. Rev. Lett.* **123** (2019) 031304 [1808.00540].

[301] S.M. Vermeulen et al., *Direct limits for scalar field dark matter from a gravitational-wave detector*, 2103.03783.

[302] L. Aiello, J.W. Richardson, S.M. Vermeulen, H. Grote, C. Hogan, O. Kwon et al., *Constraints on scalar field dark matter from co-located Michelson interferometers*, 2108.04746.

[303] H. Grote and Y.V. Stadnik, *Novel signatures of dark matter in laser-interferometric gravitational-wave detectors*, *Phys. Rev. Res.* **1** (2019) 033187 [1906.06193].

[304] E.A. Shaw, M.P. Ross, C.A. Hagedorn, E.G. Adelberger and J.H. Gundlach, *Torsion-balance search for ultralow-mass bosonic dark matter*, *Phys. Rev. D* **105** (2022) 042007 [2109.08822].

[305] P. Touboul et al., *MICROSCOPE Mission: First Results of a Space Test of the Equivalence Principle*, *Phys. Rev. Lett.* **119** (2017) 231101 [1712.01176].

[306] D. Carney et al., *Mechanical Quantum Sensing in the Search for Dark Matter*, *Quantum Sci. Technol.* **6** (2021) 024002 [2008.06074].

[307] A. Branca et al., *Search for an Ultralight Scalar Dark Matter Candidate with the AURIGA Detector*, *Phys. Rev. Lett.* **118** (2017) 021302 [1607.07327].

[308] E. Savalle, A. Hees, F. Frank, E. Cantin, P.-E. Pottie, B.M. Roberts et al., *Searching for Dark Matter with an Optical Cavity and an Unequal-Delay Interferometer*, *Phys. Rev. Lett.* **126** (2021) 051301 [2006.07055].

[309] J. Manley, M.D. Chowdhury, D. Grin, S. Singh and D.J. Wilson, *Searching for vector dark matter with an optomechanical accelerometer*, *Phys. Rev. Lett.* **126** (2021) 061301 [2007.04899].

[310] P.W. Graham, D.E. Kaplan, J. Mardon, S. Rajendran and W.A. Terrano, *Dark Matter Direct Detection with Accelerometers*, *Phys. Rev. D* **93** (2016) 075029 [1512.06165].

[311] I.M. Bloch, Y. Hochberg, E. Kuflik and T. Volansky, *Axion-like Relics: New Constraints from Old Comagnetometer Data*, *JHEP* **01** (2020) 167 [1907.03767].

[312] NASDUCK collaboration, *NASDUCK: New Constraints on Axion-like Dark Matter from Floquet Quantum Detector*, 5, 2021 [2105.04603].

[313] T. Kornack, R. Ghosh and M.V. Romalis, *Nuclear spin gyroscope based on an atomic comagnetometer*, *Physical review letters* **95** (2005) 230801.

[314] T. Wu, J.W. Blanchard, D.F.J. Kimball, M. Jiang and D. Budker, *Nuclear-spin comagnetometer based on a liquid of identical molecules*, *Physical Review Letters* **121** (2018) 023202.

[315] Z. Wang, X. Peng, R. Zhang, H. Luo, J. Li, Z. Xiong et al., *Single-Species Atomic Comagnetometer Based on ^{87}Rb Atoms*, *Phys. Rev. Lett.* **124** (2020) 193002 [1812.06830].

[316] D. Budker, P.W. Graham, M. Ledbetter, S. Rajendran and A. Sushkov, *Proposal for a Cosmic Axion Spin Precession Experiment (CASPEr)*, *Phys. Rev. X* **4** (2014) 021030 [1306.6089].

[317] S. Pustelny et al., *The Global Network of Optical Magnetometers for Exotic physics (GNOME): A novel scheme to search for physics beyond the Standard Model*, *Annalen Phys.* **525** (2013) 659 [1303.5524].

[318] S. Afach et al., *What can a GNOME do? Search targets for the Global Network of Optical Magnetometers for Exotic physics searches*, 2305.01785.

[319] S. Afach et al., *Characterization of the Global Network of Optical Magnetometers to search for Exotic Physics (GNOME)*, *Phys. Dark Univ.* **22** (2018) 162 [1807.09391].

[320] T. Ikeda, A. Ito, K. Miuchi, J. Soda, H. Kurashige and Y. Shikano, *Axion search with quantum nondemolition detection of magnons*, *Phys. Rev. D* **105** (2022) 102004 [2102.08764].

[321] Y.V. Stadnik and V.V. Flambaum, *Axion-induced effects in atoms, molecules, and nuclei: Parity nonconservation, anapole moments, electric dipole moments, and spin-gravity and spin-axion momentum couplings*, *Phys. Rev. D* **89** (2014) 043522 [1312.6667].

[322] T.S. Roussy et al., *Experimental Constraint on Axionlike Particles over Seven Orders of Magnitude in Mass*, *Phys. Rev. Lett.* **126** (2021) 171301 [2006.15787].

[323] S.P. Chang, S. Haciomeroglu, O. Kim, S. Lee, S. Park and Y.K. Semertzidis, *Axionlike dark matter search using the storage ring EDM method*, *Phys. Rev. D* **99** (2019) 083002 [1710.05271].

[324] H. Kim and G. Perez, *Oscillations of atomic energy levels induced by QCD axion dark matter*, 2205.12988.

[325] L.D. Landau and E.M. Lifshits, *Quantum Mechanics: Non-Relativistic Theory*, vol. v.3 of *Course of Theoretical Physics*, Butterworth-Heinemann, Oxford (1991).

[326] N. Arkani-Hamed, D.P. Finkbeiner, T.R. Slatyer and N. Weiner, *A Theory of Dark Matter*, *Phys. Rev. D* **79** (2009) 015014 [0810.0713].

[327] S. Aharony, N. Akerman, R. Ozeri, G. Perez, I. Savoray and R. Shaniv, *Constraining Rapidly Oscillating Scalar Dark Matter Using Dynamic Decoupling*, *Phys. Rev. D* **103** (2021) 075017 [1902.02788].

[328] W.M. Campbell, B.T. McAllister, M. Goryachev, E.N. Ivanov and M.E. Tobar, *Searching for Scalar Dark Matter via Coupling to Fundamental Constants with Photonic, Atomic and Mechanical Oscillators*, *Phys. Rev. Lett.* **126** (2021) 071301 [2010.08107].

[329] R. Oswald et al., *Search for oscillations of fundamental constants using molecular spectroscopy*, 2111.06883.

[330] A. Arvanitaki, P.W. Graham, J.M. Hogan, S. Rajendran and K. Van Tilburg, *Search for light scalar dark matter with atomic gravitational wave detectors*, *Phys. Rev. D* **97** (2018) 075020 [1606.04541].

[331] L. Badurina, D. Blas and C. McCabe, *Refined ultralight scalar dark matter searches with compact atom gradiometers*, *Phys. Rev. D* **105** (2022) 023006 [2109.10965].

[332] J.W. Foster, Y. Kahn, R. Nguyen, N.L. Rodd and B.R. Safdi, *Dark Matter Interferometry*, *Phys. Rev. D* **103** (2021) 076018 [2009.14201].

[333] Y. Chen, M. Jiang, J. Shu, X. Xue and Y. Zeng, *Dissecting Axion and Dark Photon with A Network of Vector Sensors*, 2111.06732.

[334] E.P. Wigner, *On the quantum correction for thermodynamic equilibrium*, *Phys. Rev.* **40** (1932) 749.

[335] R. Schönrich, J. Binney and W. Dehnen, *Local kinematics and the local standard of rest*, *Monthly Notices of the Royal Astronomical Society* **403** (2010) 1829 [https://academic.oup.com/mnras/article-pdf/403/4/1829/18575828/mnras0403-1829.pdf

[336] N.W. Evans, R.M. Hafner and P.T. de Zeeuw, *Simple three-integral scale-free galaxy models*, *Mon. Not. Roy. Astron. Soc.* **286** (1997) 315 [astro-ph/9611162].

[337] M.G. Abadi, J.F. Navarro, M. Steinmetz and V.R. Eke, *Simulations of galaxy formation in a λ cold dark matter universe. ii. the fine structure of simulated galactic disks*, *The Astrophysical Journal* **597** (2003) 21.

[338] S. Kazantzidis, J.S. Bullock, A.R. Zentner, A.V. Kravtsov and L.A. Moustakas, *Cold dark matter substructure and galactic disks. i. morphological signatures of hierarchical satellite accretion*, *The Astrophysical Journal* **688** (2008) 254.

[339] Á. Villalobos and A. Helmi, *Simulations of minor mergers–i. general properties of thick discs*, *Monthly Notices of the Royal Astronomical Society* **391** (2008) 1806.

[340] H.-W. Rix and J. Bovy, *The milky way's stellar disk: Mapping and modeling the galactic disk*, *The Astronomy and Astrophysics Review* **21** (2013) 1.

[341] P. Ullio, H. Zhao and M. Kamionkowski, *A Dark matter spike at the galactic center?*, *Phys. Rev. D* **64** (2001) 043504 [astro-ph/0101481].

[342] D. Merritt, *Single and binary black holes and their influence on nuclear structure*, in *Carnegie Observatories Centennial Symposium. 1. Coevolution of Black Holes and Galaxies*, 1, 2003 [astro-ph/0301257].

[343] L. Sadeghian, F. Ferrer and C.M. Will, *Dark matter distributions around massive black holes: A general relativistic analysis*, *Phys. Rev. D* **88** (2013) 063522 [1305.2619].

[344] J.E. Greene, J. Strader and L.C. Ho, *Intermediate-Mass Black Holes*, *Ann. Rev. Astron. Astrophys.* **58** (2020) 257 [1911.09678].

[345] B. Diemer and M. Joyce, *An accurate physical model for halo concentrations*, *Astrophys. J.* **871** (2019) 168 [1809.07326].

[346] J. Veltmaat and J.C. Niemeyer, *Cosmological particle-in-cell simulations with ultralight axion dark matter*, *Phys. Rev. D* **94** (2016) 123523 [1608.00802].

[347] J. Veltmaat, J.C. Niemeyer and B. Schwabe, *Formation and structure of ultralight bosonic dark matter halos*, *Phys. Rev. D* **98** (2018) 043509 [1804.09647].

[348] H.Y.J. Chan, E.G.M. Ferreira, S. May, K. Hayashi and M. Chiba, *The diversity of core–halo structure in the fuzzy dark matter model*, *Mon. Not. Roy. Astron. Soc.* **511** (2022) 943 [2110.11882].

[349] L. Spitzer, *Dynamical evolution of globular clusters* (1987).

[350] S. Weinberg, *Lectures on quantum mechanics*, Cambridge University Press (2015).

[351] D. Baumann, H.S. Chia, J. Stout and L. ter Haar, *The Spectra of Gravitational Atoms*, *JCAP* **12** (2019) 006 [1908.10370].

[352] S.L. Detweiler, *KLEIN-GORDON EQUATION AND ROTATING BLACK HOLES*, *Phys. Rev. D* **22** (1980) 2323.

[353] L. Annulli, V. Cardoso and R. Vicente, *Stirred and shaken: Dynamical behavior of boson stars and dark matter cores*, *Phys. Lett. B* **811** (2020) 135944 [2007.03700].

[354] L. Annulli, V. Cardoso and R. Vicente, *Response of ultralight dark matter to supermassive black holes and binaries*, *Phys. Rev. D* **102** (2020) 063022 [2009.00012].

[355] P.-H. Chavanis, *Landau equation for self-gravitating classical and quantum particles: application to dark matter*, *Eur. Phys. J. Plus* **136** (2021) 703 [2012.12858].

[356] P.S. Cole, G. Bertone, A. Coogan, D. Gaggero, T. Karydas, B.J. Kavanagh et al., *Disks, spikes, and clouds: distinguishing environmental effects on BBH gravitational waveforms*, 2211.01362.

[357] N. Becker, L. Sagunski, L. Prinz and S. Rastgoo, *Circularization versus eccentrification in intermediate mass ratio inspirals inside dark matter spikes*, *Phys. Rev. D* **105** (2022) 063029 [2112.09586].

[358] E. National Academies of Sciences, Medicine et al., *Pathways to Discovery in Astronomy and Astrophysics for the 2020s* (2021).

[359] J.M. Cline, S. Gao, F. Guo, Z. Lin, S. Liu, M. Puel et al., *Blazar constraints on neutrino-dark matter scattering*, 2209.02713.

[360] F. Ferrer, G. Herrera and A. Ibarra, *New constraints on the dark matter-neutrino and dark matter-photon scattering cross sections from TXS 0506+056*, 2209.06339.

[361] M.H. Chan and C.M. Lee, *Indirect Evidence for Dark Matter Density Spikes around Stellar-Mass Black Holes*, 2212.05664.

[362] X.-H. Fan, C.L. Carilli and B.G. Keating, *Observational constraints on cosmic reionization*, *Ann. Rev. Astron. Astrophys.* **44** (2006) 415 [astro-ph/0602375].

[363] D.J. Mortlock et al., *A luminous quasar at a redshift of z = 7.085*, *Nature* **474** (2011) 616 [1106.6088].

[364] E. Banados et al., *An 800-million-solar-mass black hole in a significantly neutral Universe at redshift 7.5*, *Nature* **553** (2018) 473 [1712.01860].

[365] V.F. Baldassare, A.E. Reines, E. Gallo and J.E. Greene, *A 50,000 m⊙ solar mass black hole in the nucleus of rgg 118*, *The Astrophysical Journal Letters* **809** (2015) L14.

[366] V.F. Baldassare, M. Geha and J. Greene, *Identifying agns in low-mass galaxies via long-term optical variability*, *The Astrophysical Journal* **868** (2018) 152.

[367] E.C. Moran, K. Shahinyan, H.R. Sugarman, D.O. Vélez and M. Eracleous, *Black holes at the centers of nearby dwarf galaxies*, *The Astronomical Journal* **148** (2014) 136.

[368] P. Madau and M.J. Rees, *Massive black holes as Population III remnants*, *Astrophys. J. Lett.* **551** (2001) L27 [astro-ph/0101223].

[369] S.M. Koushiappas, J.S. Bullock and A. Dekel, *Massive black hole seeds from low angular momentum material*, *Mon. Not. Roy. Astron. Soc.* **354** (2004) 292 [astro-ph/0311487].

[370] S.F.P. Zwart and S.L. McMillan, *The runaway growth of intermediate-mass black holes in dense star clusters*, *The Astrophysical Journal* **576** (2002) 899.

[371] D. Hils and P.L. Bender, *Gradual approach to coalescence for compact stars orbiting massive black holes*, *The Astrophysical Journal* **445** (1995) L7.

[372] C. Hopman and T. Alexander, *The orbital statistics of stellar inspiral and relaxation near a massive black hole: characterizing gravitational wave sources*, *The Astrophysical Journal* **629** (2005) 362.

[373] P. Ivanov, *On the formation rate of close binaries consisting of a super-massive black hole and a white dwarf*, *Monthly Notices of the Royal Astronomical Society* **336** (2002) 373.

[374] S. Sigurdsson and M.J. Rees, *Capture of stellar mass compact objects by massive black holes in galactic cusps*, *Monthly Notices of the Royal Astronomical Society* **284** (1997) 318.

[375] P. Amaro-Seoane, J.R. Gair, M. Freitag, M. Coleman Miller, I. Mandel, C.J. Cutler et al., *Astrophysics, detection and science applications of intermediate- and extreme mass-ratio inspirals*, *Class. Quant. Grav.* **24** (2007) R113 [astro-ph/0703495].

[376] D. Merritt, M. Milosavljevic, L. Verde and R. Jimenez, *Dark matter spikes and annihilation radiation from the galactic center*, *Phys. Rev. Lett.* **88** (2002) 191301 [astro-ph/0201376].

[377] D. Merritt, *Evolution of the dark matter distribution at the galactic center*, *Phys. Rev. Lett.* **92** (2004) 201304 [astro-ph/0311594].

[378] G. Bertone, A.R. Zentner and J. Silk, *A new signature of dark matter annihilations: gamma-rays from intermediate-mass black holes*, *Phys. Rev. D* **72** (2005) 103517 [astro-ph/0509565].

[379] G. Bertone, M. Fornasa, M. Taoso and A. Zentner, *Dark Matter Annihilation around Intermediate Mass Black Holes: an update*, *New J. Phys.* **11** (2009) 105016 [0905.4736].

[380] M. Maggiore, *Gravitational Waves. Vol. 1: Theory and Experiments*, Oxford Master Series in Physics, Oxford University Press (2007).

[381] M.D. Weinberg, *Self-gravitating response of a spherical galaxy to sinking satellites*, *Monthly Notices of the Royal Astronomical Society* **239** (1989) 549.

[382] M. Fujii, Y. Funato and J. Makino, *Dynamical friction on satellite galaxies*, *Publ. Astron. Soc. Jap.* **58** (2006) 743 [astro-ph/0511651].

[383] W.G. Unruh, *Absorption Cross-Section of Small Black Holes*, *Phys. Rev. D* **14** (1976) 3251.

[384] D. Traykova, K. Clough, T. Helfer, E. Berti, P.G. Ferreira and L. Hui, *Dynamical friction from scalar dark matter in the relativistic regime*, *Phys. Rev. D* **104** (2021) 103014 [2106.08280].

[385] R. Vicente and V. Cardoso, *Dynamical friction of black holes in ultralight dark matter*, *Phys. Rev. D* **105** (2022) 083008 [2201.08854].

[386] T. Robson, N.J. Cornish and C. Liu, *The construction and use of LISA sensitivity curves*, *Class. Quant. Grav.* **36** (2019) 105011 [1803.01944].

[387] B.J. Owen, *Search templates for gravitational waves from inspiraling binaries: Choice of template spacing*, *Phys. Rev. D* **53** (1996) 6749 [gr-qc/9511032].

[388] J.S. Speagle, *dynesty: a dynamic nested sampling package for estimating Bayesian posteriors and evidences*, *Mon. Not. Roy. Astron. Soc.* **493** (2020) 3132 [1904.02180].

[389] E. Seidel and W.-M. Suen, *Formation of solitonic stars through gravitational cooling*, *Phys. Rev. Lett.* **72** (1994) 2516 [gr-qc/9309015].

[390] R. Harrison, I. Moroz and K. Tod, *A numerical study of the schrödinger–newton equations*, *Nonlinearity* **16** (2002) 101.

[391] F.S. Guzman and L.A. Urena-Lopez, *Gravitational cooling of self-gravitating Bose-Condensates*, *Astrophys. J.* **645** (2006) 814 [astro-ph/0603613].

[392] L.S. Collaboration and J. Aasi, *Advanced ligo*, *Class. Quantum Gravity* **32** (2015) 074001.

[393] F. Acernese, M. Agathos, K. Agatsuma, D. Aisa, N. Allemandou, A. Allocca et al., *Advanced virgo: a 2nd generation interferometric gravitational wave detector*, *Classical and Quantum Gravity* **32** (2014) .

[394] T. Akutsu, M. Ando, K. Arai, Y. Arai, S. Araki, A. Araya et al., *Overview of kagra: Detector design and construction history*, *Progress of Theoretical and Experimental Physics* **2021** (2021) 05A101.

[395] M. Maggiore et al., *Science Case for the Einstein Telescope*, *JCAP* **03** (2020) 050 [1912.02622].

[396] C. McCabe, *The Earth's velocity for direct detection experiments*, *JCAP* **02** (2014) 027 [1312.1355].

[397] N. Bar, D. Blas, K. Blum and H. Kim, *Assessing the Fornax globular cluster timing problem in different models of dark matter*, *Phys. Rev. D* **104** (2021) 043021 [2102.11522].

[398] F. D'Eramo and A. Lenoci, *Lower mass bounds on FIMP dark matter produced via freeze-in*, *JCAP* **10** (2021) 045 [2012.01446].